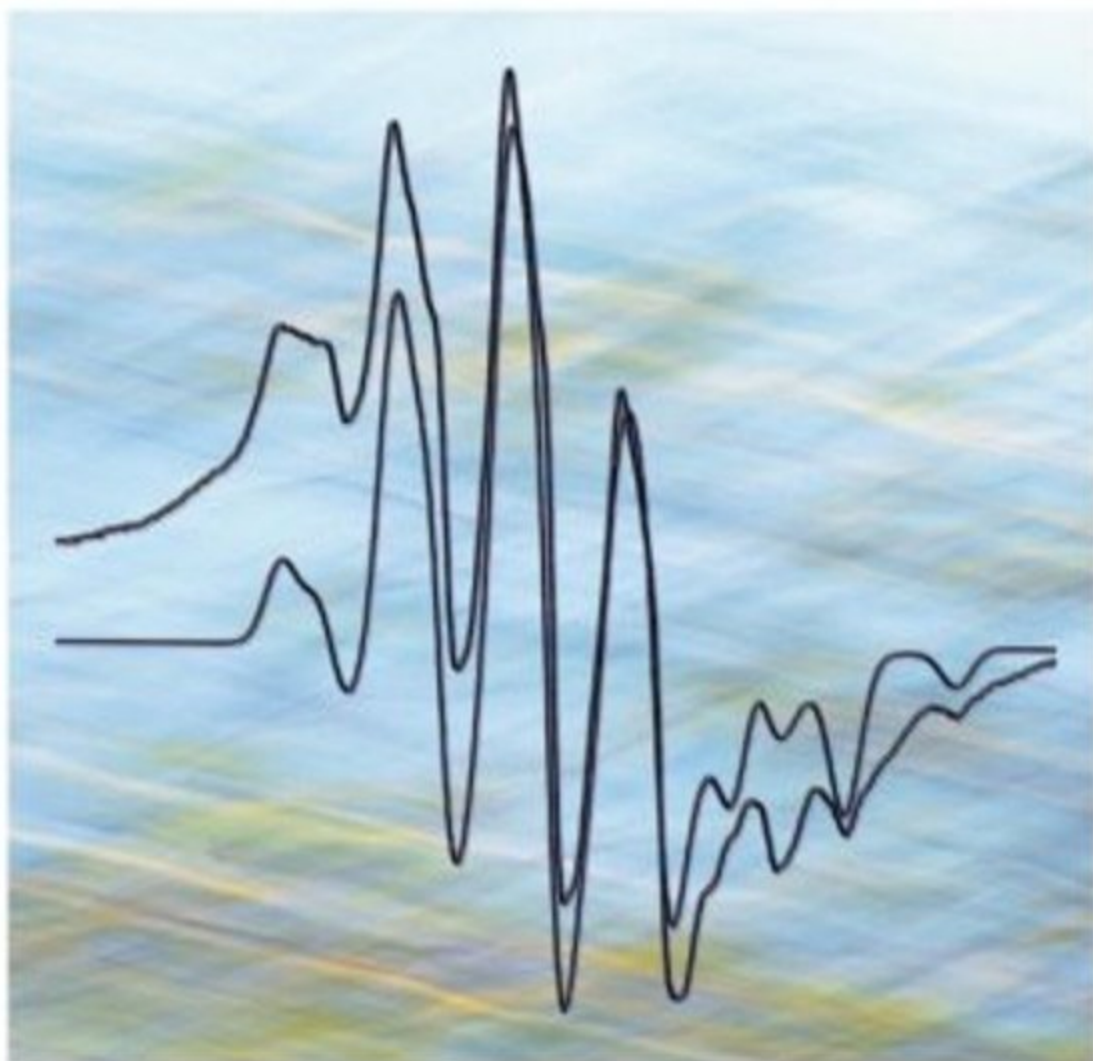Philip H Rieger

Electron Spin Resonance

Analysis and Interpretation

Electron Spin Resonance

Analysis and Interpretation

Electron Spin Resonance

Analysis and Interpretation

Philip H Rieger
Brown University, Providence, RI, USA

Preface

At the time of his death in April, 2004, Professor Philip H. Rieger had nearly finished the manuscript of this book. His intention was to present a monograph summarizing his approach to the field of Electron Spin Resonance using examples and other explanatory material developed during the course of a 40-year career of research and teaching at Brown University. Although the presentation was intended to be at the beginning graduate level, it could also serve as an introduction to the fundamentals of ESR for working research scientists in organometallic chemistry or other areas from which Phil attracted his many research collaborators. It gives the reader a thorough introduction to the analysis and interpretation of CW ESR spectra at X-band (9.5 GHz.) as applied to paramagnetic organic, inorganic and organometallic molecules.

When Professor Rieger first became interested in ESR, commercial instruments were not available. His introduction to the field, as a graduate student with George Fraenkel at Columbia University, took place in one of the few laboratories in the world at the time where ESR equipment had been built. Upon arriving at Brown his first item of business was to design and construct a spectrometer. The instrument was eventually retired once reliable, sensitive commercial instruments became available. Nevertheless, that first spectrometer enabled one of us (ALR) to begin a scientific collaboration that lasted the rest of Phil's life, and the other (RGL) to get his own career started at Brown.

In a preliminary draft of this book Phil wrote the following paragraph explaining its origin:

> This book has been many years in the making. It began with an invitation from Prof. William Trogler to write a chapter on ESR applications for the book *Organometallic Radical Processes* that was published in 1990. There are some strong resemblances to Chapter 4 of the present book. The writing was extended to a handout in 1991 when I was invited to spend a sabbatical year at the University of Bristol. It was extended a bit further when I was invited to give a series of lectures on ESR at the University of Oviedo, still further when I was invited to give some lectures at the University of Edinburgh, and still further in 1999 for a lecture series

at the University of Otago. Meanwhile, I had given a short series of lectures on ESR at Brown University most years as part of a graduate course in Physical Inorganic Chemistry.

In completing Phil's book we have retained the set of examples and explanations, and occasional commentary, as he had intended it. It has, however, been some time since a book on ESR for the non-expert has appeared. We have therefore supplemented his original manuscript in two ways. At the end of Chapter 1 is added an up-to-date list of texts and monographs on ESR which should serve the interested reader as a source of additional treatments of the subject. Secondly, in Appendix 2 we have referenced and given brief descriptions of some advanced ESR methods that have been developed in recent years and applied in various fields, including biochemistry. The modern ESR spectroscopist is now as likely to need an understanding of these techniques as of the classic X-band methods described here. We hope that this book will provide a basis for study of the newer methods.

One of Philip Rieger's most important contributions to the field of ESR, and the motivation for much of his collaborative research, was his instinctive understanding of how to analyze the powder patterns of paramagnetic inorganic complexes, often using programs for simulating and analyzing such spectra that he had developed over the years. A summary of his work in this area may be found in a review titled "Simulation and analysis of ESR powder patterns" published in the Specialist Periodical Report *Electron Spin Resonance*, Royal Society of Chemistry, Cambridge, 1993, vol 13B, ch. 4, pp. 178–199. Specism and other ESR tools written by Prof. Rieger are available from the Manchester University website at www.epr.chemistry.manchester. ac.uk. When you go to this site you will find a menu on the left with a 'Software' button which will give you access to this material.

We are particularly grateful to Elsevier Publishing Company for allowing the use, and modification, of material that originally appeared in *Organometallic Radical Processes*, *Journal of Organometallic Chemistry Library*, ed. W. C. Trogler, Elsevier, Amsterdam, 1990, vol 22. Most of Chapter 4, and also substantial parts of Chapter 3, were first published in this review. Other reviews by Professor Rieger on topics covered in this book include "Electron paramagnetic resonance studies of low-spin d^5 metal complexes", *Coord. Chem. Rev.*, 1994, **135**, 203; "Chemical insights from EPR spectra of organometallic radicals and radical ions" (with Dr. Anne L. Rieger), *Organometallics*, 2004, **23**, 154; and "Electron spin resonance", in *Physical Methods of Chemistry*, ed. A. Weissberger and B. W. Rossiter, John Wiley and Sons, Inc., New York, 1972, Part IIIA, ch.VI. pp 499–598.

Anne L. Rieger (Mrs. Philip Rieger) is grateful to Brown University for providing her with the facilities to make the completion of this project possible: office space, computers, the use of libraries, and a high speed internet connection to Professor Lawler in the mountains of New Hampshire. For many years Professor Rieger was associated with the ESR group of the Royal Society of Chemistry. The support and encouragement of many members of the group has

served as an impetus to see this project to completion and is gratefully acknowledged. Professor Neil Connelly of Bristol University, a long time collaborator and friend, has also contributed to the completion of the project and his input is very much appreciated. Finally, Ron Lawler is grateful to Margaret Merritt for her advice and support during this occasionally frustrating, but always interesting, introduction to the world of desktop publishing. We hope that our friend, companion and colleague Phil would be pleased with the result.

<div align="right">

Anne L. Rieger
Ronald G. Lawler
Pawtucket, RI, USA
Center Sandwich, NH, USA

</div>

Contents

CHAPTER 1
Introduction

1.1   What is ESR Spectroscopy?

Electron spin resonance spectroscopy (ESR), also known as electron paramagnetic resonance (EPR) or electron magnetic resonance (EMR), was invented by the Russian physicist Zavoisky[1] in 1945. It was extended by a group of physicists at Oxford University in the next decade. Reviews of the Oxford group's successes are available[2] and books by Abragam and Bleaney and by Abragam[3] cover the major points discovered by the Oxford group. In the present book, we focus on the spectra of organic and organotransition metal radicals and coordination complexes. Although ESR spectroscopy is supposed to be a mature field with a fully developed theory,[4] there have been some surprises as organometallic problems have explored new domains in ESR parameter space. We will start in this chapter with a synopsis of the fundamentals of ESR spectroscopy. For further details on the theory and practice of ESR spectroscopy, the reader is referred to one of the excellent texts and monographs on ESR spectroscopy.[3,5–36] Sources of data and a guide to the literature of ESR up to about 1990 can be found in ref. 16a. The history of ESR has also been described by many of those involved in the founding and development of the field.[37]

The electron spin resonance spectrum of a free radical or coordination complex with one unpaired electron is the simplest of all forms of spectroscopy. The degeneracy of the electron spin states characterized by the quantum number, $m_S = \pm 1/2$, is lifted by the application of a magnetic field, and transitions between the spin levels are induced by radiation of the appropriate frequency (Figure 1.1). If unpaired electrons in radicals were indistinguishable from free electrons, the only information content of an ESR spectrum would be the integrated intensity, proportional to the radical concentration. Fortunately, an unpaired electron interacts with its environment, and the details of ESR spectra depend on the nature of those interactions. The arrow in Figure 1.1 shows the transitions induced by 0.315 cm^{-1} radiation.

Two kinds of environmental interactions are commonly important in the ESR spectrum of a free radical: (i) To the extent that the unpaired electron has residual, or unquenched, orbital angular momentum, the total magnetic moment is different from the spin-only moment (either larger or smaller,

1
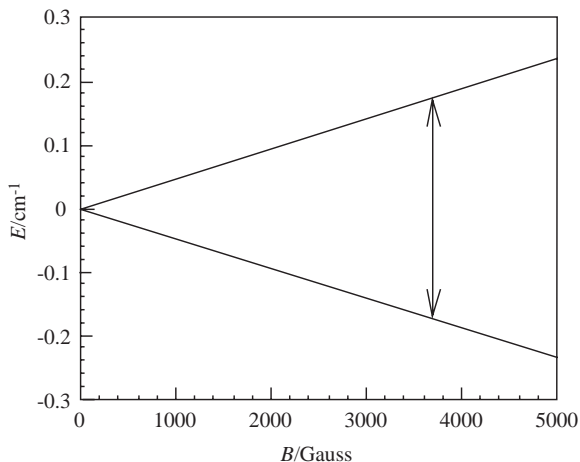
Figure 1.1   Energy levels of an electron placed in a magnetic field.
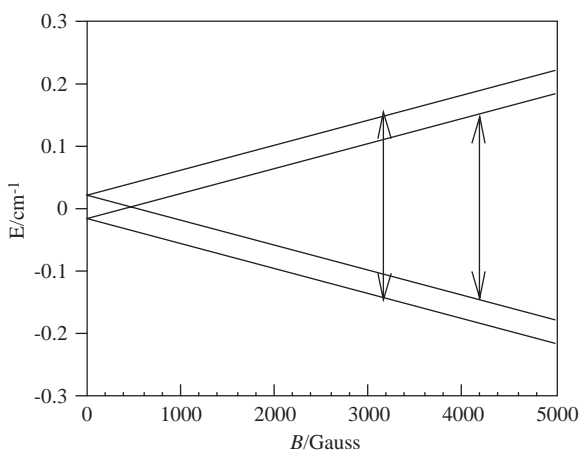
Figure 1.2   Energy levels of an unpaired electron in a magnetic field interacting with a spin-1/2 nucleus. The arrows show two allowed transitions.

depending on how the angular momentum vectors couple). It is customary to lump the orbital and spin angular momenta together in an effective spin and to treat the effect as a shift in the energy of the spin transition. (ii) The electron spin energy levels are split by interaction with nuclear magnetic moments – the nuclear hyperfine interaction. Each nucleus of spin I splits the electron spin levels into $(2I + 1)$ sublevels. Since transitions are observed between sublevels with the same values of m_I, nuclear spin splitting of energy levels is mirrored by splitting of the resonance line (Figure 1.2).

1.2 The ESR Experiment

When an electron is placed in a magnetic field, the degeneracy of the electron spin energy levels is lifted[†] as shown in Figure 1.1 and as described by the *spin Hamiltonian*:

$$\hat{H}_s = g\mu_B B \hat{S}_z \qquad (1.1)$$

In eqn (1.1), g is called the g-value (or g-factor), ($g_e = 2.00232$ for a free electron), μ_B is the Bohr magneton (9.274×10^{-28} J G^{-1}), B is the magnetic field strength in Gauss[‡], and S_z is the z-component of the spin angular momentum operator (the magnetic field defines the z-direction). The electron spin energy levels are easily found by application of $\hat{H}_s$ to the electron spin eigenfunctions corresponding to $m_S = \pm 1/2$:

$$\hat{H}_s \left| \pm \tfrac{1}{2} \right\rangle = \pm \tfrac{1}{2} g\mu_B B \left| \pm \tfrac{1}{2} \right\rangle = E_\pm \left| \pm \tfrac{1}{2} \right\rangle$$

Thus

$$E_\pm = \pm \left(\tfrac{1}{2} \right) g\mu_B B \qquad (1.2)$$

The difference in energy between the two levels:

$$\Delta E = E_+ - E_- = g\mu_B B = h\nu \qquad (1.3)$$

corresponds to the energy, $h\nu$, of a photon required to cause a transition; or in wavenumbers by eqn (1.4), where $g_e\mu_B/hc = 0.9348 \times 10^{-4}$ cm^{-1} G^{-1}:

$$\tilde{\nu} = \lambda^{-1} = \nu/c = (g\mu_B/hc)B \qquad (1.4)$$

Since the g-values of organic and organometallic free radicals are usually in the range 1.9–2.1, the free electron value is a good starting point for describing the experiment.

Magnetic fields of up to *ca.* 15000 G are easily obtained with an iron-core electromagnet; thus we could use radiation with $\tilde{\nu}$ up to 1.4 cm^{-1} ($\nu < 42$ GHz or $\lambda > 0.71$ cm). Radiation with this kind of wavelength is in the microwave region. Microwaves are normally handled using waveguides designed to transmit radiation over a relatively narrow frequency range. Waveguides look like rectangular cross-section pipes with dimensions on the order of the wavelength

---

[†] Energy level splitting in a magnetic field is called the *Zeeman effect*, and the Hamiltonian of eqn (1.1) is sometimes referred to as the electron Zeeman Hamiltonian. Technically, the energy of a magnetic dipole in a magnetic field is the negative of that shown in eqn (1.1). For electron spins, however, the parameter g is negative, *i.e.*, the magnetic moment and spin angular momentum vectors are anti-parallel, and both negative signs may be combined to give the formula as written. This has the advantage of allowing g-values to be tabulated as positive numbers.

[‡] Using the symbol "B" for the magnetic field technically implies we are using the MKS system of units in which B is given in Tesla (T). Many spectroscopists still express the magnetic field in Gauss (G) $= 10^{-4}$ T, however, and we will continue that practice here.

Table 1.1 Common frequencies used for ESR

Designation	ν (GHz)	λ (cm)	B (electron) (G)
L	1.1	27	390
S	3.0	10	1070
X	**9.5**	**3.2**	**3400**
K	24	1.2	8600
Q	35	0.85	12500
W	95	0.31	34000
–	360	0.083	128000

to be transmitted. As a practical matter for ESR, waveguides can not be too big or too small −1 cm is a bit small and 10 cm a bit large; the most common choice, called X-band microwaves, has λ in the range 3.0–3.3 cm ($\nu \approx$ 9–10 GHz); in the middle of X-band, the free electron resonance is found at 3390 G.

Although X-band is by far the most common, ESR spectrometers are available commercially or have been custom built in several frequency ranges (Table 1.1).

1.2.1 Sensitivity

As for any quantum mechanical system interacting with electromagnetic radiation, a photon can induce either absorption or emission. The experiment detects net absorption, *i.e.*, the difference between the number of photons absorbed and the number emitted. Since absorption is proportional to the number of spins in the lower level and emission is proportional to the number of spins in the upper level, net absorption, *i.e.*, absorption intensity, is proportional to the difference:

$$\text{Net absorption} \propto N_- - N_+$$

The ratio of populations at equilibrium is given by the Boltzmann distribution:

$$N_+/N_- = \exp(-\Delta E/kT) = \exp(-g\mu_B B/kT) \tag{1.5}$$

For ordinary temperatures and ordinary magnetic fields, the exponent is very small and the exponential can be accurately approximated by the expansion, $e^{-x} \approx 1 - x$. Thus

$$N_+/N_- \approx 1 - g\mu_B B/kT$$

Since $N_- \approx N_+ \approx N/2$, the population difference can be written:

$$N_- - N_+ = N_- \left[1 - (1 - g\mu_B B/kT)\right] = Ng\mu_B B/2kT \tag{1.6}$$

This expression tells us that ESR sensitivity (net absorption) increases with the total number of spins, N, with decreasing temperature and with increasing magnetic field strength. Since the field at which absorption occurs is proportional to microwave frequency, in principle sensitivity should be greater for

higher frequency K- or Q-band spectrometers than for X-band. However, the K- or Q-band waveguides are smaller, so samples are also necessarily smaller and for the same concentration contain fewer spins. This usually more than cancels the advantage of a more favorable Boltzmann factor for samples of unlimited size or fixed concentration.

Under ideal conditions, a commercial X-band spectrometer can detect about 10^{12} spins (*ca.* 10^{-12} moles) at room temperature. This number of spins in a 1 cm^3 sample corresponds to a concentration of about 10^{-9} M. By ideal conditions, we mean a single line, on the order of 0.1 G wide, with sensitivity going down roughly as the reciprocal square of the line width. When the resonance is split into two or more hyperfine lines, sensitivity decreases still further. Nonetheless, ESR is a remarkably sensitive technique, especially compared with NMR.

1.2.2 Saturation

Because the two spin levels are affected primarily by magnetic forces, which are weaker than the electric forces responsible for most other types of spectroscopy, once the populations are disturbed by radiation it takes longer for equilibrium population differences to be established. Therefore an intense radiation field, which tends to equalize the populations, leads to a decrease in net absorption which is not instantly restored once the radiation is removed. This effect is called "saturation". The return of the spin system to thermal equilibrium, *via* energy transfer to the surroundings, is a rate process called *spin–lattice relaxation*, with a characteristic time (T_1), the spin–lattice relaxation time (relaxation rate constant $= 1/T_1$). Systems with a long T_1 (*i.e.*, spin systems weakly coupled to the surroundings) will be easily saturated; those with shorter T_1 will be more difficult to saturate. Since spin–orbit coupling provides an important energy transfer mechanism, we usually find that odd-electron species with light atoms (*e.g.*, organic radicals) have long T_1s, those with heavier atoms (*e.g.*, organo-transition metal radicals) have shorter T_1s. The effect of saturation is considered in more detail in Chapter 5, where the phenomenological Bloch equations are introduced.

1.2.3 Nuclear Hyperfine Interaction

When one or more magnetic nuclei interact with the unpaired electron, we have another perturbation of the electron energy, *i.e.*, another term in the spin Hamiltonian:

$$\hat{H}_s = g\mu_B B\hat{S}_z + A\hat{I} \cdot \hat{S} \tag{1.7}$$

where A is the hyperfine coupling parameter in energy units (joule). Strictly speaking we should include the nuclear Zeeman interaction, γBI_z. However, in most cases the energy contributions are negligible on the ESR energy scale, and,

since observed transitions are between levels with the same values of m_I, the nuclear Zeeman energies cancel in computing ESR transition energies.§

The eigenfunctions of the spin Hamiltonian [eqn (1.7)] are expressed in terms of an electron- and nuclear-spin basis set $|m_S, m_I\rangle$, corresponding to the electron and nuclear spin quantum numbers m_S and m_I, respectively. The energy eigenvalues of eqn (1.7) are:

$$E\left(\tfrac{1}{2}, \tfrac{1}{2}\right) = \tfrac{1}{2}g\mu_B B + \tfrac{1}{4}A \tag{1.8A}$$

$$E\left(-\tfrac{1}{2}, -\tfrac{1}{2}\right) = -\tfrac{1}{2}g\mu_B B + \tfrac{1}{4}A \tag{1.8B}$$

$$E_+ = \tfrac{1}{2}g\mu_B B \left[1 + (A/g\mu_B B)^2\right]^{\frac{1}{2}} - \tfrac{1}{4}A \tag{1.8C}$$

$$E_- = -\tfrac{1}{2}g\mu_B B \left[1 + (A/g\mu_B B)^2\right]^{\frac{1}{2}} - \tfrac{1}{4}A \tag{1.8D}$$

The eigenfunctions corresponding the E_+ and E_- are mixtures of $|\tfrac{1}{2}, -\tfrac{1}{2}\rangle$ and $|-\tfrac{1}{2}, \tfrac{1}{2}\rangle$.

If the hyperfine coupling is sufficiently small, $A << g\mu_B B$, the second term in brackets in eqns (1.8C) and (1.8D) are negligible, which corresponds to first-order in perturbation theory, and the energies become:

$$E = \pm\tfrac{1}{2}g\mu_B B \pm \tfrac{1}{2}A \tag{1.9}$$

These are the energy levels shown in Figure 1.2. The exact energies in eqn. (1.8), which were first derived by Breit and Rabi,[38] are plotted as functions of B in Figure 1.3 for $g = 2.00$, $A/hc = 0.1$ cm^{-1}. Notice that, at zero field, there are two levels corresponding to a spin singlet ($E = -3A/4hc$) and a triplet ($E = +A/4hc$). At high field, the four levels divide into two higher levels ($m_S = +1/2$) and two lower levels ($m_S = -1/2$) and approach Figure 1.2, the first-order result, eqn. (1.9) (the first-order solution is called the high-field approximation). To conserve angular momentum, transitions among these levels can involve changes in angular momentum of only one unit. At high fields this corresponds to flipping only one spin at a time; in other words, the selection rules are $\Delta m_S = \pm 1$, $\Delta m_I = 0$ (ESR transitions) or $\Delta m_S = 0$, $\Delta m_I = \pm 1$ (NMR transitions). The latter involves much lower energy photons, and, in practice, only the $\Delta m_S = \pm 1$ transitions are observed in an ESR spectrometer. At lower fields, or when A

---

§ An exception to this rule arises in the ESR spectra of radicals with small hyperfine parameters in solids. In that case the interplay between the Zeeman and anisotropic hyperfine interaction may give rise to satellite peaks for some radical orientations (S. M. Blinder, *J. Chem. Phys.*, 1960, **33**, 748; H. Sternlicht, *J. Chem. Phys.*, 1960, **33**, 1128). Such effects have been observed in organic free radicals (H. M. McConnell, C. Heller, T. Cole and R. W. Fessenden, *J. Am. Chem. Soc.*, 1959, **82**, 766) but are assumed to be negligible for the analysis of powder spectra (see Chapter 4) where A is often large or the resolution is insufficient to reveal subtle spectral features. The nuclear Zeeman interaction does, however, play a central role in electron-nuclear double resonance experiments and related methods [Appendix 2 and Section 2.6 (Chapter 2)].
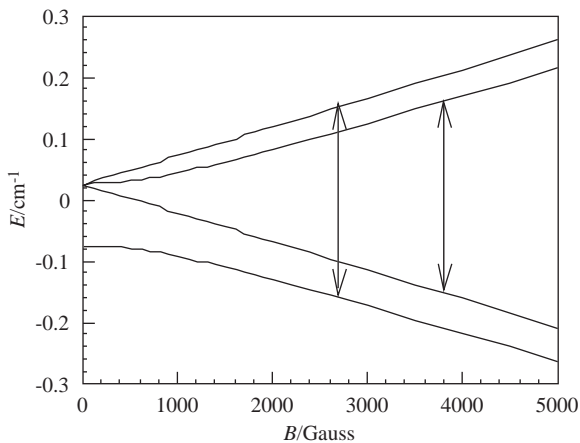
Figure 1.3 Energy levels for an electron interacting with a spin-1/2 nucleus with $A/hc = 0.1 \ \text{cm}^{-1}$. The arrows show the transitions induced by $0.315 \ \text{cm}^{-1}$ radiation.
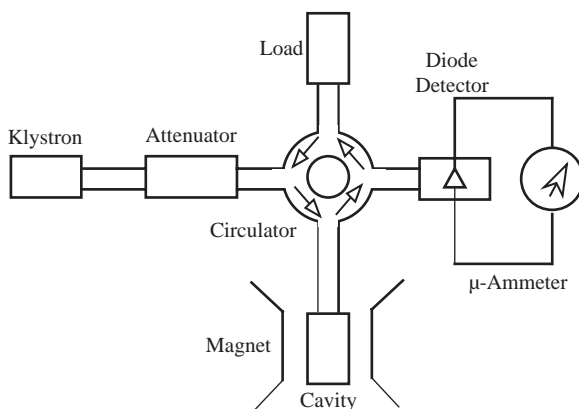
Figure 1.4 Block diagram of an ESR spectrometer.

becomes comparable in magnitude to $g\mu_B B$, the transitions may involve simultaneous flipping of electron and nuclear spins. This gives rise to second-order shifts in ESR spectra (see Chapters 2 and 3).

1.3 Operation of an ESR Spectrometer

Although many spectrometer designs have been produced over the years, the vast majority of laboratory instruments are based on the simplified block diagram shown in Figure 1.4. Plane-polarized microwaves are generated by the klystron tube and the power level adjusted with the Attenuator. The Circulator

behaves like a traffic circle: microwaves entering from the klystron are routed toward the Cavity where the sample is mounted. Microwaves reflected back from the Cavity (which is reduced when power is being absorbed) are routed to the Diode Detector, and any power reflected from the diode is absorbed completely by the Load. The diode is mounted along the *E*-vector of the plane-polarized microwaves and thus produces a current proportional to the microwave power reflected from the cavity. Thus, in principle, the absorption of microwaves by the sample could be detected by noting a decrease in current in the Microammeter. In practice, of course, such a measurement would detect noise at all frequencies as well as signal and have a far too low signal-to-noise ratio to be useful.

The solution to the signal-to-noise problem is to introduce small amplitude field modulation. An oscillating magnetic field is superimposed on the dc field by means of small coils, usually built into the cavity walls. When the field is in the vicinity of a resonance line, it is swept back and forth through part of the line, leading to an a.c. component in the diode current. This a.c. component is amplified using a frequency selective amplifier tuned to the modulation frequency, thus eliminating a great deal of noise. The modulation amplitude is normally less than the line width. Thus the detected a.c. signal is proportional to the *change* in sample absorption as the field is swept. As shown in Figure 1.5, this amounts to detection of the first derivative of the absorption curve.

It takes a little practice to get used to looking at first-derivative spectra, but there is a distinct advantage: first-derivative spectra have much better apparent resolution than do absorption spectra. Indeed, second-derivative spectra are even better resolved (though the signal-to-noise ratio decreases on further differentiation). Figure 1.6 shows the effect of higher derivatives on the resolution of a 1:2:1 triplet arising from the interaction of an electron with two equivalent $I = 1/2$ nuclei.

The microwave-generating klystron tube[¶] requires explanation. A schematic drawing of the klystron is shown in Figure 1.7. There are three electrodes: a heated cathode from which electrons are emitted, an anode to collect the electrons, and a highly negative reflector electrode that sends those electrons which pass through a hole in the anode back to the anode. The motion of the charged electrons from the hole in the anode to the reflector and back to the anode generates an oscillating electric field and thus electromagnetic radiation.

The transit time from the hole to the reflector and back again corresponds to the period of oscillation (ν). Thus the microwave frequency can be tuned (over a small range) by adjusting the physical distance between the anode and

[¶] Some modern spectrometers, especially those employing pulsed excitation (see Appendix 2), use a solid-state Gunn diode microwave source. This device makes use of the Gunn Effect, discovered by J. B. Gunn of IBM in 1963, in which electrons become "trapped" in potential wells within a solid and oscillate at a frequency that may be varied by changing the applied voltage. As with a klystron, tuning is done by varying the voltage. Gunn diode oscillators have better frequency stability and longer lifetimes than klystrons and are becoming the preferred microwave source for ESR spectrometers.
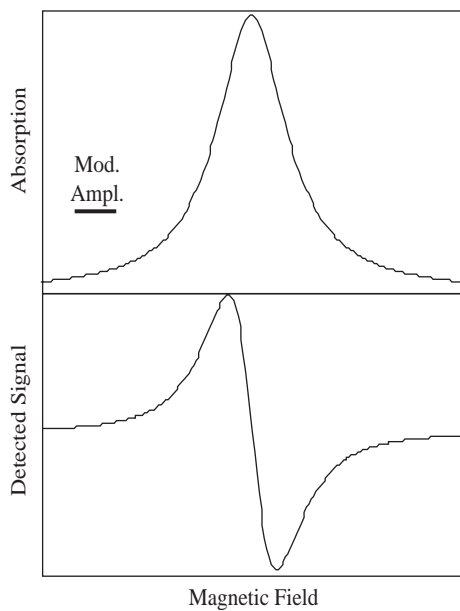
Figure 1.5   Small-amplitude field modulation converts the absorption curve into a first-derivative.
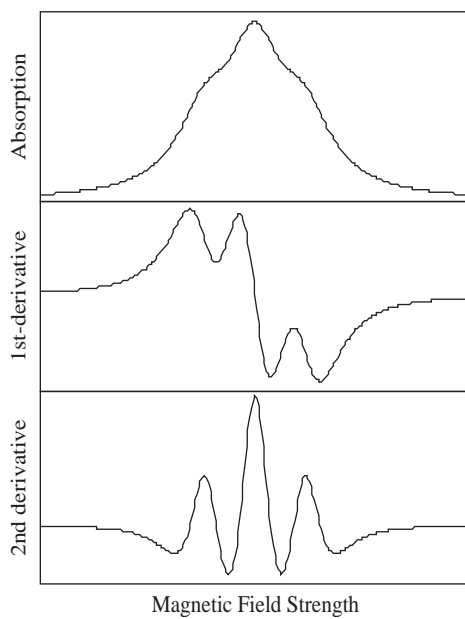
Figure 1.6   First-derivative curves show better apparent resolution than do absorption curves – and second-derivatives curves are still better.
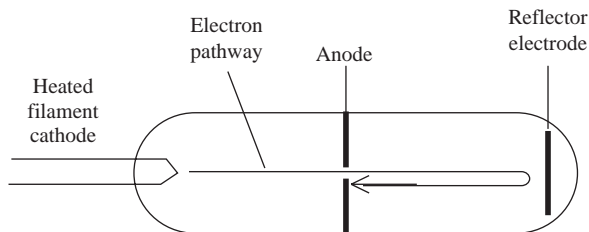
Figure 1.7   Schematic drawing of a microwave-generating klystron tube.
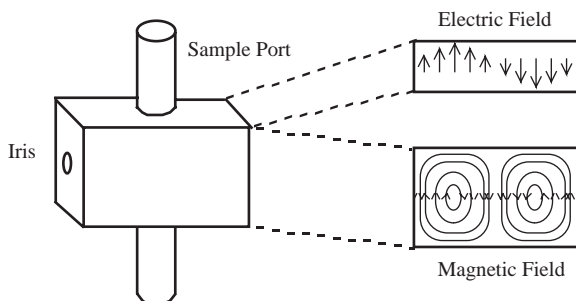
Figure 1.8   Microwave cavity.

the reflector or by adjusting the reflector voltage. In practice, both methods are used: the metal tube is distorted mechanically to adjust the distance (a coarse frequency adjustment) and the reflector voltage is adjusted as a fine control.

The sample is mounted in the microwave cavity (Figure 1.8). The cavity is a rectangular metal box, exactly one wavelength long. An X-band cavity has dimensions of about $1 \times 2 \times 3$ cm. The electric and magnetic fields of the standing wave are shown in the figure. Note that the sample is mounted in the electric field nodal plane, but at a maximum in the magnetic field. The static field, B, is perpendicular to the sample port.

The cavity length is not adjustable, but it must be exactly one wavelength. Thus the spectrometer must be tuned such that the klystron frequency is equal to the cavity resonant frequency. The tune-up procedure usually includes observing the klystron power mode. That is, the frequency is swept across a range that includes the cavity resonance by sweeping the klystron reflector voltage, and the diode detector current is plotted on an oscilloscope or other device. When the klystron frequency is close to the cavity resonance, microwave energy is absorbed by the cavity and the power reflected from the cavity to the diode is minimized, resulting in a dip in the power mode (Figure 1.9). The "cavity dip" is centered on the power mode using the coarse mechanical frequency adjustment, while the reflector voltage is used to fine tune the frequency.
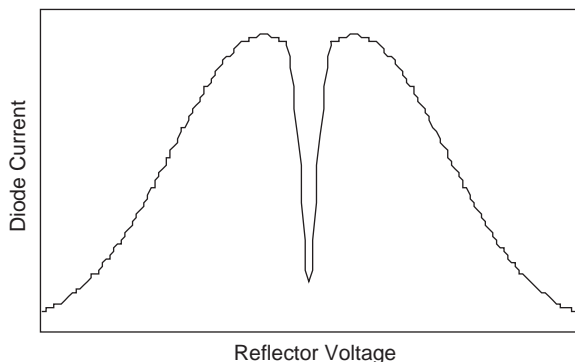
Figure 1.9 Klystron mode and cavity dip.

Table 1.2 Parameters involved in the recording of an ESR spectrum

Microwave frequency	Center field	Modulation frequency	Modulation phase
Microwave power	Sweep width	1st or 2nd harmonic	Signal gain
Sweep time	Field offset	Modulation amplitude	Filter time constant

1.4   Optimization of Operating Parameters[‖]

Determining the ESR spectrum of a sample using a typical CW spectrometer of the sort outlined in Figure 1.4, which is still the most common commercially available type of instrument, involves adjustment of the set of operating parameters described below. In the early days of ESR these adjustments would be carried out using control knobs on a console. Nowadays, of course, the settings are carried out under control of a computer interface. The purpose of these parameters and typical values, however, has remained unchanged. Such spectrometers are quite adequate for studying relatively stable samples. Characterizing transient species by ESR, however, requires substantial modification of commercial instruments or the use of a pulsed spectrometer.

There are twelve parameters that must be set or known in recording an ESR spectrum (Table 1.2). Briefly, below, each parameter is discussed and the means used to optimize or measure the parameter described.

1.4.1   Microwave Frequency

The resonant microwave frequency reaching the sample is determined by the effective length of the microwave cavity. The actual length is somewhat

---

[‖] A comprehensive discussion and illustrations of the effects of spectrometer operating parameters on ESR spectra are given by the author in Electron spin resonance, in *Physical Methods of Chemistry*, ed. A. Weissberger and B. W. Rossiter, John Wiley and Sons, Inc., New York, 1972, part IIIA, ch. VI,.

modified by the influence of the sample tube and the Dewar insert (if controlled temperature operation is required) so that the microwave frequency varies by a few percent even for the same cavity. Since the klystron frequency is locked to the cavity resonant frequency by a suitable feedback circuit, this is not an adjustable parameter. However, to compute a g-value from a spectrum, the frequency must be known quite accurately. This is normally done using a microwave frequency counter installed somewhere in the waveguide circuit.

1.4.2 Microwave Power

According to the solution of the Bloch equations (Chapter 5), the magnetic resonance absorption, sometimes called the "v-mode signal", v, is given by eqn (1.10).

$$v = \frac{\gamma B_1 M_0 T_2}{1 + T_2^2 (\omega_0 - \omega)^2 + \gamma^2 B_1^2 T_1 T_2} \tag{1.10}$$

where T_1 and T_2 are the spin–lattice and transverse relaxation times, respectively, M_0 is the bulk magnetization, γ is the magnetogyric ratio ($g\mu_B$ in ESR terms), ω_0 is the resonant frequency (proportional to B_0), ω is the angular microwave frequency (ν), and B_1 is the amplitude of the oscillating field. The microwave power is proportional to B_1^2. For small B_1, the absorption signal increases linearly with increasing B_1. However, when the third term in the denominator becomes important, v goes through a maximum when $\gamma^2 B_1^2 T_1 T_2 = 1$, and begins to decrease with increasing B_1 – the resonance begins to "saturate". At maximum v, however, the saturation term leads to an increase in apparent line width by a factor of $\sqrt{2}$. This effect is illustrated in Figure 1.10.

To simultaneously maximize signal-to-noise ratio (S/N) and minimize distortion, it is best to adjust the microwave power, as measured by the power
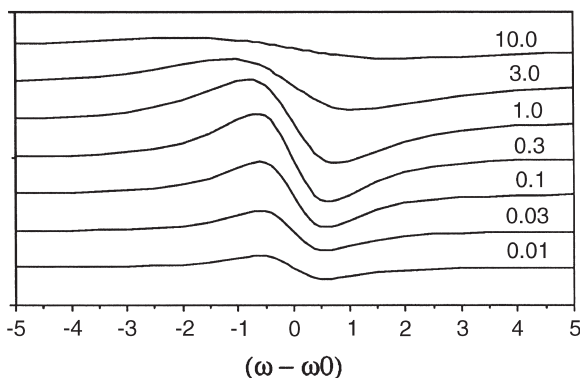
Figure 1.10   Effect of increasing microwave power on intensity and shape of an ESR line. Power increases from top to bottom of the figure. Units are relative values of B_1^2.
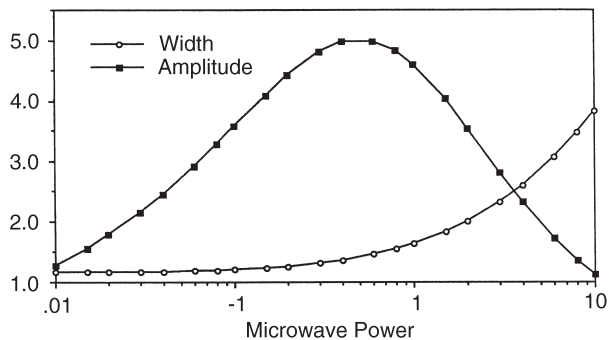
Figure 1.11 Effect of microwave power on relative width and amplitude of a line.

meter, down by a factor or 4 or 5 (6–7 db) from the maximum amplitude power. This will result in a decrease of less than 2 in signal amplitude. In practice, following this procedure would require finding the maximum amplitude by trial and error and then turning the power level down by 6–7 db. This effect is illustrated in Figure 1.11.

In general it is unnecessary to spend much time adjusting the power level. The general rule is to adjust the power to about 10 db attenuation for organic radicals and to use full power for transition metal complexes and those organometallics where the unpaired electron is primarily located on the metal.

1.4.3 Center Field, Sweep Width and Field Offset

Once you know, or can guess, the field limits of your spectrum, setting the center field and sweep width values is not very difficult. The center field corresponds to the middle of the spectrum and a sufficiently large sweep width chosen so that all of the spectrum is recorded.

If you do not know the field range occupied by your spectrum in advance, the center field must be chosen by educated guess; set the sweep width 2–4× greater than the expected width. Hopefully, you will see at least a piece of your spectrum and can make appropriate adjustments to zero in on the correct settings.

Most spectrometers measure the magnetic field by a Hall effect probe consisting of a sensor mounted on one of the pole faces of the magnet. However, such estimates of the value of B inside the cavity are not sufficiently accurate to be used for g-factor determinations. There are two ways around this problem: (i) measure the spectrum of a solid free radical such as diphenylpicrylhydrazyl (DPPH), which has a well-known g-value (2.0028), at least once during acquisition of the desired spectrum; or (ii) use of an NMR gaussmeter probe inserted in or near the cavity several times during the collection of the spectrum.

1.4.4   Sweep Time

In general, the longer the sweep time the better the sensitivity since the filter time constant parameter can be set longer with consequent improvement in signal-to-noise ratio. In practice, however, sweep times are usually set in accordance with the expected lifetime of the radical species, the stability of the instrument, and the patience of the operator. Decay of the radical or drift of the spectrometer during a scan is clearly undesirable. The sweep time is most commonly set in the range 4–10 min.

1.4.5   Modulation Frequency

With most spectrometers, you have a choice of either 100 kHz or a lower frequency of field modulation. The higher frequency generally gives better S/N, but if the lines are unusually sharp (<0.08 Gauss), 100 kHz modulation leads to "side bands", lumps in the line shape that confuse the interpretation of the spectrum. This effect is illustrated in Figure 1.12. Under such circumstances, use the lower frequency for which the sidebands are closer together and thus less likely to be a problem.
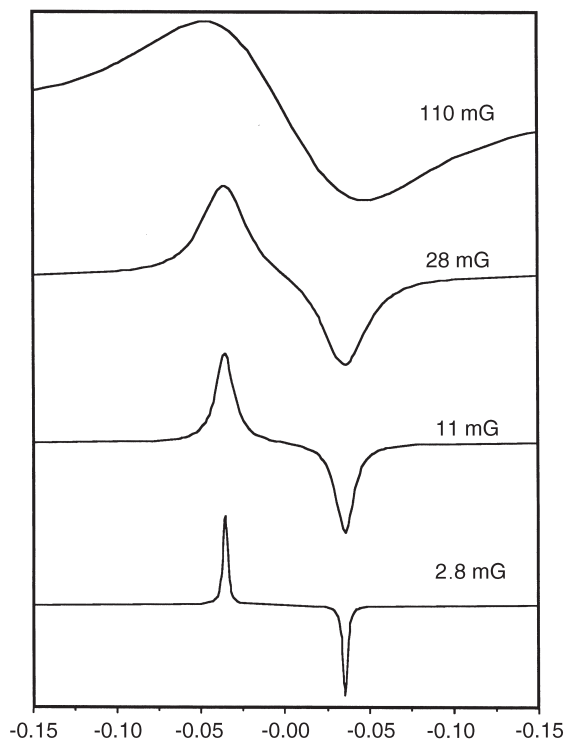
Figure 1.12   Effect of 100 kHz modulation on an ESR line of decreasing width. The *x*-axis is magnetic field, in Gauss, relative to the center of the line.

1.4.6 Second Harmonic Detection

In most cases, you will use the first harmonic and the normal first-derivative of the absorption spectrum will be presented. If your spectrum has *very* good S/N and has some regions where you would like better resolution, a second-derivative presentation may help. However, second derivatives from second harmonic detection are very costly in terms of S/N ratio and so you really do have to have a *strong* signal!

1.4.7 Modulation Amplitude

Since the absorption signal is usually detected by imposing a 100 kHz field modulation on the static field, the signal disappears when the modulation amplitude is turned to zero. In general, the signal increases more or less in proportion to the modulation amplitude, but eventually the detected lines begin to broaden and then the signal amplitude decays as well. This is illustrated in Figure 1.13.

Depending on what you want to optimize, here are some rules:

For optimum S/N ratio, but decreased resolution: Modulation amplitude = 2 × line-width.
For accurate line width measurements: Modulation amplitude = line-width/10.
For most practical work: Modulation amplitude = line-width/3.

1.4.8 Modulation Phase

To improve the S/N ratio, the modulation signal is processed by amplification with a tuned amplifier using phase-sensitive detection. This means that the detected signal must not only be at the modulation frequency, but must also be in phase with the modulation. Since the amplifier itself can introduce a bit of phase shift, there is a phase control which, in principle, should be adjusted to maximize the signal amplitude. In practice, this control needs to be adjusted only rarely and in most cases the best approach is to leave it alone.
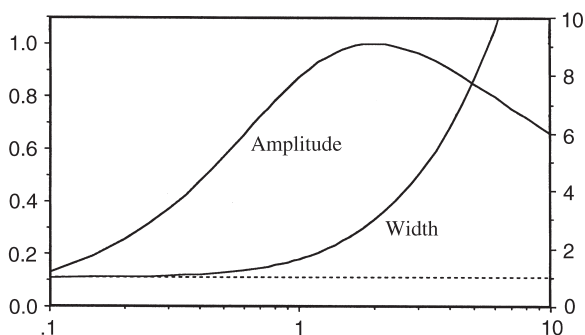
Figure 1.13 Effect of field changing (modulation/line width) on relative amplitude (left-hand axis) and observed width (right-hand axis) of an ESR line.

1.4.9   Signal Gain

Adjustment of the signal gain is straightforward. Set the gain sufficiently high that the recorded spectrum is nearly full-scale on the computer displays or recorder. If you have no idea of the strength of your expected signal, a good starting point would be 1×10^4. Too high a gain can result in amplifier overload.

1.4.10   Filter Time Constant

The output of the signal amplifier is filtered using a circuit designed to pass low-frequency, but not high frequency, signals. The cut-off frequency is the recip-rocal of the time constant setting. Thus, a time constant of 0.1 s would lead to signals with frequencies greater than about 10 Hz being attenuated. The best time constant setting thus depends critically on the sweep time. If you sweep through a line rapidly using a long time constant, you may filter out the signal altogether! With a shorter, but still too long, time constant, the line shape will be distorted, the apparent line center will shift, and the apparent line width will increase. These effects are illustrated in Figure 1.14. The best rule-of-thumb is to set the time constant to 10% of the time required to pass through the narrowest line of your spectrum.
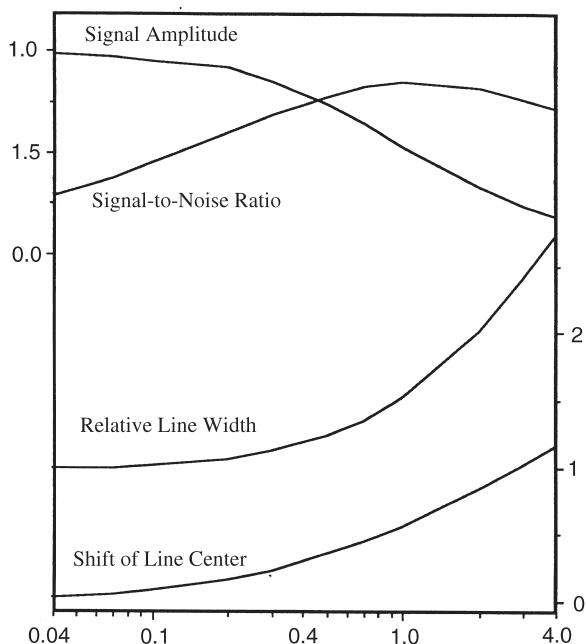
Figure   1.14   Effect of time constant/time to sweep through the line (*x*-axis) on the relative amplitude and signal-to-noise ratio (left-hand axis) and relative width and shift (right-hand axis) of an ESR line.

For example, suppose that the line width is 0.25 G, that you are scanning through 10 G in 4 min. The scan rate then is 10 G/4 min = 2.5 G min^{-1}. The time required to pass through a line is 0.25 G/2.5 G min^{-1} = 0.1 min or 6 s. The time constant should be set close to 0.6 s.

1.5   Applications of ESR Spectroscopy

1.5.1   Electronic Structure Determination

Most commonly, ESR spectroscopy is used to obtain information pertaining to the electronic structure of the species being studied. We will explore these kinds of applications extensively in subsequent chapters.

The magnetic field values at which microwaves are absorbed to produce the ESR spectrum of an isotropic sample, *e.g.*, the spectrum of a freely tumbling radical in liquid solution, can contain two principal types of chemically useful information: (i) The hyperfine coupling pattern provides information on the numbers and kinds of magnetic nuclei with which the unpaired electron interacts. (ii) The spacing of the lines and the center of gravity of the spectrum yield the hyperfine coupling constants, A_i, and *g*-value, g, which are related to the way in which the unpaired electron spin density is distributed in the molecule. In isotropic spectra the observed parameters are averaged over rotation of the molecules. In solids the parameters may also depend on molecular orientation relative to the magnetic field, B.

Structural applications range from organic, inorganic and organometallic radicals to coordination complexes and biological macromolecules containing a paramagnetic center.

Even more information is available from the spectrum of a solid-state sample, either a dilute single crystal or a frozen solution. We will discuss solid state samples later, beginning in Chapter 4.

1.5.2   Analytical Applications

Like all forms of spectroscopy, ESR intensities, through the dependence on the number of spins, N, can be used analytically to determine the concentration of a paramagnetic species. Such analytical applications usually require a standard solution to establish a calibrated intensity scale. Computer software is required in most cases to doubly integrate the spectrum (two integrations are required to convert the derivative spectrum into absorption and then to a number representing the total concentration of the species being studied). The interested reader is referred to Wertz and Bolton,[12a] who discuss the technique, point out the variables that must be controlled, and suggest intensity standards. The degree to which ESR intensities have been exploited varies widely. Experimentalists often make qualitative observations relating "strong" or "weak" spectra to chemical circumstances, but quantitative applications of integrated intensities are rare in ESR studies.

"Spin traps" which scavenge a reactive radical to give a more persistent radical may be used to detect the intermediacy of such transient radicals in sorting out a reaction mechanism.[39]

1.5.3   Determination of Rates

In some cases, ESR spectra can be used to determine the rate of a chemical reaction or the rate of a conformation change. Such applications are discussed in more detail in Chapter 5.

The spectral line widths are related to the rate of the rotational motions, which average anisotropies in the *g*- and hyperfine matrices (Chapter 5), and to the rates of fluxional processes, which average nuclear positions in a radical.

The saturation behavior of a spectrum – the variation of integrated intensity with microwave power – is related to the spin–lattice relaxation time, a measure of the rate of energy transfer between the electron spin and its surroundings. Saturation often depends on the same structural and dynamic properties as line widths.

Largely because spin–orbit coupling results in spin state admixture, electronic spin–lattice relaxation times are normally short for species containing heavy atoms such as transition metals. This has three consequences. Short relaxation times mean that saturation problems, which plague ESR spectroscopists studying organic radicals and NMR spectroscopists in general, are largely absent in organometallic ESR studies. Thus, spectra ordinarily can be recorded at full microwave power with salutary consequences for sensitivity. However, relaxation times are most easily determined by measuring spectral intensity as a function of microwave power in the saturation region. If relaxation times are short, very high power is required, which is out of the range of operation of most continuous wave spectrometers. Similarly, short relaxation times imply broad lines and reduced sensitivity. The advent of modern high power pulsed spectrometers[32,34,36] has made it possible to overcome some of the restrictions arising from relaxation behavior.

Some workers have used "spin labels" attached to a membrane or biological macromolecule to study the motion of these components of living cells (Chapter 5).

References

1. E. Zavoisky, *J. Phys. USSR*, 1945, **9**, 211, 245.
2. (*a*) B. Bleaney and K.W.H. Stevens, *Rep. Progr. Phys.*, 1953, **16**, 108; (*b*) K.D. Bowers and J. Owen, *Rep. Progr. Phys.*, 1955, **18**, 304; (*c*) D.M.S. Bagguley and J. Owen, *Rep. Progr. Phys.*, 1957, **20**, 304.
3. (*a*) A. Abragam and B. Bleaney, *Electron Paramagnetic Resonance of Transition Ions*, Clarendon Press, Oxford, 1970; (*b*) A. Abragam, *The Principles of Nuclear Magnetism*, Clarendon Press, Oxford, 1961.

4. A. Hudson, in *Electron Spin Resonance, Specialist Periodical Report*, ed. M.C.R. Symons, Royal Chemical Society, London, 1988, **11A**, 55.

Early monographs

5. D.J.E. Ingram, *Free Radicals as Studied by Electron Spin Resonance*, Butterworth, London, 1958.
6. G.E. Pake, *Paramagnetic Resonance: An Introductory Monograph*, W. A. Benjamin, New York, 1962.
7. S.A. Altshuler and B.M. Kozyrev, *Electron Paramagnetic Resonance*, Academic Press, New York, 1964.
8. M. Berson and J.C. Baird, *An Introduction to Electron Paramagnetic Resonance*, W. A. Benjamin, New York, 1966.

Standard texts and monographs

9. P.B. Ayscough, *Electron Spin Resonance in Chemistry*, Methuen, London, 1967.
10. H.M. Assenheim, *Introduction to Electron Spin Resonance*, Plenum Press, New York, 1967.
11. R.S. Alger, *Electron Paramagnetic Resonance, Techniques and Applications*, Interscience, New York, 1968.
12. (*a*) J.E. Wertz and J.R. Bolton, *Electron Spin Resonance*, McGraw-Hill, New York, 1972; (*b*) J.A. Weil, J.R. Bolton and J.E. Wertz, *Electron Paramagnetic Resonance: Elementary Theory and Practical Applications*, Wiley-Interscience, New York, 1994.
13. (*a*) N.M. Atherton, *Electron Spin Resonance: Theory and Applications*, Ellis Horwood, Chicester, 1973; (*b*) *Principles of Electron Spin Resonance*, Ellis Horwood, Chicester, 1993.
14. L.A. Blumenfeld, V.V. Voevodski and A.G. Semenov, *Monographs on Electron Spin Resonance*, Halsted Press, New York, 1974.
15. W. Gordy, *Theory and Applications of Electron Spin Resonance*, Wiley, New York, 1980.
16. *Handbook of Electron Spin Resonance*, ed. C.P. Poole, Jr. and H.A. Farach, 2 vols., AIP Press, New York, (*a*) Vol. 1, 1994, (*b*) Vol. 2, 1999.

Instrumentation

17. T.H. Wilmshurst, *Electron Spin Resonance Spectrometers*, Plenum Press, New York, 1967.
18. C.P. Poole, Jr., *Electron Spin Resonance: A Comprehensive Treatise on Experimental Techniques*, Wiley, New York, 1983.

Biological applications

19. D.J.E. Ingram, *Biological and Biochemical Applications of ESR*, Adam Hilger, London, 1969.
20. G. Feher, *Electron Paramagnetic Resonance with Applications to Selected Problems in Biology*, Gordon and Breach, New York, 1970.
21. *Biological Applications of Electron Spin Resonance*, ed. H.M. Schwartz, J.R. Bolton and D.C. Borg, Wiley-Interscience, New York, 1972.

22. M.C.R. Symons, *Chemical and Biochemical Aspects of Electron Spin Resonance*, John Wiley and Sons, New York, 1978.
23. *Paramagnetic Resonance of Metallobiomolecules*, ed. J. Telser, ACS Symposium Series, 858, Oxford Unversity Press, Oxford, 2003.
24. *Biomedical EPR*, ed. S.S. Eaton, G.R. Eaton and L.J. Berliner, Kluwer Academic/Plenum Publishers, New York, 2004.
25. L.J. Berliner, *In vivo EPR (ESR): Theory and Applications*, Baker and Taylor, Charlotte, NC, 2004.

Inorganic and organometallic applications
26. P.W. Atkins and M.C.R. Symons, *The Structure of Inorganic Radicals*, Elsevier, Amsterdam, 1967.
27. J.R. Pilbrow, *Transition Ion Electron Paramagnetic Resonance*, Clarendon Press, Oxford, 1990.
28. F.E. Mabbs and D. Collison, *Electron Paramagnetic Resonance of d Transition Metal Compounds*, Elsevier, Amsterdam, 1992.

Organic free radicals
29. F. Gerson, *High Resolution E.S.R. Spectroscopy*, John Wiley and Sons Ltd., London, 1970.
30. F. Gerson and W. Huber, *Electron Spin Resonance Spectroscopy of Organic Radicals*, Wiley-VCH, Weinheim, 2003.

Advanced methods
31. L. Kevan and L.D. Kispert, *Electron Spin Double Resonance Spectroscopy*, Wiley, New York, 1976.
32. *Time Domain Electron Spin Resonance*, ed. L. Kevan and R.N. Schwartz, Wiley-Interscience, New York, 1979.
33. *Advanced EPR – Applications in Biology and Biochemistry*, ed. A.J. Hoff, Elsevier, Amsterdam, 1989.
34. *Modern Pulsed and Continuous-Wave Electron Spin Resonance*, ed. L. Kevan and M.K. Bowman, John Wiley, New York, 1990.
35. M. Ikeya, *New Applications of Electron Spin Resonance: ESR Dating, Dosimetry and Microscopy*, World Scientific Publishing Co., London, 1993.
36. A. Schweiger and G. Jeschke, *Principles of Pulse Electron Paramagnetic Resonance*, Oxford University Press, Oxford, 2001.
37. *Foundations of Modern EPR*, ed. G.R. Eaton, S.R. Eaton and K.M. Salikhov, World Scientific, Singapore, 1998.
38. G. Breit and I.I. Rabi, *Phys. Rev.*, 1931, **38**, 2082.
39. D. Rehorek, *Chem. Soc. Rev.*, 1991, **20**, 341.

Isotropic ESR Spectra of Organic Radicals

2.1 Isotropic ESR Spectra

2.1.1 Line Positions in Isotropic Spectra

As introduced in Chapter 1, ESR spectra of radicals in liquid solution are usually interpreted in terms of a spin Hamiltonian:

$$\hat{H}_S = \mu_B g B \hat{S}_z + \sum_i A_i \hat{I}_i \cdot \hat{S} \tag{2.1}$$

where we have generalized eqn (1.7) to include the possibility of many nuclei, each with an isotropic hyperfine coupling constant A_i. The spectral information is contained in the parameters, g, the isotropic g-factor, and the set of values of A_i. Using spin functions based on the quantum numbers m_S and m_I, eqn (2.1) can be used to compute energy levels. Equating energy differences for the allowed transitions ($\Delta m_S = \pm 1$, $\Delta m_{Ii} = 0$ for all i) with the microwave photon energy ($h\nu$) [eqn (2.2)] the resonant magnetic fields can be predicted.

$$E(m_s = 1/2, m_{Ii}) - E(m_s = -1/2, m_{Ii}) = h\nu \tag{2.2}$$

As will be derived in Chapter 3, to first-order in perturbation theory, the resonant fields are:

$$B = B_0 - \sum_i a_i m_{Ii} \tag{2.3}$$

where $B_0 = h\nu/g\mu_B$ represents the center of the spectrum and $a_i = A_i/g\mu_B$ is the hyperfine coupling constant in field units.

The coupling constants in eqn (2.1) have energy units, but the energies are very small so that frequency (MHz) or wavenumber (10^{-4} cm^{-1}) units are more commonly used. Even more often, however, isotropic coupling constants are given in units of magnetic field strength, since they may be derived directly from line positions in magnetic field units. The unit usually employed for a is gauss (G) (or oersteds), although SI purists sometimes use millitesla (1 mT = 10 G).

Conversions from units of gauss into frequency or wavenumber units involves the *g*-value:

$$A_i(\text{MHz}) = 2.8025(g/g_e)a_i(\text{G}) \qquad (2.4a)$$

$$A_i(10^{-4} \text{ cm}^{-1}) = 0.93480 \ (g/g_e)a_i(\text{G}) \qquad (2.4b)$$

Note that coupling constants in 10^{-4} cm^{-1} are comparable in magnitude to those expressed in gauss. Although the units used for isotropic hyperfine coupling constants is largely a matter of taste, the components of an aniso-tropic hyperfine coupling matrix (Chapter 4) should be given in frequency or wavenumber units unless the *g*-matrix is virtually isotropic.

2.1.2 Hyperfine Coupling Patterns

Nuclear hyperfine coupling results in a multi-line ESR spectrum, analogous to the spin–spin coupling multiplets of NMR spectra. ESR spectra are simpler to understand than NMR spectra in that second-order effects normally do not alter the intensities of components; on the other hand, ESR multiplets can be much more complex when the electron interacts with several high-spin nuclei, and, as we will see in Chapter 3, there can also be considerable variation in line width within a spectrum.

   When several magnetically equivalent nuclei are present in a radical, some of the multiplet lines appear at exactly the same field position, *i.e.*, are "degenerate", resulting in variations in component intensity. Equivalent spin-1/2 nuclei such as ^{1}H, ^{19}F, or ^{31}P result in multiplets with intensities given by binomial coefficients (1:1 for one nucleus, 1:2:1 for two, 1:3:3:1 for three, 1:4:6:4:1 for four, *etc.*). One of the first aromatic organic radical anions studied by ESR spectroscopy was the naphthalene anion radical,[1] the spectrum of which is shown in Figure 2.2. The spectrum consists of 25 lines, a quintet of quintets as expected for hyperfine coupling to two sets of four equivalent protons.

   Just as in NMR, a multiplet pattern gives an important clue to the identity of a radical. For example, in the naphthalene anion radical, there are four α (positions 1, 4, 5, 8) and four β protons (positions 2, 3, 6, 7). Each proton splits the electronic energy levels in two. Since the α protons are equivalent, for example, the splitting is the same for each proton. Thus, as shown on the right side of Figure 2.1, five equally spaced energy level values result.

   The degeneracies of the levels shown in Figure 2.1 can be obtained by the following line of reasoning: Assuming that the probability that any one proton is spin up is identical to the probability that it is spin down, the probability that all four protons are spin up or spin down is $(1/2)^4 = 1/16$. Similarly, the probability that three of the four protons are spin up or spin down is 4/16 and the probability that two of the four protons are spin up or spin down is 6/16. If this pattern sounds familiar, it should be since this is just the set of binomial coefficients for $(a + b)^4 = a^4 + 4a^3b + 6a^2b^2 + 4ab^3 + b^4$. We can generate these
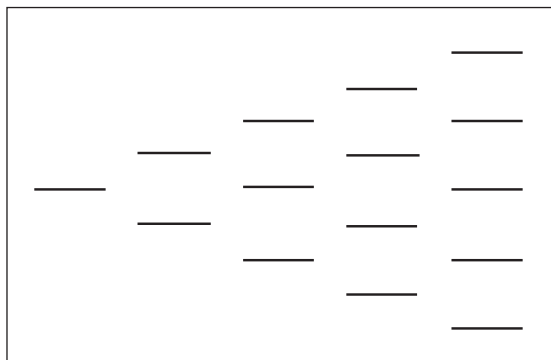
Figure 2.1 Splitting pattern for one of the electron spin energy levels coupled to four equivalent protons. Note that the degeneracies of the levels are not shown. See Section 2.5 for details.
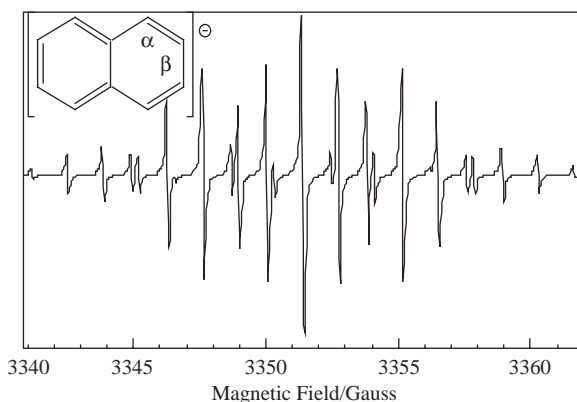
Figure 2.2 ESR spectrum of the naphthalene anion radical;[1] simulated using hyperfine couplings given in Table 2.1.

coefficients for other numbers of equivalent protons by the familiar Pascal's triangle (Figure 2.11), which is similar in structure to Figure 2.1.

Naphthalene and other aromatic hydrocarbons can be reduced by one electron to produce the anion radical. The reduction can be carried out with sodium in an ether solvent or electrochemically in a polar aprotic solvent.

The naphthalene anion radical spectrum (Figure 2.2) provided several surprises when Samuel Weissman and his associates[1] first obtained it in the early 1950s at Washington University in St. Louis. It was a surprise that such an odd-electron species would be stable, but in the absence of air or other oxidants, $[C_{10}H_8]^-$ is stable virtually indefinitely. A second surprise was the appearance of hyperfine coupling to the two sets of four equivalent protons. The odd electron was presumed (correctly) to occupy a π^* molecular orbital

(MO) with the protons in the nodal plane. The mechanism of coupling (discussed below) requires "contact" between the unpaired electron and the proton, an apparent impossibility for π electrons that have a nodal plane at the position of an attached proton. A third, pleasant, surprise was the ratio of the magnitudes of the two couplings, 5.01 G/1.79 G = 2.80. This ratio is remarkably close to the ratio of spin densities at the α and β positions, 2.62, predicted by simple Hückel MO theory for an electron placed in the lowest unoccupied MO (LUMO) of naphthalene (see Table 2.1). This result led to Hückel MO theory being used extensively in the semi-quantitative interpretation of ESR spectra of aromatic hydrocarbon anion and cation radicals.

Things get a little more complicated when a spin 1 nucleus like ^{14}N is added to the picture, but the same technique works again for the determination of the relative intensities of the ESR lines. Consider, for example, the relative intensities of the hyperfine lines arising from the pyrazine anion radical, whose spectrum is shown in Figure 2.3. Like that of the naphthalene anion radical, the spectrum observed for the pyrazine anion radical[2] consists of 25 well-resolved

Table 2.1 Hyperfine parameters and spin densities for aromatic radical anions. (Data from ref. 11.)

Compound	a^H (G)	ρ^π	Compound	a^H (G)	ρ^π
Benzene (B)	3.75	0.167	Pyrene (Py)	4.75	0.136
C_8H_8 (C)	3.21	0.125		1.09	0.000
Naphthalene (N)	5.01	0.181		2.08	0.087
	1.79	0.069	Perylene (P)	3.09	0.083
Anthracene (A)	2.74	0.096		0.46	0.013
	1.57	0.047		3.53	0.108
	5.56	0.192	Biphenylene (Bi)	0.00	0.027
				2.75	0.087

Magnetic Field/Gauss
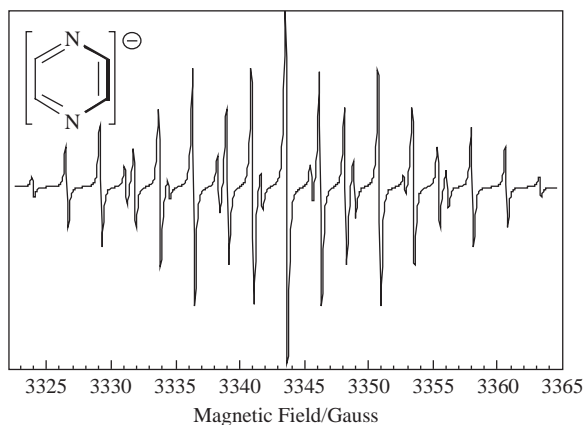
Figure 2.3 ESR spectrum of the potassium salt of pyrazine radical anion; simulated using hyperfine couplings from ref. 2.

one spin-1 nitrogen: 1   1   1

1   1   1
     1   1   1
          1   1   1

two spin-1 nitrogens: 1   2   3   2   1

$$\left[\begin{array}{c} \text{pyrazine anion structure} \end{array} \right]^{\overset{\bullet}{-}}$$

H—N ring with N and four H (pyrazine anion radical)

1 4 6 4 1
 2 8 12 8 2
plus four spin-1/2 protons: 3 12 18 12 3
   2 8 12 8 2
    1 4 6 4 1

Relative intensities: **1 4 6 2 4 8 1 12 3 8 12 2 18 2 12 8 3 12 1 8 4 2 6 4 1**
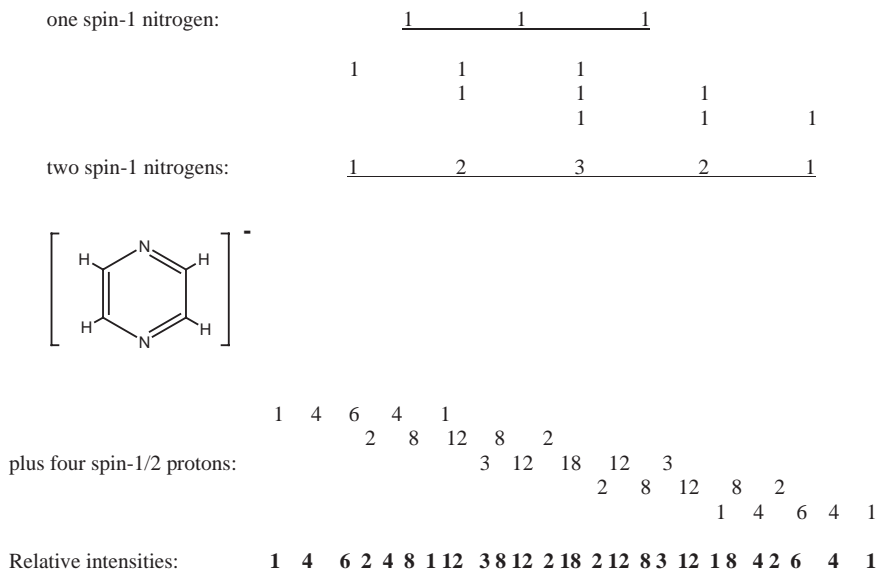
Figure 2.4 Derivation of the relative intensities of the 25 ESR lines of the pyrazine anion radical. See Section 2.5 for details of the method.

lines. In fact, the spectra in Figures 2.2 and 2.3 appear almost identical and are only distinguishable by careful examination of the intensities of the lines.

The intensities for pyrazine are derived in Figure 2.4, assuming that the ratio of hyperfine couplings, a^{N}/a^{H}, is nearly the same as a_{α}/a_{β} for naphthalene anion radical. The method used is the same as implied by the energy level splittings shown in Figure 2.1. The pattern arising from the two equivalent ^{14}N nuclei that have the larger hyperfine splitting are first derived, giving five lines with relative intensities of $1:2:3:2:1$. Each of these is then split into five lines with relative intensities of $1:4:6:4:1$, corresponding to the four equivalent protons. The relative intensities of all 25 lines are shown at the bottom of the figure in the same order in which they are appear in the observed spectrum in Figure 2.2. Section 2.5 gives a fuller explanation of this procedure.

2.1.3 Second-order Splittings

Equation (2.3) describes line positions correctly for spectra with small hyperfine coupling to two or more nuclei provided that the nuclei are not magnetically equivalent. When two or more nuclei are completely equivalent, *i.e.*, both instantaneously equivalent and equivalent over a time average, then the nuclear spins should be described in terms of the total nuclear spin quantum numbers I and m_I rather than the individual I_i and m_{Ii}. In this "coupled representation", the degeneracies of some multiplet lines are lifted when second-order shifts are included. This can lead to extra lines and/or asymmetric line shapes. The effect was first observed in the spectrum of the methyl radical, $CH_3{}^{\bullet}$, produced by

3333 3334 3335   3356 3357 3358   3379 3380 3381   3402 3403 3404

Magnetic Field/Gauss
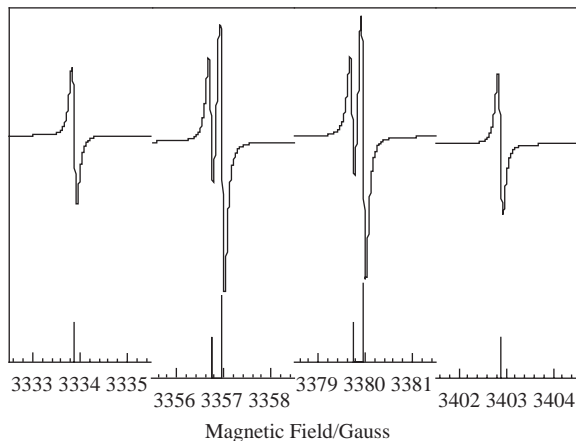
Figure 2.5   ESR spectrum of the methyl radical, $CH_3{}^{\bullet}$ (note discontinuities in magnetic field axis). Simulated using hyperfine splitting from ref. 3 and eqn (2.5).

high-energy electron irradiation of liquid methane, by Fessenden and Schuler.[3] The three equivalent protons lead to a nondegenerate nuclear spin state with $I = 3/2$ ($m_I = \pm 3/2, \pm 1/2$) and a two-fold degenerate state with $I = 1/2$ ($m_I = \pm 1/2$). Thus, six hyperfine lines are observed under conditions of high resolution (Figure 2.5).

2.1.4   Spin Hamiltonian Parameters from Spectra

Once a hyperfine pattern has been recognized, the line position information can be summarized by the spin Hamiltonian parameters, g and a_i. These parameters can be extracted from spectra by a linear least-squares fit of experimental line positions to eqn (2.3). However, for high-spin nuclei and/or large couplings, one soon finds that the lines are not evenly spaced as predicted by eqn (2.3) and second-order corrections must be made. Solving the spin Hamiltonian, eqn (2.1), to second order in perturbation theory, eqn (2.3) becomes:[4]

$$\mathbf{B} = \mathbf{B}_0 - \sum_i \left\{ a_i m_{I_i} + \left[a_i^2 / 2\mathbf{B} \right] \left[I_i (I_i + 1) - m_{I_i}^2 \right] + \ldots \right\} \qquad (2.5)$$

The magnitude of the second-order corrections is often quite significant. For example, Figure 2.5 shows the ESR spectrum of methyl radical, $CH_3{}^{\bullet}$. Notice that all lines are shifted to low field, relative to the first-order spectrum, but, as expected from eqn (2.5), the shift depends on m_I. Failure to account for the second-order terms in an analysis results in a significant error in both the g-value and in the hyperfine coupling constants For large I_i and a_i, well-resolved spectra may warrant inclusion of third- or higher-order corrections. Since the third-order corrections involve cross terms among coupling constants, in principle they permit determination of the relative signs of the coupling constants.[5] However, in the example of Figure 2.5, the third-order corrections

amount to *ca.* 1 mG. Second-order corrections are also required for accurate determinations of *g*-factors of radicals with very narrow lines[6] or in properly accounting for line positions in radicals exhibiting chemical exchange effects.[7]

Second-order effects on hyperfine structure in organometallic compounds are discussed in Chapter 3.

2.2 Interpretation of Isotropic Parameters

When ESR spectra were obtained for the benzene anion radical, $[C_6H_6]^{-\bullet}$, and the methyl radical, $CH_3^{\bullet}$, the proton hyperfine coupling constants were found to be 3.75 and 23.0 G, respectively, *i.e.* they differ by about a factor of 6. Since the carbon atom of CH_3 has a spin density corresponding to one unpaired electron and the benzene anion carries an electron spin density of 1/6, the two results suggest that the proton coupling to an electron in a π-orbital is proportional to the spin density on the adjacent carbon atom:

$$a^H = Q_{CH}^H \rho_C^\pi \tag{2.6}$$

where the parameter $Q_{CH}^H = 23.0$ G (based on CH_3), 22.5 G (based on $[C_6H_6]^-$), or -23.7 G based on a valence-bond theoretical calculation by McConnell.[8] Karplus and Fraenkel went on to analyze the origins of ^{13}C couplings in aromatic radicals.[9] Their results are summarized by eqn (2.7):

$$a^C = \left(S_C + \sum_i Q_{CX_i}^C \right) \rho_C^\pi + \sum_i Q_{X_iC}^C \rho_{X_i}^\pi \tag{2.7}$$

where $S_c = -12.7$ G, $Q_{CC'}^C = +14.4$ G, $Q_{CH}^C = +19.5$ G, and $Q_{C'C}^C = -13.9$ G. The first term refers to the spin density in the p-orbital of the carbon in question and the second term from p-orbital spin density on atoms attached to that carbon.

An isotropic hyperfine coupling to H can only arise through the so-called Fermi contact interaction of the unpaired electron at the position of the H nucleus; but this is apparently symmetry forbidden for organic π-radicals where the H nuclei lie in the nodal plane. The interaction arises in a slightly more complicated way: "spin polarization". As shown in Figure 2.6, the C $2p_z$ orbital has zero probability at the H nucleus, but there is significant overlap of the C $2p_z$ and C–H σ bond orbitals. The H 1s orbital is part of the σ-bond orbital and the C $2p_z$ part of the singly-occupied π* MO (SOMO). In the overlap region of these two MOs, there is a tendency for the unpaired spin in the SOMO to polarize the pair of electrons in the bonding MO such that the spins in the overlap region are parallel, necessarily leaving an oppositely oriented spin near the H nucleus.

For aromatic hydrocarbon radical anions, this approach works pretty well. Figure 2.7 shows a correlation plot of observed hyperfine splitting *versus* the spin density calculated from Hückel MO theory. It also correctly predicts the negative sign of a^H for protons attached to π systems.
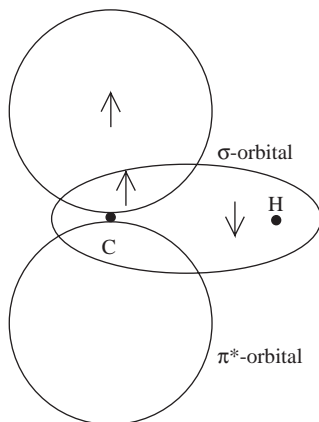
Figure 2.6 Schematic representation of spin polarization of a C–H σ-orbital by electron spin in a π* orbital. Note that the polarization effect is far from complete; only a tiny fraction of the electron density near the H nucleus is excess spin-down.
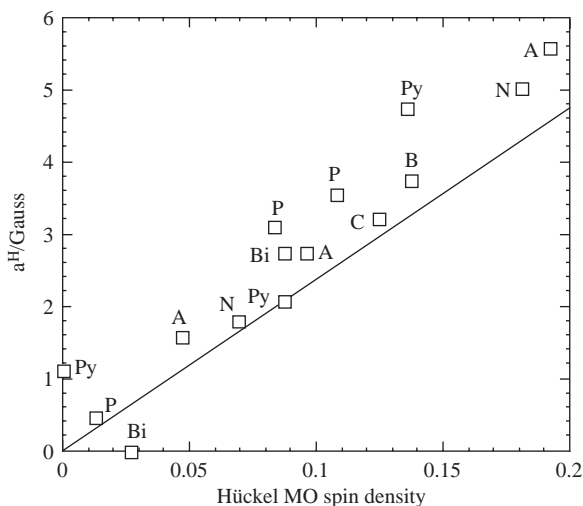
Figure 2.7 Correlation plot of observed ^{1}H coupling constant *vs.* computed spin density from Hückel MO theory. See Table 2.1 for identification of points.

Examination of Figure 2.7 shows that the largest fractional errors are for the smallest spin densities. The reason for this is related to the mechanism for aromatic proton coupling. Positions with very small spin density, according to Hückel MO theory, tend to be polarized such that a negative spin density is found at that site. Thus the zero spin density predicted for one position in pyrene leads to a coupling of a bit more than 1 G as a result of this polarization mechanism. Note that the sign of a coupling constant is not an experimental result in ordinary ESR. The alternation of the sign of a^H between positions was

confirmed by performing NMR measurements of the Knight shift of pyrene anion radical in the solid state.[10]

It is sometimes assumed that there is a relation analogous to eqn (2.6) for metal or ligand hyperfine couplings in spectra of organometallic radicals. Such an assumption is usually unwarranted. An isotropic hyperfine coupling has three contributions: (i) Fermi contact interaction between the nuclear spin and electron spin density in the valence-shell s-orbital; (ii) Fermi contact interaction between the nuclear spin and spin density in inner-shell s-orbitals arising from spin polarization by unpaired electron density in valence-shell p- or d-orbitals; and (iii) a contribution from spin–orbit coupling. The first contribution is positive (for a positive nuclear magnetic moment), the second is normally negative, and the third may be of either sign. Because direct involvement of hydrogen 1s character in the SOMO of an organic π-radical is symmetry-forbidden and spin–orbit coupling is negligible in carbon-based radicals, proton couplings in such radicals result solely from spin polarization and thus are proportional to the polarizing spin density. In contrast, all three contributions are usually significant for organometallic radicals. Although there are a few cases where polarization constants, analogous to Q_{CH}^{H}, have been estimated, they are of use only in a more complete analysis based on the results of a solid-state ESR study.

The situation with regard to protons that are attached to atoms adjacent to π centers, such as the β-protons (methyl group) of the ethyl radical, $CH_3CH_2{}^{\bullet}$, is on somewhat firmer ground. In this case a_H varies with the dihedral angle between the C–H bond and the adjacent p-orbital containing the unpaired electron. This was interpreted early on as evidence for "hyperconjugation" which delocalizes the unpaired electron onto the adjacent proton. The dependence of a_H on geometry had also proven to be a very useful tool for studying the conformations of radicals.

Most ESR studies of organic radicals were carried out in the 1950s and 1960s. They provided important tests of early developments in valence theory. The results of these early studies are nicely summarized in a review by Bowers.[11] Applications of hyperfine splittings to structure determination are discussed in many of the texts and monographs referenced in Chapter 1.

As we will see in Chapter 4, g-matrices are often difficult to interpret reliably. The interpretation of isotropic g-values is even less useful and subject to misinterpretation. Thus isotropic ESR spectra should be used to characterize a radical by means of the hyperfine coupling pattern, to study its dynamical properties through line width effects, or to measure its concentration by integration of the spectrum and comparison with an appropriate standard; but considerable caution should be exercised in interpreting the g-value or nuclear hyperfine coupling constants.

2.3 Line Widths in Isotropic Spectra

2.3.1 Incomplete Averaging of Anisotropies

Careful examination of the isotropic ESR spectra of organic radicals may reveal variations in line widths from one hyperfine component to another. Such effects

are enhanced in solvents of high viscosity or at low temperatures. The widths can often be expressed as a power series in the nuclear spin quantum numbers:

$$\text{Width} = \alpha + \sum_i \left(\beta_i m_i + \gamma_i m_i^2 + \ldots \right) \tag{2.8}$$

Much of the width arises from incomplete averaging of anisotropies in the g- and hyperfine matrices (Chapter 3). For radicals with axial symmetry the parameters of eqn (2.8) depend on $\Delta g = g_{||} - g_\perp$, $\Delta A_i = A_{i,||} - A_{i,\perp}$ and τ_R, the rotational correlation time:[12]

$$\alpha \propto \alpha_0 + (\Delta g \gamma B)^2 \tau_R \tag{2.9a}$$

$$\beta \propto \Delta g \gamma B \Delta A \tau_R \tag{2.9b}$$

$$\gamma \propto (\Delta A)^2 \tau_R \tag{2.9c}$$

Since these terms are proportional to τ_R, they increase with decreasing temperature.[†] There are several line-width contributions, included in α_0, which do not depend on m_i. These include magnetic field inhomogeneity and the spin–rotation interaction, the latter increasing with $1/\tau_R$ and thus with increasing temperature. These and other line-width effects have been studied in some detail and are discussed elsewhere.[13]

If the g- and hyperfine anisotropies are known from analysis of a solid-state spectrum, the line-width parameters β_i and γ_i can be used to compute the rotational correlation time, τ_R, a useful measure of freedom of motion. Line widths in ESR spectra of nitroxide spin labels, for example, have been used to probe the motional freedom of biological macromolecules.[14] Since τ_R is related to the molecular hydrodynamic volume, V_h, and the solution viscosity, η, by a relationship introduced by Debye:[15]

$$\tau_R = 4\pi r^3 \eta / 3kT = V_h \eta / kT \tag{2.10}$$

ESR line widths can provide a measure of the effective size of a paramagnetic molecule or ion – useful information when there is a suspicion that a radical has polymerized.

2.3.2   Rates of Fluxionality from Line Widths

ESR line widths are also sensitive to processes that modulate the g-value or hyperfine coupling constants or limit the lifetime of the electron spin state. The effects are closely analogous to those observed in NMR spectra of dynamical systems. However, since ESR line widths are typically on the order of 0.1–10 G

[†] Equations (2.9a–c) assume that the product $\tau_R \omega_0 > 1$, where ω_0 is the (angular) frequency of the microwaves. For X-band microwaves $\omega_0 = 6 \times 10^{10}$ rad s^{-1}, so these relationships hold for $\tau_R > 1.6 \times 10^{-11}$ s. Using eqn (2.10) this corresponds to the tumbling time for a molecule with a molecular weight of about 40 in water at room temperature. Equations (2.9a–c) should therefore apply to all but the smallest, *i.e.*, most rapidly tumbling, radicals in media of normal viscosity.
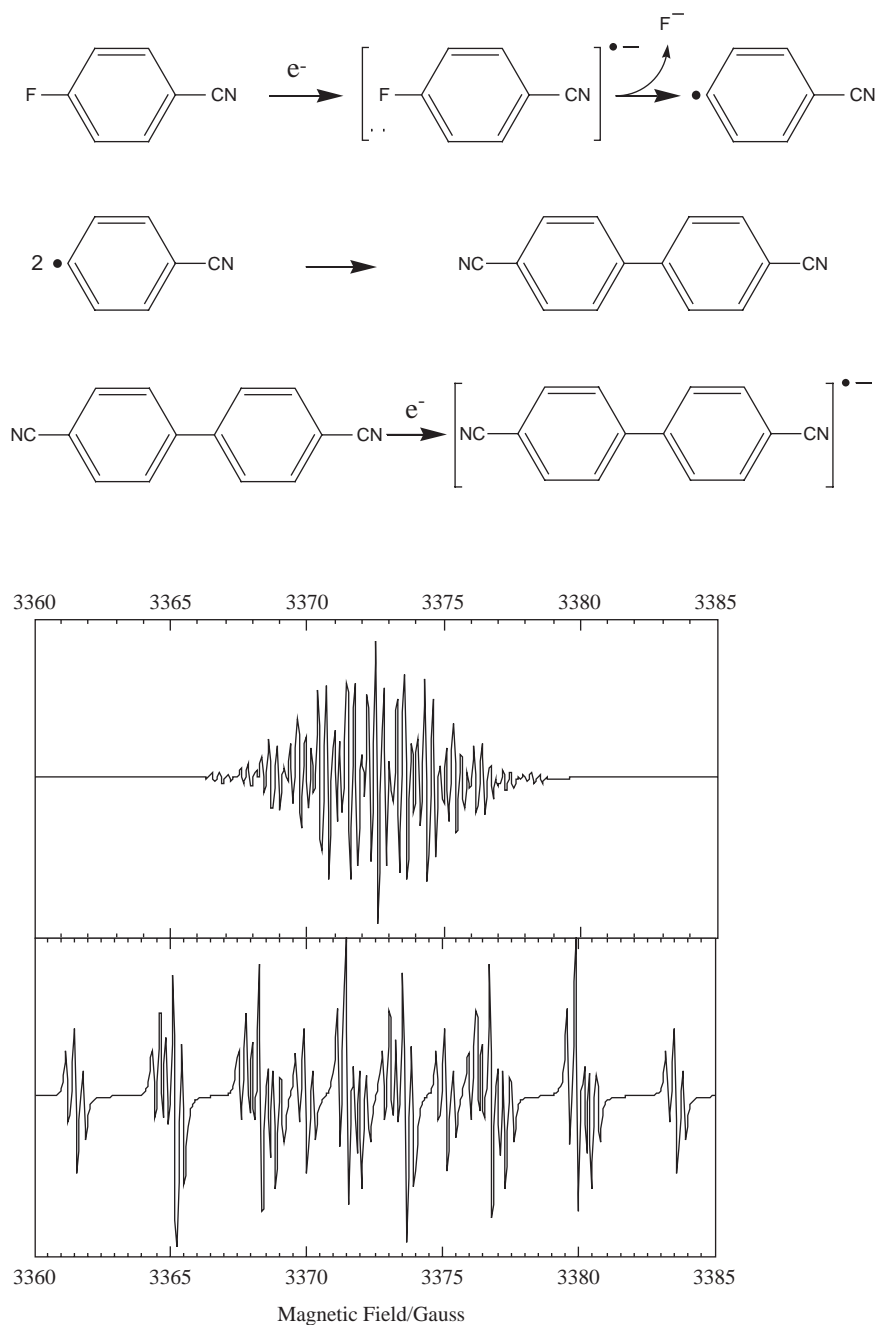
Figure 2.8 ESR spectra resulting from the reduction of PhCN (bottom) and *p*-F-PhCN (top). The top spectrum is identical to that of the 4,4′-dicyanobiphenyl anion radical. (Spectra were simulated using hyperfine couplings with permission from ref. 16, copyright (1963) American Chemical Society.)

(0.3–30 MHz), rate processes that give observable increases in line widths must be fast. Such processes are discussed in detail in Chapter 5.

2.4   Organic Radical Reactions

Sometimes the ESR spectrum obtained when an organic molecule undergoes one-electron oxidation or reduction is not of the expected cation or anion radical. Figure 2.8 shows spectra that result when benzonitrile and 4-fluorobenzonitrile are reduced electrochemically.[16] The spectrum from the reduction of benzonitrile is indeed that of $[C_6H_5CN]^{-\bullet}$, but the spectrum resulting from the reduction of FC_6H_4CN is not that of the expected radical anion. Careful examination of the spectrum shows $1:4:6:4:1$ quintets at either end of the spectrum, indicating the presence of four equivalent protons. This suggests that F^- is lost from the initially formed radical anion and that the resulting neutral radical dimerizes. In fact, the observed spectrum is identical to that obtained by one-electron reduction of 4,4′-dicyanobiphenyl, the product of radical dimerization.

   Another example from the same paper[16] involves the cyanocarbon anion, 1,1,2,3,3-pentacyanopropene. One-electron reduction produces the expected dianion radical, the spectrum of which is shown in Figure 2.9. However, further reduction leads to a very different spectrum, which results from loss of CN^- from position 2, and attachment of a proton (presumably from the solvent *N,N*-dimethylformamide) to produce the 1,1,3,3,-tetracyanopropene dianion radical the spectrum of which is also shown in Figure 2.9.

2.5   Analysis of Isotropic ESR Spectra

The analysis of an isotropic ESR spectrum is relatively straightforward if a systematic approach is used, but it can be a frustrating experience for a

3340 3342 3344 3346 3348 3350 3352 3354 3356 3358 3360
Magnetic Field/Gauss
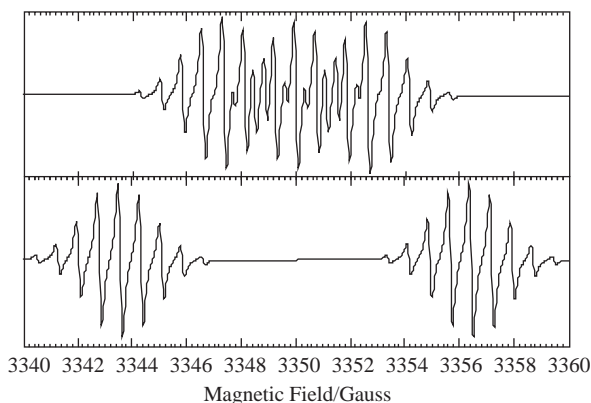
Figure   2.9   (Top) ESR spectrum of 1,1,2,3,3-pentacyanopropene dianion radical; (bottom) ESR spectrum of the dianion radical of 1,1,3,3-tetracyanopropene. Spectra were simulated using hyperfine couplings with permission from ref. 16, copyright (1963) American Chemical Society.

beginner. Given below is a series of steps which, if followed with care, will result in a successful interpretation for most reasonably well-resolved spectra.

2.5.1   Preliminary Examination of the Spectrum

(A) Check to see if the spectrum is symmetric in line positions and relative intensities. If it is not, then most likely there are two or more radical species. Variation of line widths with m_I may, in principle, cause the spectrum to appear unsymmetric, but in such a case line positions would still be at least approximately symmetrically distributed about the center.

(B) Is there a central line? If there is no central line, then there must be an even number of lines, which suggests an odd number of half-integer nuclei (*i.e.*, $I = 1/2$, $3/2$, *etc.*), which would cause splitting of any center line arising from an even number of half-integral nuclei or any number of nuclei with integer spin ($I = 1, 2$, *etc.*).

(C) Are the outermost lines visible above the noise? Observation of the lines in the "wings" of the spectrum is often crucial to successful interpretation of ESR spectra since less overlap of lines may occur there. In noisy spectra, however, it may be difficult to account for all the expected lines in the wings.

(D) How many lines are there? Count them carefully, watching for evidence of unresolved features (shoulders or bumps).

(E) What is the ratio of the amplitudes of the most intense to least intense lines in the spectrum?

2.5.2   What do you Expect to See?

(A) If the radical was produced by a chemically straightforward procedure, you usually have some idea of the identity of the radical. How many and what kinds of magnetic nuclei, *i.e.* nuclei with spins, should be present if your guess is correct?

(B) How many lines are expected from this model? The total number of nuclear spin states is $(2I_1 + 1) \times (2I_2 + 1) \times (2I_3 + 1)$ .... Thus, if the model structure has six protons ($I = 1/2$), there should be $(2 \times 1/2 + 1)^6 = 2^6 = 64$ nuclear spin states. If some of the nuclei are expected to be equivalent, then the number of lines will be less than the number of spin states, *i.e.*, some of the spin states will be degenerate (to first-order in perturbation theory). Thus, if the six protons are in three groups of two, it is as if you had three spin-1 nuclei and you expect $(2 \times 1 + 1)^3 = 3^3 = 27$ distinct lines. If there is one group of four equivalent protons and another group of two, then it is as if you had one spin-2 nucleus and one spin-1 nucleus and you expect $(2 \times 2 + 1)(2 \times 1 + 1) = 15$ lines.

If all the nuclei are non-equivalent, then all lines should have the same intensity (barring accidental overlap). If there are equivalent sets of nuclei, then the expected ratio is the product of the largest-to-smallest ratios of the various multiplets. Thus, for the above examples, three groups of two spin-1/2 nuclei gives a $1:2:1$ triplet of $1:2:1$ triplets of $1:2:1$ triplets; thus the maximum

intensity ratio would be $2 \times 2 \times 2 = 8$. If we have a $1:4:6:4:1$ quintet of $1:2:1$ triplets, then the maximum intensity ratio will be $6 \times 2 = 12$.

2.5.3 Are the Gross Features of the Spectrum Consistent with the Model?

(A) Compare the number of observed lines with the number expected. If there are more lines than expected, either the model is wrong or there is more than one radical contributing to the spectrum. If the expected and observed numbers are equal, you are in luck – the analysis should be easy. If you see fewer lines than expected (the most common case!), there may be accidental superpositions, small amplitude lines buried under large ones, or just poor resolution. The bigger the discrepancy between expected and observed numbers of lines, the less definitive the analysis will be.

(B) Compare the expected and observed largest-to-smallest intensity ratios. Accidental degeneracies (or a m_I^2 line-width dependence) may cause the observed ratio to be bigger than expected. It is rarer (but not unknown) to find a smaller ratio than expected.

(C) Is the presence or absence of a central line consistent with the odd or even number of expected lines?

(D) If the model still seems plausible after these tests, go on to a detailed analysis. If there are gross inconsistencies, the model is probably wrong.

2.5.4 An Example

We can apply these rules to the three spectra shown in Figure 2.10. The radicals in the figure are anion radicals of the three isomers of xylene (dimethylben-zene).[17] Let us see if we can figure out which is which.

The *p*-xylene anion radical is easiest. We expect to have four equivalent ring protons and six equivalent methyl protons. Thus we expect to see a $1:4:6:4:1$ quintet of $1:6:15:20:15:6:1$ septets. Spectrum (b) shows the quintet clearly, but the CH_3 proton coupling is poorly resolved. No other isomer has a quintet, so we can assign (b) to the *p*-xylene radical anion.

The *o*-xylene anion radical should have two pairs of ring protons and, again, six equivalent methyl protons. Spectrum (a) shows a $1:2:1$ triplet of multiplets, which could well be the expected quintets. The outermost lines have intensity ratios: $1:2:6:1:12:12-$, suggesting that the methyl and ring proton couplings are comparable. Apparently only one pair of ring protons has a significant coupling, but, with this assumption, spectrum (a) is consistent with *o*-xylene.

That leaves spectrum (c) for *m*-xylene. We expect two unique protons, one pair of equivalent ring protons, and six equivalent methyl protons. When we examine the wings of the spectrum, we see a $1:6:15:20:15:6$ set of doublets.

Table 2.2 gives the coupling constants for the three xylene anion radical isomers.
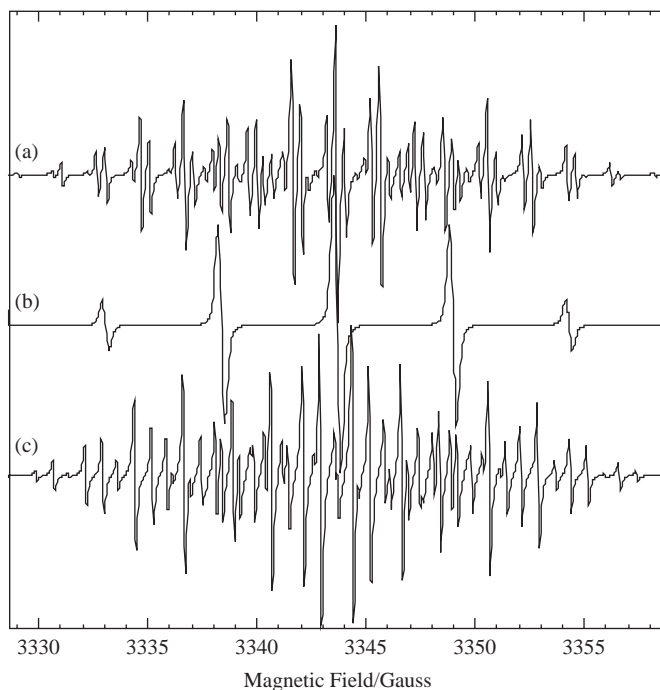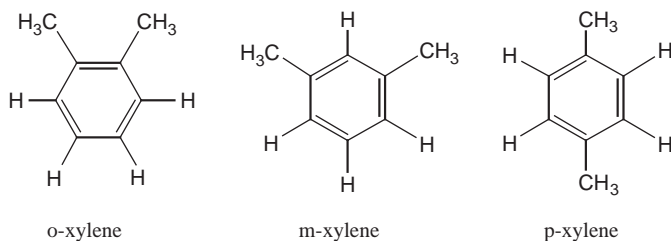
Figure 2.10 ESR spectra of *o*-, *m*-, and *p*-xylene radical anions (see text for assignment of spectra). Spectrum (a) was simulated with permission using hyperfine parameters from Ref. 17*b*, copyright (1964) American Institute of Physics; spectra (b) and (c) were simulated with permission using hyperfine parameters from ref. 17*a*, copyright (1961) Taylor and Francis (www.tandk.co.uk).

Table 2.2 Hyperfine parameters for xylene radical anions[17]

o-Xylene		*m-Xylene*		*p-Xylene*	
Number	a^H *(G)*	*Number*	a^H *(G)*	*Number*	a^H *(G)*
2 ring H	6.93	1 ring H	6.85	4 ring H	5.34
2 ring H	1.81	1 ring H	7.72	6 Me H	0.10
6 Me H	2.00	2 ring H	1.46		
		6 Me H	2.26		

2.5.5   Detailed Analysis for Determination of Parameters

(A) Measure the positions and amplitudes of all the lines in the spectrum and list them in order in a table (a spreadsheet program is convenient for this purpose). A well-defined measure of "position" in a complex spectrum is the *x*-axis point halfway between the maximum and minimum of the first-derivative line. The "amplitude" is the difference in height between the maximum and minimum. If convenient, measure the line positions in gauss; if this is inconvenient, use arbitrary units such as inches, centimeters, or recorder chart boxes measured from an arbitrary zero. In your table, also provide headings for the quantum numbers (m_1, m_2, *etc.*) for each of the line positions, for the coupling constants (a_1, a_2, *etc.*), and for the theoretical intensity (degeneracy) of each peak.

(B) The highest and lowest field lines will always have theoretical intensities of 1 and will have maximum positive and negative values for all the quantum numbers. It does not really matter whether you start with positive quantum numbers at the high-field or low-field end of the spectrum – the signs of the coupling constants are indeterminant – but, for consistency, let us agree to assign positive quantum numbers to the lowest field line (*i.e.*, pretend that the coupling constants are positive). Enter these assignments in the table. From this point on, you can work from either end of the spectrum or even from both at once. In the following, we assume that we are working from the low-field end.

(C) The spacing between the first and second lines will be the smallest coupling constant, a_1. The intensity ratio of these two lines will usually indicate the multiplet to which the coupling constant corresponds. Assign quantum numbers to the second line, compute a_1 and enter these numbers in the table. If you have started into a multiplet, you can then predict the positions and intensities of the remaining lines of the multiplet. Find them and enter the quantum numbers and new estimates of a_1 in the table.

(D) After finding all the lines of the first a_1 multiplet, find the first unassigned line as you move upfield. This will correspond to the next larger coupling constant a_2. From the ratio of its amplitude to that of the end line, you can usually figure out which multiplet this coupling constant corresponds to. Assign the quantum numbers and compute the coupling constant a_2. Enter in the table. This line will also correspond to the first line in a second a_1 multiplet, and, knowing a_1, you can predict the positions and intensities of the remaining lines of this multiplet. Find them and enter the quantum number assignments and new estimates of a_1 and a_2 in the table.

(E) If a_2 corresponds to a multiplet, the positions of the remaining lines can be predicted and located. Continue in this way through the spectrum. Small discrepancies may arise through measurement errors or because of overlapped lines. A position discrepancy larger than your estimated measurement accuracy, however, may signal a misassignment or inconsistency with the model. Notice that the spacing between the lowest and highest field lines is equal to the sum of the coupling constants. Thus, if you have found two coupling constants and know the total extent of the spectrum, you can compute the sum of the remaining couplings.

(F) When all the lines have been assigned, average all the measured values of each coupling constant and compute the standard deviation. If an arbitrary position scale was used, convert the coupling constants into gauss. Least-squares fitting of line positions to quantum numbers gives better statistics than this method, but it is impossibly tedious to do by hand in all but the simplest cases. Fortunately, computer programs and spreadsheet templates for carrying out a multiparameter least-squares analysis are now readily available.

2.5.6   Computation of Multiplet Intensity Ratios

For sets of spin-$\frac{1}{2}$ nuclei, the multiplet intensity ratios are simply the binomial coefficients found most easily from Pascal's triangle (Figure 2.11).

For higher spin nuclei, one can construct a splitting diagram. For example, for two spin-1 nuclei:

```
        first            second
      splitting         splitting       degeneracy

                                    _____ 1
                         _____
                                    _____ 2
           _____
                         _____  _____ 3
  _____
                         _____  _____ 2
                                    _____ 1
```
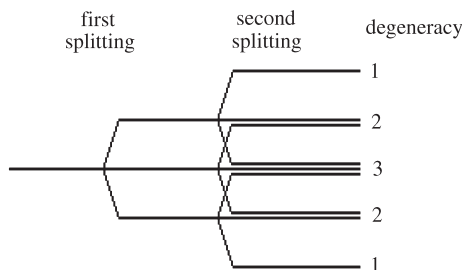
This procedure quickly gets out of hand, however, and a more compact notation is preferable. Thus if we think of each of the three lines resulting from coupling to the first spin-1 nucleus split into a $1:1:1$ triplet, we have:

	1	1	1		
		1	1	1	
			1	1	1
Add:	1	2	3	2	1

This procedure can be extended to three spin-1 nuclei by thinking of each line of a $1:1:1$ triplet split into a $1:2:3:2:1$ quintet:

	1	2	3	2	1		
		1	2	3	2	1	
			1	2	3	2	1
Add:	1	3	6	7	6	3	1

For really complicated situations, this method can be used as the basis for a computer algorithm.

```
                                    1

                                 1     1

                              1     2     1

                           1     3     3     1

                        1     4     6     4     1

                     1     5    10    10    5     1

                  1     6    15    20   15    6     1

               1     7    21    35    35   21    7     1

            1     8    28    56    70    56   28    8     1
```

**Figure 2.11**   Pascal's triangle for the determination of binomial coefficients.

2.5.7   Multiplet Patterns due to Isotopomers

We often encounter cases where an element has one or more isotopes with a nuclear spin and one or more isotopes with zero spin. The most common example is that of carbon where 1.1% of naturally occurring carbon is ^{13}C with $I = 1/2$ and 98.9% is ^{12}C with $I = 0$. Thus, in a carbon-containing radical, the probability that any given carbon is ^{13}C is 0.011. Now suppose that there are n equivalent carbon atoms in the radical. The probability that all n will be ^{12}C is $(0.989)^n$. The probability that one specific carbon is ^{13}C and the other $n-1$ ^{12}C will be $(0.011)(0.989)^{n-1}$; but, since any one of the n carbons could be ^{13}C, we see that the total probability of finding one ^{13}C is $n(0.011)(0.989)^{n-1}$. Similarly, the probability that two specific carbons are ^{13}C is $(0.011)^2(0.989)^{n-2}$, but any one of the n carbons could be ^{13}C and any of the $n-1$ remaining carbons could also be ^{13}C, so that the total probability of having two ^{13}Cs is $n(n-1)(0.011)^2(0.989)^{n-2}$. Since the two ^{13}Cs are indistinguishable, however, the coefficient must be divided by 2 to avoid double counting. On reflection, we see that the coefficients 1, n, $n(n-1)/2$, are just binomial coefficients and that the probabilities of finding 0, 1, 2, *etc.*, ^{13}Cs out of n equivalent carbon atoms are just the terms in the expansion of the expression:

$$(0.989 + 0.011)^n = (0.989)^n + n(0.989)^{n-1}(0.011)$$
$$+ n(n-1)/2(0.989)^{n-2}(0.011)^2 + \cdots$$

For example, in a radical with six equivalent carbon atoms (*e.g.*, benzene anion radical), the probabilities are: $P_0 = 0.936$, $P_1 = 0.062$, $P_2 = 0.0017$, $P_3 = 0.00003$, *etc.* In practice, we would probably see only the central line with intensity 0.936 and a pair of satellites with intensity 0.031, corresponding to splitting of the center line by a single ^{13}C (the intensity is distributed between the two resonances).

   More complex patterns can arise from atoms with a higher fraction of magnetic isotopes. Consider the case of a radical species with three equivalent
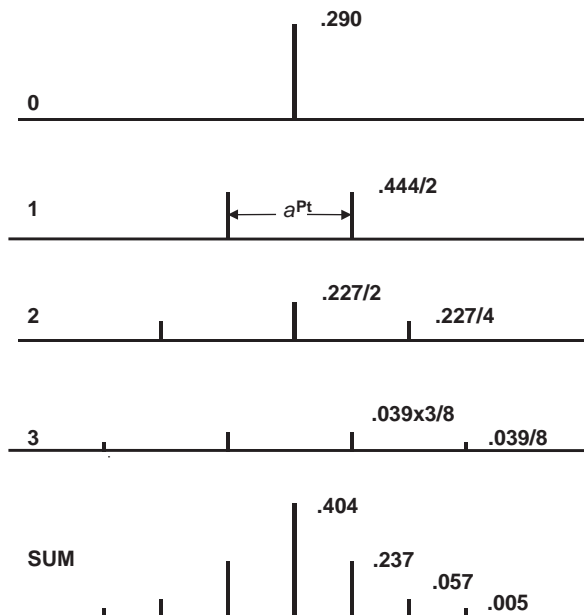
Figure 2.12 Predicted hyperfine pattern for a radical with three equivalent Pt atoms. Numbers on the left refer to the number of ^{195}Pt atoms in the radical. The intensity labels indicate the normalized probabilities of the corresponding lines which are derived from the isotope probabilities.

platinum atoms. ^{195}Pt has $I = 1/2$ and is 33.8% in natural abundance. Other Pt isotopes have $I = 0$. Thus the probabilities are: $P_0 = 0.290$, $P_1 = 0.444$, $P_2 = 0.227$, and $P_3 = 0.039$. These four isotopomers will result, respectively, in a singlet, a doublet, a $1:2:1$ triplet, and a $1:3:3:1$ quartet. However, since the platinum atoms are assumed to be equivalent, the coupling constant will be the same in each pattern and there will be some superpositions. Consequently, seven hyperfine components are expected with positions and intensities (Figure 2.12).

The relative intensities of the seven-line pattern then is expected to be approximately: $1:12:49:84:49:12:1$. With luck, all seven lines might be observable. Patterns like this are more complicated to analyze, but they also provide a fingerprint, identifying the number of equivalent nuclei involved in the multiplet pattern.

2.5.8 Second-order Shifts in Line Positions

Our analysis thus far has assumed that solution of the spin Hamiltonian to first order in perturbation theory will suffice. This is often adequate, especially for spectra of organic radicals, but when coupling constants are large (greater than about 20 gauss) or when line widths are small (so that line positions can be very accurately measured) second-order effects become important. As we see from

eqn (2.5) for a single nucleus with nuclear spin I, the hyperfine line positions are given to second order in perturbation theory by:

$$B = B_0 - am_I - \frac{a^2}{2B_0}\left[I(I+1) - m_I^2\right] \tag{2.11}$$

Thus, for example, a spin-1 nucleus with $a = 20$ G and $B_0 = 3200$ G will have lines at:

$$B = 3200 - 20(+1) - (0.0625)(2-1) = 3179.94 \text{ G}$$
$$B = 3200 - 20(0) - (0.0625)(2-0) = 3199.88 \text{ G}$$
$$B = 3200 - 20(-1) - (0.0625)(2-1) = 3219.94 \text{ G}$$

so that the line spacings are, respectively, 19.94 and 20.06 G, and the center line is shifted to low field (relative to the first-order result) by 0.12 G. This is a rather small effect and would require careful measurements to notice. When a is larger, the shifts are much more noticeable. Thus, for example, when $a = 100$ G, the line spacings become 98.44 and 101.56 G, a much more easily noticeable discrepancy.

When a spectrum results from coupling to several equivalent nuclei with couplings large enough to warrant second-order corrections, the situation becomes somewhat more complicated since we must then think of the quantum numbers I and m_I corresponding to the sum of the quantum numbers for a full set of equivalent nuclei. The second-order corrections then depend on the total I rather than the individual I_is. Thus, for example, two equivalent spin-1 nuclei will give rise to an $I = 2$ state with $m_I = \pm 2, \pm 1$, and 0. There is only one way of getting $m_I = \pm 2$ (each nucleus has $m_{Ii} = \pm 1$), but there are two ways of getting $m_I = \pm 1$ (either of the nuclei can have $m_{Ii} = 0$ and the other $m_{Ii} = \pm 1$), so there must also be a $I = 1$ state with $m_I = \pm 1$ and 0. There are three ways of getting a $m_I = 0$ state (either of the nuclei can have $m_{Ii} = \pm 1$ and the other $m_{Ii} = \pm 1$ or both nuclei can have $m_{Ii} = 0$); thus there must be a $I = 0$ state with $m_I = 0$. Substituting into eqn (2.11), to second-order, the degeneracies of the $1:2:3:2:1$ multiplet pattern are lifted and a total of $(3)^2 = 9$ individual lines would be observed. Summarizing these results in Table 2.3, we have, for $B_0 = 3200$ G, $a = 20$ G:

Table 2.3   Second-order shifts for two $I = 1$ nuclei

m_I	I	$[I(I+1) - m_I^2]/2$	B (G)
2	2	1	3159.88
1	2	5/2	3179.69
1	1	1/2	3179.94
0	2	3	3199.62
0	1	1	3199.88
0	0	0	3200.00
−1	2	5/2	3219.69
−1	1	1/2	3219.94
−2	2	1	3239.88

2.6 Related Techniques (ENDOR)

The instrumental method described in Chapter 1 and illustrated in this chapter proves to be adequate for studying many of the samples to which chemists and biologists wish to apply ESR. Indeed, even if more advanced techniques turn out to be required, CW, field-swept X-band ESR still provides the most convenient, and commonly used, method for preliminary examination of samples that are known, or suspected, to possess interesting paramagnetic properties. Nevertheless, for those who may need to extend their studies to more advanced methods Appendix 2 lists several of the most useful techniques and gives references to recent reviews and relevant papers that should serve as an entry into the still developing literature on advanced ESR.

This chapter concludes with a brief description of one advanced technique, Electron Nuclear Double Resonance (ENDOR), the capabilities for which, unlike pulsed methods, may be added as a relatively minor modification to commercial CW ESR spectrometers.

ENDOR was first developed in the mid-1950s[18] by George Feher as a means of determining unresolved nuclear hyperfine coupling parameters in solids. It has since found many other applications, including simplifying the hyperfine patterns of complex radicals in solution. The technique works by partially saturating an ESR transition at a fixed field while simultaneously sweeping the NMR frequency through nuclear spin transitions. The result, which is illustrated in Figure 2.13 for a single spin-1/2 nucleus, is an increase in absorption at the microwave frequency when an appropriate NMR transition is irradiated. In Figure 2.13 the vertical arrow on the left refers to the orientation of the electron spin and the one on the right the nuclear spin. At equilibrium, the lower and upper pairs of levels have relative populations indicated by $1+\delta$ and $1-\delta$, respectively [see Section 1.2 (Chapter 1)]. In the example, saturation of one of the ESR transitions initially equalizes the populations of the $\downarrow\uparrow$ and $\uparrow\uparrow$ levels, leading to a decrease in intensity of that transition. If the NMR transition from
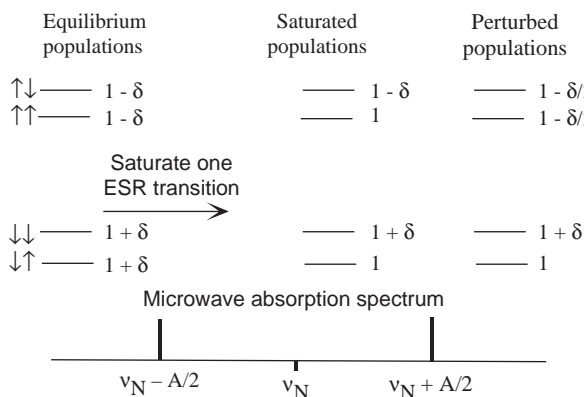
Figure 2.13 Example of an ENDOR experiment for a single spin-1/2 nucleus. See text for explanation.

Table 2.4 Hyperfine parameters for bis(*p*-methoxyphenyl)nitroxide[19]

Position	N	*o-H*	*m-H*	*Me*
a (G)	9.99(1)	1.962(2)	0.764(2)	0.249(2)

↑↑ to ↑↓ is then saturated by irradiation at the frequency of the corresponding NMR transition at, in this example, $v_N + A/2$, the resulting population change will lead to an increase in the population difference between the ↓↑ and ↑↑ levels and increased microwave absorption at the ESR frequency. Irradiation of the other NMR transition, ↓↑ to ↓↓, at frequency $v_N - A/2$, will also lead to an increase in intensity of the same saturated ESR transition. The ENDOR spectrum is generated by varying the NMR frequency and observing the corresponding increase in intensity of the saturated ESR transition. Notably, the example given here corresponds to the case where the hyperfine frequency, $A = A/h$, is less than the nuclear Zeeman frequency, v_N. For the case where $A/2 > v_N$, interpretation of the ENDOR frequencies is somewhat modified. The interested reader should consult the relevant references in Appendix 2 or one of the more general books on ESR.

An early example of an application of ENDOR to extract hyperfine couplings from a very complex, poorly resolved ESR spectrum is that of Allendoefer and Englemann[19] who studied a solution of bis(*p*-methoxyphenyl)nitroxide and obtained the results shown in Table 2.4. The figures in parentheses indicate the level of precision.

References

1. S.I. Weissman, J. Townsend, G.E. Paul and G.E. Pake, *J. Chem. Phys.*, 1953, **21**, 2227.
2. E.W. Stone and A.H. Maki, *J. Chem. Phys.*, 1963, **39**, 1635.
3. R.W. Fessenden and R.H. Schuler, *J. Chem. Phys.*, 1963, **39**, 2147.
4. R.W. Fessenden, *J. Chem. Phys.*, 1962, **37**, 747.
5. R.W. Fessenden and R.H. Schuler, *J. Chem. Phys.*, 1965, **43**, 2704.
6. R.G. Lawler, J.R. Bolton, M. Karplus and G.K. Fraenkel, *J. Chem. Phys.*, 1967, **47**, 2149.
7. (*a*) G.K. Fraenkel, *J. Chem. Phys.*, 1965, **42**, 4275; (*b*) R.D. Allendoerfer and P.H. Rieger, *J. Chem. Phys.*, 1967, **46**, 3410.
8. H.M. McConnell, *J. Chem. Phys.*, 1956, **24**, 633.
9. M. Karplus and G.K. Fraenkel, *J. Chem. Phys.*, 1961, **35**, 1312.
10. M.E. Anderson, P.J. Zandstra and T.R. Tuttle, *J. Chem. Phys.*, 1960 **33**, 1591.
11. K.W. Bowers, in *Advances in Magnetic Resonance*, ed. J. S. Waugh, 1965, **1**, 317.

12. (*a*) D. Kivelson, *J. Chem. Phys.*, 1960, **33**, 1094; (*b*) R. Wilson and D. Kivelson, *J. Chem. Phys.*, 1966, **44**, 154; (*c*) P.W. Atkins and D. Kivelson, *J. Chem. Phys.*, 1966, **44**, 169.
13. *Electron Spin Relaxation in Liquids*, ed. L.T. Muus and P.W. Atkins, Plenum Press, New York, 1972.
14. H.M. McConnell, in *Foundations of Modern EPR*, ed. G.R. Eaton, S.S. Eaton and K.M. Salikhov, World Scientific, Singapore, 1998, ch. G.5.
15. See, for example, N. Bloembergen, E.M. Purcell and R.V. Pound, *Phys. Rev.*, 1948, **73**, 579.
16. P.H. Rieger, I. Bernal, W.H. Reinmuth and G.K. Fraenkel, *J. Am. Chem. Soc.*, 1963, **85**, 683.
17. (*a*) J.R. Bolton and A. Carrington, *Mol. Phys.*, 1961, **4**, 497; (*b*) J.R. Bolton, *J. Chem. Phys.*, 1964, **41**, 2455.
18. G. Feher, *Phys. Rev.*, 1959, **114**, 1219.
19. R.D. Allendoerfer and J.H. Englemann, *Mol. Phys.*, 1971, **20**, 569.

CHAPTER 3

Isotropic Spectra of Organometallic Radicals

Most of the information content from ESR spectra of organometallic radicals and coordination complexes comes from dilute single-crystal spectra or frozen solution spectra. Nonetheless, there are some bits of information and applications that come uniquely from isotropic spectra, and we discuss those aspects in this chapter.

3.1 Second-order Effects on Line Positions

As illustrated in Chapter 2, ESR spectra of radicals in liquid solution can usually be interpreted in terms of the spin Hamiltonian:

$$\hat{H}_s = \mu_B g \mathbf{B} \cdot \hat{\mathbf{S}} + \sum_i A_i \hat{\mathbf{I}}_i \cdot \hat{\mathbf{S}} \tag{3.1}$$

This is a simplified Hamiltonian that ignores the direct interaction of any nuclear spins with the applied field, B. Because of the larger coupling, A_i, to most transition metal nuclei, however, it is often necessary to use second-order perturbation theory to accurately determine the isotropic parameters g and A. Consider, for example, the ESR spectrum of vanadium(IV) in acidic aqueous solution (Figure 3.1), where the species is $[VO(H_2O)_5]^{2+}$.

Clearly, the eight hyperfine lines ($I = 7/2$ for ^{51}V) have different widths; but careful examination also shows that the line spacing varies, increasing with increasing B. To understand the origin of this effect we must take a closer look at the solutions to Eqn. (3.1) for the case of an unpaired electron interacting with a single nucleus. This will lead us to a derivation of eqns (2.5) and (2.11) of Chapter 2.

Given the Hamiltonian eqn (3.1), it is reasonable to express the eigenfunctions in terms of the electron and nuclear spin quantum numbers: $|m_S, m_I\rangle$. Applying to this function only the two terms in the Hamiltonian operator that involve the z-direction of the field B we get:

$$\begin{aligned} \hat{H}_s |m_s, m_I\rangle &= \left(g\mu_B B \hat{S}_z + A\,\hat{S}_z \hat{I}_z \right) |m_s, m_I\rangle \\ &= \left(m_s g\mu_B B + A m_s m_I \right) |m_s, m_I\rangle \end{aligned} \tag{3.2}$$

44
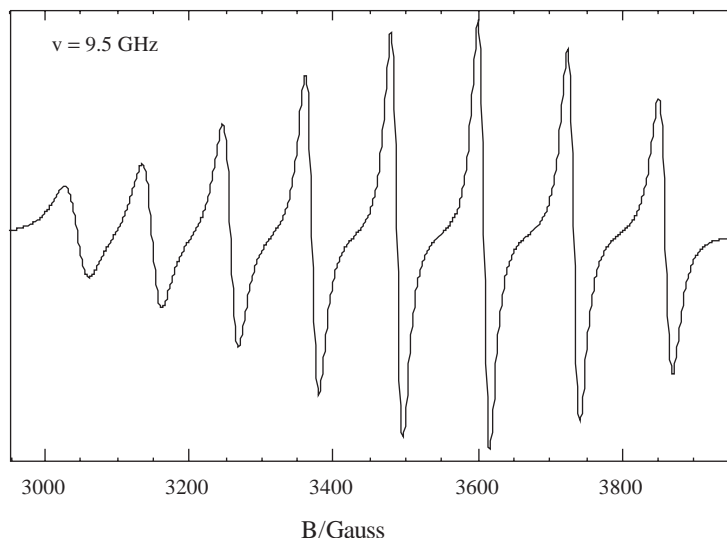
Figure 3.1 Isotropic ESR spectrum of 0.005 M vanadium(IV) in 1 M NaClO$_4$, pH 2.0. (Reproduced with permission from ref. 3, copyright (1975) American Chemical Society.)

Thus the zeroth-order, or unperturbed, energy is:

$$E^{(0)} = m_s g \mu_B B + m_s m_I A$$

or, since $m_S = \pm 1/2$:

$$E^{(0)} = \pm \tfrac{1}{2} g \mu_B B \pm \tfrac{1}{2} m_I A$$

With $I = 7/2$, $m_I = \pm 7/2, \pm 5/2, \pm 3/2, \pm 1/2$. This "first-order" solution[†] would of course lead to eight lines, equally spaced.

Now consider the application of second-order perturbation theory. First, we need to represent the $x-y$ components of the spins, S_x, S_y, I_x and I_y, in terms of their raising and lowering combinations:

$$S_\pm = S_x \pm iS_y \quad I_\pm = I_x \pm iI_y$$

$$S_x = \frac{1}{2}(S_+ + S_-) \quad I_x = \frac{1}{2}(I_+ + I_-)$$

$$S_y = -\frac{i}{2}(S_+ + S_-) \quad I_y = -\frac{i}{2}(I_+ + I_-)$$

[†] By convention, the hyperfine energy is usually referred to as a "first-order" correction to the Zeeman energy. This nomenclature will also be used here, despite the fact that the notation $E^{(0)}$ properly acknowledges that both terms are included in the "zeroth-order" energy. Strictly speaking, in this case there is no first-order perturbation.

Thus the hyperfine term of the spin Hamiltonian becomes:

$$A\mathbf{S} \cdot \mathbf{I} = A\big(S_x I_x + S_y I_y + S_z I_z\big) = A S_z I_z + \tfrac{1}{2}A(S_+ I_- + S_- I_+)$$

Operating on the spin functions with the extra hyperfine operator then gives:

$$\tfrac{1}{2}A\big(\hat{S}_+\hat{I}_- + \hat{S}_-\hat{I}_+\big)|\tfrac{1}{2}, m_I\rangle$$

$$= \frac{A}{2}\sqrt{I(I+1) - m_I(m_I+1)}\,|-\tfrac{1}{2}, m_I+1\rangle$$

$$\tfrac{1}{2}A\big(\hat{S}_+\hat{I}_- + \hat{S}_-\hat{I}_+\big)|-\tfrac{1}{2}, m_I\rangle$$

$$= \frac{A}{2}\sqrt{I(I+1) - m_I(m_I-1)}\,|\tfrac{1}{2}, m_I-1\rangle$$

Thus the matrix elements are:

$$\langle -\tfrac{1}{2}, m_I+1|\hat{H}|+\tfrac{1}{2}, m_I\rangle = \frac{A}{2}\sqrt{I(I+1) - m_I(m_I+1)}$$

$$\langle +\tfrac{1}{2}, m_I-1|\hat{H}|-\tfrac{1}{2}, m_I\rangle = \frac{A}{2}\sqrt{I(I+1) - m_I(m_I-1)}$$

and the second-order energy corrections are:

$$E^{(2)}\big(\tfrac{1}{2}, m_I\big) = \frac{A^2[I(I+1) - m_I(m_I+1)]}{4\big(E^{(0)}\big(+\tfrac{1}{2}, m_I\big) - E^{(0)}\big(-\tfrac{1}{2}, m_I+1\big)\big)}$$

$$E^{(2)}\big(-\tfrac{1}{2}, m_I\big) = \frac{A^2[I(I+1) - m_I(m_I-1)]}{4\big(E^{(0)}\big(-\tfrac{1}{2}, m_I\big) - E^{(0)}\big(+\tfrac{1}{2}, m_I-1\big)\big)}$$

or since the zeroth-order energy differences are:

$$E^{(0)}\big(+\tfrac{1}{2}, m_I\big) - E^{(0)}\big(-\tfrac{1}{2}, m_I+1\big) = g\mu_B B + \tfrac{1}{2}A(1 + 2m_I)$$

$$E^{(0)}\big(-\tfrac{1}{2}, m_I\big) - E^{(0)}\big(+\tfrac{1}{2}, m_I-1\big) = -g\mu_B B + \tfrac{1}{2}A(1 - 2m_I)$$

$$E^{(2)}\big(\tfrac{1}{2}, m_I\big) = \frac{A^2[I(I+1) - m_I(m_I+1)]}{4g\mu_B B + \tfrac{1}{2}A(1 + 2m_I)}$$

$$E^{(2)}\big(-\tfrac{1}{2}, m_I\big) = \frac{A^2[I(I+1) - m_I(m_I-1)]}{4g\mu_B B + \tfrac{1}{2}A(1 - 2m_I)}$$

We can neglect the hyperfine terms in the denominators without serious error since $4g\mu_B B \gg \tfrac{1}{2}A(1 \pm 2m_I)$. Including them would lead to energies that are third-order or higher in powers of A, making it necessary to use higher order perturbation theory.[1]

Table 3.1 Higher order effects on line positions in $[VO(H_2O)_5]^{2+}$

m_I	First-order positions	Second-order positions	Exact positions[a]	Second-order spacing[b]
7/2	3048.6	3040.8	3041.6	103.9
5/2	3165.0	3144.7	3146.2	108.8
3/2	3281.4	3253.5	3254.8	113.4
1/2	3397.8	3366.9	3367.2	117.4
−1/2	3514.2	3484.3	3483.7	121.1
−3/2	3630.6	3605.4	3604.1	124.4
−5/2	3747.0	3729.8	3728.4	127.5
−7/2	3863.4	3857.3	3856.6	

[a] Calculated to nearest 0.1 G using methods given in ref. 1 by iterative solution of the Breit-Rabi equation.
[b] 1st-order spacing of lines would be 116.4 G.

The transition energies, correct to second order in A, are:

$$\Delta E = g\mu_B B + m_I A$$

$$+\left\{ \frac{A^2[I(I+1) - m_I(m_I+1)]}{4g\mu_B B} \right\} - \left\{ -\frac{A^2[I(I+1) - m_I(m_I-1)]}{4g\mu_B B} \right\}$$

$$= g\mu_B B + m_I A + \frac{A^2\left[I(I+1) - m_I^2\right]}{2g\mu_B B}$$

and the resonant fields are:

$$B = B_0 - a m_I - \frac{a^2\left[I(I+1) - m_I^2\right]}{2B} \tag{3.3}$$

where

$$B_0 = \frac{h\nu}{g\mu_B} \qquad a = \frac{A}{g\mu_B}$$

For $[VO(H_2O)_5]^{2+}$ (Fig. 3.1), $g = 1.964$, $a = 116.4$ G, and $\nu = 9.5000$ GHz. The predicted line positions (in Gauss) are given in Table 3.1.

3.2 Understanding the Variation in Line Widths

The widths of the lines in Fig. 3.1 vary because the anisotropies of g and A (to be discussed in Chapter 4) are not completely averaged out when the molecule or ion tumbles in solution. This issue was implicit in the classic work of Bloembergen, Purcell and Pound[2a] on nuclear spin relaxation and was formulated in a useful way for EPR by Daniel Kivelson and co-workers.[2b–d] As described in Chapter 2, they showed that the widths, in units of Hz, can often be written as a power series in m_I with terms up to second-order (a third-order term is sometimes significant):

$$\text{width}(m_I) = \alpha + \beta m_I + \gamma m_I^2 \tag{3.4}$$

where

$$\alpha \propto \alpha_0 + (\Delta g \gamma B)^2 \tau_R \qquad (3.5a)$$

$$\beta \propto \Delta g \gamma B \Delta A \, \tau_R \qquad (3.5b)$$

$$\gamma \propto (\Delta A)^2 \tau_R \qquad (3.5c)$$

and τ_R is the rotational correlation time, usually expressed in an equation first introduced by Debye:[2]

$$\tau_R = \frac{4\pi r^3 \kappa}{3} \frac{\eta}{kT} \qquad (3.6)$$

where η is the viscosity of the solution, r is the radius of the (spherical) particle, and κ is a correction factor to account for deviations from sphericity. The rotational correlation time therefore provides a measure of the "hydrodynamic volume" of the tumbling molecule or ion. If values of Δg and ΔA can be determined independently, *e.g.*, from solid state spectra (Chapter 4), line width measurements may be used to evaluate τ_R as a function of η and T, allowing r to be estimated.

For example, dilute aqueous solutions of vanadium(IV) show an eight-line ESR spectrum in both acid (Fig. 3.1) and strong base, suggesting a monomeric unit under all conditions. (^{51}V has $I = 7/2$ so more than eight lines would be observed if more than one ^{51}V was coupled to the unpaired electron.) A likely structure in base would be $[VO(OH)_3(H_2O)_2]^-$, formed by removal of three protons from the species whose spectrum is shown in Fig. 3.1.[3] Previous work on the system, however, was also consistent with the formation of polymers such as $V_3O_7^{2-}$ or $V_4O_9^{2-}$ or even $V_{18}O_{42}^{12-}$ at high pH. Comparison of values of τ_R from the basic solution line widths with those obtained from spectra of acidic solutions containing $VO(H_2O)_5^{2+}$ showed that the hydrodynamic volume of the aquo cation is actually about twice that of the basic solution species, effectively ruling out the presence of ESR-active polymers in solution (Figure 3.2).[4] The slopes correspond to r values of 3.4 Å in acid solution and 2.7 Å in basic solution. The conclusion is that vanadium(IV) is monomeric in dilute basic solutions.

3.3 Puzzling Line Shapes

An example of second-order splitting, in addition to the second-order shifts described above for a single nucleus, and related to the spectrum of methyl radical discussed in Chapter 2, is seen in Fig. 3.3 for the isotropic ESR spectrum of $[PhCCo_3(CO)_9]^-$ (ref. 5). The situation is complicated by the fact that magnetically equivalent nuclei with $I > 1/2$ give less familiar multiplet intensity ratios. Thus, for example, three equivalent ^{59}Co nuclei ($I = 7/2$) give (to first-order) 22 lines with intensity ratios 1:3:6:10:15:21:28:36:42:46:48:48:46 . . . , (Figure 3.3a). The experimental spectrum of $[PhCCo_3(CO)_9]^-$ (Figure 3.3c)
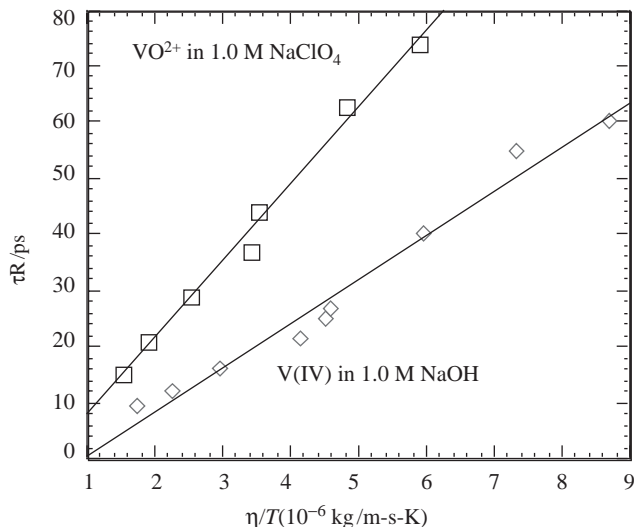
Figure 3.2 Plots of τ_R, determined from ESR line widths, *vs.* η/T for $[VO(H_2O)_5]^{2+}$ and for $[VO(OH)_3(H_2O)_2]^-$. Data from ref. 4.

does indeed exhibit a spectrum with about the expected relative intensities, and all but the weakest outermost pair of lines is visible. The observed line shapes, however, are very unsymmetrical and correspond to a marked deviation from a Lorentzian shape. Incorporating second-order splittings into the spectrum as follows solves the puzzle.

The combined spin angular momentum of three equivalent spin-7/2 ^{59}Co nuclei is properly described in terms of 11 J-states with J ranging from 21/2 to 1/2. The line positions through second-order are then calculated using Eqn. (3.3) substituting J for I. The $m_J = 17/2$ feature, for example, has three components with $J = 21/2$, 19/2, and 17/2, degeneracies of 1, 2, and 3, and second-order shifts of $97a^2/4B$, $55a^2/4B$, and $17a^2/4B$, respectively. The shifts are too small compared with the line width to be resolved, but they lead to an asymmetric absorption line envelope with apparent broadening on the low-field side, as shown in Figure 3.3(b) and in the experimental spectrum (Figure 3.3c).[5]

3.4 Use of ESR Spectra to Determine Formation Constants

Reeder and Rieger[6] used ESR spectra to identify complex ions and to estimate formation constants for aqueous oxovanadium(IV) complexes with lactic acid, thiolactic acid, glycolic acid, and thioglycolic acid. Through the use of second-harmonic detection, which produces second-derivative spectra, the resolution was good enough that several of the individual species could be separately
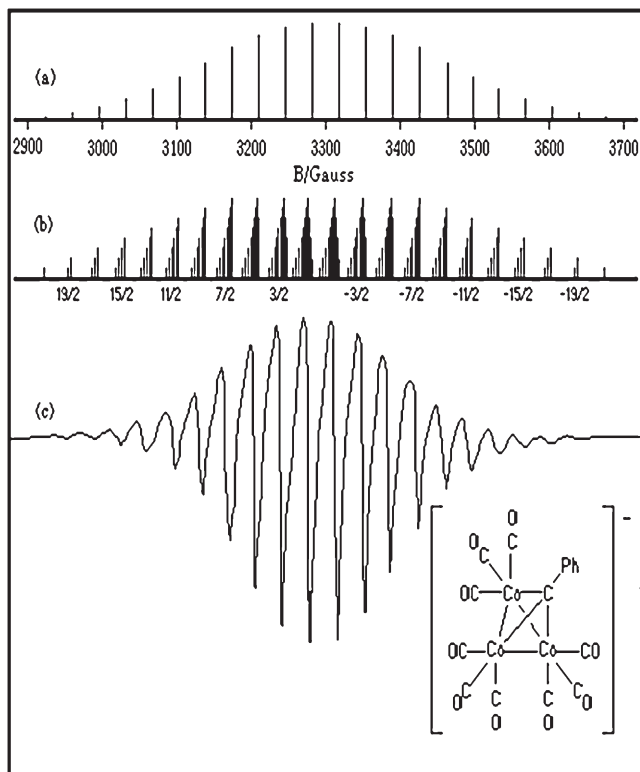
Figure 3.3 "Stick spectrum" showing hyperfine pattern for coupling to three equiva-
lent ^{59}Co nuclei ($I = 7/2$) computed to (a) first-order and (b) second-order
in perturbation theory. (Adapted from ref. 7.) (c) Isotropic ESR spectrum
of $[PhCCo_3(CO)_9]^-$ in THF solution at 40°C.
(Experimental spectrum, reprinted from ref. 5 with permission, copyright
(1979) American Chemical Society.)

detectable. The key requirement was that the ^{51}V coupling constant varied with
the nature of the ligands, the coupling constant decreasing with each additional
ligand coordinated. For each acid, H_2A, the equilibria were:

$$VO^{2+} + HA^- \rightleftharpoons VO(HA)^+$$

$$VO(HA)^+ + HA^- \rightleftharpoons VO(HA)_2$$

$$VO(HA)^+ \rightleftharpoons VO(A) + H^+$$

$$VO(HA)_2 \rightleftharpoons VO(A)(HA)^- + H^+$$

$$VO(A)(HA)^- \rightleftharpoons VO(A)_2^{2-} + H^+$$
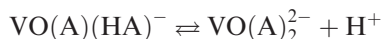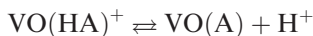
where HA^- indicates ionization of the carboxyl group but retention of the
hydroxyl or sulfhydryl proton. For example, for VO^{2+}/lactic acid mixtures at
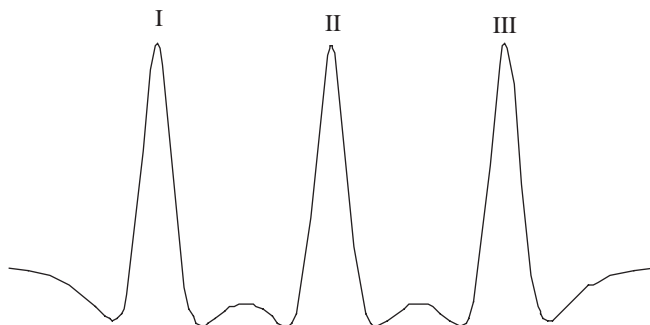
Figure 3.4 Second-derivative ESR spectrum of the low-field line of the VO^{2+} octet for a 1:4 mole ratio mixture of VO^{2+} and lactic acid at pH 3.5 and 25°C. The separation between peaks is approximately 25 Gauss.
(Reprinted with permission from ref. 6, copyright (1971) American Chemical Society.)

pH 3.5, the low-field hyperfine line (in second-derivative presentation) appears as shown in Figure 3.4.

Peak I was assigned to the superposition of peaks resulting from $VO(H_2O)_5^{2+}$ and $VO(HA)(H_2O)_3^+$; peak II was assigned to $VO(HA)_2(H_2O)$, and peak III to the superposition of $VO(A)(H_2O)_3$ and $VO(A)(HA)(H_2O)^-$. From the variation in peak heights with pH, a reasonable set of formation constants was deduced for each of the complexes.

References

1. N.M. Atherton, *Electron Spin Resonance: Theory and Practice*, John Wiley and Sons, Inc., New York, 1973, section 3.12. For solutions through fourth-order see also: R.W. Fessenden and R.H. Schuler, *J. Chem. Phys.*, 1965, **43**, 2704.
2. (*a*) N. Bloembergen, E.M. Purcell and R.V. Pound, *Phys. Rev.*, 1948 **73**, 679; (*b*) D. Kivelson, *J. Chem. Phys.*, 1960, **33**, 1094; (*c*) R. Wilson and D. Kivelson, *J. Chem. Phys.*, 1966, **44**, 154; (*d*) P. W. Atkins and D. Kivelson, *J. Chem. Phys.*, 1966, **44**, 169.
3. M.M. Iannuzzi and P.H. Rieger, *Inorg. Chem.*, 1975, **14**, 2895.
4. M.M. Iannuzzi, C.P. Kubiak and P.H. Rieger, *J. Phys. Chem.*, 1976, **80**, 541.
5. B.M. Peake, P.H. Rieger, B.H. Robinson and J. Simpson, *Inorg. Chem.*, 1979, **18**, 1000.
6. R.R. Reeder and P.H. Rieger, *Inorg. Chem.*, 1971, **10**, 1258.
7. P.H. Rieger, *Journal of Organometallic Chemistry Library*, ed. W.C. Trogler, Elsevier, Amsterdam, 1990, vol. 22, ch. 8.

CHAPTER 4[†]
Anisotropic ESR Spectra

4.1 Introduction

The anisotropies that lead to line broadening in isotropic ESR spectra influence solid-state spectra more directly. Accordingly a more complex spin Hamiltonian is required to interpret such spectra:

$$\hat{H}_s = \mu_B \vec{\mathbf{B}} \cdot \mathbf{g} \cdot \vec{\mathbf{S}} + \sum_i \vec{\mathbf{I}}_i \cdot \mathbf{A}_i \cdot \vec{\mathbf{S}} \tag{4.1}$$

In eqn (4.1), g and A_i are 3×3 matrices representing the anisotropic Zeeman and nuclear hyperfine interactions. In general, a coordinate system can be found – the g-matrix principal axes – in which g is diagonal. If g and A_i are diagonal in the same coordinate system, we say that their principal axes are coincident.

In species with two or more unpaired electrons, a fine structure term must be added to the spin Hamiltonian to represent electron spin–spin interactions. We confine our attention here to radicals with one unpaired electron ($S = 1/2$) but will address the $S > 1/2$ problem in Chapter 6.

Nuclear quadrupole interactions introduce line shifts and forbidden transitions in spectra of radicals with nuclei having $I > 1/2$. In practice, quadrupolar effects are observable only in very well-resolved spectra or in spectra of radicals with nuclei having small magnetic moments and large quadrupole moments. The most extreme case of a small magnetic moment to quadrupole moment ratio is that of ^{191}Ir and ^{193}Ir. The spectra of [Ir(CN)$_6$]$^{3-}$ (ref. 1), [Ir(CN)$_5$Cl]$^{4-}$ and [Ir(CN)$_4$Cl$_2$]$^{4-}$ (ref. 2), and [Ir$_2$(CO)$_2$(PPh$_3$)$_2$(μ-RNNNR)$_2$]$^+$, R = p-tolyl (ref. 3), show easily recognizable quadrupolar effects. Other nuclei for which quadrupolar effects might be expected include ^{151}Eu/^{153}Eu, ^{155}Gd and ^{157}Gd, ^{175}Lu, ^{181}Ta, ^{189}Os, and ^{197}Au. When quadrupolar effects are important, it is usually necessary to take account of the nuclear Zeeman interaction as well. The nuclear quadrupole and nuclear Zeeman interactions add two more terms

---

[†]This chapter has been taken in part from material first published by Elsevier Publishing in The Journal of Organometallic Chemistry Library Series, *Organometallic Radical Processes*, ed. D. Trogler, 1990, ch. 8. The material from that chapter has been somewhat modified and is republished here with permission from the publisher. Figures reprinted from the chapter are designated by an "**[E]**".

to the spin Hamiltonian. Since these terms considerably complicate an already complex situation, we will deal with quadrupole effects in Chapter 7 and confine our attention here to nuclei for which quadrupolar effects can be neglected.

When a radical is oriented such that the magnetic field direction is located by the polar and azimuthal angles, θ and φ, relative to the g-matrix principal axes, the resonant field is given, to first order in perturbation theory, by:[4]

$$B = B_0 - \sum_i \frac{A_i m_i}{g\mu_B} \tag{4.2}$$

where

$$B_0 = \frac{h\nu}{g\mu_B} \tag{4.3}$$

$$g^2 = \left(g_x^2 \cos^2 \varphi + g_y^2 \sin^2 \varphi\right) \sin^2 \theta + g_z^2 \cos^2 \theta \tag{4.4}$$

$$A_i^2 = A_{ix}^2 S_{ix}^2 + A_{iy}^2 S_{iy}^2 + A_{iz}^2 S_{iz}^2 \tag{4.5}$$

$$S_{ik} = \frac{\left[g_x \sin \theta \cos \varphi \, l_{ixk} + g_y \sin \theta \cos \varphi \, l_{iyk} + g_z \cos \theta \, l_{izk}\right]}{g} \tag{4.6}$$

and the l_{ijk} are direction cosines indicating the orientation of the kth principal axis of the ith hyperfine matrix relative to the jth g-matrix principal axis. When the matrix principal axes are coincident, only one of the l_{ijk} in eqn (4.6) will be nonzero. When the hyperfine matrix components are large, second-order terms[4] must be added to eqn (4.2); these result in down-field shifts, proportional to m_i^2.

4.2 Solid-state ESR Spectra

So long as they are dilute (to avoid line broadening from intermolecular spin exchange), radicals can be studied in the solid state as solutes in single crystals, powders, glasses or frozen solutions. Radicals can be produced *in situ* by UV- or γ-irradiation of a suitable precursor in a crystalline or glassy matrix. While many organometallic radicals have been studied in this way,[5] it is often easier to obtain solid-state ESR spectra by freezing the liquid solution in which the radical is formed. Various techniques then can be used to generate radicals, *e.g.*, chemical reactions, electrochemical reduction or oxidation, or photochemical methods. Furthermore, the radical is studied under conditions more closely approximating those in which its reaction chemistry is known. Not all solvents give a satisfactory frozen solution. Highly symmetrical solvent molecules like benzene tend to freeze with semi-crystalline regions, which leads to undesirable orientation of the solute molecules. The goal is a completely random

arrangement of solutes. Toluene gives a good random glass, as do mixtures of CH_2Cl_2 and $C_2H_4Cl_2$ or of tetrahydrofuran and CH_2Cl_2.

4.2.1 Spectra of Dilute Single Crystals

Spectra of radicals in a dilute single crystal are obtained for various orientations, usually with the field perpendicular to one of the crystal axes. Each spectrum usually can be analyzed as if they were isotropic to obtain an effective g-value and hyperfine coupling constants for that orientation. Since the g- and hyperfine-matrix principal axes are not necessarily the same as the crystal axes, the matrices, written in the crystal axis system, usually will have off-diagonal elements. Thus, for example, if spectra are obtained for various orientations in the crystal xy-plane, the effective g-value is:

$$g_\varphi^2 = \left(g_{xx}\cos\varphi + g_{yx}\sin\varphi\right)^2 + \left(g_{xy}\cos\varphi + g_{yy}\sin\varphi\right)^2 \\ + \left(g_{xz}\cos\varphi + g_{yz}\sin\varphi\right)^2 \tag{4.7}$$

or

$$g_\varphi^2 = K_1 + K_2\cos 2\varphi + K_3\sin 2\varphi \tag{4.8}$$

where

$$K_1 = \frac{1}{2}\left(g_{xx}^2 + g_{yy}^2 + g_{xz}^2 + g_{yz}^2 + 2g_{xy}^2\right) \tag{4.9a}$$

$$K_2 = \frac{1}{2}\left(g_{xx}^2 - g_{yy}^2 + g_{xz}^2 - g_{yz}^2\right) \tag{4.9b}$$

$$K_3 = g_{xy}g_{xx} + g_{xy}g_{yy} + g_{xz}g_{yz} \tag{4.9c}$$

A sinusoidal plot of g_φ^2 *vs.* φ can be analyzed to determine K_1, K_2, and K_3. Exploration of another crystal plane gives another set of Ks that depend on other combinations of the g_{ij}; eventually enough data are obtained to determine the six independent values of g_{ij} (g is a symmetric matrix so that $g_{ij} = g_{ji}$). The g-matrix is then diagonalized to obtain the principal values and the transformation matrix, elements of which are the direction cosines of the g-matrix principal axes relative to the crystal axes. An analogous treatment of the effective hyperfine coupling constants leads to the principal values of the A^2-matrix and the orientation of its principal axes in the crystal coordinate system.

In their 1967 book, Atkins and Symons[6a] summarized much of the early ESR work on small inorganic radicals, many of which were produced by photolysis or radiolysis of single crystals of the precursor molecules. A good example of the application of the information that can be obtained from such single-crystal studies is the analysis of the spectrum of NO_3, produced by γ-irradiation of KNO_3 crystals by Livingston and Zeldes.[6b] Table 4.1 summarizes the results.

Table 4.1 ESR parameters for NO$_3$[6b]

$g_{xx} = 2.0232$	$g_{yy} = 2.0232$	$g_{zz} = 2.0031$
$A_{xx} = 3.46$ G	$A_{yy} = 3.46$ G	$A_{zz} = 4.31$ G

The data clearly show that NO$_3$ in this medium has axial symmetry, most likely with a three-fold axis passing through the nitrogen atom. Furthermore, the relatively small ^{14}N hyperfine splitting is consistent with spin density localized to a large degree on the oxygen atoms. While the geometry may in principle also be obtained from vibrational and rotational spectra, the spin density distribution would be inferred only indirectly without the ESR data.
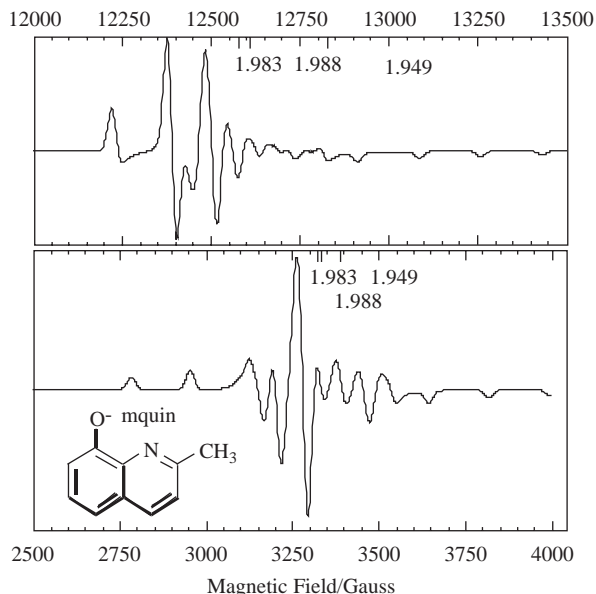
Dilute solutions of well-oriented paramagnetic molecules can also sometimes be prepared by co-crystallization with a suitable diamagnetic host. Much of the early work by Bleaney and co-workers (Chapter 1, ref. 2) on transition metal ions was carried out this way. In such samples one may often obtain not only the desired ESR parameters but also determine the orientation of the paramagnetic molecule within the host crystal. A good example of this approach is the work by Collison and Mabbs[7] who studied [VO(mquin)$_2$] (mquin = 2-methylquinolin-8-olate) dissolved in a single crystal of [GaCl(mquin)$_2$], using both X- and Q-band spectrometers. As it happened, [GaCl-(mquin)$_2$] was not the perfect host and the ESR matrix axes differed from the crystal axes by 11.7°. Furthermore, the g-matrix axes were not coincident with the A-matrix axes, being displaced in the *xy*-plane by $\alpha = 27.5°$. The frozen solution spectrum (in toluene) of [VO(mquin)$_2$] and the powder spectrum of [VO(mquin)$_2$] in [GaCl(mquin)$_2$] are nearly identical. Simulations of the powder spectra at X- and Q-band are shown in Figure 4.1. The spectra of Figure 4.1 illustrate one of the advantages of higher frequencies over X-band ESR spectra: The various g-components are better separated and the spectrum is more easily analyzed.

The next section deals with the analysis of frozen solution spectra.

4.2.2 Analysis of Frozen Solution Spectra

Since ESR spectra are normally recorded as the first derivative of absorption *vs.* field, observable features in the spectrum of a powder correspond to molecular orientations for which the derivative is large in magnitude or changes in sign. For any spin Hamiltonian, there will be minimum and maximum resonant fields at which the absorption changes rapidly from zero, leading to a large value of the derivative and features that resemble positive-going and negative-going absorption lines. Peaks in the absorption envelope correspond to derivative sign changes and lead to features resembling isotropic derivative lines. The interpretation of a powder spectrum thus depends on the connection of the positions of these features to the g- and hyperfine-matrix components.

Frozen solution spectra must be taken in solvents that form good glasses. A random but homogeneous distribution of the species to be studied is required to obtain a well-resolved spectrum. Notably, some solvents, such as toluene, can "crack" when frozen, thus giving rise to more features than predicted as spectra

from different regions of the sample will be overlapped. Thawing and refreezing of the sample often corrects the problem; but it is well to keep the predicted number of features in mind when attempting to interpret the results. Drago has given a list of good glass-forming solvents and mixtures.[8]

Early treatments of powder patterns attempted to deal with the spatial distribution of resonant fields by analytical mathematics.[9] This approach led to some valuable insights but the algebra is much too complex when non-axial hyperfine matrices are involved. Consider the simplest case: a single resonance line without hyperfine structure. The resonant field is given by eqn (4.3). Features in the first derivative spectrum correspond to discontinuities or turning points in the absorption spectrum that arise when $\partial B/\partial \theta$ or $\partial B/\partial \varphi$ are zero:

$$\frac{\partial B}{\partial \theta} = \frac{h\nu}{\mu_B} \frac{g_z^2 - g_\perp^2}{g^3} \sin \theta \cos \theta = 0 \tag{4.10a}$$

$$\frac{\partial B}{\partial \phi} = \frac{h\nu}{\mu_B} \frac{g_x^2 - g_y^2}{g^3} \sin^2 \theta \sin \phi \cos \phi = 0 \tag{4.10b}$$

and

$$g_\perp^2 = g_x^2 \cos^2 \varphi + g_y^2 \sin^2 \varphi$$

These equations have three solutions: (i) $\theta = 0$; (ii) $\theta = 90°$, $\varphi = 0$; and (iii) $\theta = \varphi = 90°$. Since θ and φ are in the g-matrix axis system, observable features are expected for those fields corresponding to orientations along the principal axes of the g-matrix. This being the case, the principal values of the g-matrix are obtained from a straightforward application of eqn (4.10).

Powder spectra with hyperfine structure often can be interpreted similarly with spectral features identified with orientation of the magnetic field along one of the g- and hyperfine-matrix principal axes. However, this simple situation often breaks down. Using a first-order theory and one hyperfine coupling, Ovchinnikov and Konstantinov[10] have shown that eqns (4.10) may have up to six solutions corresponding to observable spectral features. Three of these correspond to orientation of B along principal axes, but the "extra lines" correspond to less obvious orientations. Even more extra lines may creep in when the spin Hamiltonian is treated to second-order or when there is more than one hyperfine coupling. The problem is illustrated by the resonant field *vs.* $\cos \theta$ and φ surface shown in Figure 4.2, corresponding to $m_{Cu} = -3/2$ in the spectrum of Cu(acac)$_2$ ($g = 2.0527, 2.0570, 2.2514$; $A^{Cu} = 27.0, 19.5,$
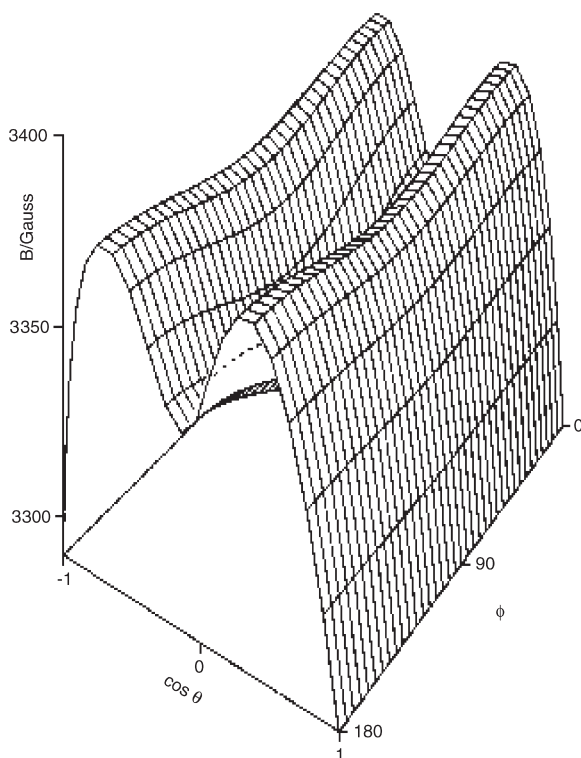
Figure 4.2 [E] Resonant field as a function of $\cos \theta$ and φ for the $m_{Cu} = -3/2$ "line" of the frozen solution spectrum of Cu(acac)$_2$, ESR parameters from ref 10. (Figure reproduced from ref. 13.)

193.4×10^{-4} cm^{-1}).[10] The minimum resonant field, $B = 3290.7$ G, corresponds to B along the z-axis ($\cos\theta = \pm 1$). With B along the x-axis ($\cos\theta = 0$, $\varphi = 0°$), the surface shows a saddle point at 3344.3 G (which corresponds to a maximum in the absorption spectrum and therefore appears with closely spaced maximum and minimum first-derivative features), and with B along the y-axis ($\cos\theta = 0$, $\varphi = 90°$) there is a local minimum at 3325.5 G. In addition, another saddle point occurs in the yz-plane at $B = 3371.2$ G ($\cos\theta = \pm 0.482$, $\varphi = 90°$); the only maximum is in the xz-plane at $B = 3379.0$ G ($\cos\theta = \pm 0.459$, $\varphi = 0°$). Thus five features are expected and indeed are shown in the computer-simulated spectrum of Cu(acac)$_2$ shown in Figure 4.3. Interestingly, the two most intense features, high-field, correspond to off-axis field orientations and thus are "extra lines". The situation is more complex when the g- and hyperfine-matrix principal axes are non-coincident (see below); in this case, none of the features need correspond to the orientation of B along a principal axis direction.

Since the analytical approach is so complicated, powder patterns have usually been analyzed by comparing the experimental spectrum with a computer-simulated spectrum using estimates of the g- and hyperfine-matrix components.[11] Parameters are then adjusted and another simulation computed until the fit is satisfactory (or the experimentalist loses patience with the problem). The most straightforward computer simulation method[10] involves computation of the resonant magnetic field using eqn (4.2) for $ca.$ 10^5 values of $\cos\theta$ and φ for each set of nuclear spin quantum numbers. The field is then divided into equal increments and the number of times the resonant field falls between B_i and B_{i+1} is plotted $vs.$ B to give an approximation to the unbroadened absorption spectrum. The absorption spectrum is then broadened by numerical convolution with a line shape function and differentiated to give the desired simulation. Although such a "cut and try" approach to spectrum
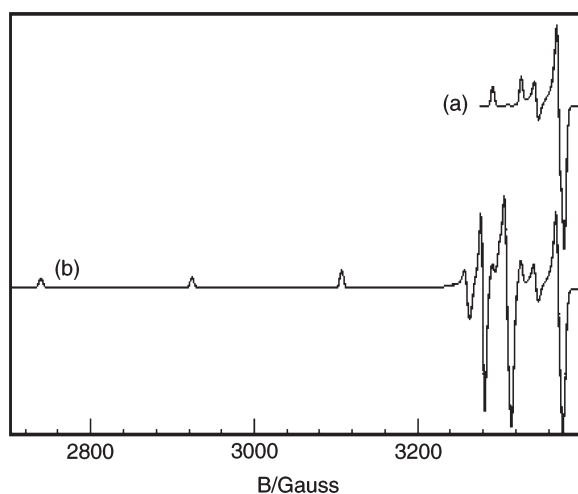
Figure 4.3 [E] Computer-simulated first-derivative ESR powder spectrum of Cu(acac)$_2$. (a) Features corresponding to $m_{Cu} = -3/2$, (b) the complete spectrum.

analysis works reasonably well when there are small numbers of parameters, analysis of a complex spectrum is exceedingly tedious.

DeGray and Rieger[12] have developed a computer algorithm to locate powder pattern features in spectra, given estimates of the spin Hamiltonian parameters. The method employs a search of the resonant field surface in $\cos\theta$, φ space for maxima, minima, and saddle points. Since the search procedure requires computation of B for only ~ 100 orientations, the method is much faster than a complete simulation. The predicted locations of spectral features are then compared with the experimental values and the parameters are refined using a nonlinear least-squares method. Using this method, relatively complex powder patterns can be analyzed, provided that the spectrum is sufficiently well-resolved that enough features can be located and identified to provide statistically significant estimates of the parameters. Even with least-squares fitting, however, comparison of the experimental spectrum with a high-resolution computer simulation is required to check the assignments of spectral features.

4.3 Interpretation of the *g*-Matrix

The *g*-value of a free electron is a scalar, $g_e = 2.00232$. In a radical species, g becomes a matrix because of the admixture of orbital angular momentum into S through spin–orbit coupling. The components of the *g*-matrix thus differ from g_e to the extent that p-, d-, or f-orbital character has been incorporated, and they differ from one another, depending on which p-, d-, or f-orbitals are involved.

In general, the components of the *g*-matrix are given by:

$$g_{ij} = g_e \delta_{ij} + 2 \sum_k \sum_{m \neq 0} \frac{\zeta_k \langle m | l_{ki} | 0 \rangle \langle 0 | l_{kj} | m \rangle}{E_0 - E_m} \qquad (4.11)$$

where the indices i and j refer to molecular coordinate axes (x, y, z), k sums over atoms with unpaired electron density, and m sums over filled and empty molecular orbitals with energy E_m (E_0 is the energy of the SOMO); ζ_k is the spin–orbit coupling constant for atom k, and l_{ki} is the i-component orbital angular momentum operator for atom k. The integrals $\langle m | l_{ki} | n \rangle$ are easily computed for an electron centered on a single atom if the MOs are written as linear combinations of real p or d atomic orbitals. Table 4.2 shows the results of operation by l_i on these functions. Thus, for example, in the usual shorthand notation for p and d orbitals:

$$\langle z | l_x | y \rangle = i \quad \text{and} \quad \langle z^2 | l_y | xz \rangle = -\sqrt{3}i$$

The orbital angular momentum operations needed to calculate integrals for other orbitals are summarized in Table 4.2.

Notice that d_{z^2} is unique among the d-orbitals in that l_z does not couple it to any other orbital. Thus if the major metal contribution to the SOMO is d_{z^2}, g_z will be close to the free electron value. Accordingly, when one *g*-matrix

Table 4.2 [E] Angular momentum operations on the real p and d orbitals

	l_x	l_y	l_z
$\lvert x \rangle$	0	$-i\lvert z \rangle$	$i\lvert y \rangle$
$\lvert y \rangle$	$i\lvert z \rangle$	0	$-i\lvert x \rangle$
$\lvert z \rangle$	$-i\lvert y \rangle$	$i\lvert x \rangle$	0
$\lvert x^2 - y^2 \rangle$	$-i\lvert yz \rangle$	$-i\lvert xz \rangle$	$2i\lvert xy \rangle$
$\lvert xy \rangle$	$i\lvert xz \rangle$	$-i\lvert yz \rangle$	$-2i\lvert x^2 - y^2 \rangle$
$\lvert yz \rangle$	$i\lvert x^2 - y^2 \rangle + \sqrt{3}i\lvert z^2 \rangle$	$i\lvert xy \rangle$	$-i\lvert xz \rangle$
$\lvert xz \rangle$	$-i\lvert xy \rangle$	$i\lvert x^2 - y^2 \rangle - \sqrt{3}i\lvert z^2 \rangle$	$i\lvert yz \rangle$
$\lvert z^2 \rangle$	$-\sqrt{3}i\lvert yz \rangle$	$\sqrt{3}i\lvert xz \rangle$	0

component is found close to the free electron value, it is often taken as evidence for a d_{z^2}-based SOMO; such reasoning should be applied with caution, however, since cancellation of negative and positive terms in eqn (4.11) could have the same effect.

Spin–orbit coupling to empty MOs ($E_0 - E_m < 0$) gives a negative contribution to g_{ij} whereas coupling to filled MOs has the opposite effect. Thus, for example, ESR spectra of d[1] vanadium(IV) complexes generally have g-values less than g_e (admixture of empty MOs) whereas d[9] copper(II) complexes have g-values greater than g_e (admixture of filled MOs).

Since the g-matrix has only three principal values and there are almost always many potentially interacting molecular orbitals, there is rarely sufficient information to interpret a g-matrix with complete confidence. When a well-resolved and reliably assigned optical spectrum is available, the energy differences, $E_0 - E_m$, are known and can be used in eqn (4.11) to estimate the contribution of the corresponding MOs to the g-matrix. Extended Hückel MO (EHMO) calculations can be useful (but do not trust EHMO energies!), but one is most commonly reduced to arguments designed to show that the observed g-matrix is consistent with the interpretation placed on the hyperfine matrix.

4.4 Interpretation of the Hyperfine Matrix

Electron–nuclear hyperfine coupling arises mainly through two mechanisms: (i) The Fermi contact interaction between the nuclear spin and s-electron spin density; this contribution, designated A, is isotropic and has been discussed in Chapters 2 and 3. (ii) The electron spin–nuclear spin magnetic dipolar interaction; this contribution is almost entirely anisotropic, i.e., neglecting spin–orbit coupling, the average dipolar contribution to the hyperfine coupling is zero.

The general form of the dipolar contribution to the hyperfine term of the Hamiltonian is:

$$\hat{\boldsymbol{H}}_{\text{dipolar}} = g_e g_N \mu_B \mu_N \left\langle \psi_{\text{SOMO}} \left| \frac{\vec{\boldsymbol{S}} \cdot \vec{\boldsymbol{I}}}{r^3} - \frac{3(\vec{\boldsymbol{S}} \cdot \vec{\mathbf{r}})(\vec{\boldsymbol{I}} \cdot \vec{\mathbf{r}})}{r^5} \right| \psi_{\text{SOMO}} \right\rangle \tag{4.12}$$

where g_e and g_N are the electron and nuclear g-values, μ_B and μ_N are the Bohr and nuclear magnetons, and the matrix element is evaluated by integration over the spatial coordinates, leaving the spins as operators. Equation (4.12) can then be written:

$$\hat{H}_{\text{dipolar}} = \vec{I} \cdot A_d \cdot \vec{S} \tag{4.13}$$

where A_d is the dipolar contribution to the hyperfine matrix, and the total hyperfine coupling is:

$$A = AE + A_d \tag{4.14}$$

(E is the unit matrix). In evaluating the matrix element of eqn (4.12), the integration over the angular variables is quite straightforward.[14] The integral over r, however, requires a good atomic orbital wavefunction. Ordinarily, the integral is combined with the constants as a parameter:

$$P = g_e g_N \mu_B \mu_N \langle r^{-3} \rangle \tag{4.15}$$

P has been computed using Hartree–Fock atomic orbital wavefunctions and can be found in several published tabulations[14–17] and in Appendix 1. Because of the $\langle r^{-3} \rangle$ dependence of P, dipolar coupling of a nuclear spin with electron spin density on another atom is usually negligible.

If an atom contributes p_x, p_y, and p_z atomic orbitals to the SOMO:

$$c_x |x\rangle + c_y |y\rangle + c_z |z\rangle \tag{4.16}$$

the total p-orbital spin density is (in the Hückel approximation, *i.e.*, neglecting overlap):

$$\rho^p = c_x^2 + c_y^2 + c_z^2 \tag{4.17}$$

and the dipolar contribution to the hyperfine matrix can be written:

$$(A_d)_{ij} = \frac{2}{5} P l_{ij} \tag{4.18}$$

where the l_{ij} are:

$$l_{xx} = 2c_x^2 - c_y^2 - c_z^2 \tag{4.19a}$$

$$l_{yy} = 2c_y^2 - c_x^2 - c_z^2 \tag{4.19b}$$

$$l_{zz} = 2c_z^2 - c_x^2 - c_y^2 \tag{4.19c}$$

$$l_{ij} = -3c_i c_j \quad (i \neq j) \tag{4.19d}$$

The factor of 2/5 and the weighting of the orbital coefficients is determined by the angular factors.[14] Equations (4.17–4.19) can therefore be combined in matrix notation to write the dipolar hyperfine matrix for p-orbitals as:

$$A_d = (2/5)P\rho^p \begin{pmatrix} 2 & 0 & 0 \\ 0 & -1 & 0 \\ 0 & 0 & -1 \end{pmatrix} \qquad (4.20)$$

where ρ^p, the spin density, is defined by eqn (4.17). The p-orbital axis corresponds to the positive principal value of the matrix. When the p-orbitals are written as hybrids, the orbital shape is unchanged, but the principal axes of the hyperfine matrix, which reflect the spatial orientation of the hybrid p-orbital, differ from those in which the SOMO was formulated. Thus, for example, a p-hybrid with $c_x = c_z$ and $c_y = 0$ corresponds to a p-orbital with the major axis in the xz-plane and halfway between the x- and z-axes (Euler angle $\beta = 45°$).

Similarly, if an atom contributes d atomic orbitals to the SOMO,

$$c_{z^2}|z^2\rangle + c_{yz}|yz\rangle + c_{xz}|xz\rangle + c_{x^2-y^2}|x^2 - y^2\rangle + c_{xy}|xy\rangle \qquad (4.21)$$

the total d-orbital spin density is (in the Hückel approximation):

$$\rho^d = (c_{z^2})^2 + (c_{yz})^2 + (c_{xz})^2 + (c_{x^2-y^2})^2 + (c_{xy})^2 \qquad (4.22)$$

and the dipolar contribution to the hyperfine matrix is:[18]

$$(A_d)_{ij} = \frac{2}{7}Pl_{ij} \qquad (4.23)$$

where P is given by eqn (4.15) and the l_{ij} are:

$$\begin{aligned} l_{xx} = &- (c_{z^2})^2 - 2(c_{yz})^2 + (c_{xz})^2 \\ &+ (c_{x^2-y^2})^2 + (c_{xy})^2 - 2\sqrt{3}(c_{z^2})(c_{x^2-y^2}) \end{aligned} \qquad (4.24a)$$

$$\begin{aligned} l_{yy} = &- (c_{z^2})^2 - 2(c_{yz})^2 + (c_{xz})^2 \\ &+ (c_{x^2-y^2})^2 + (c_{xy})^2 + 2\sqrt{3}(c_{z^2})(c_{x^2-y^2}) \end{aligned} \qquad (4.24b)$$

$$l_{zz} = 2(c_{z^2})^2 + (c_{yz})^2 + (c_{xz})^2 - 2(c_{x^2-y^2})^2 - 2(c_{xy})^2 \qquad (4.24c)$$

$$l_{xy} = -2\sqrt{3}(c_{z^2})(c_{xy}) + 3(c_{yz})(c_{xz}) \qquad (4.24d)$$

$$l_{yz} = \sqrt{3}(c_{z^2})(c_{yz}) + 3(c_{xz})(c_{xy}) - 3(c_{yz})(c_{x^2-y^2}) \qquad (4.24e)$$

$$l_{xz} = \sqrt{3}(c_{z^2})(c_{xz}) + 3(c_{yz})(c_{xy}) + 3(c_{xz})(c_{x^2-y^2}) \qquad (4.24f)$$

The dipolar contribution to the hyperfine matrix for a pure d-orbital is:

$$A_{\mathrm{d}} = (\pm \tfrac{2}{7}) P \rho^{\mathrm{d}} \begin{pmatrix} 2 & 0 & 0 \\ 0 & -1 & 0 \\ 0 & 0 & -1 \end{pmatrix} \qquad (4.25)$$

where the positive sign applies for d_{z^2} and the negative sign to the other four orbitals. Hybrid combinations of d_{yz}, d_{xz}, and d_{xy} or $d_{x^2-y^2}$ and d_{xy} give a d-orbital of the same shape and the same dipolar matrix, though the principal axes in general are different from the axes in which the SOMO was formulated. Other hybrid orbitals are generally of different shape, reflected by different principal values of the dipolar matrix, usually with different principal axes.

Spin–orbit coupling perturbs these results, adding terms to the diagonal matrix components on the order of $P(g_{\mathrm{i}}-g_{\mathrm{e}})$. These can be neglected only when the g-matrix anisotropy is small. Calculation of the spin–orbit coupling corrections is fairly straightforward for mononuclear complexes where the SOMO is composed mainly of d-orbitals from a single metal.[19–21] In radicals with two or more transition metals, the spin–orbit coupling calculation is seriously nontrivial. A major part of the problem is that the solution must be gauge-invariant, *i.e.*, it must not depend on the choice of coordinate system. This problem was addressed in the context of spin–orbit coupling corrections to the g-matrix,[22] with eqn (4.11) as the result, but it has received only cursory examination with regard to spin–orbit contributions to hyperfine matrices.[23] Fortunately, polynuclear radicals containing first-row transition metals generally have g-matrix components sufficiently close to g_{e} that the problem can be ignored. As organometallic radicals with second- and third-row transition metals appear, the problem will become more urgent; it is to be hoped that some future theoretician will deem the problem worthy of attention.

The AO composition of the SOMO can often be deduced from the dipolar hyperfine matrix, particularly when the radical has enough symmetry to restrict possible hybridization. Thus an axial hyperfine matrix can usually be interpreted in terms of coupling to a SOMO composed of a single p- or d-orbital. A departure from axial symmetry may be due to spin–orbit coupling effects, if (for example) $A_{\parallel} = A_z$ and $A_x - A_y \approx P(g_x - g_y)$. If the departure from axial symmetry is larger, it is usually caused by d-orbital hybridization. The procedure is best illustrated by examples.

4.5   Organometallic Examples

### 4.5.1   A Low-spin Manganese(II) Complex

The spectrum of the low-spin manganese(II) complex, [Mn(dppe)$_2$(CO)(CN-Bu)]$^{2+}$, (dppe = Ph$_2$PCH$_2$CH$_2$PPh$_2$), in a CH$_2$Cl$_2$/THF glass is shown in Figure 4.4(a).[24] The spin Hamiltonian parameters, obtained from least-squares

fitting of the field positions of the spectral features, are given in Table 4.3, and a simulation based on those parameters is shown in Figure 4.4(b). In this case the principle axes of the g- and hyperfine-matrices are coincident.

[Mn(dppe)$_2$(CO)(CNBu)]$^{2+}$ has approximate C_{2v} symmetry, although the actual symmetry is reduced to C_2, depending on the conformation of the CH$_2$CH$_2$ bridges of the dppe ligands. Since it has a nominal d^5 configuration, the SOMO is expected to be one of the "t$_{2g}$" orbitals of an idealized octahedral complex – d$_{xz}$ (b_1), d$_{yz}$ (b_2), or d$_{x^2-y^2}$ (a_1), where the representations refer to C_{2v}. The energies of the d$_{xz}$ and d$_{yz}$ orbitals are expected to be lowered by

Table 4.3 **[E]** ESR parameters for [Mn(dppe)$_2$(CO)(CNBu)]$^{2+}$

g_{ii}	$10^4 A_{ii}^{Mn}$ (cm^{-1})	$10^4 A_{ii}^{P}$ (cm^{-1})
2.107	30.2	27.2
2.051	20.6	25.3
1.998	146.9	26.4
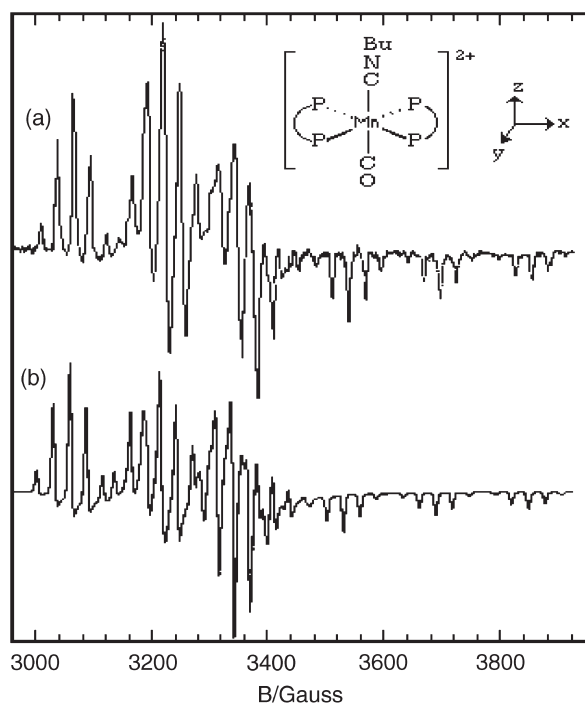
Figure 4.4 **[E]** (a) ESR spectrum of [Mn(dppe)$_2$(CO)(CNBu)]$^{2+}$ in frozen CH$_2$Cl$_2$/THF glass.
(Reproduced with permission from ref. 24, copyright (1987) Royal Society of Chemistry). (b) Computer simulation using the parameters in Table 4.3.

back-donation into the π* orbitals of the CO and CNBu ligands so that the SOMO is likely based on $d_{x^2-y^2}$:

$$|SOMO\rangle = a|z^2\rangle + b|x^2 - y^2\rangle + \cdots \quad (4.26)$$

Although the isotropic spectrum was not sufficiently resolved to unambiguously determine A^{Mn}, other closely related species give isotropic couplings on the order of 60–70 G;[25] if we assume an isotropic coupling in this range, all three matrix components must have the same sign. If the isotropic hyperfine coupling is negative, as expected if it arises mostly through polarization of inner-shell s orbitals, we have $A^{Mn} = -65.9 \times 10^{-4}$ cm^{-1}. Assuming that the SOMO is mostly $d_{x^2-y^2}$, ($b >> a$) and including the appropriate spin–orbit coupling corrections, we have:[21,26]

$$A_z - A^{Mn} = P\left[\frac{4}{7}(a^2 - b^2) - \frac{2}{3}\Delta g_z - \frac{5}{42}(\Delta g_x + \Delta g_y)\right] \quad (4.27)$$

With $\Delta g_z = -0.004$, $(\Delta g_x + \Delta g_y) = 0.154$, and $P = 207.6 \times 10^{-4}$ cm^{-1} (ref. 14), we get $(a^2-b^2) = -0.655$. The departure from axial symmetry is due to spin–orbit coupling and/or $d_{x^2-y^2}/d_{z^2}$ hybridization,

$$A_x - A_y = P\left[-\frac{8\sqrt{3}}{7}ab + \frac{17}{14}(\Delta g_x - \Delta g_y)\right] \quad (4.28)$$

Substituting the parameters, we have $ab = \pm 0.058$. (The upper sign applies if the components are listed in the order x, y, z in Table 4.3, the lower sign if the order is y, x, z.) Finally, we get $b^2 = 0.660$, $a^2 = 0.005$. The d_{z^2} component is not really significant, given the accuracy of the data and the theory, *i.e.*, most of the departure from axial symmetry can be explained by the spin–orbit coupling correction.

Using eqn (4.11), the deviations of the g-matrix components from the free-electron value, g_e, are found to be:

$$\Delta g_{xx} = 2\zeta_{Mn} \sum_k \frac{b^2 c_{yz,k}^2}{E_0 - E_k} \quad (4.29a)$$

$$\Delta g_{yy} = 2\zeta_{Mn} \sum_k \frac{b^2 c_{xz,k}^2}{E_0 - E_k} \quad (4.29b)$$

$$\Delta g_{zz} = 2\zeta_{Mn} \sum_k \frac{4b^2 c_{xy,k}^2}{E_0 - E_k} \quad (4.29c)$$

If we assume coupling with single pure d_{yz}, d_{xz}, and d_{xy} orbitals, we have $\Delta E_{yz} = 16\zeta$, $\Delta E_{xz} = 19\zeta$, $\Delta E_{xy} = -1100\zeta$, which is qualitatively consistent with the expected MO energy level scheme.

4.5.2   Some Cobalt(0) Radical Anions

ESR spectra of [CpCo(1,3-COD)]$^-$ in frozen THF solution and [CpCo(1,5-COD)]$^-$ in frozen DMF have been reported by Geiger and co-workers[27] and are reproduced in Figures 4.5(a) and 4.6(a). These spectra have been

[CpCo(1,3-COD)]$^-$ [CpCo(1,5-COD)]$^-$ [(C$_5$Ph$_5$)Co(CO)$_2$]$^-$

B/Gauss
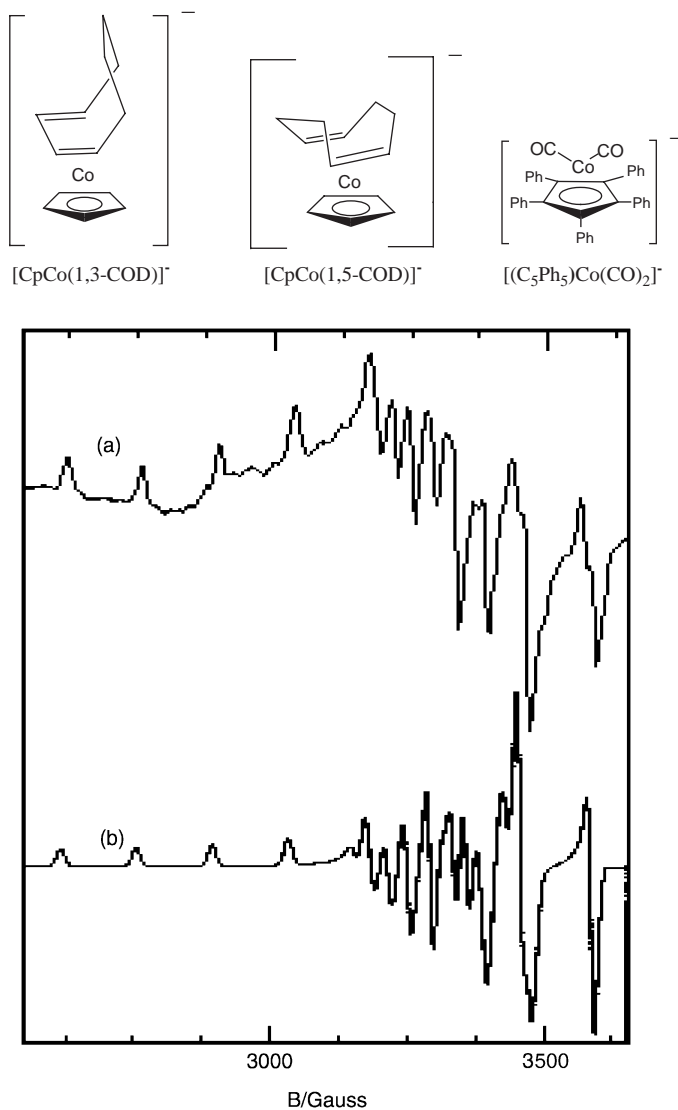
Figure   4.5   [E] ESR spectrum of [CpCo(1,3-COD)]$^-$: (a) experimental spectrum in frozen THF solution.
(Reproduced with permission from ref. 27, copyright (1981) American Chemical Society.) (b) Computer simulation, based on the parameters in Table 4.4.
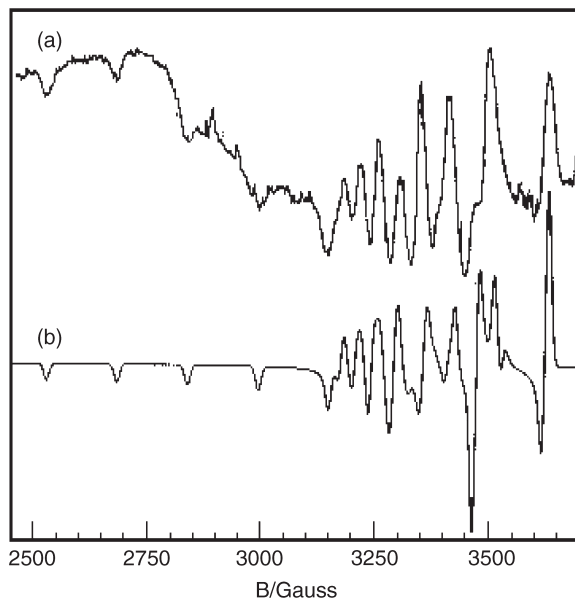
Figure 4.6 [E] (a) ESR spectrum of [CpCo(1,5-COD)]$^-$ in frozen DMF solution. (Reproduced with permission from ref. 27, copyright (1981) American Chemical Society.) (b) Computer simulation, based on the parameters in Table 4.4.

Table 4.4 [E] ESR parameters for cobalt(0) radical anions

Radical anion	g_x	g_y	g_z	$10^4 A_x (cm^{-1})$	$10^4 A_y (cm^{-1})$	$10^4 A_z (cm^{-1})$
[CpCo(1,5-COD)]$^{-a}$	2.171	2.027	1.985	158.6	36.7	45.8
[CpCo(1,3-COD)]$^{-a}$	2.151	2.027	1.997	139.2	36.4	38.2
[(C$_5$Ph$_5$)Co(CO)$_2$]$^{-b}$	2.018	2.041	1.995	157.9	16.8	44.1

[a] From ref. 27.
[b] From ref. 20.

reinterpreted to give the parameters shown in Table 4.4; computer-simulated spectra based on these parameters are shown in Figures 4.5(b) and 4.6(b). Also shown in Table 4.4 are the ESR parameters for [(C$_5$Ph$_5$)Co(CO)$_2$]$^-$.[20]

The ^{59}Co hyperfine matrix components must have identical signs in order that the average values match the observed isotropic couplings; we assume the signs are negative since the isotropic couplings almost certainly arise from polarization of inner shell s orbitals (see below).

The SOMO in these radicals is expected from extended Hückel MO calculations[27–29] to be primarily cobalt 3d$_{yz}$ in character. In the C_s symmetry of the radicals, d$_{yz}$ belongs to the a'' representation and d-hybridization is possible only with d$_{xy}$. Assuming that such hybridization is negligible, the g-matrix

Table 4.5 **[E]** Electron spin densities in cobalt($_0$) radical anions

Radical anion	ρ^d	$A_s{}^a$	A_s/Q_d
[CpCo(1,5-COD)]$^{-b}$	0.681	−97.0	0.740
[CpCo(1,3-COD)]$^{-b}$	0.591	−87.2	0.666
[(C_5Ph_5)Co(CO)$_2$]$^{-c}$	0.540	−77.4	0.591

^{a} In units of 10^{-4} cm^{-1}.
^{b} From ref. 27.^{c} From ref. 20.

components are given by:[20]

$$\Delta g_{xx} = 2\zeta_{Co} \sum_k \frac{a^2\left(c_{x^2-y^2,k}\right)^2 + 3a^2\left(c_{z^2,k}\right)^2}{E_0 - E_k} \tag{4.30a}$$

$$\Delta g_{yy} = 2\zeta_{Co} \sum_k \frac{a^2\left(c_{xy,k}\right)^2}{E_0 - E_k} \tag{4.30b}$$

$$\Delta g_{zz} = 2\zeta_{Co} \sum_k \frac{a^2\left(c_{xz,k}\right)^2}{E_0 - E_k} \tag{4.30c}$$

The dipolar contribution to the hyperfine matrix is given by eqn (4.20), but spin–orbit coupling contributions are significant. These often can be expressed in terms of the g-matrix components, as in the Mn(II) example discussed above, but here spin–orbit coupling with the four other d-orbitals contributes somewhat differently to the g-matrix and to the hyperfine matrix. The simplest way of expressing the hyperfine matrix is in terms of the isotropic coupling, the x-component, and the departure from axial symmetry. With the assumed signs of the hyperfine components of Table 4.4, eqn (4.31b) can be used unambiguously to compute $a^2 = \rho^d$ with the results shown in Table 4.5.

$$A = A_s + \frac{1}{3}P\left(\Delta g_{xx} + \Delta g_{yy} + \Delta g_{zz}\right) \tag{4.31a}$$

$$A_x - A = P\left[-\frac{4}{7}a^2 + \frac{2}{3}\Delta g_{xx} - \frac{5}{42}\left(\Delta g_{yy} + \Delta g_{zz}\right)\right] \tag{4.31b}$$

$$A_y - A_z = \frac{17P}{14}\left(\Delta g_{yy} + \Delta g_{zz}\right) + \frac{6a^2\zeta P}{7}\left(\frac{1}{\Delta E_{x^2-y^2}} - \frac{1}{\Delta E_{z^2}}\right) \tag{4.31c}$$

Since 3d$_{yz}$/4s admixture is symmetry-forbidden for these radicals, the Fermi contact contribution to the isotropic coupling, A_s, must be entirely from spin polarization,

$$A_s = Q_d\rho^d \tag{4.32}$$

Thus we can obtain an independent estimate of the d-electron spin density from the values of A_s, taking $Q_d = -131 \times 10^{-4}$ cm^{-1} – estimated from the isotropic Co coupling in $[PhCCo_3(CO)_9]^-$ (ref. 18). The results are shown in the last column of Table 4.5. The spin densities estimated from the isotropic couplings are consistently about 10% higher than those from the dipolar coupling matrix, suggesting a systematic error in one of the parameters, but a reliable ordering of the spin densities.

The *g*-matrix presents an interesting problem in these cases. EHMO calculations[27,28,29] suggest that the SOMO is the highest-energy MO, which is primarily cobalt 3d in character. At lower energy is an orbital with d_{xz} character and still lower, but grouped at about the same energy, are MOs with $d_{x^2-y^2}$, d_{xy}, and d_{z^2} contributions. Equations (4.30) then would suggest that $\Delta g_{xx}/4 \approx \Delta g_{yy} < \Delta g_{zz}$. With the assignments of Table 4.4, the first relationship is approximately correct for $[CpCo(1,3\text{-}COD)]^-$ and $[CpCo(1,5\text{-}COD)]^-$, but very poor for $[(C_5Ph_5)Co(CO)_2]^-$. The second relationship is not found for any of the anions. Reversing the *y* and *z* assignments makes the agreement worse. In discussing this problem for $[(C_5Ph_5)Co(CO)_2]^-$,[20] we postulated admixture of some cobalt 4p$_y$ character in the SOMO,

$$|\text{SOMO}\rangle = a|yz\rangle + b|y\rangle + \cdots \qquad (4.33)$$

which would result in additional contributions to g_{xx} and g_{zz}:

$$g_{xx}(\text{p}) = 2\zeta_p b^2/\Delta E_z \text{ and } g_{zz}(\text{p}) = 2\zeta_p b^2/\Delta E_x \qquad (4.34)$$

where ζ_p is the cobalt 4p spin–orbit coupling parameter ($\zeta_p \approx \zeta_d/3$). If MOs with significant p$_z$ or p$_x$ character lie just above the SOMO, then g_{xx} and g_{zz} would be less positive than expected from eqns (4.30), and possibly even negative. The component g_{xx} is indeed smaller than expected for $[(C_5Ph_5)Co(CO)_2]^-$ and EHMO calculations do indeed suggest an MO with significant p$_z$ character just above the SOMO in energy; this orbital is apparently substantially higher in energy in $[CpCo(1,3\text{-}COD)]^-$ and $[CpCo(1,5\text{-}COD)]^-$. An MO with significant p$_x$ character, at about the same energy for all three anions, is implied by these results but is unsubstantiated by the reported EHMO calculations.

4.6 Organic Examples of Solid-state ESR Spectra

Far less effort has been directed at organic solid-state spectra than at organometallics and coordination complexes. Much of the work on organic systems was done by Walter Gordy and his students at Duke University in the 1960s and 1970s. We review a couple of these experiments here. More information is available in Gordy's book.[30]

4.6.1 Irradiated Single Crystal of Glycylglycine

Katayama and Gordy[31] studied ESR spectra of γ-irradiated single crystals of glycylglycine. The data were analyzed as described above to yield the

parameters shown in Table 4.6. The axes were defined as follows: z is along the CH bond, y is in the NCHC plane $\perp$ to CH, and x is $\perp$ to the NCHC plane.

The conclusion was that the radical produced by γ-irradiation was that pictured in Table 4.6. This conclusion was based on the larger coupling to H than to N, but nonetheless there is a significant coupling to N.

## 4.6.2 X-irradiated Single Crystal of Methylene Diphosphonic Acid

Lucken and co-workers[32] subjected a single crystal of methylene diphosphonic acid to X-irradiation. The ESR spectrum indicated that the radicals produced were those pictured in Tables 4.7 and 4.8. The spectra were analyzed as described above and the results are also summarized in the tables. The species shown in Table 4.7 is the more abundant of the two. The methylene group freely rotates at room temperature but is stationary at 77 K, where splitting from two non-equivalent protons is observed for some orientations of the crystal.

Table 4.6 ESR parameters for the glycylglycine radical.[31] (H and N hyperfine splittings from nuclei in structure shown in boldface.)
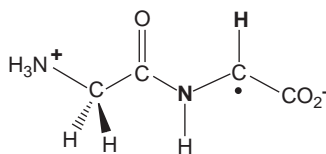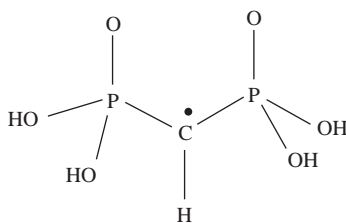

Axis	g	$a^H(G)$	$a^N(G)$
x	2.0028	19	4
y	2.0035	28	3
z	2.0033	9	2

Table 4.7 ESR parameters for the phosphonylmethyl radical[32]
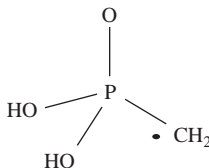
Axis	g	$a^H(G)$	$a^P(G)$
x	2.0024	16.3	38.7
y	2.0029	27.2	44.3
z	2.0022	20.4	41.4

Table 4.8 ESR parameters for the diphosphonyl-methyl radical[32]

Axis	g	$a^H(G)$	$a^P(G)$
x	2.0024	12.7	36.5
y	2.0029	30.0	38.1
z	2.0022	18.5	40.4

Table 4.9 **[E]** Symmetry restrictions on *g*-matrix components

Symmetry	Triclinic	Monoclinic	Orthorhombic	Axial
Point groups	C_1, C_i	C_2, C_s, C_{2h}	C_{2v}, D_2, D_{2h}	$C_n, C_{nv}, C_{nh}, D_n,$ $D_{nd}, D_{nh}, n > 2$
Restrictions on diagonal elements	None	None	None	$g_{xx} = g_{yy}$
Restrictions on off-diagonal elements	None	$g_{xz} = g_{yz} = 0$	$g_{xz} = g_{yz} = g_{xy} = 0$	$g_{xz} = g_{yz} = g_{xy} = 0$
Required matrix axes	None	z	x,y,z	x,y,z

4.7 Non-coincident Matrix Axes

In general, the *g*- and nuclear hyperfine coupling matrices, **g** and $\mathbf{A}_i$, can be written in diagonal form with three principal values, *i.e.*, g_x, g_y, g_z and A_{ix}, A_{iy}, A_{iz}. In textbooks on ESR[6a,30,33–35] it is usually assumed that the same set of principal axes diagonalizes all the relevant matrices. While this is sometimes true, there are many instances where the principal axes are non-coincident.[36]

4.7.1 Symmetry Considerations

Kneubühl[37,38] has given a detailed group theoretical analysis of symmetry restrictions on the orientations of *g*- and hyperfine matrix principal axes. His results are summarized in Table 4.9.

For a nucleus sharing all the molecular symmetry elements (*e.g.*, the metal nucleus in a mononuclear complex), the hyperfine matrix is subject to the same

restrictions as the *g*-matrix. In orthorhombic or axial symmetry, such nuclear hyperfine matrices necessarily share principal axes with the *g*-matrix. In monoclinic symmetry, one hyperfine axis is also a *g*-matrix axis, but the other two may be different. In triclinic symmetry (C_1 or C_i), none of the three principal axes need be shared by the *g*-matrix and hyperfine matrix. The hyperfine matrix for a ligand atom (or for a metal in polynuclear complexes) is constrained only by the symmetry elements that the nucleus shares with the molecule.

Although symmetry considerations often permit *g*- and hyperfine matrix principal axes to be non-coincident, there are relatively few cases of such non-coincidence reported in the literature. Most of the examples discussed by Pilbrow and Lowrey in their 1980 review[36] cite cases of transition metal ions doped into a host lattice at sites of low symmetry. This is not to say that matrix axis non-coincidence is rare but that the effects have only rarely been recognized.

4.7.2   Experimental Determination of Matrix Axis Orientations

We have seen that spectra of dilute single crystals are analyzed in a way that gives the orientations of the *g*- and hyperfine-matrix principal axes relative to the crystal axes. Historically, most of the information on noncoincident matrix axes is derived from such studies.

At first glance, it would appear that all orientation dependence should be lost in the spectrum of a randomly oriented sample and that location of the *g*- and hyperfine-matrix principal axes would be impossible. While it is true that there is no way of obtaining matrix axes relative to molecular axes from a powder pattern, it is frequently possible to find the orientation of a set of matrix axes relative to those of another matrix.

The observable effects of matrix axis non-coincidence on powder patterns range from blatantly obvious to negligible. In general, the effects of axis non-coincidence will be more noticeable if two (or more) matrices have large anisotropies that are comparable in magnitude, *e.g.*, $\Delta g \mu_B B \approx \Delta A$. This follows from the fact that minimum and maximum resonant fields are determined by a competition between extrema in the angle-dependent values of *g* and *A*. Consider the case of non-coincident *g*- and hyperfine-matrix axes. For large values of $|m_I|$, the field extrema will be determined largely by the extrema in the effective hyperfine coupling and will occur at angles close to the hyperfine matrix axes, but for small $|m_I|$ the extrema will be determined by extrema in the effective *g*-value and will correspond to angles close to the *g*-matrix axes. The result of such a competition is that a series of features that would be equally spaced (to first-order) acquires markedly uneven spacings.

Two corollaries stem from this generalization. Since a spin-1/2 nucleus gives only two hyperfine lines, there can be no variation in spacings. Thus powder spectra cannot be analyzed to extract the orientations of hyperfine matrix axes for such important nuclei as ^{1}H, ^{13}C, ^{19}F, ^{31}P, ^{57}Fe, and ^{103}Rh. Secondly, since the observable effects in powder spectra depend on the magnitude of the matrix

anisotropies, the principal axes of the hyperfine matrix for a nucleus with small hyperfine coupling generally cannot be located from a powder spectrum, even though the relative anisotropy may be large.

4.8 Organometallic Examples of Non-coincident Matrix Axes

4.8.1 A Chromium Nitrosyl Complex

A good example of the effect of *g*- and hyperfine matrix axis noncoincidence is the ESR spectrum of $[CpCr(CO)_2NO]^-$, studied by Geiger and co-workers;[39] a simulation is shown in Figure 4.7.
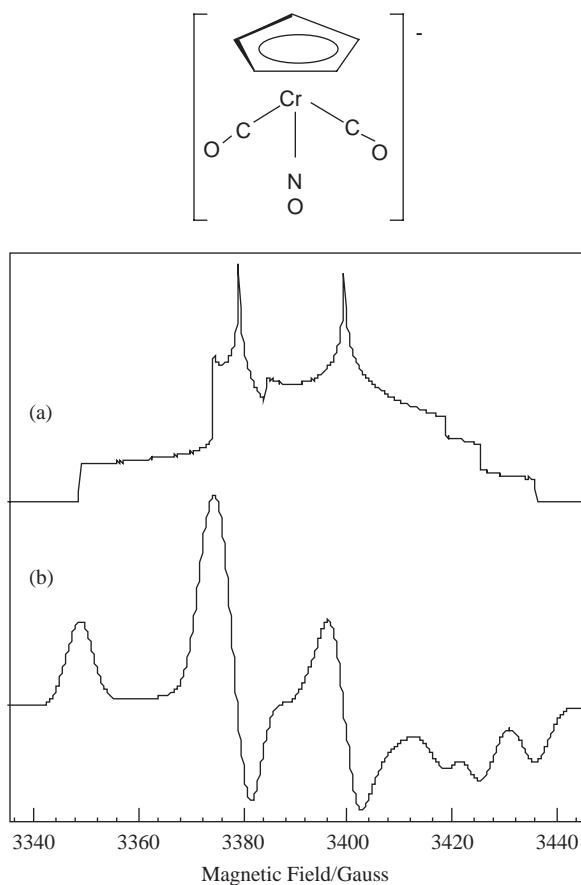
Figure 4.7 (a) Computer simulation of an absorption spectrum, zero line-width, showing positions $m_A = -1, 0, +1$. (b) First-derivative spectrum in frozen DMF.
(Reproduced with permission from ref. 39, copyright (1984) American Chemical Society.)

The *g*- and ^{14}N hyperfine matrices are approximately axial for this radical, but the $g_\parallel$ axis lies close to the perpendicular plane of the hyperfine matrix. If the $g_\parallel$ axis was exactly in the $A_\perp$ plane, the three negative-going $g_\parallel$, $A_\perp$ features, corresponding to resonant field maxima, would be evenly spaced. In fact, the spacings are very uneven – far more so than can be explained by second-order shifts. The effect can be understood, and the spectrum simulated virtually exactly, if the $g_\parallel$ axis is about 15° out of the $A_\perp$ plane.

4.8.2   Iron Pentacarbonyl Ions

Two particularly interesting organometallic examples have been reported by Morton, Preston and co-workers.[40,41] Spectra of single crystals of $Cr(CO)_6$, doped with ^{13}C- or ^{57}Fe-enriched $Fe(CO)_5$ and γ-irradiated at 77 K, showed two different radicals. One species, identified as $Fe(CO)_5{}^+$, showed coupling to ^{57}Fe and to a unique ^{13}C nucleus with axial hyperfine matrices sharing principal axes with the *g*-matrix.[40] Coupling was also observed to four other ^{13}C nuclei with identical coupling matrices but with the major axis approximately along the *g*-matrix *x*-axis for two nuclei and along the *g*-matrix *y*-axis for the other two. Table 4.10 lists the parameters.

If the radical is square pyramidal (C_{4v}) $Fe(CO)_5{}^+$ (**1**), the principal axes of the *g*-matrix must be the molecular axes (the C_4 axis and normals to the reflection planes). The iron atom and the carbon of the axial CO group would have the full symmetry of the group and so these hyperfine matrices would share principal axes with the *g*-matrix. The four equatorial carbonyl carbons, on the other hand, lie in reflection planes, but not on the C_4-axis and so are symmetry-required to share only one principal axis with the *g*-matrix. In fact, the major matrix axes for the equatorial carbons are tilted slightly in the $-z$ direction from the ideal locations along the $\pm x$ and $\pm y$ axes. The *g*-matrix suggests that the metal contribution is d_{z^2} and the iron hyperfine matrix then can be used to estimate about 55% iron 3d and 34% axial carbon $2p_z$ spin density. The spin density on the equatorial carbons then is mostly negative and due to spin polarization.

The other species observed in irradiated $Fe(CO)_5$-doped crystals of $Cr(CO)_6$ also showed coupling to ^{57}Fe, to a unique ^{13}C, and to four other carbons. However, in this case *g*, A^{Fe}, and A^{C1} have only one matrix axis in common (that corresponding to the third component of each matrix listed in Table 4.10).

Table 4.10   [E] ESR parameters for $Fe(CO)_5{}^+$ and $Fe(CO)_5{}^{-a}$

$Fe(CO)_5^+$	$g_\parallel = 2.001$	$A_\parallel{}^{Fe} = 9.4$	$A_\parallel{}^{C1} = 19.6$	$A_\parallel{}^{C2\text{-}C5} = (+)6.4$
	$g_\perp = 2.081$	$A_\perp{}^{Fe} = 6.2$	$A_\perp{}^{C1} = 17.6$	$A_\perp{}^{C2\text{-}C5} = (+)8.6$
$Fe(CO)_5^-$	$g_1 = 1.989$	$A_1{}^{Fe} = 6.7$	$A_1{}^{C1} = 87.4$	
	$g_2 = 2.003$	$A_2{}^{Fe} = 4.5$	$A_2{}^{C1} = 70.7$	
	$g_3 = 2.010$	$A_3{}^{Fe} = 3.2$	$A_3{}^{C1} = 65.7$	

^{a} Coupling constants in units of 10^{-4} cm^{-1}. Data from refs. 40 and 41.

The other ^{57}Fe hyperfine axes are rotated by about 27° and those of the ^{13}C hyperfine matrix by about 48° relative to the g-matrix axes. Insufficient data were accumulated to determine the complete hyperfine matrices for the other four carbons, but the components are considerably smaller (4–15×10^{-4} cm^{-1}). The hyperfine matrices suggest about 38% iron $3d_{z^2}$, 18% carbon 2p, and 6% carbon 2s spin densities. Using detailed arguments regarding the orientation of the g-matrix axes relative to the crystal axes, the authors conclude that the carbon 2p axis is oriented at about 106° relative to the Fe–C bond axis and that the Fe–C–O bond angle is about 119°.
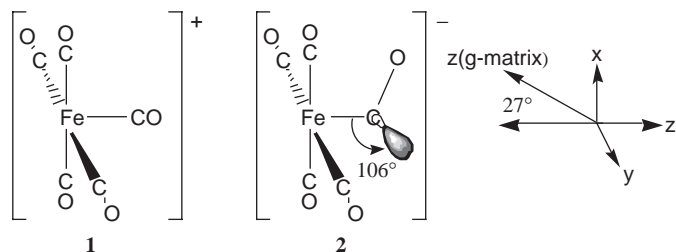
The most striking feature of these results is the orientation of the unique ^{13}C hyperfine matrix axes, relative to those of the ^{57}Fe hyperfine axes. This orientation led Fairhurst *et al.*[41] to assign the spectrum to [Fe(CO)$_5$]$^-$ (**2**) and to describe the species as a substituted acyl radical. However, these authors did not discuss the orientation of the g-matrix axes. The y-axis, normal to the reflection plane, is common to all three matrices. The x- and z-axes of the g-matrix, however, are oriented about 27° away from the corresponding ^{57}Fe hyperfine matrix axes. Since the iron d-orbital contribution to the SOMO appears to be nearly pure d_{z^2}, the ^{57}Fe hyperfine matrix major axis must correspond to the local z-axis, assumed to be essentially the Fe–C bond. Thus we must ask: Why are the g-matrix axes different? The SOMO can be written:

$$|\text{SOMO}\rangle = a|z^2, \text{Fe}\rangle + b_x|x, \text{C}\rangle + b_z|z, \text{C}\rangle \tag{4.35}$$

where $a = 0.62$, $b_x = -0.41$, and $b_z = 0.12$. Spin–orbit coupling will mix the SOMO with MOs having iron d_{yz} or d_{xz} character, but d_{yz} is involved in the π orbitals of the C $=$ O group:

$$|\pi\rangle = c_{yz}|yz, \text{Fe}\rangle + c_y|y, \text{C}\rangle \tag{4.36}$$

Assuming that there is only one π orbital close enough in energy to couple significantly, eqn (4.11) gives the g-matrix components:

$$\Delta g_{xx} = 2\zeta_{\text{Fe}} \frac{3a^2 c_{yz}^2 + \sqrt{3}ab_z c_{yz} c_y}{\Delta E_\pi} \tag{4.37a}$$

$$\Delta g_{yy} = 2\zeta_{\text{Fe}} \frac{3a^2 c_{xz}^2}{\Delta E_{xz}} \tag{4.37b}$$

$$\Delta g_{zz} = 0 \tag{4.37c}$$

$$g_{xz} = -2\zeta_{\text{Fe}} \frac{\sqrt{3}ab_x c_{yz} c_y}{\Delta E_\pi} \tag{4.37d}$$

The g-matrix can be diagonalized by rotation about the y-axis by the angle β:

$$\tan 2\beta = \frac{2g_{xz}}{g_{xx} - g_{zz}} = \frac{-2\sqrt{3}ab_x}{3a^2(c_{yz}/c_y) + \sqrt{3}ab_z} \tag{4.38}$$

With $\beta = 27°$, this expression gives $c_{yz}/c_y \approx 0.5$, a reasonable result.

This may be a rather general effect; if the unpaired electron in a radical is delocalized asymmetrically, and other MOs are similarly delocalized, the g-matrix will have off-diagonal elements that may be large enough to shift the principal axes away from the molecular coordinate system.

4.8.3 Another Low-spin Manganese(II) Complex

The low-spin manganese(II) complex $[Mn(dppe)_2\text{-}(CO)(CNBu)]^{2+}$ gave us a textbook example of a well-behaved ESR spectrum characterized by coincident g- and hyperfine-matrix principal axes. The nearly identical complex $[Mn(dppm)_2(CO)(CN)]^+$, (dppm = $Ph_2PCH_2PPh_2$) (ref. 25) provides us with a good example of non-coincident principal axes. The frozen solution spectrum (Figure 4.8) shows that the "parallel" features are not evenly spaced.
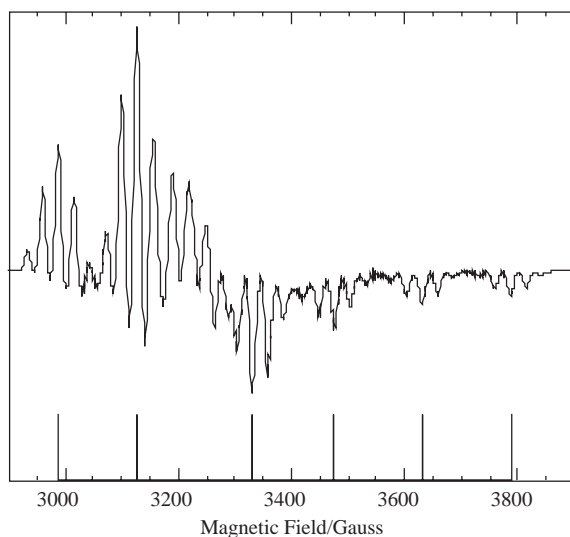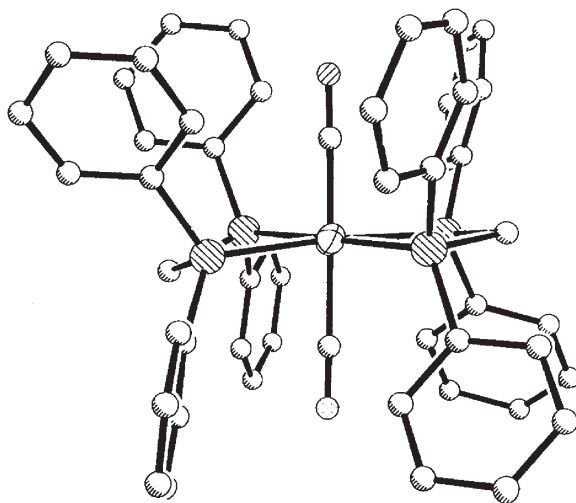

Figure 4.8   ESR spectrum of the Mn(II) complex $[Mn(dppm)_2(CO)(CN)]^+$ in CH_2Cl_2/$C_2H_4Cl_2$ at 90 K.
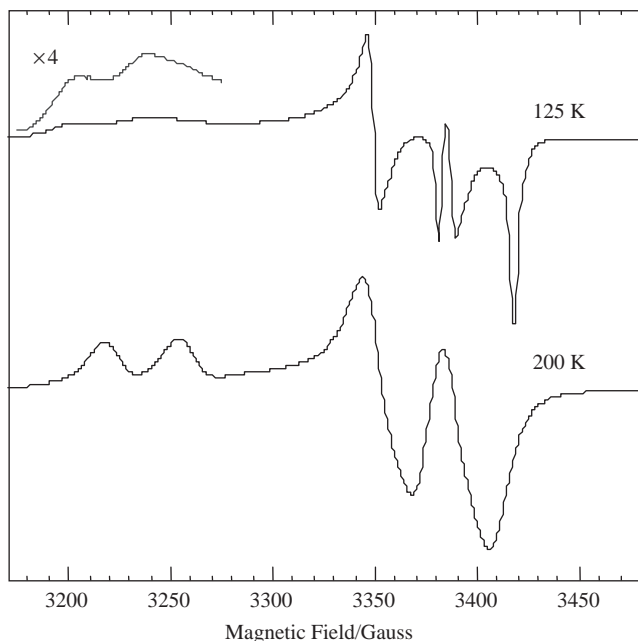(Reproduced with permission from ref. 25, copyright (1993) Royal Society of Chemistry.)

The spectrum can be understood if the *z*-axes of the *g*- and *A*-matrices are displaced by $\beta = 19.6°$. This, of course, tells us that the molecule does not have C_{2v} symmetry, and that, unlike the dppe analog, $d_{x^2-y^2}$ is not the only Mn contribution to the SOMO. One way of interpreting the results is that the Mn contribution to the SOMO incorporates a small amount of d_{xz} character. The consequence of this hybridization would be to tilt the "*x*" lobes of $d_{x^2-y^2}$ up and down, *i.e.*, rotation about the *y*-axis. The reason for this hybridization is not difficult to discover. If the CH_2 groups of the dppm ligands were coplanar with Mn, the "*x*" lobes of the $d_{x^2-y^2}$ SOMO would be directed toward the carbon atoms and an anti-bonding interaction would result. To avoid this interaction, two things happen: (1) incorporation of d_{xz} character tilts the lobes up and down, away from the C atoms. At the same time, the X-ray structure of the Mn(II) cation (Figure 4.9) shows that the CH_2 groups tilt down and up, further decreasing the anti-bonding interaction. With only one electron in the SOMO, the anti-bonding interaction is strong enough to produce this distortion. With two electrons, the neutral parent Mn(I) complex would be expected to be even more distorted, and an X-ray structure shows that the up and down displacements of the CH_2 groups is approximately doubled.

4.8.4   Chromium(I) Piano-stool Complex

Ordinarily, there is no way of extracting the orientation of the principal axes of the *g*-matrix from a powder or frozen solution ESR spectrum. However, there are exceptional circumstances in which nature is kind to the experimentalist!

Figure 4.9 X-ray structure showing methylene groups tilted up and down to avoid anti-bonding interaction with the Mn $d_{x^2-y^2}$ SOMO in the complex $[Mn(dppm)_2(CO)(CN)]^+$.
(Reproduced with permission from ref. 25, copyright (1993) Royal Society of Chemistry.)

Figure   4.10   Spectra of $[(\eta\text{-}C_5Ph_5)Cr(CO)_2PMe_3]$ in toluene at 125 and 200 K. (Reproduced with permission from ref. 28, copyright (1996) American Chemical Society.)

Spectra of the low-spin d^5 Cr(I) complex $[(C_5Ph_5)Cr(CO)_2PMe_3]^{28}$ are shown at 125 and 200 K in Figure 4.10. The low-temperature spectrum shows three sets of doublets, corresponding to the three g-components (2.104, 2.013, 1.994), each a doublet due to hyperfine coupling to ^{31}P. As the sample is warmed to 200 K, above the freezing point of toluene, the spectrum still appears as a "powder pattern", but the low-field "perpendicular" features are nearly averaged and the "parallel" features have shifted slightly upfield ($g_{\|} = 2.090$, $g_\perp = 2.012$).

The exceptionally bulky C_5Ph_5 ligand apparently moves very slowly at 200 K but on the ESR time scale the $Cr(CO)_2PMe_3$ moiety rotates quickly, producing a spectrum averaged about the Cr–C_5 axis. With this interpretation, we can assign this axis as the principal axis for $g_{\|}$ measured at 200 K and, noting that the $g_{\|}$ axis differs from the g_z axis by the angle β and that g_y and g_x are averaged according to:

$$2g_{\|}^2 = g_z^2 + g_x^2 + (g_z^2 + g_x^2)\cos^2 2\beta$$

Substitution of the g-components gives $\beta = 15°$.

The symmetry of the static complex is at most C_s, requiring one of the g-matrix principal axes to be normal to the plane of symmetry – this is assumed

to be xz. π-Back-bonding to the CO ligands is expected to lead to a hybrid SOMO. If, as suggested by extended Hückel MO calculations, the SOMO and first HOMO are of a' symmetry, and the second HOMO of a'' symmetry:

$$|\text{SOMO}\rangle = a_1|x^2 - y^2\rangle + a_2|z^2\rangle + a_3|xz\rangle$$
$$|\text{HOMO}_1\rangle = b_1|x^2 - y^2\rangle + b_2|z^2\rangle + b_3|xz\rangle$$
$$|\text{HOMO}_2\rangle = c_1|xy\rangle + c_2|yz\rangle$$

the g-matrix components can be computed:[42]

$$g_{xx} = g_e + \frac{\zeta_{Cr}(a_1 c_2 + \sqrt{3} a_2 c_2 + a_3 c_1)^2}{E_0 - E_2}$$

$$g_{zz} = g_e + \frac{\zeta_{Cr}(2a_1 c_1 + a_3 c_2)^2}{E_0 - E_2}$$

$$g_{yy} = g_e + \frac{\zeta_{Cr}[a_1 b_3 - a_3 b_1 + \sqrt{3}(a_3 b_2 + a_2 b_3)]^2}{E_0 - E_1}$$

$$g_{xz} = -\frac{\zeta_{Cr}(2a_1 c_1 + a_3 c_2)(a_1 c_2 + \sqrt{3} a_2 c_2 + a_3 c_1)}{E_0 - E_2}$$

Rotation about the y-axis by β diagonalizes the matrix, and we find:

$$\tan 2\beta = -\frac{2g_{xz}}{g_{zz} - g_{xx}}$$

The single experimental observable, β, is hardly enough to evaluate the LCAO coefficients for the SOMO and second HOMO, but we can compare the results of an extended Hückel MO calculation. (Since ζ_{Cr} and $E_0 - E_2$ cancel in the calculation of $\tan 2\beta$, the EHMO calculation could come close.) The results are: $a_1 = 0.538$, $a_2 = 0.216$, $a_3 = -0.194$, $c_1 = 0.582$, $c_2 = -0.061$, $\beta = 14.8°$. Nevertheless, if we were to substitute these LCAO coefficients, but also use the EHMO estimate of the energy difference, into the expressions for g_{xx}, g_{yy}, g_{zz}, and g_{xz}, the results would be in very poor agreement with experiment; the moral here is that EHMO calculations, lacking charge self-consistency, usually have large errors in the energies, but the MO wavefunctions are often fairly accurate.

4.8.5 $[(RCCR')Co_2(CO)_6]^-$ and $[SFeCo_2(CO)_9]^-$

Non-coincident matrix axis effects are seen in the frozen solution spectra of $[(RCCR')Co_2(CO)_6]^-$ (**3**)[18] and $[SFeCo_2(CO)_9]^-$ (**4**),[43] but the effects are rather more subtle than those discussed above.
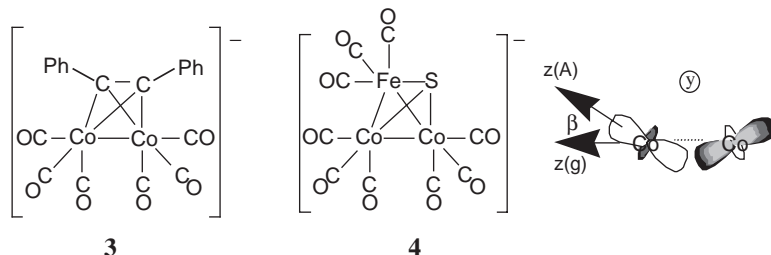
In these cases, the *g*-matrix is nearly isotropic, but the principal axes of the two ^{59}Co hyperfine matrices are non-coincident. The largest hyperfine matrix component ($a_y = 66.0$ G in the case of the Co-Co-Fe-S cluster) results in 15 features, evenly spaced (apart from small second-order shifts). Another series of features, less widely spaced, shows some variation in spacing and, in a few cases, resolution into components. This behavior can be understood as follows: Suppose that the hyperfine matrix *y*-axes are coincident and consider molecular orientations with the magnetic field in the *xz*-plane. To first order, the resonant field then is:

$$B = B_o - m_1 a_+ - m_2 a_- \tag{4.39}$$

where $B_o = h\nu/g\mu_B$ and:

$$a_\pm^2 = a_z^2 \cos^2(\theta \pm \beta) + a_x^2 \sin^2(\theta \pm \beta) \tag{4.40}$$

where β describes the orientation of the hyperfine matrix *z*-axes relative to the *g*-matrix *z*-axis. Since *g* is nearly isotropic, the extrema in *B* are determined mostly by the hyperfine term. When $m_1 = m_2$, a_+ and a_- are equally weighted and the extrema occur at $\theta = 0$ or $90°$, but when $m_1 \neq m_2$, the extrema correspond to other angles. Consider, for example, the five components of the $m = m_1 + m_2 = +3$ feature. With $a_z = 53.6$ G, $a_x = 15.5$ G, $\beta = 18°$, the hyperfine contributions to the field extrema and the corresponding values of θ are given in Table 4.11. In the experimental spectrum of the Co-Co-Fe-S cluster, two resolved field maximum features were seen, corresponding to the first two and the last three of the above components. Since the resolution is sensitive to the non-coincidence, it was possible to fit the experimental spectrum to obtain β quite accurately.

Table 4.11 **[E]** Splitting of $m = 3$ features in the $[SFeCo_2(CO)_9]^-$ spectrum[43]

(m_1, m_2)	θ_{min} (°)	$(B-B_0)^{min}$ (G)	θ_{max} (°)	$(B-B_0)_{max}$ (G)
+7/2,−1/2	−20	37.0	+67	166.1
−1/2,+7/2	+20	37.0	−67	166.1
+5/2,+1/2	−15	55.3	+78	156.9
+1/2,+5/2	+15	55.3	−78	156.9
+3/2,+3/2	0	66.5	90	153.6

It is relatively easy to understand the significance of the non-coincident matrix axes in these cases. For the Co_2C_2 cluster, the C_{2v} molecular symmetry permits a specific prediction of the possible matrix axis orientations. The *g*-matrix principal axes must be coincident with the molecular symmetry axes. The two cobalt nuclei are located in a reflection plane (which we label *xz*) so that symmetry requires the *y*-axis to be a principal axis for all three matrices. The other two axes may be rotated, relative to the molecular *x*- and *z*-axes, by $\pm\beta$. (Since the two nuclei are symmetrically equivalent, the rotations must be equal and opposite.)

Since the magnitudes and probable signs of the cobalt hyperfine matrices suggest a SOMO predominantly d_{z^2} in character, the major axes of the hyperfine matrices approximate the local *z*-axes at the cobalt atoms and the angular displacement indicates a bent Co–Co anti-bonding interaction, as shown in the structure, where the C–C or Fe–S bond axis (the molecular *y*-axis) is perpendicular to the plane of the page. Comparison with the crystal structure of neutral $(Ph_2C_2)Co_2(CO)_6$[44] shows that these local axes are roughly in the direction of the axial carbonyl ligands (the Co–CO bond is tilted 28° away from the Co–Co vector). Thus it seems reasonable to say that the local axes on a metal are determined primarily by the more strongly interacting ligands and that bonds to other atoms can be described as bent.

4.8.6   (*o*-Xylylene)-Mn(dmpe)$_2$

As part of a study of Mn(II) dialkyls, Wilkinson, Hursthouse, and co-workers[45] reported the ESR spectrum of the approximately octahedral (*o*-xylylene)Mn(dmpe)$_2$ (Figure 4.11a) (dmpe = $Me_2PCH_2CH_2PMe_2$).

The spectrum was interpreted assuming coincident *g*- and hyperfine-matrix axes, but a simulation based on the reported parameters gave a very poor fit to the published spectrum. On closer examination, it was realized that this is a rather extreme example of a spectrum influenced by non-coincident *g*- and hyperfine matrix principal axes. The clue evident in the spectrum is the large gap between the $m_{Mn} = -1/2$ and $+1/2$ "parallel" features, suggesting one or more extra features. Figure 4.12 shows a set of simulated spectra for a hypothetical low-spin Mn(II) species; all seven spectra correspond to the same *g*- and hyperfine-matrices, but the angle β, between the *g*- and hyperfine matrix *z*-axes, varies from 0 to 90°. As shown in Figure 4.12, it is possible to obtain spectra with more than six resolved "parallel" features. Indeed, the spectrum is sufficiently sensitive to the angle that β can be evaluated quite precisely. The final parameters, based on least-squares fitting of the positions of the resolved features and the isotropic parameters, are given in Table 4.12; a computer simulation using these parameters is shown in Figure 4.11(b).

[(*o*-Xylylene)Mn(dmpe)$_2$] has approximate C_{2v} symmetry, but the ethylene bridges of the dmpe ligands destroy the reflection planes; the X-ray structure[45] shows a small fold at the methylene groups of the *o*-xylylene ligand, which destroys the C_2 axis. Thus the molecule can be regarded, with increasing
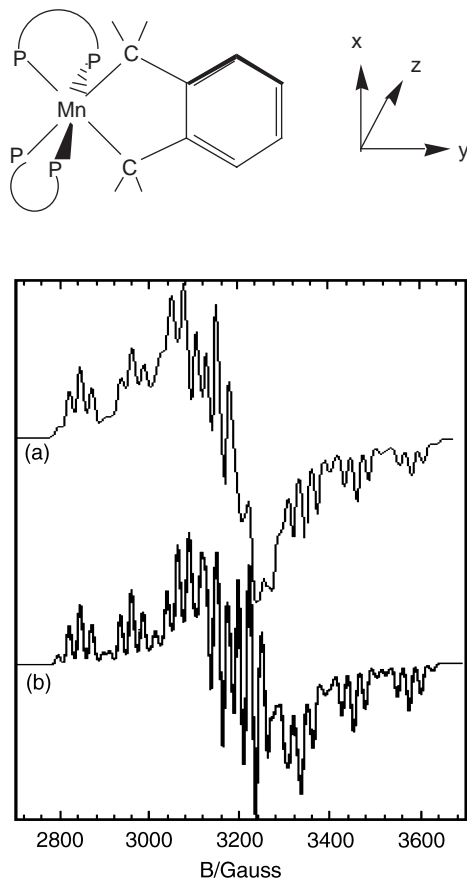
Figure   4.11   [E] (a) ESR spectrum of (*o*-xylylene)Mn(dmpe)$_2$ in frozen toluene
solution.
(Reproduced with permission from ref. 45, copyright (1983) Royal
Society of Chemistry.) (b) Computer simulation of spectrum using
parameters of Table 4.12.

accuracy, as C_{2v}, Cs, C_2, or C_1. To explain the matrix axis non-coincidence, the
metal contribution to the SOMO must be a d-hybrid. Since it is a low-spin d^5
Mn(II) species, the SOMO is expected to be dominated by one of the orbitals of
the octahedral t_{2g} set – d$_{xz}$, d$_{yz}$, or d$_{x^2-y^2}$. This is consistent with a clue
contained in the ESR parameters. The four ^{31}P couplings are apparently
equivalent, and all are relatively small. Thus no lobe of the SOMO can be
directed toward a phosphorus atom, and major d$_{xy}$ or d$_{z^2}$ contributions to the
SOMO can be ruled out. Consider the twelve binary hybrids based on these
orbitals, which are listed in Table 4.13.

Since we know that the hyperfine matrix major axis is not a *g*-matrix
principal axis, we can immediately reject hybrids 1, 3, 4, 7, 8, and 10 for which
the major axis is a common axis. Hybrids 2 and 6, 5 and 9, and 11 and 12 differ
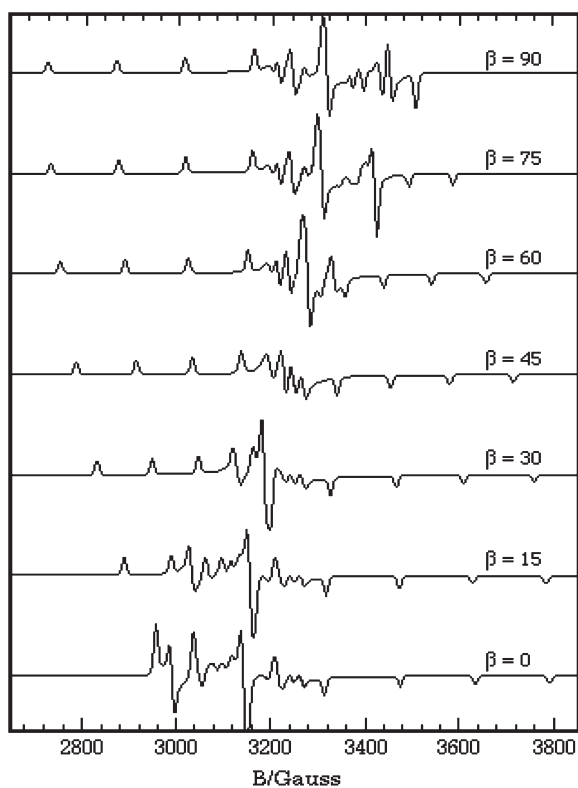
Figure 4.12 **[E]** Computer-simulated ESR spectra for a hypothetical low-spin Mn(II) radical with $g = (2.100, 2.050, 2.000)$, $A^{Mn} = (150, 25, 25) \times 10^{-4}$ cm^{-1}, for various values of β, the Euler angle between the g-matrix and hyperfine matrix z-axes.

Table 4.12 **[E]** ESR parameters for (*o*-xylylene)Mn(dmpe)$_2$ ($\beta = 41°$)

g	$10^4 A^{Mn}$ (*cm^{-1}*)	$10^4 A^P$ (*cm^{-1}*)
2.110	27	24.5
2.035	27	24.5
2.000	125	24.5

only in the *x*- and *y*-labels and are essentially indistinguishable, so that there are only three cases to consider in detail.

Hybrid 6 can be written:

$$|SOMO\rangle = a|x^2 - y^2\rangle + b|xz\rangle \tag{4.41}$$

Table 4.13 [E] SOMO candidates: binary d-hybrids

	Representation		Major	Minor	Approx. major	Common
#	C_s	C_2	d-AO	d-AO	HF axis	axis
1	a'	a	$d_{x^2-y^2}$	d_{z^2}	z	x,y,z
2	a'	–	$d_{x^2-y^2}$	d_{yz}	z	x
3	a'	–	d_{yz}	$d_{x^2-y^2}$	x	x
4	a'	–	d_{yz}	d_{z^2}	x	x
5	a''	–	d_{xz}	d_{xy}	y	x
6	–	a	$d_{x^2-y^2}$	d_{xz}	z	y
7	–	a	d_{xz}	$d_{x^2-y^2}$	y	y
8	–	a	d_{xz}	d_{z^2}	y	y
9	–	b	d_{yz}	d_{xy}	x	y
10	–	–	$d_{x^2-y^2}$	d_{xy}	z	z
11	–	–	d_{xz}	d_{yz}	y	z
12	–	–	d_{yz}	d_{xz}	x	z

Straightforward application of eqns (4.24) yields a hyperfine matrix that can be diagonalized by rotation about the *y*-axis by the angle β:

$$\tan 2\beta = -2b/a \tag{4.42}$$

The *g*-matrix can be written in relatively simple form if we assume that the only MOs close enough in energy to contribute significantly are the filled MOs, primarily d_{xz} and d_{yz} in character. With this assumption, we obtain a matrix which can be diagonalized by rotation about the *y*-axis by β',

$$\tan 2\beta' = -\frac{2b/a}{1-(b/a)^2} \tag{4.43}$$

For reasonable values of the hybridization ratio, b/a up to about 0.5, β and β' can differ by only a few degrees and this kind of hybrid cannot explain the matrix axis non-coincidence. Following the same reasoning with *x* and *y* interchanged, exactly the same conclusions can be reached for hybrid 2.

Hybrids 11 and 12 are:

$$|\text{SOMO}\rangle = a|xz\rangle + b|yz\rangle \tag{4.44}$$

In this case, the hyperfine matrix remains axial, independent of the hybridization ratio, although the principal axes are rotated in the *xy*-plane by an angle α equal to angle β of eqn (4.43). Assuming that only MOs with predominantly d_{xz}, d_{yz}, or $d_{x^2-y^2}$ character contribute, a *g*-matrix is found that can be diagonalized by rotation in the *xy*-plane by the angle α', also given by eqn (4.43). Thus this hybrid gives identical *g*- and hyperfine matrix principal axes for all hybridization ratios.

Finally, hybrid 9:

$$|\text{SOMO}\rangle = a|yz\rangle + b|xy\rangle \tag{4.45}$$

gives an axial hyperfine matrix with principal axes rotated in the xz-plane by an angle β, given by eqn (4.43). The g-matrix is somewhat more complicated:

$$\frac{\Delta g}{2\zeta} = \begin{pmatrix} \dfrac{\left(ac_{x^2-y^2}\right)^2}{\Delta E_{x^2-y^2}} + \dfrac{(bc_{xz})^2}{\Delta E_{xz}} & 0 & -\dfrac{2ab\left(c_{x^2-y^2}\right)^2}{\Delta E_{x^2-y^2}} - \dfrac{ab(c_{xz})^2}{\Delta E_{xz}} \\ 0 & \dfrac{(bc_{yz})^2}{\Delta E_{yz}} & 0 \\ -\dfrac{2ab\left(c_{x^2-y^2}\right)^2}{\Delta E_{x^2-y^2}} - \dfrac{ab(c_{xz})^2}{\Delta E_{xz}} & 0 & \dfrac{\left(2bc_{x^2-y^2}\right)^2}{\Delta E_{x^2-y^2}} + \dfrac{(ac_{xz})^2}{\Delta E_{xz}} \end{pmatrix} \tag{4.46}$$

Diagonalization requires rotation about the y-axis by the angle β',

$$\tan 2\beta' = -\frac{2b}{a}\left[\frac{2Q+1}{Q-1-(b/a)^2(4Q-1)}\right] \tag{4.47}$$

where

$$Q = \frac{\left(c_{x^2-y^2}\right)^2}{\Delta E_{x^2-y^2}} \bigg/ \frac{(c_{xz})^2}{\Delta E_{xz}} \tag{4.48}$$

Since the energy differences, $\Delta E_{x^2-y^2}$ and ΔE_{xz} are expected to be comparable, the parameter Q is probably not far from unity. For $Q = 1$, eqn (4.47) has a particularly simple form, $\tan 2\beta' = +2a/b$ so that, for small b/a, we expect $\beta \approx 0$ and $\beta' \approx 45°$, which is entirely consistent with experiment. The axial hyperfine matrix is in agreement with experiment, and the principal values of the g-matrix can also be rationalized with reasonable values of Q and b/a. A small rotation of d_{yz} about the y-axis might reflect the small displacements of the phosphorus atoms from the idealized octahedral positions.

An extended Hückel MO calculation supports the assumptions made in the above analysis in that the three "t_{2g}" orbitals are indeed close together in energy and remain nearly nonbonding metal-based d-orbitals. The detailed agreement is less satisfactory: the SOMO is predicted to be primarily $d_{x^2-y^2}$ with a small d_{xz} admixture (hybrid 6 of Table 4.13), a result that can be ruled out from our analysis of the ESR results. The EHMO overlap matrix based on the X-ray structure suggests that the molecule is much closer to C_2 symmetry than to *Cs*. If we accept that conclusion, then d_{xz}/d_{xy} hybridization is less likely than d_{yz}/d_{xy}, as we tacitly assumed above.

Several alternative explanations were considered for the matrix axis non-coincidence. In particular, it seemed possible that delocalization of spin density into the *o*-xylylene ligand, either through the σ-bonds or into the π-system, might lead to significant contributions to the off-diagonal terms of the g-matrix. While the EHMO calculations suggest that the MOs containing $d_{x^2-y^2}$ and d_{yz} do have contributions from the carbon atoms of the *o*-xylylene group, the amount is far too small to rationalize rotation of the g-matrix axes by 41°; indeed, to explain the effect in this way would require each of several carbon

atoms to contribute 5% or more to the MOs with $d_{x^2-y^2}$ or d_{yz} character, which is unreasonably large considering the poor overlap of these metal d-orbitals with the relevant carbon orbitals.

4.8.7 Cobalt Dithiolene Complexes

In the 1960s and 1970s, dithiolene complexes were very popular subjects for investigation by inorganic chemists. An ESR spectrum was reported[46] for one such complex, the structure of which is shown in Figure 4.13, coordinated with an axial PPh$_3$ ligand. A simulation based on a redetermination of the ESR parameters[47] is also shown in Figure 4.13.

Careful examination of the spacings of the ^{59}Co hyperfine lines in the spectrum reveals that the g and A-axes are non-coincident. This tells us that the symmetry cannot be as high as C_{2v}. This is surprising since several crystal structures obtained for iron dithiolene complexes are textbook examples of square pyramidal complexes of C_{2v} symmetry. Accordingly, Carpenter, et al.[47] determined the structure of the above complex and obtained ESR spectra for various complexes with different steric requirements. The non-coincidence angle α is given in Table 4.14.
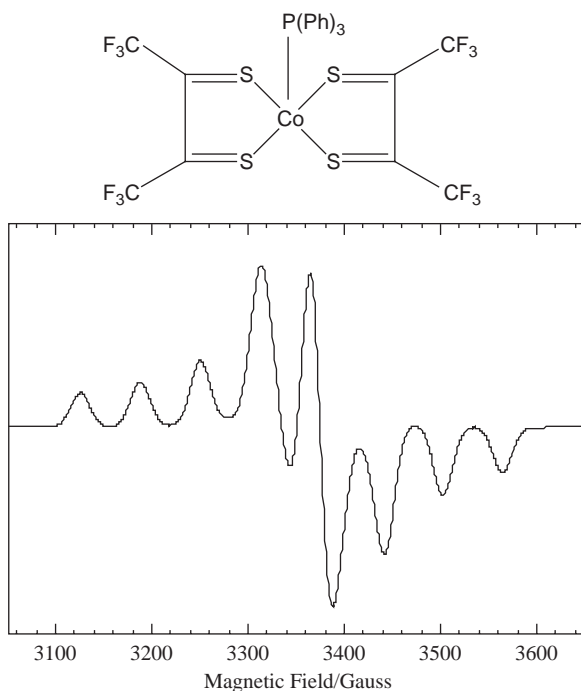
Figure 4.13 Simulation of ESR spectrum of the above cobalt dithiolene complex in frozen toluene at 77 K.
(Reproduced with permission from ref. 47, copyright (1994) Royal Society of Chemistry.)

Table 4.14 Non-coincidence angles for [Co{S$_2$C$_2$R$_2$}$_2$L]. (Data reproduced with permission from ref. 47, copyright (1994) Royal Society of Chemistry.)

R	L	α (°)
CN	Pet$_3$	2 ± 2
CF$_3$	P(OPh)$_3$	11 ± 5
CF$_3$	**PPh$_3$**	**16 ± 1**
Ph	P(OPh)$_3$	11 ± 5
Ph	PPh$_3$	24 ± 1
4-MePh	Pet$_3$	10 ± 2
4-MePh	PPh$_3$	24 ± 1
4-MeOPh	PPh$_3$	31 ± 2

Clearly, from inspection of Table 4.14, there is a good correlation between the steric bulk of R and L and the non-coincidence angle α. Furthermore, analysis of the hyperfine parameters leads to the conclusion that only about 25% of the electron spin resides in Co orbitals (mainly d$_{xz}$), and crystal structures of the R = CF$_3$, L = PPh$_3$ and P(OPh)$_3$ complexes do indeed show distortions. The difference between iron and cobalt is just one electron, but this electron occupies a dithiolene π* orbital, which makes the cobalt complexes much more easily distorted.

4.9 "g-Strain"

ESR spectral lines in a frozen solution or powder spectrum are sometimes peculiarly broad. The phenomenon is sometimes called "g-strain". In most cases, the matter is dropped at that point and no attempt to explain further is made. A successful interpretation of the effect has, however, been made for some organometallic radicals.[48]

Figure 4.14 shows the ESR spectrum of [Mn(CO)(dmpe)Cp]$^+$. Clearly, the "parallel" features are rather variable in line width, with the low-field lines broad and the high-field lines narrow. The ESR parameters for this spectrum[49] are given in Table 4.15 where β is the angle between the g-matrix z-axis and the hyperfine matrix z-axis.

Because of the non-coincidence of the g- and A-matrix principal axes, the various "parallel" features correspond to different orientations of the magnetic field in the g-matrix principal axis system. These orientations are given in Table 4.16.

If the excess width is associated with orientation along the g-matrix z-axis, we expect all widths to increase in the order $m_I = -1/2 < -3/2 < -5/2 << +5/2 < +3/2 < +1/2$, and this is observed. The field position of a spectral feature can be written as:

$$B = \frac{h\nu - km_I}{g_{\text{eff}}\mu_{\text{B}}} \tag{4.49}$$
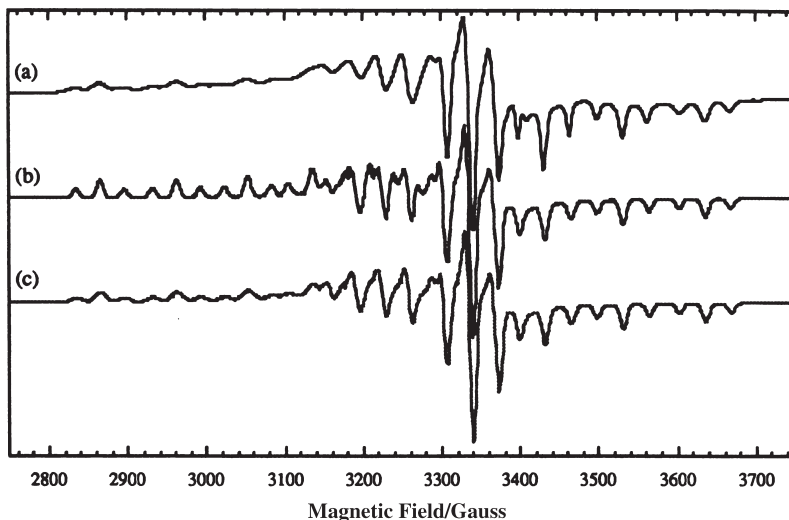
Figure 4.14 ESR spectrum of [Mn(CO)(dmpe)Cp]$^+$ in 1:1 CH$_2$Cl$_2$:C$_2$H$_4$Cl$_2$.
(Reproduced from ref. 48, with permission.) (a) Experimental spectrum at
120 K, (b) simulation with parameters of Table 4.15 and constant 4.1 G
Gaussian line widths, (c) simulation with constant 4.1 G line widths, w_g =
0.0049. (Reproduced with permission from ref. 48, copyright (1997)
American Chemical Society.)

Table 4.15 ESR parameters for [Mn(CO)(dmpe)Cp]$^{+48}$

g_1	g_2	g_3	$10^4 A_1$ (cm^{-1})	$10^4 A_2$ (cm^{-1})	$10^4 A_3$ (cm^{-1})	β $(°)$
2.000	2.021	2.187	35.6	ca. 0	115.3	45.4

where k is the angle-dependent hyperfine coupling and g_{eff} is given by eqn
(4.50):

$$g_{eff} = \sqrt{g_z^2 \cos^2 \theta + \left(g_x^2 \cos^2 \varphi + g_y^2 \sin^2 \varphi\right) \sin^2 \theta} \qquad (4.50)$$

Differentiating B with respect to g_z, we see that the line width of a feature depends
not only on the orientation in the field but also on the magnitude of the field:

$$\frac{\partial B}{\partial g_z} = -\frac{B g_z}{g_{eff}^2} \cos^2 \theta \qquad (4.51)$$

Values of $|\partial B/\partial g_z|$ are given in Table 4.16, as are values of w_{excess} [computed from
eqn (4.52)].

$$w_{excess} = w_g |\partial B/\partial g_z| = w_g B/g_z \qquad (4.52)$$

Table 4.16 Analysis of widths of "parallel" features of the spectrum of $[Mn(CO)(dmpe)Cp]^+$.[48] (Data from ref. 48 with permission, copyright (1997) American Chemical Society.)

m_I	5/2	3/2	1/2	−1/2	−3/2	−5/2
$B_\parallel$ (G)	2865	2962	3053	3432	3532	3636
$\theta_\parallel$ (°)	14.5	9.4	3.3	86.4	81.1	78.6
$\lvert\partial B/\partial g_z\rvert$ (G)	1240	1324	1392	8	46	105
w (G)	7.2	7.5	8.2	3.1	4.1	5.4
w_{excess} (G)	5.9	6.2	7.2		0	
w_g	0.0048	0.0047	0.0051			

The experimental value of w_{excess} is defined by $w_{excess} = \sqrt{w_{low}^2 - w_{high}^2}$ where $w_{high} = 4.1$ G (the $-3/2$ line was used since the $-1/2$ line was subject to destructive interferences by a divergence feature). The simulation in Figure 4.14(c) is based on $w_g = 0.0049$ G. A very similar explanation deals with the broader low-field features in the ESR spectrum of $[Cr(CO)_2(PMe_3)(\eta\text{-}C_5Ph_5)]$ (ref. 28) (Figure 4.10).

References

1. N.V. Vugman, A.O. Caride and J. Danon, *J. Chem. Phys.*, 1973, **59**, 4418.
2. N.V. Vugman and N.M. Pinhal, *Mol. Phys.*, 1983, **49**, 1315.
3. J.A. DeGray, P.H. Rieger, N.G. Connelly and G. Garcia Herbosa, *J. Magn. Reson.*, 1990, **88**, 376.
4. P.H. Rieger, *J. Magn. Reson.*, 1982, **50**, 485.
5. M.C.R. Symons, J.R. Morton and K.F. Preston, in *High-Energy Processes in Organometallic Chemistry*, ed. K.S. Suslick, American Chemical Society, Washington, DC, 1987, p. 169.
6. (*a*) P.W. Atkins and M.C.R. Symons, *The Structure of Inorganic Radicals*, Elsevier, Amsterdam, 1967; (*b*) R. Livingston and H. Zeldes, *J. Chem. Phys.*, 1964, **41**, 4011.
7. D. Collison, B. Gahan and F.E. Mabbs, *J. Chem. Soc., Dalton Trans.*, 1987, 111.
8. R.S. Drago, *Physical Methods in Chemistry*, Saunders, New York, 1977, p. 318.
9. P.C. Taylor, J.F. Baugher and H.M. Kriz, *Chem. Rev.*, 1975, **75**, 203.
10. I.V. Ovchinnikov and V.N. Konstantinov, *J. Magn. Reson.*, 1978, **32**, 179.
11. P.C. Taylor and P.J. Bray, *J. Magn. Reson.*, 1970, **2**, 305.
12. J.A. DeGray and P.H. Rieger, *Bull. Magn. Reson.*, 1987, **8**, 95.
13. P.H. Rieger, in *Organometallic Processes*, ed. W.C. Trogler, 1990, Ch. 8.
14. J.R. Morton and K.F. Preston, *J. Magn. Reson.*, 1978, **30**, 577.
15. B.A. Goodman and J.B. Raynor, *Adv. Inorg. Chem. Radiochem.*, 1971 **13**, 136.

16. A.K. Koh and D.J. Miller, *Atom. Data Nucl. Data Tab.*, 1985, **33**, 235.
17. P.H. Rieger, *J. Magn. Reson.*, 1997, **124**, 140.
18. B.M. Peake, P.H. Rieger, B.H. Robinson and J. Simpson, *J. Am. Chem. Soc.*, 1980, **102**, 156.
19. N.M. Atherton, *Electron Spin Resonance*, Ellis Horwood, Chicester, 1973.
20. N.G. Connelly, W.E. Geiger, G.A. Lane, S.J. Raven and P.H. Rieger, *J. Am. Chem. Soc.*, 1986, **108**, 6219.
21. B.R. McGarvey, in *Electron Spin Resonance of Metal Complexes*, ed. T.F. Yen, Plenum Press, New York, 1969, p. 1.
22. A.J. Stone, *Proc. Roy. Soc. (London)*, 1963, **A271**, 424.
23. T. Kawamura, K. Fukamachi, T. Sowa, S. Hayashida and T. Yonezawa, *J. Am. Chem. Soc.*, 1981, **103**, 364.
24. G.A. Carriedo, V. Riera, N.G. Connelly and S.J. Raven, *J. Chem. Soc., Dalton Trans.*, 1987, 1769.
25. G.A. Carriedo, N.G. Connelly, E. Perez-Carreno, A.G. Orpen, A.L. Rieger, P.H. Rieger, V. Riera and G.M. Rosair, *J. Chem. Soc., Dalton Trans.*, 1993, 3103.
26. J.A. DeGray, Q. Meng and P.H. Rieger, *J. Chem. Soc., Faraday I*, 1987, **83**, 3565.
27. T.A. Albright, W.E. Geiger, J. Moraczweski and B. Tulyathan, *J. Am. Chem. Soc.*, 1981, **103**, 4787.
28. D.J. Hammack, M.M. Dillard, M.P. Castellani, A.L. Rheingold, A.L. Rieger and P.H. Rieger, *Organometallics*, 1996, **15**, 4791.
29. T.A. Albright and R. Hoffmann, *Chem. Ber.*, 1978, **111**, 1390.
30. W. Gordy, *Theory and Applications of Electron Spin Resonance*, John Wiley, New York, 1980.
31. M. Katayama and W. Gordy, *J. Chem. Phys.*, 1961, **35**, 117.
32. M. Geoffroy, L. Ginet and E.A.C. Lucken, *Mol. Phys.*, 1974, **28**, 1289.
33. P.B. Ayscough, *Electron Spin Resonance in Chemistry*, Methuen, London, 1967.
34. A. Abragam and B. Bleaney, *Electron Paramagnetic Resonance of Transition Ions*, Clarendon Press, Oxford, 1970.
35. J.E. Wertz and J.E. Bolton, *Electron Spin Resonance*, McGraw-Hill, New York, 1972.
36. (*a*) J.R. Pilbrow and M.R. Lowrey, *Rep. Prog. Phys.*, 1980, **43**, 433; (*b*) A recent example that illustrates the intricacies involved in extracting information about axis orientations may be found in C.J. Adams, I.M. Bartlett, S. Boonyuen, N.G. Connelly, D.J. Harding, O.D. Hayward, E.J.L. McInnes, A.G. Orpen, M.J. Quayle and P.H. Rieger, *Dalton Trans.*, 2006, 3466.
37. F.K. Kneubühl, *Phys. Kondens. Mat.*, 1963, **1**, 410; 1965, 4, 50.
38. For a summary of Kneubühl's methods, see ref. 36.
39. W.E. Geiger, P.H. Rieger, B. Tulyathan and M.C. Rausch, *J. Am. Chem. Soc.*, 1984, **106**, 7000.
40. T. Lionel, J.R. Morton and K.F. Preston, *J. Chem. Phys.*, 1982, **76**, 234.

41. S.A. Fairhurst, J.R. Morton and K.F. Preston, *J. Chem. Phys.*, 1982 **77**, 5872.
42. P.H. Rieger, *Coord. Chem. Rev.*, 1994, **135**, 203.
43. B.M. Peake, P.H. Rieger, B.H. Robinson and J. Simpson, *Inorg. Chem.*, 1981, **20**, 2540.
44. F.A. Cotton, J.D. Jamerson and B.R. Stults, *J. Am. Chem. Soc.*, 1976, **98**, 1774.
45. C.G. Howard, G.S. Girolami, G. Wilkinson, M. Thornton-Pett and M.B. Hursthouse, *J. Chem. Soc., Dalton Trans.*, 1983, 2631.
46. A.L. Balch, *Inorg. Chem.*, 1967, **6**, 2158.
47. G.B. Carpenter, G.S. Clark, A.l. Rieger, P.H. Rieger and D.A. Sweigart, *J. Chem. Soc., Dalton Trans.*, 1994, 2903.
48. M.P. Castellani, N.G. Connelly, R.D. Pike, A.L. Rieger and P.H. Rieger, *Organometallics*, 1997, **16**, 4369.
49. R.D. Pike, A.L. Rieger and P.H. Rieger, *J. Chem. Soc., Faraday Trans. I*, 1989, **85**, 3913.

CHAPTER 5
ESR Kinetic Studies

One of the first uses of ESR spectra to measure the rate of a chemical reaction was by Ward and Weissman in the early 1950s.[1] They made use of a form of the Heisenberg uncertainty principle (eqn 5.1) to relate the lifetime of a spin state to the uncertainty in the energy of the state.

$$\delta E \delta t \geq \hbar \qquad (5.1)$$

Thus, if the lifetime of a spin state is δt, the energy level is broadened by an amount $\hbar/\delta t$, with consequences for ESR line widths. Ward and Weissman[1] added some unreduced naphthalene to a solution of the radical anion, and, from the observed broadening, computed δt, and from δt the rate constant for the electron transfer reaction:

$$C_{10}H_8 + [C_{10}H_8]^- \rightleftharpoons [C_{10}H_8]^- + C_{10}H_8$$
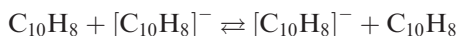
The result is very rapid electron exchange, as expected, with $k = 1 \times 10^6$ L mol^{-1} s^{-1}.

   This approach works well for electron transfer reactions where the rate is simply related to the broadening, but to proceed further in kinetic applications of ESR spectroscopy we must deal with the Bloch equations and modified Bloch equations.

   The phenomenological equations proposed by Felix Bloch in 1946[2] have had a profound effect on the development of magnetic resonance, both ESR and NMR, on the ways in which the experiments are described (particularly in NMR), and on the analysis of line widths and saturation behavior. Here we will describe the phenomenological model, derive the Bloch equations and solve them for steady-state conditions. We will also show how the Bloch equations can be extended to treat inter- and intramolecular exchange phenomena and give examples of applications.

5.1   Bloch's Phenomenological Model

When a magnetic field is applied to an electron or nuclear spin, the spin quantization axis is defined by the field direction. Spin magnetic moments

aligned with the field are only slightly lower in energy than those aligned opposed to the field. If we consider an ensemble of spins, the vector sum of all the spin magnetic moments will be a non-zero net magnetic moment or macroscopic magnetization:

$$\vec{M} = \underset{i}{\Sigma} \, \vec{\mu}_i \tag{5.2}$$

At equilibrium $\vec{M}$ is in the direction of the field $\vec{B}$. If somehow $\vec{M}$ is tilted away from $\vec{B}$ there will be a torque that causes $\vec{M}$ to precess about $\vec{B}$ with the equation of motion:

$$\frac{d\vec{M}}{dt} = \gamma \vec{B} \times \vec{M} \tag{5.3}$$

where $\gamma = 2\pi g \mu_B / h$ (or $g \mu_B / \hbar$). In addition to the precessional motion, there are two relaxation effects.

If M_0 is the equilibrium magnetization along $\vec{B}$ and M_z is the z-component under non-equilibrium conditions, then we assume that M_z approaches M_0 with first-order kinetics:

$$\frac{dM_Z}{dt} = -\frac{M_Z - M_o}{T_1} \tag{5.4}$$

where T_1 is the characteristic time for approach to equilibrium (the reciprocal of the rate constant). Since this process involves transfer of energy from the spin system to the surroundings (conventionally called the "lattice"), T_1 is called the *spin–lattice relaxation time*. Since electrons are much more strongly coupled to molecular interactions than are nuclei (which are buried in a sea of inner-shell electrons), it is not surprising that T_1 for electrons is usually much shorter (on the order of microseconds) than are nuclear T_1s (on the order of seconds).

There is a second kind of relaxation process that is at least as important for magnetic resonance as the T_1 process. Suppose that $\vec{M}$ is somehow tilted down from the z-axis toward the x-axis and the precessional motion is started. Each individual magnetic moment undergoes this precessional motion, but the individual spins may precess at slightly different rates. Local shielding may cause small variations in $\vec{B}$ or the effective g-factor may vary slightly through the sample. Thus an ensemble of spins that all start out in phase will gradually lose phase coherence – the individual spins will get out of step. We assume that there is a characteristic time for this process, called the *transverse relaxation time*, T_2, and that the transverse magnetization components decay to the equilibrium value of zero accordingly:

$$\frac{dM_x}{dt} = -\frac{M_x}{T_2} \quad \frac{dM_y}{dt} = -\frac{M_y}{T_2} \tag{5.5}$$

Notice that dephasing of the transverse magnetization does not affect M_z; a T_2 process involves no energy transfer but, being a spontaneous process, does involve an increase in the entropy of the spin system.

It should be emphasized that the approach to equilibrium by a T_1 process, in which M_z approaches M_0, also causes M_x and M_y to approach zero. Thus, the T_2 of eqn (5.5) must include both the effects of spin–lattice relaxation as well as the dephasing of the transverse magnetization. Transverse relaxation is often much faster than spin–lattice relaxation and T_2 is then determined mostly by spin dephasing. In general, however, we should write:

$$\frac{1}{T_2} = \frac{1}{T_1} + \frac{1}{T_{2'}} \tag{5.6}$$

where $T_{2'}$ is the spin dephasing relaxation time, and T_2 is the observed transverse relaxation time.

In ESR, it is also customary to classify relaxation processes by their effects on electron and nuclear spins. A process that involves an electron spin flip necessarily involves energy transfer to or from the lattice and is therefore a contribution to T_1; we call such a process *nonsecular*. A process that involves no spin flips, but which results in loss of phase coherence, is termed *secular*. Processes that involve nuclear spin flips but not electron spin flips are, from the point of view of the electron spins, nonsecular, but because the energy transferred is so small (compared with electron spin flips) these processes are termed *pseudosecular*.

5.1.1 Derivation of the Bloch Equations

Combining eqns (5.3)–(5.5), we have:

$$\frac{\mathrm{d}\vec{M}}{\mathrm{d}t} = \gamma\vec{B} \times \vec{M} - \hat{\boldsymbol{i}}\frac{M_x}{T_2} - \hat{\boldsymbol{j}}\frac{M_y}{T_2} - \hat{\boldsymbol{k}}\frac{M_z - M_0}{T_1} \tag{5.7}$$

In a magnetic resonance experiment, we apply not only a static field B_0 in the z-direction but an oscillating radiation field B_1 in the xy-plane, so that the total field is:

$$\vec{B} = \hat{\boldsymbol{i}}\,B_1\,\cos\,\omega t + \hat{\boldsymbol{j}}\,B_1\,\sin\,\omega t + \hat{\boldsymbol{k}}\,B_0 \tag{5.8}$$

Note that there are other possible ways to impose a time-dependent B_1. The one described in eqn (5.8) corresponds to a circularly polarized field initially aligned along the x-axis and rotating about the z-axis in a counterclockwise direction.

The vector product of eqn (5.7) then becomes:

$$\vec{B} \times \vec{M} = -\hat{\boldsymbol{i}}\big[B_0 M_y - B_1 M_z \sin\,\omega t\big] + \hat{\boldsymbol{j}}\big[B_0 M_x - B_1 M_z \cos\,\omega t\big]$$
$$+ \hat{\boldsymbol{k}}\,B_1\big[M_y \cos\,\omega t - M_x \sin\,\omega t\big]$$

Inserting this expression in eqn (5.7) and separating it into components, we get:

$$\frac{\mathrm{d}M_x}{\mathrm{d}t} = -\gamma B_0 M_y + \gamma B_1 M_z \sin\,\omega t - \frac{M_x}{T_2} \tag{5.9a}$$

$$\frac{\mathrm{d}M_y}{\mathrm{d}t} = \gamma B_0 M_x - \gamma B_1 M_z \cos \omega t - \frac{M_y}{T_2} \tag{5.9b}$$

$$dM_z/dt = \gamma B_1 \left[M_y \cos \omega t - M_x \sin \omega t \right] - (M_z - M_0)/T_1 \tag{5.9c}$$

It is convenient to write Mx and My as:

$$M_x = u \cos \omega t + v \sin \omega t \tag{5.10a}$$

$$M_y = u \sin \omega t - v \cos \omega t \tag{5.10b}$$

or

$$u = M_x \cos \omega t + M_y \sin \omega t \tag{5.11a}$$

$$v = M_x \sin \omega t - M_y \cos \omega t \tag{5.11b}$$

This is equivalent to transformation into a coordinate system that rotates with the oscillating field; u is that part of M_x which is in-phase with B_1 and v is the part which is 90° out of phase. Differentiating eqn (5.11a) and substituting eqns (5.9a) and (5.9b), we get:

$$\frac{\mathrm{d}u}{\mathrm{d}t} = \frac{\mathrm{d}M_x}{\mathrm{d}t} \cos \omega t - M_x \omega \sin \omega t + \frac{\mathrm{d}M_y}{\mathrm{d}t} \sin \omega t + M_y \omega \cos \omega t$$

$$= [\gamma B_0 - \omega] \left[M_x \sin \omega t - M_y \cos \omega t \right] - \frac{M_x \cos \omega t + M_y \sin \omega t}{T_2}$$

and substituting from eqns (5.11):

$$\frac{\mathrm{d}u}{\mathrm{d}t} = -[\omega - \gamma B_0] v - \frac{u}{T_2} \tag{5.12a}$$

Similarly, we obtain:

$$\frac{\mathrm{d}v}{\mathrm{d}t} = [\omega - \gamma B_0] u - \frac{v}{T_2} + \gamma B_1 M_z \tag{5.12b}$$

$$\frac{\mathrm{d}M_z}{\mathrm{d}t} = -\gamma B_1 v - \frac{M_z - M_0}{T_1} \tag{5.12c}$$

Equations (5.12a–c) are the Bloch equations in the rotating coordinate frame.

5.1.2 Steady-state Solution

In a continuous wave (CW) magnetic resonance experiment, the radiation field B_1 is continuous and B_0 is changed only slowly compared with the relaxation rates (so-called *slow passage* conditions). Thus a steady-state solution to eqns

(5.12) is appropriate. Setting the derivatives to zero and solving the three simultaneous equations, we get:

$$u = \frac{\gamma B_1 M_0 (\omega_0 - \omega) T_2^2}{1 + T_2^2 (\omega_0 - \omega)^2 + \gamma^2 B_1^2 T_1 T_2} \tag{5.13a}$$

$$v = \frac{\gamma B_1 M_0 T_2}{1 + T_2^2 (\omega_0 - \omega)^2 + \gamma^2 B_1^2 T_1 T_2} \tag{5.13b}$$

$$M_z = \frac{M_0 \left[1 + T_2^2 (\omega_0 - \omega)^2 \right]}{1 + T_2^2 (\omega_0 - \omega)^2 + \gamma^2 B_1^2 T_1 T_2} \tag{5.13c}$$

where $\omega_0 = \gamma B_0$ is called the *Larmor frequency* and corresponds, in a quantum mechanical description of the experiment, to the (angular) frequency of the energy level transition.

Notice that as B_1 approaches zero, u and v go to zero and M_z approaches M_0, as expected. That is, it is the transverse oscillating field that causes the magnetization to have a non-equilibrium value. On the other hand, as B_1 increases, M_z decreases (moves away from equilibrium); u and v at first increase with increasing B_1, but eventually they decrease as the third term in the denominator begins to dominate.

Recall that u is the transverse magnetization component in-phase with the driving field B_1. In general a response that is exactly in phase with a driving signal does not absorb power from the signal source and in spectroscopy corresponds to *dispersion* – in optical spectroscopy dispersion results from a small reduction of the speed of light as it traverses the medium; but the problem can also be formulated so that optical dispersion is described in a way closely analogous to the Bloch equations description. An out-of-phase response, in contrast, corresponds to *absorption*. In magnetic resonance, it is usually the absorption, or v-mode, that is detected and so we confine our attention to eqn (5.13b) in what follows.

When the microwave or radiofrequency power, proportional to $B_1{}^2$, is small so that $\gamma^2 B_1{}^2 T_1 T_2 \ll 1$, eqn (5.13b) becomes:

$$v = \frac{\gamma B_1 M_0 T_2}{1 + T_2^2 (\omega_0 - \omega)^2} \tag{5.14}$$

A plot of *v vs.* $T_2(\omega_0 - \omega)$ is shown in Figure 5.1. Equation (5.14) corresponds to the classical *Lorentzian line shape* function and the absorption curve of Figure 5.1 is a Lorentzian "line". The half-width at half-height is easily found to be:

$$\Delta\omega = \frac{1}{T_2} \quad \text{or} \quad \Delta\nu = \frac{1}{2\pi T_2} \quad \text{or} \quad \Delta B = \frac{\hbar}{g\mu_{\mathrm{B}} T_2}$$

where the last form is appropriate when (as in CW ESR) B_0 is changed while keeping ω constant.
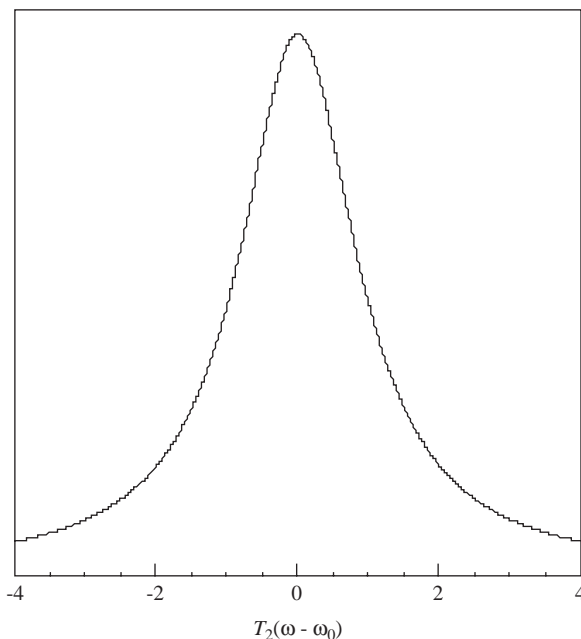
Figure 5.1 A Lorentzian absorption line.

When the absorption is detected *via* small amplitude field modulation, the signal is proportional to the first derivative of absorption:

$$\frac{\mathrm{d}v}{\mathrm{d}\omega} = \frac{2\gamma B_1 M_0 T_2^3 (\omega_0 - \omega)}{\left[1 + T_2^2 (\omega_0 - \omega)^2\right]^2} \tag{5.15}$$
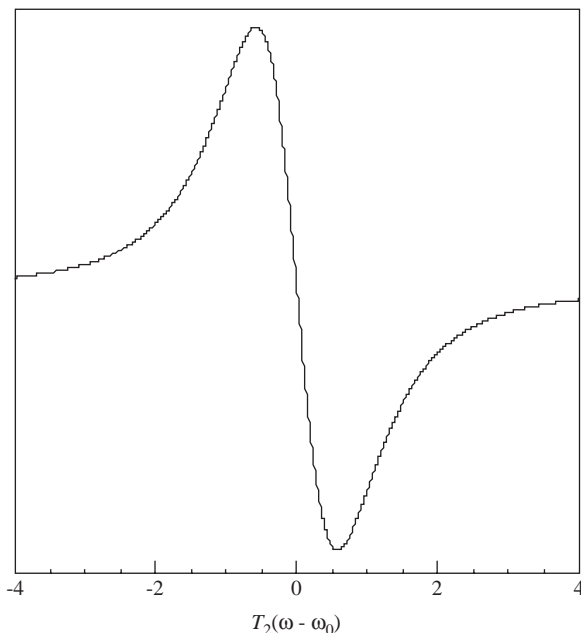
Figure 5.2 shows a Lorentzian derivative line.

In first-derivative spectra, it is most convenient to describe the line width as the separation between derivative extrema. This width may be computed by taking the second derivative and finding the zeros, obtaining:

$$\Delta\omega = \frac{2}{\sqrt{3}T_2} \quad \text{or} \quad \Delta v = \frac{1}{\sqrt{3\pi}T_2} \quad \text{or} \quad \Delta B = \frac{h}{\sqrt{3}\pi g \mu_B T_2}$$

The absorption derivative amplitude is proportional to T_2^2 whereas the width is proportional to T_2^{-1}. In other words, the derivative amplitude is inversely proportional to the square of the line width. Furthermore, the product of the amplitude and the square of the width is independent of T_2 and is sometimes taken as a measure of the intensity of the line, *i.e.*, proportional to M_0.

Notice that in the limit of small B_1 [where eqns (5.14) and (5.15) are valid] the derivative amplitude increases linearly with B_1, that the width is independent of B_1 and that neither width nor amplitude depends on T_1. At higher power, $\gamma^2 B_1^2 T_1 T_2$ cannot be neglected in eqn (5.13b), the amplitude is no longer linear

Figure 5.2 A Lorentzian first-derivative line.

in B_1 and both amplitude and width depend on T_1. Eventually, the amplitude begins to decrease with increasing B_1 and we say that the resonance is *saturated*. In quantum mechanical language this corresponds to equalization of the energy level populations and reduction of net absorption.

5.2   Chemical Exchange – The Modified Bloch Equations

Suppose we have a system in which a spin can exist in either of two different sites, A or B, and that these are distinguished by different resonant frequencies, ω_A and ω_B, and/or by different relaxation times, T_{2A} and T_{2B}. If there is no exchange between sites, site A spins and site B spins can be described separately and independently by sets of Bloch equations. When exchange takes place, however, additional rate terms – completely analogous to terms in chemical rate equations – must be added to the Bloch equations.

The algebra we are about to get into can be compacted somewhat by introducing the complex magnetization, $G = u + iv$, so that eqns (5.12a) and (5.12b) can be combined to obtain:

$$\frac{\mathrm{d}G}{\mathrm{d}t} = \frac{\mathrm{d}u}{\mathrm{d}t} + i\frac{\mathrm{d}v}{\mathrm{d}t} = -\frac{G}{T2} + i(\omega_0 - \omega)G + i\gamma B_1 M_0 \qquad (5.16)$$

In eqn (5.16), we have ignored the difference between M_0 and M_z and so have assumed that B_1 is small.

Spins at site A will have magnetization G_A and those at site B will have magnetization G_B. We now assume that A and B are interconverted by first-order kinetics with an A $\rightarrow$ B rate constant τ_A^{-1} and a B $\rightarrow$ A rate constant τ_B^{-1}. The site A magnetization thus decreases with a rate term $-G_A/\tau_A$ and increases with rate G_B/τ_B. Combining these terms with eqn (5.16) for site A:

$$\frac{dG_A}{dt} = -\frac{G_A}{T_{2A}} - \frac{G_A}{\tau_A} + \frac{G_B}{\tau_B} + i(\omega_A - \omega)G_A + i\gamma B_1 M_{0A} \tag{5.17a}$$

and a similar expression for site B:

$$\frac{dG_B}{dt} = -\frac{G_B}{T_{2B}} + \frac{G_A}{\tau_A} - \frac{G_B}{\tau_B} + i(\omega_B - \omega)G_B + i\gamma B_1 M_{0B} \tag{5.17b}$$

The rather fearsome algebra can be somewhat simplified by defining:

$$\alpha_A = T_{2A}^{-1} - i(\omega_A - \omega), \quad \alpha_B = T_{2B}^{-1} - i(\omega_B - \omega)$$

and noting that, at chemical equilibrium:

$$\frac{p_A}{p_B} = \frac{\tau_A}{\tau_B} \quad \text{and} \quad p_A + p_B = 1$$

where p_A and p_B are the fractions of the population at sites A and B. Defining a mean lifetime:

$$\tau = \frac{\tau_A \tau_B}{\tau_A + \tau_B}$$

several useful relations result:

$$p_A = \frac{\tau_A}{\tau_A + \tau_B} \quad p_B = \frac{\tau_B}{\tau_A + \tau_B}$$

$$\tau = p_A \tau_B = p_B \tau_A$$

Also, if M_0 is the total equilibrium magnetization, we can write:

$$M_{0A} = p_A M_0 \quad M_{0B} = p_B M_0$$

With these relations, it is possible to find the steady-state solution to eqns (5.17):

$$G = G_A + G_B = i\gamma B_1 M_0 \frac{\tau_A + \tau_B + \tau_A \tau_B (p_A \alpha_A + p_B \alpha_B)}{(1 + \tau_A \alpha_A)(1 + \tau_B \alpha_B) - 1} \tag{5.18}$$

The absorption signal, of course, is the imaginary part of eqn (5.18); the equation is too horrible to contemplate, but computer-simulations, such as those shown in Figures 5.3 and 5.4, are relatively easy to produce. There are two limiting cases where the equations are easier to understand. In the *slow exchange limit*, where τ_A^{-1} and τ_B^{-1} are both small compared with $|\omega_A - \omega_B|$, the
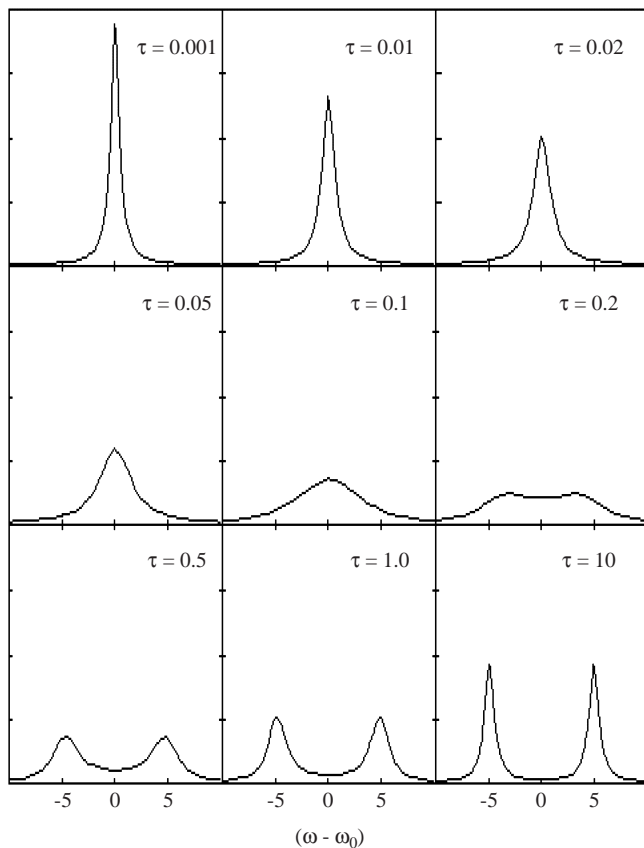
Figure 5.3 Absorption curves, computed using eqn (5.18) for various values of τ, and $\omega_A = \omega_0 - 5$, $\omega_B = \omega_0 + 5$, $T_{2A}^{-1} = T_{2B}^{-1} = 0.5$, $P_A = P_B = 0.5$.

absorption, $v = \text{Im}(G)$, is:

$$v = \frac{\gamma B_1 M_0 P_A \left(T_{2A}^{-1} + \tau_A^{-1}\right)}{\left(T_{2A}^{-1} + \tau_A^{-1}\right)^2 + (\omega_A - \omega)^2} + \frac{\gamma B_1 M_0 P_B \left(T_{2B}^{-1} + \tau_B^{-1}\right)}{\left(T_{2B}^{-1} + \tau_B^{-1}\right)^2 + (\omega_B - \omega)^2} \tag{5.19}$$

which corresponds to two Lorentzian lines centered at ω_A and ω_B and with widths $(T_{2A^{-1}} + \tau_{A^{-1}})$ and $(T_{2B^{-1}} + \tau_{B^{-1}})$. In other words, the lines are unshifted but are broadened by an amount proportional to the reciprocal of the lifetimes.

In the *fast exchange limit*, where τ_A^{-1} and τ_B^{-1} are both large compared with $|\omega_A - \omega_B|$, the absorption is:

$$v = \frac{\gamma B_1 M_0 T_2^{-1}}{T_2^{-2} + (\omega_0 - \omega)^2} \tag{5.20}$$
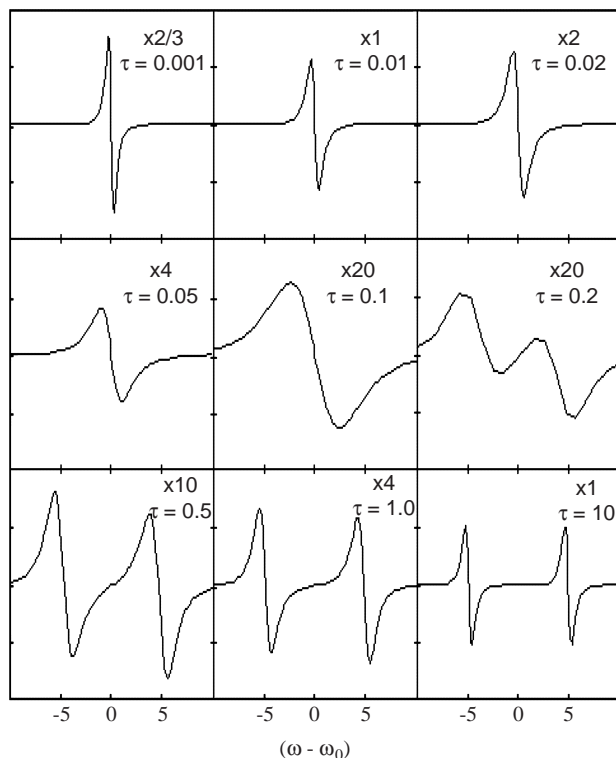
Figure 5.4 First-derivative curves, computed using eqn (5.18) for various values of τ, and $\omega_A = \omega_0 - 5$, $T_{2A^{-1}} = T_{2B^{-1}} = 0.5$, $p_A = p_B = 0.5$; note that the vertical scale differs – the plots are magnified by the factors shown.

where

$$\omega_0 = p_A\omega_A + p_B\omega_B$$

$$\frac{1}{T_2} = \frac{p_A}{T_{2A}} + \frac{p_B}{T_{2B}} + p_A p_B (\omega_A - \omega_B)^2 \tau$$

Thus a single Lorentzian line is obtained that is centered at a weighted average resonant frequency and has a width proportional to a weighted average T_2^{-1} plus a term proportional to the average lifetime and the square of the separation of the slow exchange resonances.

In the so-called *intermediate exchange region*, eqn (5.18) is not easily tractable and recourse is usually made to computer simulations. Qualitatively, however, it is clear that as the rate increases, the separate resonances of the slow exchange limit broaden, shift together, coalesce and then begin to sharpen into the single line of the fast exchange limit.

Simulations spanning all three exchange regions are shown in Figures 5.3 and 5.4.

5.3   Further Discussion of Line Shapes

Lorentzian line shapes are expected in magnetic resonance spectra whenever the Bloch phenomenological model is applicable, *i.e.*, when the loss of magnetization phase coherence in the *xy*-plane is a first-order process. As we have seen, a chemical reaction meets this criterion, but so do several other line broadening mechanisms such as averaging of the *g*- and hyperfine matrix anisotropies through molecular tumbling (rotational diffusion) in solution.

Some sources of line broadening, however, cannot be thought of as first-order rate processes. For example, when the magnetic field is inhomogeneous and varies over the sample, not all the molecules are at resonance at the same nominal field. It is usually reasonable to guess that the field has a *Gaussian* distribution (*i.e.*, a normal error distribution), so that the resonance line will also have a Gaussian shape. Various other effects can lead to such *inhomogeneous broadening* and thus to Gaussian line shapes. For example, the instantaneous chemical environment may vary from one radical to another because of different degrees of solvation or ion pairing. Probably for such reasons, Gaussian line shapes are commonly observed in frozen solution ESR spectra. Unresolved hyperfine couplings also often give a resonance line with an approximately Gaussian shape.

The Gaussian line shape function can be written:

$$S(\omega) = e^{-(\omega-\omega_0)^2/2\delta^2} \tag{5.21}$$

so that the half-width at half-height is

$$\text{Half width} = \sqrt{2}\ln 2\,\delta = 0.980\,\delta$$

and the derivative width (between extrema) is exactly 2δ.

A Gaussian line and its first derivative are shown in Figures 5.5 and 5.6. Comparison with Figures 5.1 and 5.2 shows that the Gaussian line is somewhat fatter near the middle but lacks the broad wings of the Lorentzian line.

5.4   Applications of the Modified Bloch Equations

ESR spectra of the radical anion of bis-(diphenylphosphino)maleic anhydride (BMA),[3] are shown in Figure 5.7. These spectra provide a good example of dynamical line-width effects. This radical shows a 1:2:1 triplet spectrum at higher temperatures, $a^P = 3.52$ G at 240 K, but the phosphorus coupling is strongly temperature dependent and extra lines appear at 200 K and below, indicating a dynamical equilibrium between two isomeric forms of the radical, one having two equivalent P nuclei (1:2:1 triplet spectrum), the other two non-equivalent P nuclei (doublet of doublets spectrum). The lines broaden with increasing temperature and coalesce at about 220 K.
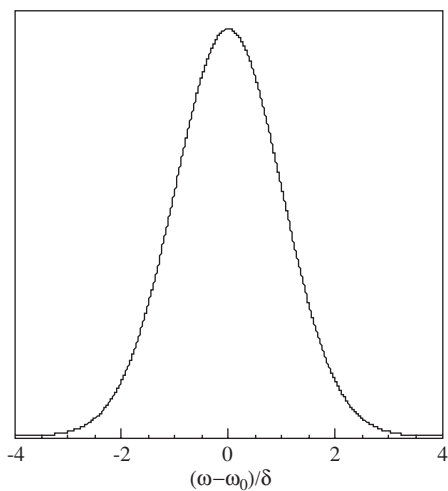
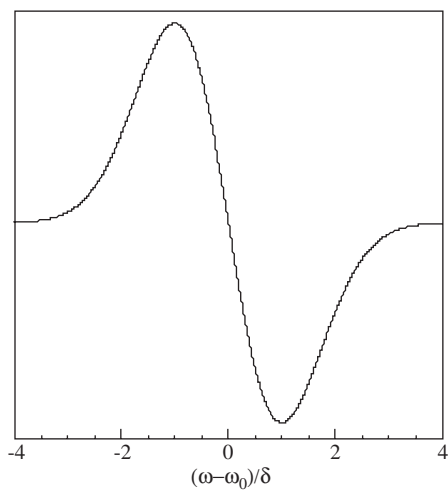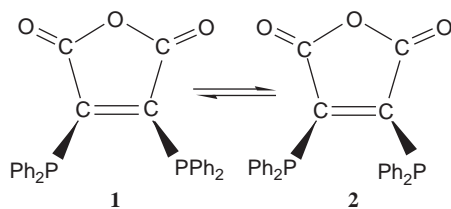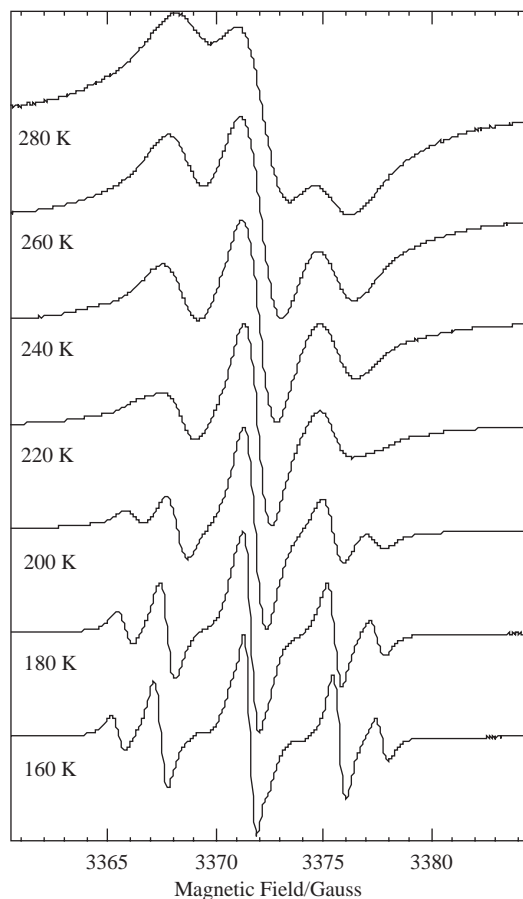**Figure 5.5** Gaussian absorption line.

Figure 5.6 First-derivative Gaussian line.

These data can be understood in terms of two rotational isomers of BMA^- (**1** and **2**).

Figure 5.7   Isotropic ESR spectra of the BMA radical anion in THF solution at various temperatures.
(Reproduced with permission from ref. 3, copyright (1998) American Chemical Society.)

Detailed analysis led to the thermodynamic and kinetic parameters: $\Delta H^\circ = 0.8 \pm 0.2$ kJ mol^{-1}, $\Delta S^\circ = -4 \pm 1$ J mol^{-1} K^{-1} ($K_{160} = 3.0$); $\Delta H^\ddagger = 18.2 \pm 0.4$ kJ mol^{-1}, $\Delta S^\ddagger = -30 \pm 2$ J mol^{-1} K^{-1} ($k_{200} = 1.9 \times 10^6$ s^{-1}).

A very similar application of the modified Bloch equations was based in the work of Adams and Connelly.[4] ESR spectra (Figure 5.8) of [Mo{P(OMe)$_3$}$_2$(MeC≡CMe)Cp] show the expected triplet (two equivalent ^{31}P nuclei) at 280 K, but only a doublet at 160 K. At intermediate temperatures, the lines broaden. The interpretation is that the alkyne undergoes a pendulum oscillation, which in the extrema diverts spin density from one or the other phosphite. Interestingly, the diamagnetic cation undergoes a similar motion on the NMR time scale, but then the alkyne undergoes a complete rotation. Thus, analysis of the effect leads to a measure of the rate of the oscillation. The
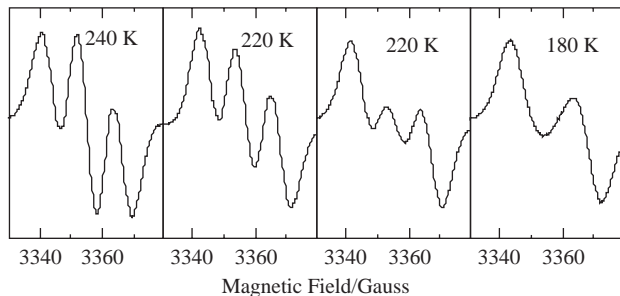
Figure 5.8 ESR spectra of [Mo{P(OMe)$_3$}$_2$(MeC$\equiv$CMe)-Cp] in 2:1 THF–CH$_2$Cl$_2$. (Reproduced with permission from ref. 4, copyright (2001) Royal Society of Chemistry.)
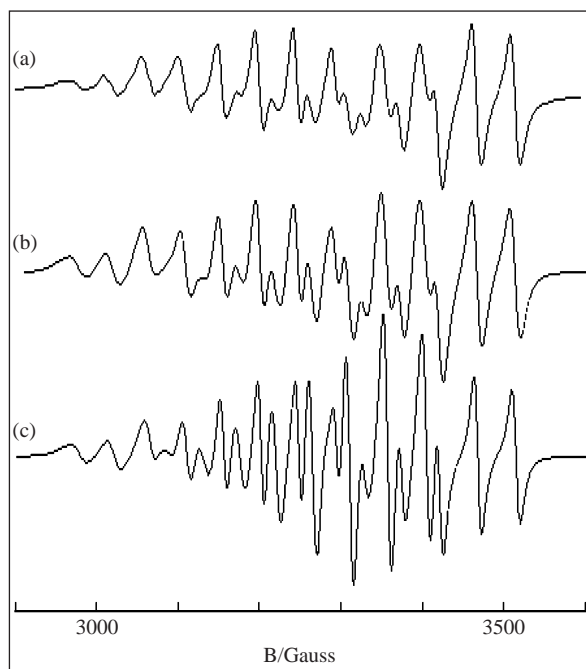
**Figure 5.9** (a) Experimental spectrum of (Ph$_2$C$_2$)Co(CO)[P(OMe)$_3$]$_2$ in THF solution at 270 K; (b and c) Computer-simulated spectra: (b) the m_{Co} and m_P line width dependence and (c) the m_{Co} line width dependence only. (Adapted from ref. 5 with permission, copyright (1984) American Chemical Society.)

resulting kinetic parameters are $\Delta H^{\dagger} = 13.2 \pm 0.3$ kJ mol^{-1}, $\Delta S^{\dagger} = -14 \pm 2$ J mol^{-1} K^{-1}, $k_{298} = 1.0 \times 10^9$ s^{-1}.

Casagrande *et al.*[5] have used line-width effects to study the rate of fluxionality in (Ph$_2$C$_2$)Co(CO)[P(OMe)$_3$]$_2$. The experimental spectrum (Figure 5.9a),

can be described as a 1:2:1 triplet of octets ($I = 7/2$ for ^{59}Co); the spectrum is complicated by a large line width dependence on m_{Co}, but, as demonstrated in Figure 5.9(b) and 5.9(c), the central lines of the triplets are much broader than the outer lines. This radical has a distorted tetrahedral structure with the singly occupied molecular orbital (SOMO) largely cobalt 3 d_{z^2} in character.[6] Thus the ligand sites can be described as axial or equatorial relative to the unique z-axis. Several isomers are possible, but the ^{31}P couplings distinguish between the isomer with an axial phosphite (ax,eq) and those with either CO or the acetylene axial and both phosphites equatorial (eq,eq). The rate of interconversion between (eq,eq) and (ax,eq) isomers (**3** and **4**) was estimated from the relative widths of the $m_P = \pm 1$ and 0 lines, given the isotropic coupling constants for the various ^{31}P nuclei (which were determined from the frozen solution spectrum[5]). The average rate was found to be approximately 2×10^{10} s^{-1} ($E_a = 17 \pm 2$ kJ mol^{-1}) at 298 K.
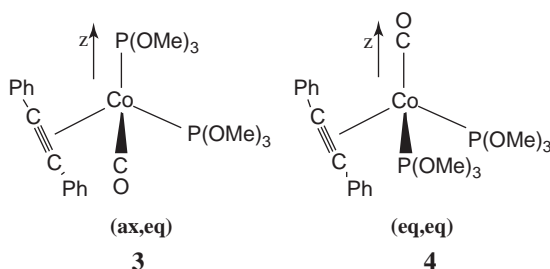
F. A. Walker *et al.* studied the rate of base exchange with VO(acac)$_2$ in benzene solution:[7]

$$VO(acac)_2 + Base \rightleftharpoons VO(acac)_2 \cdot Base$$
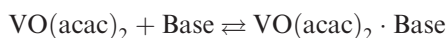
where Base = pyridine, 3-picoline, 4-picoline, 3,4-lutidine, 3,5-lutidine, and piperidine, by using ESR line broadening. Line widths were fitted to a power-series expression:

$$T_2^{-1} = \alpha + \beta m_I + \gamma m_I^2 + \delta m_I^3$$

Table 5.1 shows the spin Hamiltonian parameters for some of the complexes. The equilibrium constants and rate constants are given in Table 5.2.

**Table 5.1**   ESR parameters for VO(acac)$_2 \cdot$ Base[7]

	g	$10^4 A^V$ *(cm^{-1})*
VO(acac)$_2$-pyridine	1.9693	99.5
VO(acac)$_2$-2-picoline	1.9697	96.7
VO(acac)$_2$-piperidine	1.9690	96.9

Table 5.2 Equilibrium and rate constants for VO(acac)$_2$ · Base exchange. (Reproduced from ref. 7a with permission, copyright (1966) American Institute of Physics.)

Base	T (°C)	K (M^{-1})^a	k$_r$ (s^{-1})	k$_r$ (M^{-1} s^{-1})
Pyridine	18	78	1.3 × 10^7	1.0 × 10^9
2-Picoline	16	0.78^b	7.2 × 10^7	5.0 × 10^6
Piperidine	17	1400	<0.2 × 10^7	<2.8 × 10^9

^{a} Ref. 7b.
^{b} Using estimated $\Delta H°$.
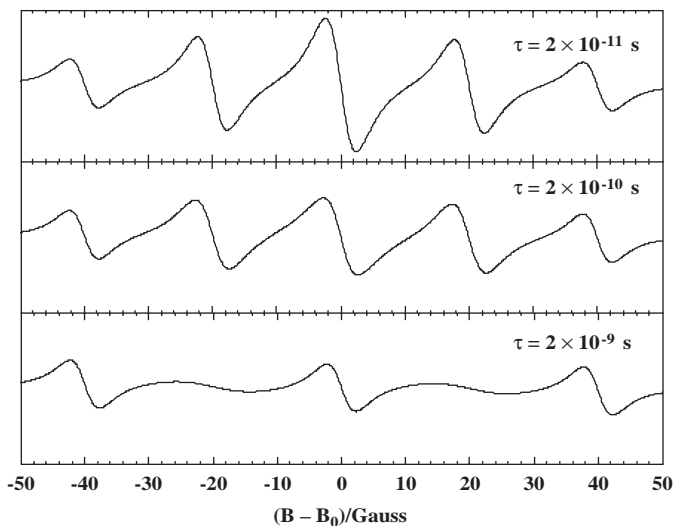
Figure 5.10 Simulations of the ESR spectrum of the dinitrodurene radical anion. Parameters taken from ref. 8.

5.5 Alternating Line Width Effects

Several examples were found during the 1950s and 1960s of spectra of organic radical ions in which the line widths were alternatively sharp and broad. One example of this is the ESR spectrum of dinitrodurene (**5**) (Figure 5.10).


5
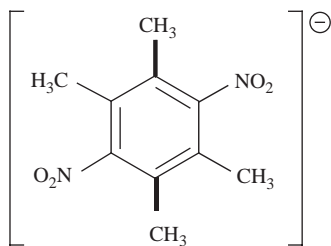
Table 5.3 Effect of cation and solvent on hopping rate
in durosemiquinone

Cation/solvent[a]	Log A	E_a (kJ mol^{-1})
K$^+$/THF	10.7	24
Rb$^+$/THF	10.9	22
Cs$^+$/THF	11.1	20
Na$^+$/DME		12
K$^+$/DME		28

[a] THF = tetrahydrofuran (ref. 9); DME = dimethoxyethane (ref. 10).

This spectrum was at first quite puzzling, but, on reflection, the explanation became clear.[8] The unpaired electron is mostly on the electron-withdrawing nitro groups in the *p*-dinitrobenzene radical anion but, in the present case, the methyl groups do not allow the two nitro groups to be coplanar with the ring simultaneously. Thus the unpaired electron hops back and forth between the two nitro groups, with the one having the unpaired electron coplanar with the ring. The simulations in Figure 5.10 show the effect of rate on the shape of the spectrum.

Another example of alternating line width effect was found in the spectra of durosemiquinone (**6**),[9,10] where the effect is due to alkali metal ions hopping back and forth from one oxygen atom to the other. The rates depend on the alkali metal as shown in Table 5.3.

6
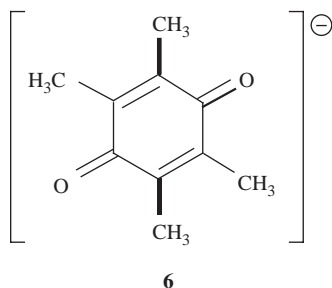
Another example is the *m*-dinitrobenzene anion radical in aqueous solution,[11,12] where the effect is due to asymmetric solvation (one nitro group solvated, the other not), an effect very similar to that with dinitrodurene anions. In this case the mean lifetime of one solvation state was 0.8 µs at 291 K and 4.5 µs at 282 K. Still more examples are mentioned in the reviews by Atkins in the early 1970s.[13]
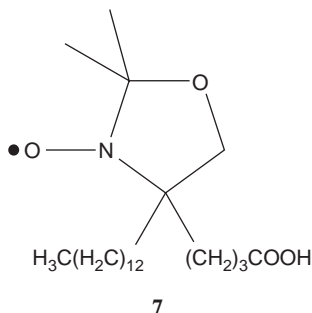
5.6 Spin Labels

One of the many advances in ESR spectroscopy introduced by Harden McConnell is the idea of labeling a biological membrane or macromolecule with a stable free radical (typically a nitroxide).[14] Since in a nitroxide the spin is primarily in a nitrogen 2p orbital, $A_{\parallel} \neq A_{\perp}$, and the isotropic line widths give a good indication of the freedom of motion of the nitroxide. Moro and Freed[15] developed an algorithm for the analysis of ESR spectra to give motional

lifetimes. The subject has been reviewed nearly annually in the Specialist Periodical Report, *Electron Spin Resonance* and other monographs.[16] The effects of decrease in the rate of rotation motion on the appearance of nitroxide ESR is shown qualitatively in Figure 5.11.

Applications of spin labels to problems in structural biology have continued to grow over the four decades since McConnell's original proposal. We mention here only two examples, which provided early support for the method.

Morrisett, *et al.*[17] studied phase transitions in *E. coli* membranes using three different spin labels, including 5-doxyl stearate (5-DS) (**7**).

7

They observed abrupt changes in the slope of Arrhenius plots for reactions catalyzed by NADH oxidase and *p*-lactate oxidase that correlate well with phase transitions detected by the ESR spectra of the nitroxide spin labels bound covalently to the enzymes (Table 5.4).

Another example comes from the work of Johnson, *et al.*[18] These workers studied spin labels dissolved in lipid bilayer dispersions of dipalmitoylphosphatidylcholine and cholesterol (9:1 by weight) in the hope that anisotropic rotational diffusion of the spin label would mimic the motion of the bilayer components. In addition to 5-DS, which is sensitive to rotational motion about the NO bond, they used the steroidal nitroxide **8**, which tends to rotate about an axis perpendicular to the N–O bond. ESR measurements were carried out at both 9 and 35 GHz and at temperatures ranging from –30 to 30 °C. Rather different results were obtained with the two spin labels, largely as a result of the different axes of rotation. Because the rotation rates were very slow, ESR spectra appeared as powder patterns rather than isotropic spectra and special methods were needed to extract the motional data.

8
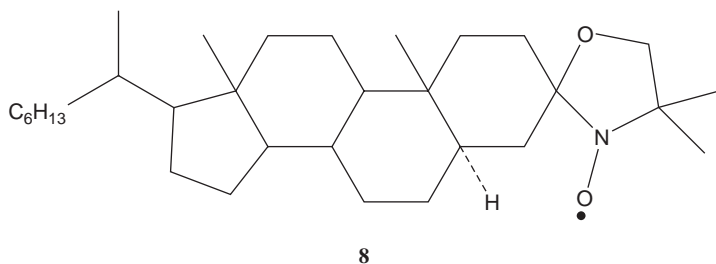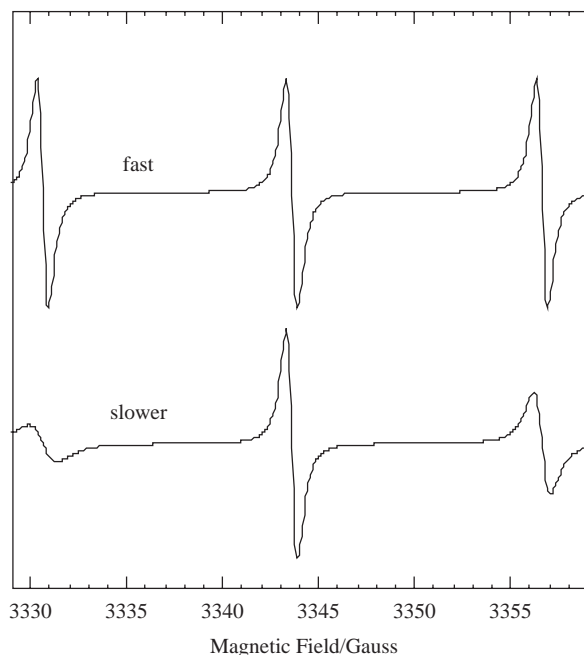
Figure 5.11 Effect of a slowing of the rate of rotational motion on the simulated ESR spectrum of a typical nitroxide spin label. Broadening becomes even more pronounced and non-uniform as the rate is further decreased.

Table 5.4 Transition temperatures for enzyme activity and nitroxide motion[17]

	Activity	*Activity*	*ESR*
	NADH oxidase	*p-Lactate oxidase*	*Phase trans. temp* (°C)
T_{2b} (°C)[a]	27		29.0
T_{2m} (°C)[a]	32	31	31.0
T_{2e} (°C)[a]		36	33.0

[a] T_{2b} = transition beginning; T_{2m} = transition mid-point; T_{2e} = transition endpoint.

References

1. R.L. Ward and S.I. Weissman, *J. Am. Chem. Soc.*, 1954, **76**, 3612.
2. F. Bloch, *Phys. Rev.*, 1946, **70**, 460.
3. N.W. Duffy, R.R. Nelson, M.G. Richmond, A.L. Rieger, P.H. Rieger, B.H. Robinson, D.R. Tyler, J.C. Wang and K. Yang, *Inorg. Chem.*, 1998, **37**, 4849.
4. C.J. Adams, N.G. Connelly and P.H. Rieger, *Chem. Commun.*, 2001, 2458.
5. L.V. Casagrande, T. Chen, P.H. Rieger, B.H. Robinson, J. Simpson and S.J. Visco, *Inorg. Chem.*, 1984, **23**, 2019.

6. J.A. DeGray, Q. Meng and P.H. Rieger, *J. Chem. Soc., Faraday Trans. I*, 1987, **83**, 3565.

7. (*a*) F.A. Walker, R.L. Carlin and P.H. Rieger, *J. Chem. Phys.*, 1966 **45**, 4181; (*b*) R.L. Carlin and F.A. Walker, *J. Am. Chem. Soc.*, 1965 **87**, 2128.

8. J.H. Freed and G.K. Fraenkel, *J. Chem. Phys.*, 1962, **37**, 1156.

9. L. Pasimeni, M. Brustoon and C. Corvaia, *J. Chem. Soc., Faraday Trans. II*, 1972, 223.

10. P.S. Gill and T.E. Gough, *Trans. Faraday Soc.*, 1968, **64**, 1997.

11. D. Jones and M.C.R. Symons, *Trans. Faraday Soc.*, 1971, **67**, 961.

12. J.H. Freed, P.H. Rieger and G.K. Fraenkel, *J. Chem. Phys.*, 1962, **37**, 1881.

13. P. W. Atkins, *Electron Spin Resonance*, Specialist Periodical Report, Royal Society of Chemistry, London, 1973, **1**, 47; 1974, **2**, 52; 1976, **3**, 35; 1977, **4**, 1.

14. T.J. Stone, T. Buckman, P.L. Nordio and H.M. McConnell, *Proc. Nat. Acad. Sci. U.S.A.*, 1965, **54**, 1010.

15. G. Moro and J.H. Freed, *J. Chem. Phys.*, 1981, **74**, 3757, **75**, 3157.

16. T. Lund and J. B. Raynor, *Electron Spin Resonance*, Specialist Periodical Report, Royal Society of Chemistry, London, 1974, **2**, 295; J. B. Raynor, *ibid.* 1976, **3**, 256; P. F. Knowles and B. Peake, *ibid.* 1977, **4**, 212; B. M Peake, *ibid.* 1978, **5**, 256; B. M. Peake, *ibid.* 1980, **6**, 233; B. H. Robinson, *ibid.* 1981, **7**, 293; B. H. Robinson and A. H. Beth, *ibid.* 1983, **8**, 346; C.-S. Lai, *ibid.* 1983, **8**, 378; C.-S. Lai, *ibid.* 1984, **9**, 246; C.-S. Lai, *ibid.* 1987, **10A**, 116; C.-S. Lai, *ibid.* 1991, **12A**, 74; D. Marsh, *ibid.* 1993, **14**, 166; P. Tordo, *ibid.* 1997, **16**, 116; *Spin Labeling Theory and Applications*, ed. L. J. Berliner, Academic Press, New York, 1976; M. J. Davies, *Electron Paramagnetic Resonance 18*, Royal Society of Chemistry, Cambridge, UK, 2003, ch 2, pp. 47–75.

17. J.D. Morrisett, H.J. Pownall, R.T. Plumlee, L.C. Smith, Z.E. Zehner, M. Eseahani and S.J. Wakil, *J. Biol. Chem.*, 1975, **250**, 6969.

18. M.E. Johnson, L. Lee and L.W.-M. Fung, *Biochemistry*, 1982, **21**, 4459.

CHAPTER 6

ESR Spectra of Biradicals, Triplet States, and other $S > 1/2$ Systems

6.1 Biradicals

Molecules with two or more unpaired electrons may be divided into two classes: by far the most common examples are molecules where the unpaired electrons are contained in a set of degenerate atomic or molecular orbitals with qualitatively similar spatial distributions, *e.g.*, an octahedral Cr(III) ($^4A_{2g}$) or Ni(II) ($^3A_{2g}$) complex, a ground state triplet molecule like O_2, or the excited triplet states of naphthalene or benzophenone.

A second class of molecules with two unpaired electrons has the two electrons localized, to a first approximation, in different parts of the molecule. We refer to such molecules as *biradicals* (or, with three or more unpaired electrons, triradicals, *etc.*). Examples are the dinitroxides (*e.g.* **1**), and certain binuclear vanadium(IV) and copper(II) complexes.

1
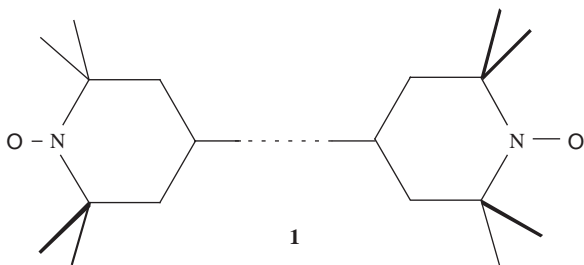
From the point of view of ESR spectroscopy, the distinction between molecules with one unpaired electron and those with more than one lies in the fact that electrons interact with one another; these interactions lead to additional terms in the spin Hamiltonian and additional features in the ESR spectrum. The most important electron–electron interaction is coulombic repulsion; with two unpaired electrons, repulsion leads to the singlet–triplet splitting. As we will see, this effect can be modeled by adding a term, $J\vec{S}_1 \cdot \vec{S}_2$, to the spin Hamiltonian,

where J is called the *exchange coupling constant* and turns out to be equal to energy difference between the singlet and triplet states, *i.e.* the singlet–triplet splitting.

In many cases, the singlet–triplet splitting is large compared with kT, as well as any other term in the spin Hamiltonian, and we can safely ignore the singlet state, focusing entirely on the triplet. The simplification of being able to ignore the singlet state is more than compensated for by the introduction of a *fine structure term* into the spin Hamiltonian.

This term, which has the form shown in eqn (6.1) introduces considerable complication into the shape and interpretation of ESR spectra.

$$D\left[S_Z^2 - \tfrac{1}{3}S(S+1)\right] + E\left(S_x^2 - S_y^2\right) \qquad (6.1)$$

Further complicating the situation is the fact that the same term can arise from two quite different physical effects: *electron–electron dipolar interaction* and *spin–orbit coupling*.

The distinction between a biradical and an ordinary triplet state molecule is often somewhat fuzzy. For our purposes, we consider a molecule a biradical if the exchange interaction between the two electrons is relatively weak – comparable in energy to the electron–nuclear hyperfine interaction. When the exchange interaction is weak, the singlet–triplet splitting is small and (as we will see) singlet–triplet mixing has an effect on the ESR spectrum. J falls off with electron–electron distance as $1/r$, whereas the dipolar coupling constant D falls off as $1/r^3$. Thus when J is small, D is negligible (though spin–orbit effects may contribute).

6.1.1 Exchange Coupling

In this section we consider the spin Hamiltonian appropriate to a biradical with weak dipolar coupling and see how ESR spectra of such species should appear. Obviously, it is possible to find triradicals, tetraradicals, *etc.*; treatment of such species is similar, though of course somewhat more complicated.

The spin Hamiltonian for a biradical consists of terms representing the electron Zeeman interaction, the exchange coupling of the two electron spins, and hyperfine interaction of each electron with the nuclear spins. We assume that there are two equivalent nuclei, each strongly coupled to one electron and essentially uncoupled to the other. The spin Hamiltonian is:

$$H_s = g\mu_B B\left(S_{1z} + S_{2z}\right) + A\left(\vec{S_1} \cdot \vec{I_1} + \vec{S_2} \cdot \vec{I_2}\right) + J\,\vec{S_1} \cdot \vec{S_2} \qquad (6.2)$$

where J is the exchange coupling constant. Notice that we have also assumed that the g-values for the two electrons are the same. To simplify matters, we will assume that $|A| \ll g\mu_B B$ so that a first-order treatment of the hyperfine term will suffice. We choose as basis functions the singlet and triplet electron spin functions:

$$|S_0\rangle = \tfrac{1}{\sqrt{2}}\left(|\tfrac{1}{2}, -\tfrac{1}{2}\rangle - |-\tfrac{1}{2}, \tfrac{1}{2}\rangle\right) \qquad (6.3a)$$

$$|T_0\rangle = \tfrac{1}{\sqrt{2}}(|\tfrac{1}{2}, -\tfrac{1}{2}\rangle + |-\tfrac{1}{2}, \tfrac{1}{2}\rangle) \tag{6.3b}$$

$$|T_1\rangle = |\tfrac{1}{2}, \tfrac{1}{2}\rangle \tag{6.3c}$$

$$|T_{-1}\rangle = |-\tfrac{1}{2}, -\tfrac{1}{2}\rangle \tag{6.3d}$$

The singlet function corresponds to zero total electron spin angular momentum, $S=0$; the triplet functions correspond to $S=1$. Operating on these functions with the spin Hamiltonian, we get:

$$\hat{H}_s|T_1\rangle = \left[g\mu_B B + \tfrac{1}{4}J + \tfrac{1}{2}A\,(m_1 + m_2)\right]|T_1\rangle$$

$$\hat{H}_s|T_{-1}\rangle = \left[-g\mu_B B + \tfrac{1}{4}J - \tfrac{1}{2}A\,(m_1 + m_2)\right]|T_{-1}\rangle$$

$$\hat{H}_s|T_0\rangle = \tfrac{1}{4}J|T_0\rangle + \tfrac{1}{2}A\,(m_1 - m_2)|S_0\rangle$$

$$\hat{H}_s|S_0\rangle = -\tfrac{3}{4}J|S_0\rangle + \tfrac{1}{2}A\,(m_1 - m_2)|T_0\rangle$$

Thus $|T_1\rangle$ and $|T_{-1}\rangle$ are eigenfunctions of $\hat{H}_s$, but $|T_0\rangle$ and $|S_0\rangle$ are mixed. (Notice, however, that if there were no hyperfine coupling, $A=0$, then $|T_0\rangle$ and $|S_0\rangle$ would be eigenfunctions as well.) In the absence of a hyperfine interaction, the triplet energy is $J/4$ and the singlet energy is $-3J/4$; J is normally negative so that the triplet lies lower in energy.

To get the eigenvalues resulting from the admixture of $|T_0\rangle$ and $|S_0\rangle$, we solve the secular equation:

$$\begin{vmatrix} \tfrac{J}{4} - E & \tfrac{A}{2}(m_1 - m_2) \\ \tfrac{A}{2}(m_1 - m_2) & -\tfrac{3J}{4} - E \end{vmatrix}$$

$$= E^2 + \tfrac{1}{2}JE - \tfrac{3}{16}J^2 - \tfrac{1}{4}A^2(m_1 - m_2)^2 = 0$$

The roots are:

$$E = -\tfrac{1}{4}J \pm \tfrac{1}{2}\sqrt{J^2 + A^2(m_1 - m_2)^2}$$

or, defining:

$$R = \sqrt{J^2 + A^2(m_1 - m_2)^2}$$

we have:

$$E = -\frac{J}{4} \pm \frac{R}{2}$$

The eigenfunctions corresponding to these energies may be found by inserting a value of E into one of the linear equations that lead to the secular equation:

$$\left(\tfrac{1}{4}J - E\right)c_T + \tfrac{1}{2}A(m_1 - m_2)\,c_S = 0$$

$$\tfrac{1}{2}A(m_1 - m_2)\,c_T + \left(-\tfrac{3}{4}J - E\right)c_S = 0$$

where c_T and c_S are the coefficients of $|T_0\rangle$ and $|S_0\rangle$ in the eigenfunction corresponding to $E(c_T^2 + c_S^2 = 1)$. The resulting eigenfunctions and energies are:

$$E_1 = g\mu_B B + \frac{J}{4} + \frac{A}{2}(m_1 + m_2) \qquad |1\rangle = |T_1\rangle$$

$$E_2 = -\frac{J}{4} + \frac{R}{2} \qquad |2\rangle = \sqrt{\frac{R+J}{2R}}|T_0\rangle + \sqrt{\frac{R-J}{2R}}|S_0\rangle$$

$$E_3 = -\frac{J}{4} - \frac{R}{2} \qquad |3\rangle = \sqrt{\frac{R-J}{2R}}|T_0\rangle - \sqrt{\frac{R+J}{2R}}|S_0\rangle$$

$$E_4 = -g\mu_B B + \frac{J}{4} - \frac{A}{2}(m_1 + m_2) \qquad |4\rangle = |T_{-1}\rangle$$

Remembering that each of these is further split by the hyperfine interaction, there are obviously several possible transitions among these four energy levels. To find out which are important, we must evaluate the transition dipole moment matrix elements, $\langle i|S_x|j\rangle$, since the absorption intensity is proportional to the square of these matrix elements. The operator S_x can be written:

$$\hat{S}_x = \hat{S}_{1x} + \hat{S}_{2x} = \tfrac{1}{2}\left(\hat{S}_{1+} + \hat{S}_{1-} + \hat{S}_{2+} + \hat{S}_{2-}\right)$$

Applying S_x to $|1\rangle$ and $|4\rangle$, we have:

$$\hat{S}_x|1\rangle = \tfrac{1}{2}\left(\hat{S}_{1+} + \hat{S}_{1-} + \hat{S}_{2+} + \hat{S}_{2-}\right)|\tfrac{1}{2}, \tfrac{1}{2}\rangle$$
$$= \tfrac{1}{2}\left(|-\tfrac{1}{2}, \tfrac{1}{2}\rangle + |\tfrac{1}{2}, -\tfrac{1}{2}\rangle\right) = \sqrt{2}|T_0\rangle$$

$$\hat{S}_x|4\rangle = \tfrac{1}{2}\left(\hat{S}_{1+} + \hat{S}_{1-} + \hat{S}_{2+} + \hat{S}_{2-}\right)|-\tfrac{1}{2}, -\tfrac{1}{2}\rangle$$
$$= \tfrac{1}{2}\left(|\tfrac{1}{2}, -\tfrac{1}{2}\rangle + |-\tfrac{1}{2}, \tfrac{1}{2}\rangle\right) = \sqrt{2}|T_0\rangle$$

Thus the matrix elements are:

$$\left\langle 1\middle|\hat{S}_x\middle|1\right\rangle = \left\langle 4\middle|\hat{S}_x\middle|4\right\rangle = \left\langle 1\middle|\hat{S}_x\middle|4\right\rangle = \left\langle 4\middle|\hat{S}_x\middle|1\right\rangle = 0$$

$$\left\langle 2\middle|\hat{S}_x\middle|1\right\rangle = \left\langle 2\middle|\hat{S}_x\middle|4\right\rangle = \left\langle 1\middle|\hat{S}_x\middle|2\right\rangle = \left\langle 4\middle|\hat{S}_x\middle|2\right\rangle = \sqrt{\frac{R+J}{R}}$$

$$\left\langle 3\middle|\hat{S}_x\middle|1\right\rangle = \left\langle 3\middle|\hat{S}_x\middle|4\right\rangle = \left\langle 1\middle|\hat{S}_x\middle|3\right\rangle = \left\langle 4\middle|\hat{S}_x\middle|3\right\rangle = \sqrt{\frac{R-J}{R}}$$

Since the relative intensity of a transition is proportional to the square of the corresponding matrix element of $\hat{S}_x$, we see that there are four allowed transitions:

$$\Delta E_{42} = g\mu_{\mathrm{B}}B + \frac{1}{2}(R - J) + \frac{1}{2}A(m_1 + m_2)$$

$$\text{Relative intensity} = \frac{R + J}{R}$$

$$\Delta E_{43} = g\mu_{\mathrm{B}}B - \frac{1}{2}(R + J) + \frac{1}{2}A(m_1 + m_2)$$

$$\text{Relative intensity} = \frac{R - J}{R}$$

$$\Delta E_{31} = g\mu_{\mathrm{B}}B + \frac{1}{2}(R + J) + \frac{1}{2}A(m_1 + m_2)$$

$$\text{Relative intensity} = \frac{R - J}{R}$$

$$\Delta E_{21} = g\mu_{\mathrm{B}}B - \frac{1}{2}(R - J) + \frac{1}{2}A(m_1 + m_2)$$

$$\text{Relative intensity} = \frac{R + J}{R}$$

Consider now the limiting case of strong exchange coupling. When $|J| >> |A|$, $R \approx J$, and the 43 and 31 transitions are forbidden. The 42 and 21 transitions are at equal energy and so we have only:

$$\Delta E = g\mu_{\mathrm{B}}B + \tfrac{1}{2}A(m_1 + m_2) \tag{6.4}$$

Thus in the limit of strong exchange interaction, the resulting spectrum is identical to that which would be observed if one electron interacted with two equivalent nuclei with coupling constant $A/2$.

In the limiting case of weak coupling, $|J| \ll |A|$, $R \approx A(m_1 - m_2)$, and all four transitions have equal relative intensities; the transition energies then are:

$$\Delta E_{42} = \Delta E_{31}$$

$$= g\mu_{\mathrm{B}}B + \frac{A}{2}(m_1 - m_2) + \frac{A}{2}(m_1 + m_2) \tag{6.5a}$$

$$= g\mu_{\mathrm{B}}B + Am_1$$

$$\Delta E_{43} = \Delta E_{21}$$

$$= g\mu_{\mathrm{B}}B - \frac{A}{2}(m_1 - m_2) + \frac{A}{2}(m_1 + m_2) \tag{6.5b}$$

$$= g\mu_{\mathrm{B}}B + Am_2$$

Thus in the limit of negligible exchange interaction, we expect a spectrum identical to that observed for two independent radicals.
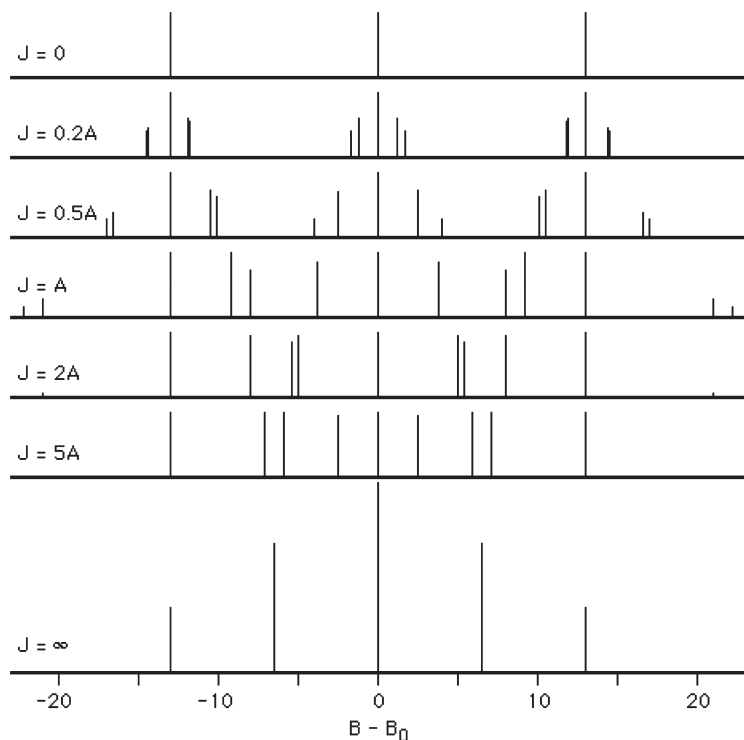
Figure 6.1 Stick spectra for a dinitroxide biradical with $a = 13$ G for various values of the exchange coupling constant J. (Several very small, widely spaced resonances have been omitted for $J = 2A$ and $J = 5A$.)

Now consider a concrete example. Suppose we have a nitroxide biradical with $a^N = 13$ G. In the strong exchange limit, we expect a five-line spectrum with a spacing of 6.5 G and the usual 1:2:3:2:1 intensity ratios for two equivalent spin-1 nuclei. In the weak exchange limit, we expect a three-line spectrum with a spacing of 13 G and intensity ratios 1:1:1. In intermediate cases, up to 15 lines are expected, as shown in Figure 6.1.

In a classic early study of biradicals, Glarum and Marshall[1] were able to vary the exchange coupling between two nitroxide radicals by changing the temperature, solvent, and the number of atoms linking the two groups. Most of their spectra corresponded to the intermediate exchange region where $J \approx A$.

6.2 Organic Triplet State Molecules and the Dipolar Interaction

The Hamiltonian term for the electron–electron dipolar interaction is:

$$\hat{H}_d = g^2 \mu_B^2 \left[\frac{\vec{s}_1 \cdot \vec{s}_2}{r^3} - 3 \frac{(\vec{s}_1 \cdot \vec{r})(\vec{s}_2 \cdot \vec{r})}{r^5} \right] \tag{6.6}$$

where r is the vector pointing from electron 1 to electron 2. We have used a lower-case s for the one-electron spin operators, reserving upper-case S for the total electron spin operators. The dot products can be expanded to give:

$$\hat{H}_d = g^2 \mu_B^2 \left[\frac{(r^2 - 3x^2)}{r^5} \hat{s}_{1x}\hat{s}_{2x} + \frac{(r^2 - 3y^2)}{r^5} \hat{s}_{1y}\hat{s}_{2y} \right.$$
$$+ \frac{(r^2 - 3z^2)}{r^5} \hat{s}_{1z}\hat{s}_{2z} - \frac{3xy}{r^5} \left(\hat{s}_{1x}\hat{s}_{2y} + \hat{s}_{2y}\hat{s}_{1x} \right)$$
$$\left. - \frac{3yz}{r^5} \left(\hat{s}_{1y}\hat{s}_{2z} + \hat{s}_{1z}\hat{s}_{2y} \right) - \frac{3zx}{r^5} \left(\hat{s}_{1z}\hat{s}_{2x} + \hat{s}_{1x}\hat{s}_{2z} \right) \right]$$

Our next goal is to transform this expression into one based on the total electron spin operator, $S = s_1 + s_2$. The first three terms can be simplified by making use of the identity (derived using raising and lowering operators):

$$2s_{1i}s_{2i} = S_i^2 - \tfrac{1}{2} \qquad (i = x, y, z)$$

When these are substituted in the above expression, the terms arising from $-1/2$ cancel since $x^2 + y^2 + z^2 = r^2$. Transformation of the last three terms makes use of the identities:

$$2(s_{1i}s_{2j} + s_{1j}s_{2i}) = S_iS_j + S_jS_i$$

The transformed Hamiltonian then is:

$$\hat{H}_d = \frac{1}{2} g^2 \mu_B^2 \left[\frac{r^2 - 3x^2}{r^5} \hat{S}_x^2 + \frac{r^2 - 3y^2}{r^5} \hat{S}_z^2 \right.$$
$$+ \frac{r^2 - 3z^2}{r^5} \hat{S}_z^2 - \frac{3xy}{r^5} \left(\hat{S}_x\hat{S}_y + \hat{S}_y\hat{S}_x \right)$$
$$\left. - \frac{3yz}{r^5} \left(\hat{S}_y\hat{S}_z + \hat{S}_z\hat{S}_y \right) - \frac{3zx}{r^5} \left(\hat{S}_z\hat{S}_x + \hat{S}_x\hat{S}_z \right) \right]$$

The coefficients of the spin operators must be evaluated using the electron wave function, an operation that is not usually possible in practice. However, we can parameterize the problem, defining the matrix D with elements:

$$D_{ij} = \frac{1}{2} g^2 \mu_B^2 \left\langle \frac{r^2 \delta_{ij} - 3ij}{r^5} \right\rangle \qquad (6.7)$$

where the angle brackets indicate averaging over the spatial coordinates of the wave function.

It is possible to choose an axis system in which the D-matrix is diagonal – the principal axes. In many cases, these axes will also be the principal axes of the g-matrix and we will so assume in the following.

Since the trace of D ($D_{xx} + D_{yy} + D_{zz}$) is zero, there are really only two independent parameters. The conventional choice of these parameters is:

$$D = \tfrac{3}{2} D_{zz} \quad E = \tfrac{1}{2} \left(D_{xx} - D_{yy} \right)$$

or:

$$D_{zz} = \tfrac{2}{3}D \quad D_{xx} = -\tfrac{1}{3}D + E \quad D_{yy} = -\tfrac{1}{3}D - E$$

The Hamiltonian then becomes:

$$\hat{H}_{d} = D_{xx}\hat{S}_x^2 + D_{yy}\hat{S}_y^2 + D_{zz}\hat{S}_z^2 \tag{6.8a}$$

or:

$$\hat{H}_{d} = D\left[\hat{S}_z^2 - \tfrac{1}{3}\left(\hat{S}_x^2 + \hat{S}_y^2 + \hat{S}_z^2\right)\right] + \tfrac{1}{2}E\left(\hat{S}_x^2 + \hat{S}_y^2\right) \tag{6.8b}$$

We can somewhat simplify the Hamiltonian by noting that $S_x{}^2 + S_y{}^2 + S_z{}^2 = S^2$ and the eigenvalue of S^2 is $S(S+1)$, and that S_x and S_y can be written in terms of the raising and lowering operators:

$$\hat{H}_{d} = D\left[\hat{S}_z^2 - \tfrac{1}{3}S(S+1)\right] + E\left(\hat{S}_+^2 + \hat{S}_-^2\right) \tag{6.9}$$

We will see that a Hamiltonian term identical in form also arises from spin–orbit coupling, but first we will pause to see the effect of this Hamiltonian on the energy levels and ESR spectrum of a triplet-state molecule. The spin triplet wave functions can be written in the notation $|S,m_S\rangle$:

$$\hat{H}_{d}|1, 1\rangle = D\left(1 - \tfrac{2}{3}\right)|1, 1\rangle + E|1, -1\rangle$$

$$\hat{H}_{d}|1, 0\rangle = D\left(0 - \tfrac{2}{3}\right)|1, 0\rangle$$

$$\hat{H}_{d}|1, -1\rangle = D\left(1 - \tfrac{2}{3}\right)|1, -1\rangle + E|1, 1\rangle$$

The Hamiltonian matrix then is:

$$\begin{pmatrix} \tfrac{1}{3}D & 0 & E \\ 0 & -\tfrac{2}{3}D & 0 \\ E & 0 & \tfrac{1}{3}D \end{pmatrix}$$

Solution of the corresponding secular equation leads to energy levels, $-2D/3$ and $D/3 \pm E$. The splitting pattern is shown in Figure 6.2.

Notice that if the molecule has axial symmetry, $D_{xx} = D_{yy}$ so that $E = 0$. If the molecule has octahedral symmetry, $D_{xx} = D_{yy} = D_{zz}$ so that $D = E = 0$. Thus the appearance of a zero-field splitting into two or three levels tells the spectroscopist something about the symmetry of the molecule. It is possible, of course, to do spectroscopy on these energy levels at zero magnetic field. Our concern here is the effect of zero-field splitting on the ESR spectrum where a magnetic field is applied.

When we include the Zeeman interaction term, $g\mu_B B \cdot S$, in the spin Hamiltonian a complication arises. We have been accustomed to evaluating the dot product by simply taking the direction of the magnetic field to define the z-axis (the axis of quantization). When we have a strong dipolar interaction, the
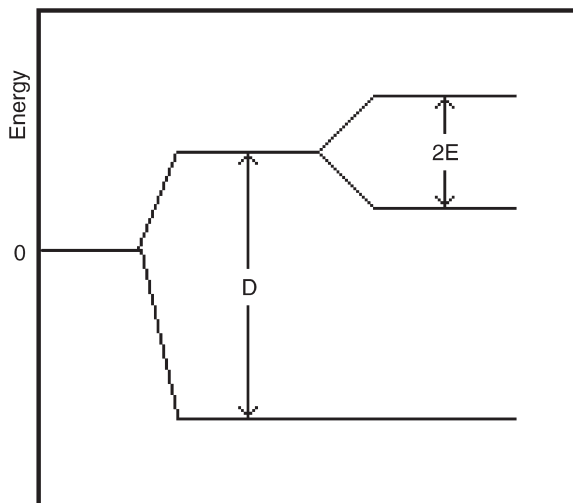
Figure 6.2   Zero-field splitting of a triplet state.

molecule defines a quantization axis for itself. Thus, in general, the $\boldsymbol{B} \cdot \boldsymbol{S}$ term has three components. It is possible to deal with the general case, but the algebra is very messy and not very enlightening. Instead we will assume that the triplet molecule is in a dilute single crystal and that we can orient the crystal in the field with $\boldsymbol{B}$ along one of the internal coordinate axes.

Suppose that we orient the crystal with $\boldsymbol{B}$ in the z-direction. The spin Hamiltonian then is:

$$\hat{H}_s = g\mu_B B\hat{S}_z + D\left[\hat{S}_z^2 - \tfrac{1}{3}S(S+1)\right] + \tfrac{1}{2}E\left(\hat{S}_+^2 + \hat{S}_-^2\right)$$

Operating on the triplet wave functions as before, we get the Hamiltonian matrix:

$$\begin{pmatrix} g\mu_B B + \tfrac{1}{3}D & 0 & E \\ 0 & -\tfrac{2}{3}D & 0 \\ E & 0 & -g\mu_B B + \tfrac{1}{3}D \end{pmatrix}$$

Solution of the secular equation leads to the energies:

$$-\tfrac{2}{3}D, \ \tfrac{1}{3}D \pm \sqrt{g^2\mu_B^2 B^2 + E^2}$$

These are plotted *vs.* magnetic field in Figure 6.3, using $D = 0.1003$ cm^{-1}, $E = -0.0137$ cm^{-1} – parameters appropriate to the excited triplet of naphthalene.[2]

The energies of the allowed transitions are:

$$\Delta E = \sqrt{g^2\mu_B^2 B^2 + E^2} \pm D$$

At constant frequency, $v_0 = \Delta E/h$, the resonant fields are:

$$B = \frac{1}{g\mu_B} \sqrt{(hv_0 \pm D)^2 - E^2}$$

With the magnetic field oriented along the x-axis, the Hamiltonian is:

$$\hat{H}_s = g\mu_B B \hat{S}_x + D\left[\hat{S}_z^2 - \tfrac{1}{3}S(S+1)\right] + \tfrac{1}{2}E\left(\hat{S}_+^2 + \hat{S}_-^2\right)$$

The Hamiltonian matrix is:

$$\begin{pmatrix} \tfrac{1}{3}D & \tfrac{1}{\sqrt{2}}g\mu_B B & E \\ \tfrac{1}{\sqrt{2}}g\mu_B B & -\tfrac{2}{3}D & \tfrac{1}{\sqrt{2}}g\mu_B B \\ E & \tfrac{1}{\sqrt{2}}g\mu_B B & \tfrac{1}{3}D \end{pmatrix}$$

The cubic secular equation factors; the resulting energies are:

$$\frac{D}{3} - E, \quad -\frac{D - 3E}{6} \pm \sqrt{g^2 \mu_B^2 B^2 + \frac{1}{4}(D+E)^2}$$

These energies are also plotted in Figure 6.3; energies of the allowed transitions are:

$$\Delta E = \sqrt{g^2 \mu_B^2 B^2 + \tfrac{1}{4}(D+E)^2} \pm \tfrac{1}{2}(D - 3E)$$

The resonant fields then are:

$$B = \frac{1}{g\mu_B} \sqrt{\left(hv_0 \pm \frac{1}{2}(D - 3E)\right)^2 - \frac{1}{4}(D+E)^2}$$
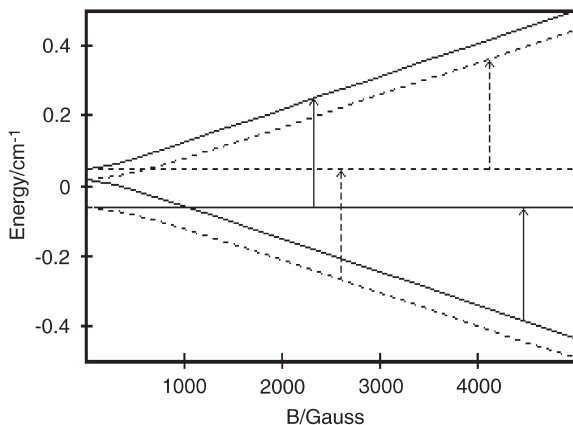
Figure 6.3 Energy level diagram for the triplet state of naphthalene ($D = 0.1003$ cm^{-1}, $E = -0.0137$ cm^{-1}, $g = 2.003$). Solid lines correspond to orientation of the magnetic field along the z-axis, dashed lines for orientation along the x-axis. Arrows show the allowed transitions for 9.50 GHz microwave radiation.

6.2.1   Organic Triplet State Molecules

The phosphorescent triplet state of naphthalene, for which the energy levels are shown in Figure 6.3, is produced by irradiation of naphthalene doped into a single crystal of durene. This prevents relaxation effects due to rapid transfer of energy between triplet and ground state naphthalene molecules. The triplet state is long-lived at 77 K. The energy-level diagram (Figure 6.3) predicts two transitions: at 2315 and 4465 G when the field is oriented along the z-axis, and at 2595 and 4125 G for orientation along the x-axis ($v_0 = 9.50$ GHz).

The experimental determination of D and E for a dilute single crystal is not trivial, even when the crystal axes are known. Durene, for example, has two molecules per unit cell with different orientations of the molecular plane. Thus for any orientation there are four resonances, two from each type of site. Sorting out the data is a challenging exercise.[2]

Triplet state powder spectra (or frozen solution glasses) are generally easier to interpret and much easier to get experimentally than dilute single crystal spectra. The features of the derivative spectrum correspond to orientations along the principal axis directions. Thus, six features can be found in the spectrum of naphthalene in glassy THF solution at 77 K (after irradiation). The problem, as is usual with powder spectra, is that there is no way to assign the features to molecular axes; recourse must be made to theoretical considerations or to analogy with a related system studied in a dilute single crystal. Since the resonances are spread over a large field range and are very orientation dependent, there is little hope of detecting the resonance of a triplet state molecule in liquid solution, even if the triplet state lifetime could be made long enough.

What do we make of the parameters D and E once we have extracted them from a spectrum? Seven examples are given in Table 6.1.
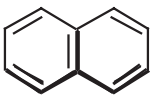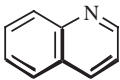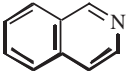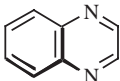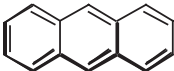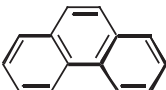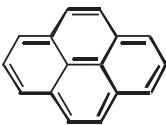
There are some qualitative trends that make some sense. Since D is a measure of the dipolar interaction of the two unpaired electrons, we might expect that D would be large when both electrons are forced to be close together, and naphthalene and the related nitrogen heterocyclics do indeed give the largest values of D. When the π-system remains about the same size but heteroatoms are substituted, we might expect that D would not change by much, and we see that naphthalene and related nitrogen heterocyclics do indeed have nearly the same values of D. When the π-system gets bigger, we might expect D to decrease, and anthracene and pyrene fulfill this expectation, but phenanthrene seems anomalous. To go beyond a qualitative explanation of D or to explain E at all requires rather sophisticated valence theory calculations. Indeed electron dipolar interaction parameters provide one of the more challenging tests of valence theory.

6.3   Transition Metal Complexes with $S > 1/2$

6.3.1   Spin–Orbit Coupling

We now will show that spin–orbit coupling can give a spin Hamiltonian term identical to that we obtained from the electron dipolar interaction. Consider the

Table 6.1 ESR data for some organic triplet-state molecules

Molecule	Structure	D (cm^{-1})	E (cm^{-1})	Ref
Naphthalene (in durene)		0.1003	–0.0137	2
Quinoline (in durene)		0.1030	–0.0162	3
Isoquinoline (in durene)		0.1004	–0.0117	3
Quinoxaline (in durene)		0.1007	–0.0182	4
Anthracene (in biphenyl)		0.0716	–0.0084	5
Phenanthrene (in biphenyl)		0.1004	–0.0466	6
Pyrene (in fluorene)		0.0678	–0.0314	7

spin Hamiltonian including orbital angular momentum and the usual spin–orbit coupling term:

$$\hat{H} = \mu_B \vec{B} \cdot \left(\vec{L} + g_e \vec{S} \right) + \lambda \vec{L} \cdot \vec{S} \tag{6.10}$$

where λ is the spin–orbit coupling constant. The zero-order ground state wave function will be characterized by the quantum numbers L, m_L, S, m_S, and we

assume that the wave function is orbitally nondegenerate, i.e., $m_L = 0$. Thus we write the ground state wave function as $|m_L, m_S\rangle = |0, m_S\rangle$. With $\boldsymbol{B}$ defining the z-axis, the energy is easily found to first order in perturbation theory:

$$E^{(1)} = g\mu_B B m_s \tag{6.11}$$

since $L_z|0,m_S\rangle = 0$. The second-order energy is not so simple since the excited states in general have nonzero m_L. Thus we get second-order contributions from matrix $|0,m_S\rangle$ elements connecting with excited state functions:

$$E^{(2)} = -\sum_i \frac{\left[\langle 0, m_{S,0}|\left(\mu_B\vec{B} + \lambda\vec{S}\right)\cdot\vec{L} + g_e\mu_B\vec{B}\cdot\vec{S}|m_{L,i}, m_{S,i}\rangle\right]^2}{E_i^{(1)} - E_0^{(1)}} \tag{6.12}$$

The matrix element can be expanded and written as:

$$\langle 0, m_{S,0}|\left(\mu_B\vec{B} + \lambda\vec{S}\right)|m_{S,i}\rangle \cdot \langle 0|\vec{L}|m_{L,i}\rangle$$
$$+ g_e\mu_B\vec{B}\cdot\langle m_{S,0}|\vec{S}|m_{S,i}\rangle\langle 0|m_{L,i}\rangle$$

Since the orbital functions, $\langle 0|$ and $|m_{L,i}\rangle$ are orthogonal, the second term vanishes. The absolute value square of the matrix element of a Hermitean operator can be written as:

$$|\langle i|\boldsymbol{Op}|j\rangle|^2 = \langle i|\boldsymbol{Op}|j\rangle\langle j|\boldsymbol{Op}|i\rangle$$

Thus we can write $E^{(2)}$ as:

$$E^{(2)} = \sum_{m_S'}^{\infty}\left\{\langle m_{S,0}|\mu_B\vec{B} + \lambda\vec{S}|m_S'\rangle\right.$$
$$\cdot\left(\sum_i \frac{\langle 0|\vec{L}|m_L\rangle\langle m_L|\vec{L}|0\rangle}{E_i^{(1)} - E_0^{(1)}}\right)$$
$$\left.\cdot\langle m_S'|\mu_B\vec{B} + \lambda\vec{S}|m_{S,0}\rangle\right\}$$

Defining:

$$\overleftrightarrow{\Lambda} = \sum_i \frac{\langle 0|\vec{L}|m_L\rangle\langle m_L|\vec{L}|0\rangle}{E_i^{(1)} - E_0^{(1)}} \tag{6.13}$$

we can write $E^{(2)}$ as:

$$E^{(2)} = \sum_{m_S'}^{\infty}\left\{\mu_B^2\langle m_S|\vec{B}\cdot\overleftrightarrow{\Lambda}\cdot\vec{B}|m_S'\rangle + \lambda^2\langle m_S|\vec{S}\cdot\overleftrightarrow{\Lambda}\cdot\vec{S}|m_S'\rangle\right.$$
$$\left. + 2\lambda\mu_B\langle m_S|\vec{B}\cdot\overleftrightarrow{\Lambda}\cdot\vec{S}|m_S'\rangle\right\} \tag{6.14}$$

We now notice that we could write a Hamiltonian operator that would give the same matrix elements we have here, but as a first-order result. Including the electron Zeeman interaction term, we have the resulting spin Hamiltonian:

$$\hat{H}_s = g_e \mu_B \vec{B} \cdot \vec{S} + \mu_B^2 \vec{B} \cdot \overset{\leftrightarrow}{A} \cdot \vec{B} + 2\lambda \mu_B \vec{B} \cdot \overset{\leftrightarrow}{A} \cdot \vec{S} + \lambda^2 \vec{S} \cdot \overset{\leftrightarrow}{A} \cdot \vec{S} \qquad (6.15)$$

The $\mu_B^2 \vec{B} \cdot \overset{\leftrightarrow}{A} \vec{B}$ term is independent of spin state and so changes all levels by the same amount. Although the term would be important to the thermodynamic properties of the system, it is uninteresting to spectroscopists and we will ignore it. The first and third terms can be combined to obtain the g-tensor:

$$g = g_e E + 2\lambda \overset{\leftrightarrow}{A} \qquad (6.16)$$

where E is the unit matrix. We can also define the fine structure tensor D as:

$$D = \lambda^2 \overset{\leftrightarrow}{A} \qquad (6.17)$$

so that the spin Hamiltonian reduces to:

$$H_s = \mu_B \vec{B} \cdot g \cdot \vec{S} + \vec{S} \cdot D \cdot \vec{S} \qquad (6.18)$$

Notice that the fine structure term found here has the same form (and the tensor is given the same symbol) as that obtained from the electron dipolar interaction. Unlike the dipolar D-tensor, however, the spin–orbit coupling D-tensor in general does not have zero trace. Nonetheless, we introduce analogous parameters:

$$D = D_{zz} - \tfrac{1}{2}(D_{xx} - D_{yy})$$

$$E = \tfrac{1}{2}(D_{xx} - D_{yy})$$

In the coordinate system that diagonalizes g, the related D-tensor is also diagonal. Expanding the fine structure term in the principal axis system, we have:

$$\vec{S} \cdot D \cdot \vec{S} = D_{xx} S_x^2 + D_{yy} S_y^2 + D_{zz} S_z^2$$

and substituting:

$$\vec{S} \cdot D \cdot \vec{S} = D\left[S_z^2 - \tfrac{1}{3}\left(S_x^2 + S_y^2 + S_z^2 \right) \right]$$
$$+ E\left(S_x^2 - S_y^2 \right)$$
$$+ \tfrac{1}{3}(D_{xx} + D_{yy} + D_{zz})\left(S_x^2 + S_y^2 + S_z^2 \right)$$

Since $S^2 = S_x^2 + S_y^2 + S_z^2$ and the eigenvalue of S^2 is $S(S+1)$ we have:

$$\vec{S} \cdot D \cdot \vec{S} = D\left[S_z^2 - \tfrac{1}{3}S(S+1) \right]$$
$$+ E\left(S_x^2 - S_y^2 \right)$$
$$+ \tfrac{1}{3}(D_{xx} + D_{yy} + D_{zz})S(S+1)$$

The last term (which would be zero if $\boldsymbol{D}$ came from the dipolar interaction and thus had zero trace) raises all levels equally and so has no effect on spectroscopy and can be dropped. Thus, again, only two parameters, D and E, are required to completely specify the fine structure interaction.

Although it is unfortunate that spin–orbit coupling and the electron dipolar interaction give fine structure terms of the same form, it is possible to separate the effects. Since the spin–orbit contribution to $\boldsymbol{D}$ is related to the g-tensor:

$$\boldsymbol{D}_{\text{so}} = \frac{\lambda}{2}(\boldsymbol{g} - g_e\boldsymbol{E})$$

the parameters D_{so} and E_{so} can be computed:

$$D_{\text{so}} = \frac{\lambda}{2}\left[g_{zz} - \frac{1}{2}(g_{xx} + g_{yy})\right]$$

$$E_{\text{so}} = \frac{\lambda}{4}(g_{xx} - g_{yy})$$

The difference between the fine structure parameters computed from the experimental g-tensor and those measured from the spectrum are presumed to be the electron dipolar contributions.

In the above derivation, we have made no explicit assumption about the total electron spin quantum number S so that the results should be correct for $S = 1/2$ as well as higher values. However, the fine structure term is not usually included in spin Hamiltonians for $S = 1/2$ systems. The fine structure term can be ignored since in that case the results of operating on a spin-1/2 wave function is always zero:

$$\left\{D\left[S_z^2 - \tfrac{1}{3}S(S+1)\right] + \tfrac{1}{2}E\left(S_+^2 + S_-^2\right)\right\}|\tfrac{1}{2}, \pm\tfrac{1}{2}\rangle$$
$$= \left\{D\left[\tfrac{1}{4} - \tfrac{1}{3} \times \tfrac{1}{2} \times \tfrac{3}{2}\right] + \tfrac{1}{2}E \times 0\right\}|\tfrac{1}{2}, \pm\tfrac{1}{2}\rangle = 0$$

6.3.2 High-spin Transition Metal Ions

For axially symmetric complexes, the parameter E is zero, and the spin functions $|S, m_S\rangle$ are eigenfunctions of the spin Hamiltonian:

$$H_s = \mu_B \vec{B} \cdot g \cdot \vec{S} + D\left[S_z^2 - \tfrac{1}{3}S(S+1)\right]$$

For example, consider a d^3 Cr(III) complex in an axial ligand field with $g = 1.98$, $D = 0.0455$ cm^{-1}, $E = 0$. For the magnetic field along the molecular z-axis, the energies are:

$$E\left(\pm\tfrac{3}{2}\right) = \pm\tfrac{3}{2}g_{\parallel} + D$$
$$E\left(\pm\tfrac{1}{2}\right) = \pm\tfrac{1}{2}g_{\parallel} - D$$

These energies are plotted *vs.* magnetic field in Figure 6.4.

Transitions among these levels have intensities proportional to the square of the matrix element of S_x. These are easily found to be:

$$\langle \tfrac{3}{2}, \pm\tfrac{3}{2}|S_x|\tfrac{3}{2}, \pm\tfrac{1}{2}\rangle = \tfrac{\sqrt{3}}{2}$$

$$\langle \tfrac{3}{2}, \tfrac{1}{2}|S_x|\tfrac{3}{2}, -\tfrac{1}{2}\rangle = 1$$

Thus the $-3/2 \to -1/2$ and $1/2 \to 3/2$ transitions, at $B = h\nu_0(1 \pm 2D)/g\mu_B$, have relative intensities of 3/4 the intensity of the $-1/2 \to 1/2$ transition, at $h\nu_0/g\mu_B$.

When the magnetic field is oriented along the x-axis, the Hamiltonian matrix is:

$$\begin{pmatrix} D & \tfrac{\sqrt{3}}{2}g_\perp\mu_B B & 0 & 0 \\ \tfrac{\sqrt{3}}{2}g_\perp\mu_B B & -D & g_\perp\mu_B B & 0 \\ 0 & g_\perp\mu_B B & -D & \tfrac{\sqrt{3}}{2}g_\perp\mu_B B \\ 0 & 0 & \tfrac{\sqrt{3}}{2}g_\perp\mu_B B & D \end{pmatrix}$$

Unfortunately, the secular equation doesn't factor and the energies must be computed numerically. A plot of the computed energies is shown in Figure 6.4 as a function of magnetic field.

As we might expect from the nondiagonal Hamiltonian matrix, the spin functions are thoroughly mixed when the field is in the x-direction. The immediate consequence of this mixing is that the selection rules are complicated, and the transition from the lowest level to the highest level becomes allowed. (For the field along the z-axis, this would be a forbidden two-quantum transition.) When $B = 1000$ G, corresponding to the lowest-to-highest transition, the wave functions are:

$$E = -0.179 \, \text{cm}^{-1}, \quad |1\rangle = -0.255 \left(|\tfrac{3}{2}\rangle - |-\tfrac{3}{2}\rangle\right)$$
$$+ 0.660\left(|\tfrac{1}{2}\rangle - |-\tfrac{1}{2}\rangle\right)$$
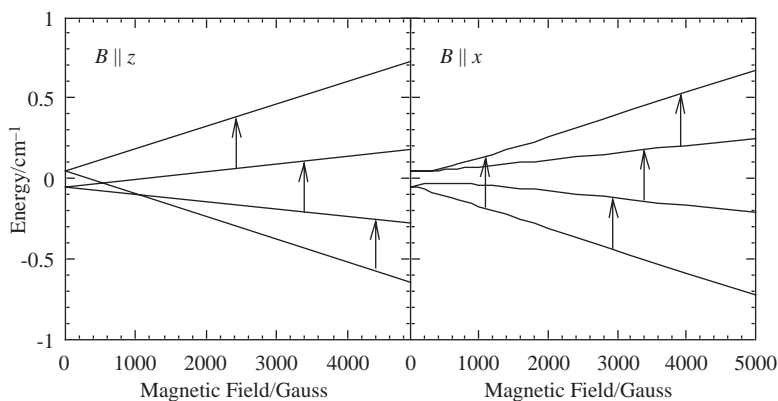
Figure 6.4 Energy levels and allowed transitions for a Cr(III) complex with $g = 1.98$, $D = 0.0455 \, \text{cm}^{-1}$, for the magnetic field along the x- and z-axes.

$$E = -0.037\,\mathrm{cm}^{-1}, \quad |2\rangle = -0.513\left(\left|\tfrac{3}{2}\right\rangle + \left|-\tfrac{3}{2}\right\rangle\right)$$
$$+ 0.487\left(\left|\tfrac{1}{2}\right\rangle + \left|-\tfrac{1}{2}\right\rangle\right)$$

$$E = +0.079\,\mathrm{cm}^{-1}, \quad |3\rangle = 0.660\left(\left|\tfrac{3}{2}\right\rangle - \left|-\tfrac{3}{2}\right\rangle\right)$$
$$+ 0.255\left(\left|\tfrac{1}{2}\right\rangle - \left|-\tfrac{1}{2}\right\rangle\right)$$

$$E = +0.137\,\mathrm{cm}^{-1}, \quad |4\rangle = 0.487\left(\left|\tfrac{3}{2}\right\rangle + \left|-\tfrac{3}{2}\right\rangle\right)$$
$$+ 0.513\left(\left|\tfrac{1}{2}\right\rangle + \left|-\tfrac{1}{2}\right\rangle\right)$$

When the field is along the z-axis, transition intensities are proportional to the square of the S_z^2 matrix element. The S_z^2 matrix for $B = 1000$ G is:

$$\begin{pmatrix} 0 & 1.197 & 0 & 0.0011 \\ 1.197 & 0 & 0.794 & 0 \\ 0 & 0.794 & 0 & 0.508 \\ 0.0011 & 0 & 0.508 & 0 \end{pmatrix}$$

The $1 \rightarrow 4$ transition is only weakly allowed compared with the $1 \rightarrow 2$, $2 \rightarrow 3$, and $3 \rightarrow 4$ transitions; however, it is often observed, particularly in powder spectra since it tends to be considerably sharper than the other transitions. Notice that the $1 \rightarrow 3$ and $2 \rightarrow 4$ transitions are still forbidden. Since the wave functions are field-dependent, the S_z matrix elements also depend on the field. Thus the observed $1 \rightarrow 2$, $2 \rightarrow 3$, and $3 \rightarrow 4$ transitions would be different than predicted from the S_z^2 matrix at 1000 G.

For Cr(III) complexes, D is relatively small (comparable to the X-band microwave quantum, $0.317\,\mathrm{cm}^{-1}$) and all three fine structure lines are observable. This is not always the case. Consider high-spin Fe(III) in an axial ligand field with $D >> h\nu_0$, $E = 0$. With the same Hamiltonian as above and the magnetic field along the z-axis, the energies are:

$$E\left(\pm\tfrac{5}{2}\right) = \pm\tfrac{5}{2}g_\parallel\mu_\mathrm{B}B + \tfrac{10}{8}D$$
$$E\left(\pm\tfrac{3}{2}\right) = \pm\tfrac{3}{2}g_\parallel\mu_\mathrm{B}B - \tfrac{2}{3}D$$
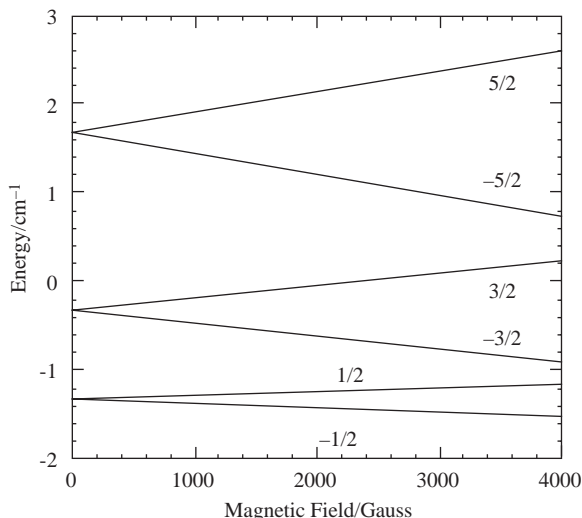$$E\left(\pm\tfrac{1}{2}\right) = \pm\tfrac{1}{2}g_\parallel\mu_\mathrm{B}B - \tfrac{8}{3}D$$

These are plotted *vs.* B in Figure 6.5.

The transition energies are:

$$E\left(\tfrac{5}{2}\right) - E\left(\tfrac{3}{2}\right) = g_\parallel\mu_\mathrm{B}B + 4D$$

$$E\left(\tfrac{3}{2}\right) - E\left(\tfrac{1}{2}\right) = g_\parallel\mu_\mathrm{B}B + 2D$$

$$E\left(\tfrac{1}{2}\right) - E\left(-\tfrac{1}{2}\right) = g_\parallel\mu_\mathrm{B}B$$

Figure 6.5 Energies of an $S = 5/2$ spin system with $D = 0.5$ cm^{-1} for B along the z-axis.

$$E\left(-\tfrac{1}{2}\right) - E\left(-\tfrac{3}{2}\right) = g_{\parallel}\mu_{\mathrm{B}}B - 2D$$

$$E\left(-\tfrac{3}{2}\right) - E\left(-\tfrac{5}{2}\right) = g_{\parallel}\mu_{\mathrm{B}}B - 4D$$

However, if $D > h\nu_{\mathrm{o}}$, only the $-1/2 \rightarrow 1/2$ transition will be observable. The first two transitions are always higher in energy then $h\nu_{\mathrm{o}}$ and it is usually not possible to make B large enough to bring the last two transitions into resonance.

Now consider what happens when the field is applied perpendicular to the symmetry axis. The large value of D ensures that z will continue to be the quantization axis. We ought to solve a 6×6 secular equation, but we can get a reasonable approximation more easily. Since D is big, the $\pm 5/2$ and $\pm 3/2$ levels are well separated from the $\pm 1/2$ levels before application of the magnetic field. Thus mixing of $|3/2\rangle$ with $|1/2\rangle$ will be much less important than mixing of $|1/2\rangle$ with $|-1/2\rangle$. Thus we can solve just the middle 2×2 block for the energies of $m_S = \pm 1/2$ levels:

$$\begin{pmatrix} -\tfrac{8}{3}D & \tfrac{3}{2}g_{\perp}\mu_{\mathrm{B}}B \\ \tfrac{3}{2}g_{\perp}\mu_{\mathrm{B}}B & -\tfrac{8}{3}D \end{pmatrix}$$

The expanded block gives:

$$\left(-\tfrac{8}{3}D - E\right)^2 - \left(\tfrac{3}{2}g_{\perp}\mu_{\mathrm{B}}B\right)^2 = 0$$

so that the energies are:

$$E = -\tfrac{8}{3}D \pm \tfrac{3}{2}g_{\perp}\mu_{\mathrm{B}}B$$

and the energy difference is:

$$E\left(\tfrac{1}{2}\right) - E\left(-\tfrac{1}{2}\right) = 3g_{\perp}\mu_{\mathrm{B}}B$$

The apparent g-value for the transition is $3g_{\perp}$, $g_{\mathrm{eff}} = 6$ if $g_{\perp} = 2$.

Thus, for example, high-spin d^5 Fe(III) in an axial ligand field should show a resonance around $g = 2$ and another resonance near $g = 6$ when B is perpendicular to the symmetry axis. In solution, where the complex tumbles rapidly and averages the g-values, the resonance is expected to be so broad as to be undetectable, but, in frozen solution, both resonances should be observable.

6.3.3   Examples: K₃Cr(CN)₆ and K₄V(CN)₆

These two salts were studied by the Oxford physics group in the early days of ESR spectroscopy.[8] The Cr(III) and V(II) salts were doped into diamagnetic single crystals of $K_3Co(CN)_6$ and $K_4Fe(CN)_6$, respectively. The spin–orbit coupling parameters found from the spectroscopic study are listed, together with the g-components, in Table 6.2.

Let us see what the energy levels look like for these two systems and try to understand how Baker, Bleaney, and Bowers determined the values given in Table 6.2. The spin Hamiltonian is:

$$\hat{H} = \mu_{\mathrm{B}}\vec{S}\cdot\overline{\overline{g}}\cdot\vec{B} + D\left[S_z^2 - \tfrac{1}{3}S(S+1)\right] + E\left(S_x^2 - S_y^2\right) + \vec{I}\cdot\overline{\overline{A}}\cdot\vec{S}$$

with eigenfunctions $|3/2\rangle$, $|1/2\rangle$, $|-1/2\rangle$, and $|-3/2\rangle$ for Cr, and $|1\rangle$, $|0\rangle$, and $|-1\rangle$ for V (the ^{51}V hyperfine coupling is essentially isotropic and equal to -55.5×10^{-4} cm^{-1}). With the field along the z-axis, using the Hamiltonian on the eigenfunctions gives for Cr(CN)$_6^{3-}$:

$$\hat{H}\left|\tfrac{3}{2}\right\rangle = \left[\tfrac{3}{2}\mu_{\mathrm{B}}g_zB + D\right]\left|\tfrac{3}{2}\right\rangle$$

$$\hat{H}\left|\tfrac{1}{2}\right\rangle = \left[\tfrac{1}{2}\mu_{\mathrm{B}}g_zB - D\right]\left|\tfrac{1}{2}\right\rangle$$

$$\hat{H}\left|-\tfrac{1}{2}\right\rangle = \left[-\tfrac{1}{2}\mu_{\mathrm{B}}g_zB - D\right]\left|-\tfrac{1}{2}\right\rangle$$

$$\hat{H}\left|-\tfrac{3}{2}\right\rangle = \left[-\tfrac{3}{2}\mu_{\mathrm{B}}g_zB + D\right]\left|-\tfrac{3}{2}\right\rangle$$

and for V(CN)$_6^{4-}$:

$$\hat{H}|1\rangle = \left[\mu_{\mathrm{B}}g_zB + \tfrac{1}{3}D\right]|1\rangle$$

$$\hat{H}|0\rangle = \left[-\tfrac{2}{3}D\right]|0\rangle$$

$$\hat{H}|-1\rangle = \left[-\mu_{\mathrm{B}}B + \tfrac{1}{3}D\right]|-1\rangle$$

Table 6.2 ESR parameters for two high-spin complexes[8]

Complex	D (cm^{-1})	E (cm^{-1})	g_x	g_y	g_z
$Cr(CN)_6^{3-}$	0.083	0.011	1.993	1.991	1.991
$V(CN)_6^{4-}$	−0.0264	−0.0972	1.9919	1.9920	1.9920
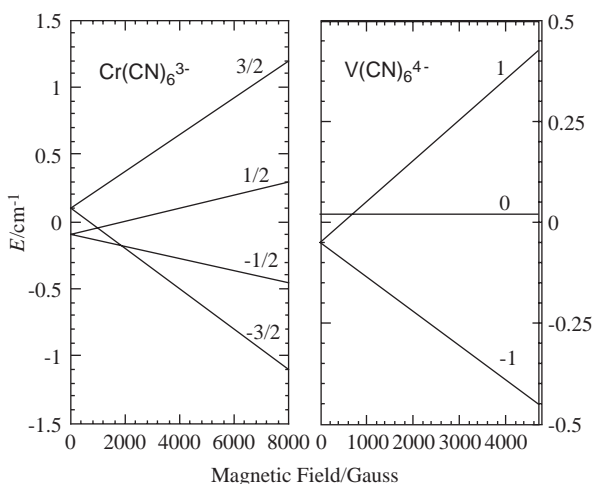
Figure 6.6 Energy levels for $Cr(CN)_6^{3-}$ and $V(CN)_6^{4-}$ for B along the z-axis.[8]

Substituting the values from Table 6.2 into these equations, we get the energy levels shown in Figure 6.6.

Given the measured positions of the transitions, the values of g_z and D can be determined. Orienting the field along x and y gives g_x, g_y, and E. Ligand-field theory was still in its infancy in 1956, so one of the goals of Baker, Bleaney, and Bowers[8] was a test of the theory – of course it passed with flying colors. In the same paper, $K_3Fe(CN)_6$ and $K_4Mn(CN)_6$ were also studied. With the CN^- ligand, which is high in the spectrochemical series, it was expected that both complexes would be low spin and, sure enough, they were.

Because the d^5 configuration is spherically symmetric, high-spin Mn(II) and Fe(III) usually have nearly isotropic g-matrices and Mn(II) usually has a nearly isotropic A-matrix. This means that there usually is not much information in the ESR spectrum of these high-spin species. Indeed, high-spin Mn(II) is usually an unwanted interference for those interested in low-spin Mn(II); the ESR spectrum is very characteristic with six hyperfine lines with a coupling constant of 80–100 G. Because the g- and A-matrices are nearly isotropic, the six-line spectrum persists in frozen solutions.

In part because the high-spin Mn(II) signal is so easily detected, several workers have doped Mn(II) into crystals for which a phase transition was indicated. Thus Das and Pal[9] have doped $CoSiF_6 \cdot 6H_2O$ and $Co_{1-x}Zn_x$-$SiF_6 \cdot 6H_2O$ with Mn(II), replacing some of the Co(II). For $CoSiF_6 \cdot 6H_2O$,

Table 6.3 ESR parameters for Mn(II) in $PbCl_2$[10]

	g	A^a	D^a	E^a
x	1.9996(2)	79.7(5)	463.8(1)	127.9(1)
y	2.0004(2)	79.6(2)		
z	2.003(1)	80.9(2)		

^{a} A, D, and E in units of 10^{-4} cm^{-1}. Estimated errors in last significant
   figure shown in parentheses.

following the ESR spectrum as a function of temperature, they found a change
in the dipolar parameter D from -176 to -274×10^{-4} cm^{-1} while the hyperfine
coupling changed from 93 to 96×10^{-4} cm^{-1}. These changes correlate with the
phase transition. The temperature of the phase transition depended on the
Mn(II) content; for $X_{Mn} = 0.082$ and 0.182, the transitions occurred at 205, 218
K and 175, 185 K, respectively.

   Hirota[10] reported a very similar experiment in which $PbCl_2$ was doped with
Mn(II). In this experiment, the goal was to study Mn(II) in an ionic medium.
The results are summarized in Table 6.3.

References

1. S.H. Glarum and J.H. Marshall, *J. Chem. Phys.*, 1967, **47**, 1374.
2. C.A. Hutchison and C.W. Mangum, *J. Chem. Phys.*, 1958, **29**, 952; 1961, **34**, 908.
3. J.S. Vincent and A.H. Maki, *J. Chem. Phys.*, 1965, **42**, 865.
4. J.S. Vincent and A.H. Maki, *J. Chem. Phys.*, 1964, **39**, 3088.
5. J. Grivet, *Chem. Phys. Lett.*, 1969, **4**, 104.
6. R.W. Brandon, R.E. Gerkin and C. A. Hutchison, *J. Chem. Phys.*, 1964, **41**, 3717.
7. O.H. Griffith, *J. Phys. Chem.*, 1965, **69**, 1429.
8. J.M. Baker, B. Bleaney and K.D. Bowers, *Proc. Phys. Soc.*, 1956, **B69**, 1205.
9. M. Das and A.K. Pal, *J. Phys. Chem. Solids*, 1987, **48**, 903.
10. T. Hirota, *Jpn. J. Appl. Phys.*, 1988, **27**, 493.

CHAPTER 7
Perturbation Theory Calculations

7.1 Second-order Perturbation Theory Treatment of Spin Hamiltonian with Non-coincident *g*- and *A*-axes

In Chapter 4 (Sections 4.7 and 4.8) several examples were presented to illustrate the effects of non-coincident *g*- and *A*-matrices on the ESR of transition metal complexes. Analysis of such spectra requires the introduction of a set of Eulerian angles, α, β, and γ, relating the orientations of the two coordinate systems. Here is presented a detailed description of how the spin Hamiltonian is modified, to second-order in perturbation theory, to incorporate these new parameters in a systematic way. Most of the calculations in this chapter were first executed by Janice DeGray.[1] Some of the details, in the notation used here, have also been published in ref. 8.

The key to success turns out to be taking careful account of the various axis systems (Table 7.1).

7.1.1 The Electron Zeeman Term

$$H = \mu_\mathrm{B} \vec{S} \cdot \bar{\bar{g}} \cdot \vec{B}$$

$\vec{S}$ is quantized along $\bar{\bar{g}} \cdot \vec{B}$ *i.e.*:

$$\vec{S} \cdot \bar{\bar{g}} \cdot \vec{B} = gBS_{z'}$$

Table 7.1 Various axis systems

Coordinate system	Coordinates
g-Matrix principal axes	*x*, *y*, *z*
A-Matrix principal axes	*X*, *Y*, *Z*
Electron spin quantization axes	*x'*, *y'*, *z'*
Nuclear spin quantization axes	*x''*, *y''*, *z''*

Since $S = (S_{x'}, S_{y'}, S_{z'})$, it is necessary that:

$$\bar{\bar{g}} \cdot \vec{B} = \begin{pmatrix} 0 \\ 0 \\ gB \end{pmatrix}$$

The x,y,z coordinate system is defined by the g-matrix principal axes:

$$\bar{\bar{g}} = \begin{pmatrix} g_x & 0 & 0 \\ 0 & g_y & 0 \\ 0 & 0 & g_z \end{pmatrix}$$

The magnetic field vector in that coordinate system is:

$$\vec{B} = \begin{pmatrix} B\sin\theta\cos\phi \\ B\sin\theta\sin\phi \\ B\cos\theta \end{pmatrix}$$

where θ and φ are the usual polar angles.

We therefore have:

$$\bar{\bar{g}} \cdot \vec{B} = \begin{pmatrix} g_x B\sin\theta\cos\phi \\ g_y B\sin\theta\sin\phi \\ g_z B\cos\theta \end{pmatrix}$$

The transformation from the x,y,z axes to x',y',z' (the axis system in which $\vec{S}$ is quantized) must then take this form to:

$$\bar{\bar{g}} \cdot \vec{B} = \begin{pmatrix} g_x B\sin\theta\cos\phi \\ g_y B\sin\theta\sin\phi \\ g_z B\cos\theta \end{pmatrix} \Rightarrow \begin{pmatrix} 0 \\ 0 \\ gB \end{pmatrix}$$

$$\bar{\bar{Q}} \cdot \bar{\bar{g}} \cdot \vec{B} = \bar{\bar{Q}} \cdot \begin{pmatrix} g_x B\sin\theta\cos\phi \\ g_y B\sin\theta\sin\phi \\ g_z B\cos\theta \end{pmatrix} = \begin{pmatrix} 0 \\ 0 \\ gB \end{pmatrix}$$

where $\bar{\bar{Q}}$ is a transformation matrix corresponding to rotations of the axes by the Euler angles ζ (rotation about y-axis), ξ (rotation about new z-axis), χ (rotation about new y-axis) (Whittaker definitions[2,3]):

$$\bar{\bar{Q}} = \begin{pmatrix} Q_{11} & Q_{12} & Q_{13} \\ Q_{21} & Q_{22} & Q_{23} \\ Q_{31} & Q_{32} & Q_{33} \end{pmatrix}$$

where:

$$Q_{11} = \cos\zeta\cos\xi\cos\chi - \sin\zeta\sin\chi$$

$$Q_{12} = \sin\zeta\cos\xi\cos\chi + \cos\zeta\sin\chi$$

$$Q_{13} = -\sin\xi\cos\chi$$

$$Q_{21} = -\cos\zeta\cos\xi\sin\chi - \sin\zeta\cos\chi$$

$$Q_{22} = -\sin\zeta\cos\xi\sin\chi + \cos\zeta\cos\chi$$

$$Q_{23} = \sin\xi\sin\chi \quad Q_{31} = \cos\zeta\sin\xi$$

$$Q_{32} = \sin\zeta\sin\xi \quad Q_{33} = \cos\xi$$

Thus:

$$Q_{11}g_x\sin\theta\cos\varphi + Q_{12}g_y\sin\theta\sin\varphi + Q_{13}g_z\cos\theta = 0$$

$$Q_{21}g_x\sin\theta\cos\varphi + Q_{22}g_y\sin\theta\sin\varphi + Q_{23}g_z\cos\theta = 0$$

$$Q_{31}g_x\sin\theta\cos\varphi + Q_{32}g_y\sin\theta\sin\varphi + Q_{33}g_z\cos\theta = g$$

These equations are satisfied with:

$$g^2 = g_\perp^2\sin^2\theta + g_z^2\cos^2\theta$$

$$g_\perp^2 = g_x^2\cos^2\phi + g_y^2\sin^2\phi$$

if:

$$\cos\zeta = \frac{g_x}{g_\perp}\cos\phi \quad \sin\zeta = \frac{g_y}{g_\perp}\sin\phi$$

$$\cos\xi = \frac{g_z}{g}\cos\theta \quad \sin\xi = \frac{g_\perp}{g}\sin\theta$$

Note that the angle χ is left indeterminant by this transformation. This amounts to saying that S_x and S_y are not fixed in space by the quantization of $\vec{S}$ along $\bar{g}\vec{B}$. The above result was used in deriving eqn (4.4) in Chapter 4.

7.1.2 Nuclear Hyperfine Interaction

$$H_{\text{hf}} = \vec{S}\cdot\bar{\bar{A}}\cdot\vec{I}$$

where the principal axes of A are (X, Y, Z), which are related to the principal axes of g by the transformation matrix $\bar{\bar{R}}$, which depends in the Euler angles α, β, and γ in the same way that $\bar{\bar{Q}}$ depends on ζ, ξ, and χ. Following Blinder,[4] we assume that $\vec{I}$ is quantized along the effective or resultant field due to the applied field B and the hyperfine field due to the unpaired electron:

$$\vec{B}_{\text{hf}} = \vec{S}\cdot\bar{\bar{A}}$$

To a first approximation, we neglect $\vec{B}$ compared with $\vec{B}_{\text{hf}}$. For $B \approx 3000$ G, *i.e.* X-band ESR, this will be a good approximation for most metal nuclei and for protons or fluorines with hyperfine couplings greater than *ca.* 20 G.

We label the nuclear spin quantization axes (x'', y'', z'') and require that the $S_{z'}$ term has the form $KS_{z'}I_z$.

The hyperfine term may be written in the (x',y',z') system:

$$H_{\mathrm{hf}} = \vec{S} \cdot \overline{\overline{Z}} \cdot \vec{I}$$

where:

$$\overline{\overline{Z}} = \overline{\overline{S}}^{-1} \cdot \overline{\overline{A}} \cdot \overline{\overline{S}} \qquad \overline{\overline{S}} = \overline{\overline{Q}} \cdot \overline{\overline{R}}$$

That is, matrix $\overline{\overline{R}}$ transforms from (X,Y,Z) to (x,y,z) and matrix $\overline{\overline{Q}}$ transforms from (x,y,z) to (x',y',z'), so that matrix $\overline{\overline{S}}$ transforms from (X,Y,Z) to (x',y',z'). In the (x',y',z') coordinate system:

$$
\begin{aligned}
\vec{S} \cdot \overline{\overline{Z}} \cdot \vec{I} = & S_{x'}\left(Z_{11}I_{x'} + Z_{12}I_{y'} + Z_{13}I_{z'}\right) \\
& + S_{y'}\left(Z_{21}I_{x'} + Z_{22}I_{y'} + Z_{23}I_{z'}\right) \\
& + S_{z'}\left(Z_{31}I_{x'} + Z_{32}I_{y'} + Z_{33}I_{z'}\right)
\end{aligned}
$$

In the nuclear spin quantization axis system, the last term has the form, $KS_{z'}I_{z''}$ where K is the effective hyperfine coupling for the particular orientation. Thus:

$$I_{z''} = \frac{1}{K}\left(Z_{31}I_{x'} + Z_{32}I_{y'} + Z_{33}I_{z'}\right)$$

where:

$$K^2 = Z_{31}^2 + Z_{32}^2 + Z_{33}^2$$

As it happens, the only components of the S-matrix we will need to know (for the perturbation theory treatment) are S_{31}, S_{32} and S_{33}:

$$
\begin{aligned}
S_{31} = & Q_{31}R_{11} + Q_{32}R_{21} + Q_{33}R_{31} \\
= & \frac{g_x}{g}\sin\theta\cos\phi(\cos\alpha\cos\beta\cos\gamma - \sin\alpha\sin\gamma) \\
& + \frac{g_y}{g}\sin\theta\sin\phi(-\cos\alpha\cos\beta\sin\gamma - \sin\alpha\cos\gamma) \\
& + \frac{g_z}{g}\cos\theta\cos\alpha\sin\beta
\end{aligned} \qquad (7.1a)
$$

$$
\begin{aligned}
S_{32} = & Q_{31}R_{12} + Q_{32}R_{22} + Q_{33}R_{32} \\
= & \frac{g_x}{g}\sin\theta\cos\phi(\sin\alpha\cos\beta\cos\gamma + \cos\alpha\sin\gamma) \\
& + \frac{g_y}{g}\sin\theta\sin\phi(-\sin\alpha\cos\beta\sin\gamma + \cos\alpha\cos\gamma) \\
& + \frac{g_z}{g}\cos\theta\sin\alpha\sin\beta
\end{aligned} \qquad (7.1b)
$$

$$
\begin{aligned}
S_{33} = & Q_{31}R_{13} + Q_{32}R_{23} + Q_{33}R_{33} \\
= & -\frac{g_x}{g}\sin\theta\cos\phi\sin\beta\cos\gamma \\
& + \frac{g_y}{g}\sin\theta\sin\phi\,\sin\beta\sin\gamma + \frac{g_z}{g}\cos\theta\cos\beta
\end{aligned} \qquad (7.1c)
$$

Consider the matrix which transforms the $\vec{I}$ vector from the nuclear-spin into the electron-spin quantization axes:

$$\overline{\overline{Q}}_I \cdot \begin{pmatrix} I_{x''} \\ I_{y''} \\ I_{z''} \end{pmatrix} = \begin{pmatrix} I_{x'} \\ I_{y'} \\ I_{z'} \end{pmatrix}$$

where $\overline{\overline{Q}}_I$ can be written in terms of Euler angles α, β and γ. Since the hyperfine term can be written:

$$\begin{pmatrix} S_{x'} \\ S_{y'} \\ S_{z'} \end{pmatrix} \cdot \begin{pmatrix} Z_{11} & Z_{12} & Z_{13} \\ Z_{21} & Z_{22} & Z_{23} \\ Z_{31} & Z_{32} & Z_{33} \end{pmatrix} \cdot \begin{pmatrix} I_{x'} \\ I_{y'} \\ I_{z'} \end{pmatrix} =$$
$$\begin{pmatrix} S_{x'} \\ S_{y'} \\ S_{z'} \end{pmatrix} \cdot \begin{pmatrix} Z_{11} & Z_{12} & Z_{13} \\ Z_{21} & Z_{22} & Z_{23} \\ Z_{31} & Z_{32} & Z_{33} \end{pmatrix} \cdot \overline{\overline{Q}}_I \cdot \begin{pmatrix} I_{x''} \\ I_{y''} \\ I_{z''} \end{pmatrix}$$

we also have:

$$I_{x'} = (\cos \alpha \cos \beta \cos \gamma - \sin \alpha \sin \gamma) I_{x''}$$
$$+ (\sin \alpha \cos \beta \cos \gamma + \cos \alpha \sin \gamma) I_{y''} - \sin \beta \cos \gamma I_{z''}$$

$$I_{y'} = (- \cos \alpha \cos \beta \sin \gamma - \sin \alpha \cos \gamma) I_{x''}$$
$$+ (- \sin \alpha \cos \beta \sin \gamma + \cos \alpha \cos \gamma) I_{y''} + \sin \beta \sin \gamma I_{z''}$$

$$I_{z'} = \cos \alpha \sin \beta I_{x''} + \sin \alpha \sin \beta I_{y''} + \cos \beta I_{z''}$$

where:

$$\cos \alpha \sin \beta = Z_{31}/K$$

$$\sin \alpha \sin \beta = Z_{32}/K$$

$$\cos \beta = Z_{33}/K$$

Thus the angles α and β are determined, but γ (like χ) remains indeterminant. However, in this case we have a means of approximating γ. If Q_I were used to transform Z into the nuclear spin quantization axis system, the trace of the matrix would remain constant. We are multiplying Z from one side only, so that the trace is not necessarily invariant. However, we can write:

$$Z_{11}(\cos \alpha \cos \beta \cos \gamma - \sin \alpha \sin \gamma)$$
$$+ Z_{12}(- \cos \alpha \cos \beta \sin \gamma - \sin \alpha \cos \gamma) + Z_{13} \cos \alpha \sin \beta$$
$$+ Z_{21}(\sin \alpha \cos \beta \cos \gamma + \cos \alpha \sin \gamma)$$
$$+ Z_{22}(- \sin \alpha \cos \beta \sin \gamma + \cos \alpha \cos \gamma) + Z_{23} \sin \alpha \sin \beta$$
$$\approx Z_{11} + Z_{22} + Z_{33} - K$$

Collecting terms in $\cos \gamma$ and $\sin \gamma$:

$$A \cos \gamma + B \sin \gamma + Z_{13} \cos \alpha \sin \beta + Z_{23} \sin \alpha \sin \beta$$
$$\approx Z_{11} + Z_{22} + Z_{33} - K$$

where:

$$A = Z_{11} \cos \alpha \cos \beta$$
$$- Z_{12} \sin \alpha + Z_{21} \sin \alpha \cos \beta + Z_{22} \cos \alpha$$

$$B = - Z_{11} \sin \alpha - Z_{12} \cos \alpha \cos \beta$$
$$+ Z_{21} \cos \alpha - Z_{22} \sin \alpha \cos \beta$$

If this were not an approximation, we could evaluate the components of the Z-matrix, the angles α and β, and solve for γ. The nature of the approximation causes this approach to fail, but we can still look for the value of γ that brings the function closest to a solution. Differentiating with respect to γ, we have:

$$- A \sin \gamma + B \cos \gamma = 0$$

or:

$$\tan \gamma = \frac{B}{A}$$

In practice, we must check this result to make sure that we have a minimum and not a maximum. Now assume that the hyperfine term can be written in the form:

$$\vec{S} \cdot \overline{\overline{Z}} \cdot \vec{I} = \left(S_{x'} S_{y'} S_{z'} \right) \begin{pmatrix} D_x & E_x & F_x \\ D_y & E_y & F_y \\ 0 & 0 & K \end{pmatrix} \begin{pmatrix} I_{x''} \\ I_{y''} \\ I_{z''} \end{pmatrix}$$

$$\vec{S} \cdot \overline{\overline{Z}} \cdot \vec{I} = S_{x'} \left(D_x I_{x''} + E_x I_{y''} + F_x I_{z''} \right)$$
$$+ S_{y'} \left(D_y I_{x''} + E_y I_{y''} + F_y I_{z''} \right) + K S_{z'} I_{z''}$$

Given values of α, β and γ, calculation of the new parameters D_x, D_y, E_x, E_y, F_x and F_y is straightforward using perturbation theory.

7.1.3 Perturbation Theory Treatment of Hyperfine Term

If we expand the hyperfine term of the spin Hamiltonian and write the operators in terms of raising and lowering operators:

$$S_\pm = S_{x'} \pm i S_{y'} \quad I_\pm = I_{x''} \pm i I_{y''}$$

$$H_{\text{hf}} = KS_{z'}I_{z''} + \tfrac{1}{2}\left(F_x - iF_y\right)S_+I_{z''} + \tfrac{1}{2}\left(F_x + iF_y\right)S_-I_{z''}$$
$$+ \tfrac{1}{4}\left[\left(D_x - E_y\right) - i\left(D_y + E_x\right)\right]S_+I_+$$
$$+ \tfrac{1}{4}\left[\left(D_x - E_y\right) + i\left(D_y + E_x\right)\right]S_-I_-$$
$$+ \tfrac{1}{4}\left[\left(D_x + E_y\right) - i\left(D_y - E_x\right)\right]S_+I_-$$
$$+ \tfrac{1}{4}\left[\left(D_x + E_y\right) + i\left(D_y - E_x\right)\right]S_-I_+$$

The unperturbed and perturbation Hamiltonians then are:

$$H_0 = g\mu_{\text{B}}BS_{z'} + KS_{z'}I_{z''}$$

$$H_1 = \tfrac{1}{2}\left(F_x - iF_y\right)S_+I_{z''} + \tfrac{1}{2}\left(F_x + iF_y\right)S_-I_{z''}$$
$$+ \tfrac{1}{4}\left[\left(D_x - E_y\right) - i\left(D_y + E_x\right)\right]S_+I_+ + \tfrac{1}{4}\left[\left(D_x - E_y\right) + i\left(D_y + E_x\right)\right]S_-I_-$$
$$+ \tfrac{1}{4}\left[\left(D_x + E_y\right) - i\left(D_y - E_x\right)\right]S_+I_- + \tfrac{1}{4}\left[\left(D_x + E_y\right) + i\left(D_y - E_x\right)\right]S_-I_+$$

Operating on the zero-order wavefunctions:

$$\left|\tfrac{1}{2}, m_s; I, m_I\right\rangle$$

we have

$$H_0\left|\tfrac{1}{2}, m_s; I, m_I\right\rangle = (g\mu_{\text{B}}BS_{z'} + KS_{z'}I_{z''})\left|\tfrac{1}{2}, m_s; I, m_I\right\rangle$$
$$= (m_s g\mu_{\text{B}}B + m_s m_I K)\left|\tfrac{1}{2}, m_s; I, m_I\right\rangle$$

$$H_1\left|\tfrac{1}{2}, m_s; I, m_I\right\rangle$$
$$= \left[\tfrac{1}{2}\left(F_x - iF_y\right)S_+I_{z''} + \tfrac{1}{2}\left(F_x + iF_y\right)S_-I_{z''}\right]\left|\tfrac{1}{2}, m_s; I, m_I\right\rangle$$
$$+ \tfrac{1}{4}\left[\left(D_x - E_y\right) - i\left(D_y + E_x\right)\right]S_+I_+\left|\tfrac{1}{2}, m_s; I, m_I\right\rangle$$
$$+ \tfrac{1}{4}\left[\left(D_x - E_y\right) + i\left(D_y + E_x\right)\right]S_-I_-\left|\tfrac{1}{2}, m_s; I, m_I\right\rangle$$
$$+ \tfrac{1}{4}\left[\left(D_x + E_y\right) + i\left(D_y - E_x\right)\right]S_-I_+\left|\tfrac{1}{2}, m_s; I, m_I\right\rangle$$
$$+ \tfrac{1}{4}\left[\left(D_x + E_y\right) - i\left(D_y - E_x\right)\right]S_+I_-\left|\tfrac{1}{2}, m_s; I, m_I\right\rangle$$

$$H_1\left|\tfrac{1}{2}, \tfrac{1}{2}; I, m_I\right\rangle = \left[\tfrac{m_I}{2}\left(F_x + iF_y\right)\right]\left|\tfrac{1}{2}, -\tfrac{1}{2}; I, m_I\right\rangle$$
$$+ \tfrac{1}{4}\left[\left(D_x - E_y\right) + i\left(D_y + E_x\right)\right]$$
$$\times \left[I(I + 1) - m_I(m_I - 1)\right]^{\frac{1}{2}}\left|\tfrac{1}{2}, -\tfrac{1}{2}; I, m_I - 1\right\rangle$$
$$+ \tfrac{1}{4}\left[\left(D_x + E_y\right) + i\left(D_y - E_x\right)\right]$$
$$\times \left[I(I + 1) - m_I(m_I + 1)\right]^{\frac{1}{2}}\left|\tfrac{1}{2}, -\tfrac{1}{2}; I, m_I + 1\right\rangle$$

$$H_1 \left| \tfrac{1}{2}, -\tfrac{1}{2}; I, m_I \right\rangle = \left[\frac{m_I}{2} \left(F_x - iF_y \right) \right] \left| \tfrac{1}{2}, \tfrac{1}{2}; I, m_I \right\rangle$$
$$+ \tfrac{1}{4} \left[(D_x - E_y) - i(D_y + E_x) \right]$$
$$\times \left[I(I+1) - m_I(m_I + 1) \right]^{\frac{1}{2}} \left| \tfrac{1}{2}, \tfrac{1}{2}; I, m_I + 1 \right\rangle$$
$$+ \tfrac{1}{4} \left[(D_x + E_y) - i(D_y - E_x) \right]$$
$$\times \left[I(I+1) - m_I(m_I - 1) \right]^{\frac{1}{2}} \left| \tfrac{1}{2}, \tfrac{1}{2}; I, m_I - 1 \right\rangle$$

Thus the significant matrix elements are:

$$\left\langle \tfrac{1}{2}, -\tfrac{1}{2}; I, m_I \left| H_1 \right| \tfrac{1}{2}, \tfrac{1}{2}; I, m_I \right\rangle = \frac{m_I}{2} \left(F_x + iF_y \right)$$

$$\left\langle \tfrac{1}{2}, -\tfrac{1}{2}; I, m_I - 1 \left| H_1 \right| \tfrac{1}{2}, \tfrac{1}{2}; I, m_I \right\rangle$$
$$= \tfrac{1}{4} \left[(D_x - E_y) + i(D_y + E_x) \right] \sqrt{I(I+1) - m_I(m_I - 1)}$$

$$\left\langle \tfrac{1}{2}, -\tfrac{1}{2}; I, m_I + 1 \left| H_1 \right| \tfrac{1}{2}, \tfrac{1}{2}; I, m_I \right\rangle$$
$$= \tfrac{1}{4} \left[(D_x + E_y) + i(D_y - E_x) \right] \sqrt{I(I+1) - m_I(m_I + 1)}$$

$$\left\langle \tfrac{1}{2}, \tfrac{1}{2}; I, m_I \left| H_1 \right| \tfrac{1}{2}, -\tfrac{1}{2}; I, m_I \right\rangle = \frac{m_I}{2} \left(F_x - iF_y \right)$$

$$\left\langle \tfrac{1}{2}, \tfrac{1}{2}; I, m_I + 1 \left| H_1 \right| \tfrac{1}{2}, -\tfrac{1}{2}; I, m_I \right\rangle$$
$$= \tfrac{1}{4} \left[(D_x - E_y) - i(D_y + E_x) \right] \sqrt{I(I+1) - m_I(m_I + 1)}$$

$$\left\langle \tfrac{1}{2}, \tfrac{1}{2}; I, m_I - 1 \left| H_1 \right| \tfrac{1}{2}, -\tfrac{1}{2}; I, m_I \right\rangle$$
$$= \tfrac{1}{4} \left[(D_x + E_y) - i(D_y - E_x) \right] \sqrt{I(I+1) - m_I(m_I - 1)}$$

Thus the zero-, first-, and second-order energies are:

$$E_{\pm 1/2}^{(0)} = \pm \tfrac{1}{2} g \mu_B B \pm \tfrac{1}{2} K m_I$$

$$E_{\pm 1/2}^{(1)} = 0$$

$$E_{1/2}^{(2)} = \frac{m_I^2}{4hv} \left(F_x^2 + F_y^2 \right)$$
$$+ \frac{1}{16hv} \left[(D_x - E_y)^2 + (D_y + E_x)^2 \right] \left[I(I+1) - m_I(m_I - 1) \right]$$
$$+ \frac{1}{16hv} \left[(D_x + E_y)^2 + (D_y - E_x)^2 \right] \left[I(I+1) - m_I(m_I + 1) \right]$$

$$E^{(2)}_{-1/2} = -\frac{m_I^2}{4hv}\left(F_x^2 + F_y^2\right)$$

$$-\frac{1}{16hv}\left[\left(D_x - E_y\right)^2 + \left(D_y + E_x\right)^2\right]\left[I(I+1) - m_I(m_I+1)\right]$$

$$-\frac{1}{16hv}\left[\left(D_x + E_y\right)^2 + \left(D_y - E_x\right)^2\right]\left[I(I+1) - m_I(m_I-1)\right]$$

For the "allowed" transitions, $\Delta m_S = +1$, $\Delta m_I = 0$, the energy is:

$$\Delta E = hv = g\mu_B B + Km_I + \frac{m_I^2}{2hv}\left(F_x^2 + F_y^2\right)$$
$$+ \frac{m_I}{4hv}\left[D_x^2 + E_y^2 + D_y^2 + E_x^2\right]\left[I(I+1) - m_I^2\right] \tag{7.2}$$

Defining:

$$F_1 = F_x^2 + F_y^2$$

$$F_2 = D_x^2 + D_y^2 + E_x^2 + E_y^2$$

the transition energy can be written:

$$\Delta E = hv = g\mu_B B + Km_I + \frac{(2F_1 - F_2)m_I^2}{4hv} + \frac{F_2 I(I+1)}{4hv} \tag{7.3}$$

and the field:

$$B = \frac{hv}{g\mu_B} - \frac{Km_I}{g\mu_B} - \frac{(2F_1 - F_2)m_I^2 + F_2 I(I+1)}{4g\mu_B hv} \tag{7.4}$$

Thus we must express F_1 and F_2 in parameters of the original spin Hamiltonian.

Starting with the two ways of expressing the hyperfine Hamiltonian term, we equate the coefficients of $S_x{}'$, $S_y{}'$ and $S_z{}'$:

$$Z_{11}I_{x'} + Z_{12}I_{y'} + Z_{13}I_{z'} = D_x I_{x''} + E_x I_{y''} + F_x I_{z''}$$
$$Z_{21}I_{x'} + Z_{22}I_{y'} + Z_{23}I_{z'} = D_y I_{x''} + E_y I_{y''} + F_y I_{z''}$$
$$Z_{31}I_{x'} + Z_{32}I_{y'} + Z_{33}I_{z'} = K$$

or:

$$Z_{11}I_{x'} + Z_{12}I_{y'} + Z_{13}I_{z'} = D_x\left(a_1 I_{x'} + b_1 I_{y'} + c_1 I_{z'}\right)$$
$$+ E_x\left(a_2 I_{x'} + b_2 I_{y'} + c_2 I_{z'}\right)$$
$$+ F_x\left(a_3 I_{x'} + b_3 I_{y'} + c_3 I_{z'}\right)$$

$$Z_{21}I_{x'} + Z_{22}I_{y'} + Z_{23}I_{z'} = D_y\left(a_1 I_{x'} + b_1 I_{y'} + c_1 I_{z'}\right)$$
$$+ E_y\left(a_2 I_{x'} + b_2 I_{y'} + c_2 I_{z'}\right)$$
$$+ F_y\left(a_3 I_{x'} + b_3 I_{y'} + c_3 I_{z'}\right)$$

Equating coefficients of $I_{x'}$, $I_{y'}$ and $I_{z'}$, we have:

$$Z_{11} = D_x a_1 + E_x a_2 + F_x a_3$$
$$Z_{12} = D_x b_1 + E_x b_2 + F_x b_3$$
$$Z_{13} = D_x c_1 + E_x c_2 + F_x c_3$$

Squaring and summing:

$$Z_{11}^2 + Z_{12}^2 + Z_{13}^2 = D_x^2 \left(a_1^2 + b_1^2 + c_1^2\right)$$
$$+ E_x^2 \left(a_2^2 + b_2^2 + c_2^2\right) + F_x^2 \left(a_3^2 + b_3^2 + c_3^2\right)$$
$$+ 2D_x E_x (a_1 a_2 + b_1 b_2 + c_1 c_2)$$
$$+ 2D_x F_x (a_1 a_3 + b_1 b_3 + c_1 c_3)$$
$$+ 2E_x F_x (a_2 a_3 + b_2 b_3 + c_2 c_3)$$

or:

$$Z_{11}^2 + Z_{12}^2 + Z_{13}^2 = D_x^2 + E_x^2 + F_x^2$$

Similarly:

$$Z_{21}^2 + Z_{22}^2 + Z_{23}^2 = D_y^2 + E_y^2 + F_y^2$$

Since:

$$a_1 a_3 + b_1 b_3 + c_1 c_3 = 0, \quad c_1 = -\frac{a_1 a_3 + b_1 b_3}{c_3}$$

Thus:

$$Z_{11} = D_x a_1 + E_x a_2 + F_x a_3$$
$$Z_{12} = D_x b_1 + E_x b_2 + F_x b_3$$
$$Z_{13} = - D_x \left(\frac{a_1 a_3 + b_1 b_3}{c_3}\right) - E_x \left(\frac{a_2 a_3 + b_2 b_3}{c_3}\right) + F_x c_3$$

or:

$$a_3 Z_{11} = D_x a_1 a_3 + E_x a_2 a_3 + F_x a_3^2$$
$$b_3 Z_{12} = D_x b_1 b_3 + E_x b_2 b_3 + F_x b_3^2$$
$$c_3 Z_{13} = - D_x (a_1 a_3 + b_1 b_3) - E_x (a_2 a_3 + b_2 b_3) + F_x c_3^2$$

Summing, we have:

$$F_x = a_3 Z_{11} + b_3 Z_{12} + c_3 Z_{13}$$

or:

$$F_x = \frac{1}{K} (Z_{31} Z_{11} + Z_{32} Z_{12} + Z_{33} Z_{13})$$

Similarly:

$$F_y = \frac{1}{K}(Z_{31}Z_{21} + Z_{32}Z_{22} + Z_{33}Z_{23})$$

Expanding the Z matrix in terms of A_x, A_y and A_z and the components of the S-matrix, and simplifying making use of the orthonormality of rows of the S-matrix, we have:

$$Z_{33}Z_{13} + Z_{32}Z_{12} + Z_{31}Z_{11}$$
$$= A_x^2 S_{31} S_{11} + A_y^2 S_{32} S_{12} + A_z^2 S_{33} S_{13}$$

$$Z_{33}Z_{23} + Z_{32}Z_{22} + Z_{31}Z_{21}$$
$$= A_x^2 S_{31} S_{21} + A_y^2 S_{32} S_{22} + A_z^2 S_{33} S_{23}$$

Thus:

$$F_1 = F_x^2 + F_y^2 = \frac{1}{K^2}\left(A_x^4 S_{31}^2 + A_y^4 S_{32}^2 + A_z^4 S_{33}^2 - K^4\right) \tag{7.5}$$

$$K^2 = Z_{11}^2 + Z_{12}^2 + Z_{13}^2 = A_z^2 S_{13}^2 + A_y^2 S_{12}^2 + A_x^2 S_{11}^2$$

$$D_x^2 + E_x^2 = Z_{11}^2 + Z_{12}^2 + Z_{13}^2 - F_x^2$$

$$K^2\left(Z_{11}^2 + Z_{12}^2 + Z_{13}^2\right) - K^2 F_x^2$$
$$= (S_{33}S_2 - S_{32}S_3)^2 A_y^2 A_z^2$$
$$+ (S_{33}S_1 - S_{31}S_3)^2 A_x^2 A_z^2$$
$$+ (S_{32}S_1 - S_{31}S_2)^2 A_x^2 A_y^2$$

$$D_y^2 + E_y^2 = Z_{21}^2 + Z_{22}^2 + Z_{23}^2 - F_y^2$$

$$Z_{21}^2 + Z_{22}^2 + Z_{23}^2 = A_z^2 S_{23}^2 + A_y^2 S_{22}^2 + A_x^2 S_{21}^2$$

$$K^2\left(Z_{21}^2 + Z_{22}^2 + Z_{23}^2\right) - K^2 F_y^2$$
$$= (S_{33}S_{22} - S_{32}S_{23})^2 A_y^2 A_z^2$$
$$+ (S_{33}S_{21} - S_{31}S_{23})^2 A_x^2 A_z^2$$
$$+ (S_{32}S_{21} - S_{31}S_{22})^2 A_x^2 A_y^2$$

$$F_2 = \frac{1}{K^2}\Big[A_y^2 A_z^2\left(S_{33}^2 + S_{32}^2\right)$$
$$+ A_x^2 A_z^2\left(S_{33}^2 + S_{31}^2\right) + A_x^2 A_y^2\left(S_{32}^2 + S_{31}^2\right)\Big] \tag{7.6}$$

7.1.4 Example Application of these Results

Robert Pike has prepared various low-spin Mn(II) complexes. Figure 7.1 shows the ESR spectrum of $[Mn(CO)_2(PPh_3)(C_5H_5)]^+$ in frozen $CH_2Cl_2/C_2H_4Cl_2$ (see also Tables 7.2 and 7.3). Some of Pike's spectra, and an analysis of the spectrum simulated in Figure 7.1, have been published.[5]

   We will now see how to apply the equations derived above. As a first step, we notice that the ^{31}P coupling is virtually isotropic. Thus, things can be simplified by taking the average of the 5/2,1/2 and 5/2,−1/2 assignments, *etc.*:

   The next thing to notice is that the widely spaced features are very approximately equally spaced. This suggests that the *g*- and *A*-matrix principal axes are non-coincident. You might think that a simple application of the above equations would suffice for a complete analysis. It is not quite so simple, and a nonlinear least-squares program is required.[1,6] Table 7.4 shows the fitted parameters.
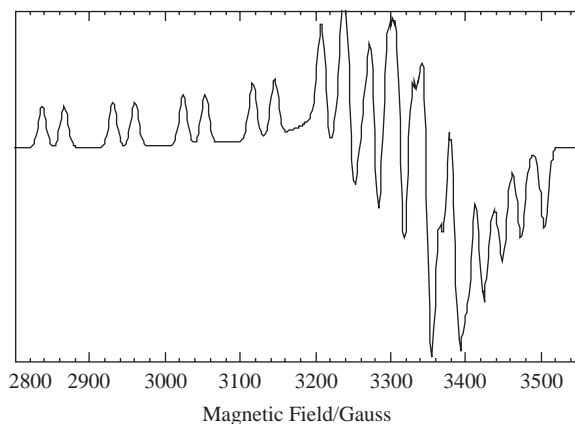
Figure 7.1   Frozen solution ESR spectrum ($v = 9.45$ GHz) of $[Mn(CO)_2(PPh_3)(C_5H_5)]^+$. Simulated using parameters in ref. 5.

Table 7.2   Measured line positions (m_{Mn}, m_P) for $[Mn(CO)_2(PPh_3)(C_5H_5)]^{+a}$

	5/2,1/2	3/2,1/2	1/2,1/2	−1/2,1/2	−3/2,1/2	−5/2,1/2
Min	2836.3	2930.4	3024.1	3116.1	3207.4	3295.3
Sp	3215.1	3246.5	3279.5	3314.0	3350.4	3388.3*
Max	3309.1*	3320.2	3340.6	3372.4	3417.1	3473.6

	5/2,−1/2	3/2,−1/2	1/2,−1/2	−1/2,−1/2	−3/2,−1/2	−5/2,−1/2
Min	2865.5	2959.6	3053.4	3145.9	3236.6	3324.6
Sp	3246.5	3277.8	3310.8	3245.5	3381.8	3419.7*
Max	3340.8*	3352.0	3372.4*	3404.3	3448.8	3505.1

[a] Min = minimum, Sp = saddle point, and Max = maximum; those indicated with an asterisk (*) are poorly resolved.

Table 7.3 Line positions for $[Mn(CO)_2(PPh_3)(C_5H_5)]^+$. Averaged over m_P[5]

m_{Mn}	Min	SP	Max
5/2	2850.94	3230.77	3324.94
3/2	2945.04	3262.15	3336.12
1/2	3038.68	3295.16	3356.51
−1/2	3131.28	3379.81	3388.34
−3/2	3222.05	3366.09	3432.99
−5/2	3309.96	3404.00	3489.34

Table 7.4 ESR parameters for $[Mn(CO)_2(PPh_3)(C_5H_5)]^{+5}$

	x	y	z
g	2.188	2.034	2.002
A^{Mn}	*ca.* 10	32.9	98.4
A^P	29.8	29.8	29.8
Euler angles (°)	$\alpha = 0$	$\beta = 73.9°$	$\gamma = 0$

7.2 Quadrupole Coupling

The spectra discussed in Chapter 4 were analyzed by neglecting the effects of nuclear quadrupole coupling on the nuclear hyperfine structure. Presented here is the way such effects may be incorporated into the spectra using perturbation theory.

The quadrupole coupling term in the spin Hamiltonian can be written as:

$$H_Q = \vec{I} \cdot \overline{\overline{P}} \cdot \vec{I}$$

where $\overline{\overline{P}}$ is the quadrupole coupling matrix:

$$\overline{\overline{P}} = \begin{pmatrix} -P(1-\eta) & 0 & 0 \\ 0 & -P(1+\eta) & 0 \\ 0 & 0 & 2P \end{pmatrix}$$

Assuming identical principal axes for $\overline{\overline{A}}$ and $\overline{\overline{P}}$, the Hamiltonian term would have the form in the (x'',y'',z'') coordinate system:

$$\vec{I} \cdot \overline{\overline{P}} \cdot \vec{I} = \left(I_{x''} I_{y''} I_{z''}\right) \begin{pmatrix} P_{11} & P_{12} & P_{13} \\ P_{12} & P_{22} & P_{23} \\ P_{13} & P_{23} & P_{33} \end{pmatrix} \begin{pmatrix} I_{x''} \\ I_{y''} \\ I_{z''} \end{pmatrix}$$

$$= P_{33}I_{z''}^2 - \frac{1}{4}P_{33}(I_+I_- + I_-I_+) + \frac{1}{2}(P_{13} + iP_{23})(I_-I_z + I_zI_-)$$

$$+ \frac{1}{2}(P_{13} - iP_{23})(I_+I_z + I_zI_+) - \frac{i}{2}P_{12}(I_+^2 - I_-^2)$$

$$+ \frac{1}{4}(P_{11} - P_{22})(I_+^2 + I_-^2)$$

Note that transformation by a general coordinate transformation matrix leaves the quadrupole matrix symmetrical, *i.e.*, $P_{ij} = P_{ji}$ and with zero trace, $P_{11} + P_{22} = -P_{33}$.

7.2.1 Perturbation Theory Treatment of Quadrupole Term

Operating on the spin functions, we have:

$$
\begin{aligned}
H_Q|I,m\rangle = {}&\tfrac{1}{2}P_{33}\left[3m^2 - I(I+1)\right]|I,m\rangle \\
&\times \tfrac{1}{2}(P_{13} + iP_{23})(2m-1)\sqrt{I(I+1) - m(m-1)}|I,m-1\rangle \\
&+ \tfrac{1}{2}(P_{13} - iP_{23})(2m+1)\sqrt{I(I+1) - m(m+1)}|I,m+1\rangle \\
&+ \tfrac{1}{4}(P_{11} - P_{22} - 2iP_{12})\sqrt{\left[I(I+1) - (m+1)^2\right]^2 - (m+1)^2}|I,m+2\rangle \\
&+ \tfrac{1}{4}(P_{11} - P_{22} + 2iP_{12})\sqrt{\left[I(I+1) - (m-1)^2\right]^2 - (m-1)^2}|I,m-2\rangle
\end{aligned}
$$

which leads to matrix elements:

$$
\langle I,m|H_Q|I,m\rangle = \tfrac{1}{2}P_{33}\left[3m^2 - I(I+1)\right]
$$

$$
\langle I,m-1|H_Q|I,m\rangle = \tfrac{1}{2}(P_{13} + iP_{23})(2m-1)\sqrt{I(I+1) - m(m-1)}
$$

$$
\langle I,m+1|H_Q|I,m\rangle = \tfrac{1}{2}(P_{13} - iP_{23})(2m+1)\sqrt{I(I+1) - m(m+1)}
$$

$$
\begin{aligned}
&\langle I,m+2|H_Q|I,m\rangle \\
&= \tfrac{1}{4}(P_{11} - P_{22} - 2iP_{12})\sqrt{\left[I(I+1) - (m+1)^2\right]^2 - (m+1)^2}
\end{aligned}
$$

$$
\begin{aligned}
&\langle I,m-2|H_Q|I,m\rangle \\
&= \tfrac{1}{4}(P_{11} - P_{22} + 2iP_{12})\sqrt{\left[I(I+1) - (m-1)^2\right]^2 - (m-1)^2}
\end{aligned}
$$

First- and second-order energy corrections then are:

$$
E^{(1)} = \tfrac{1}{2}P_{33}\left[3m^2 - I(I+1)\right]
$$

$$
\begin{aligned}
E^{(2)} = {}&\pm\frac{4m}{K}\left(P_{13}^2 + P_{23}^2\right)\left[I(I+1) - \left(2m^2 + \tfrac{1}{4}\right)\right] \\
&\mp\frac{m}{2K}\left[(P_{11} - P_{22})^2 + 4P_{12}^2\right]\left[I(I+1) - \left(m^2 + \tfrac{1}{2}\right)\right]
\end{aligned}
$$

where K is the angle-dependent hyperfine coupling defined in the previous section and the upper sign corresponds to $m_s = +1/2$, the lower to $-1/2$.

In the electron-spin quantization system (x',y',z'), the quadrupole interaction matrix is:

$$\begin{pmatrix} S_{11} & S_{12} & S_{13} \\ S_{21} & S_{22} & S_{23} \\ S_{31} & S_{32} & S_{33} \end{pmatrix} \begin{pmatrix} -P(1-\eta) & 0 & 0 \\ 0 & -P(1+\eta) & 0 \\ 0 & 0 & 2P \end{pmatrix} \begin{pmatrix} S_{11} & S_{21} & S_{31} \\ S_{12} & S_{22} & S_{32} \\ S_{13} & S_{23} & S_{33} \end{pmatrix}$$

Since we can transform from the (x',y',z') coordinate system into (x'',y'',z'') by:

$$\begin{pmatrix} I_{x''} \\ I_{y''} \\ I_{z''} \end{pmatrix} = \begin{pmatrix} a_1 & b_1 & c_1 \\ a_2 & b_2 & c_2 \\ a_3 & b_3 & c_3 \end{pmatrix} \begin{pmatrix} I_{x'} \\ I_{y'} \\ I_{z'} \end{pmatrix}$$

the reverse transformation must be:

$$\begin{pmatrix} I_{x'} \\ I_{y'} \\ I_{z'} \end{pmatrix} = \begin{pmatrix} a_1 & a_2 & a_3 \\ b_1 & b_2 & b_3 \\ c_1 & c_2 & c_3 \end{pmatrix} \begin{pmatrix} I_{x''} \\ I_{y''} \\ I_{z''} \end{pmatrix}$$

We next transform the $\bar{\bar{P}}$ matrix, using the a,b,c-matrix and compute P_{33}, $F_3 = P_{13}{}^2 + P_{23}{}^2$, and $F_4 = (P_{11} - P_{22})^2 + 4P_{12}{}^2$, simplifying the expressions using the relations:

$$a_1 b_1 + a_2 b_2 + a_3 b_3 = 0 \quad a_1 c_1 + a_2 c_2 + a_3 c_3 = 0$$
$$b_1 c_1 + b_2 c_2 + b_3 c_3 = 0 \quad a_1^2 + a_2^2 + a_3^2 = 1$$
$$b_1^2 + b_2^2 + b_3^2 = 1 \quad c_1^2 + c_2^2 + c_3^2 = 1$$
$$a_1 b_2 - a_2 b_1 = c_3 \quad a_1 c_2 - a_2 c_1 = -b_3$$
$$b_1 c_2 - b_2 c_1 = a_3$$

with similar expressions relating components of the S-matrices:

$$P_{33} = 3(c_3 S_{33} + b_3 S_{23} + a_3 S_{13})^2 P - P$$
$$+ (c_3 S_{31} + b_3 S_{21} + a_3 S_{11})^2 P\eta$$
$$- (c_3 S_{32} + b_3 S_{22} + a_3 S_{12})^2 P\eta$$

$$F_3 = 9 F_{3a} P^2 + F_{3b} P^2 \eta + F_{3c} P^2 \eta^2$$

$$F_{3a} = (c_3 S_{33} + b_3 S_{23} + a_3 S_{13})^2 - (c_3 S_{33} + b_3 S_{23} + a_3 S_{13})^4$$

$$F_{3b} = 2(c_3 S_{33} + b_3 S_{23} + a_3 S_{13})^2 \times \left[(c_3 S_{32} + b_3 S_{22} + a_3 S_{12})^2 \right.$$
$$\left. - (c_3 S_{31} + b_3 S_{21} + a_3 S_{11})^2 \right]$$

$$F_{3c} = (c_3 S_{32} + b_3 S_{22} + a_3 S_{12})^2$$
$$+ (c_3 S_{31} + b_3 S_{21} + a_3 S_{11})^2$$
$$- \left[(c_3 S_{32} + b_3 S_{22} + a_3 S_{12})^2 \right.$$
$$\left. -(c_3 S_{31} + b_3 S_{21} + a_3 S_{11})^2 \right]^2$$

$$F_4 = 9 F_{4a} P^2 + F_{4b} P\eta + F_{4c} P^2 \eta^2$$

$$F_{4a} = 1 - 2(c_3 S_{33} + b_3 S_{23} + a_3 S_{13})^2 + (c_3 S_{33} + b_3 S_{23} + a_3 S_{13})^4$$

$$F_{4b} = 2 \left[(a_3 S_{13} + b_3 S_{23} + c_3 S_{33})^2 + 1 \right]$$

$$F_{4c} = 4(a_3 S_{13} + b_3 S_{23} + c_3 S_{33})^2$$
$$+ \left[(a_3 S_{11} + b_3 S_{21} + c_3 S_{31})^2 \right.$$
$$\left. -(a_3 S_{12} + b_3 S_{22} + c_3 S_{32})^2 \right]^2$$

but:

$$c_3 S_{31} + b_3 S_{21} + a_3 S_{11} = \frac{A_x S_{31}}{K}$$

$$c_3 S_{32} + b_3 S_{22} + a_3 S_{12} = \frac{A_y S_{32}}{K}$$

$$c_3 S_{33} + b_3 S_{23} + a_3 S_{13} = \frac{A_z S_{33}}{K}$$

Finally:

$$F_i = P^2 \left(9 F_{ia} + 3\eta F_{ib} + \eta^2 F_{ic} \right)$$

$$P_{33} = \frac{P}{K^2} \left[2 A_z^2 S_{33}^2 - A_\perp^2 (1 - S_{33}^2) + \eta \left(A_x^2 S_{31}^2 - A_y^2 S_{32}^2 \right) \right]$$

$$F_3 = \frac{P^2}{K^4} \left[(9 + \eta^2) A_\perp^2 A_z^2 S_{33}^2 (1 - S_{33}^2) \right.$$
$$\left. + 6\eta A_z^2 S_{33}^2 \left(A_y^2 S_{32}^2 - A_x^2 S_{31}^2 \right) + 4\eta^2 A_x^2 S_{31}^2 A_y^2 S_{32}^2 \right]$$

$$F_4 = \frac{P^2}{K^4} \left[9 A_\perp^4 (1 - S_{33}^2)^2 + 6\eta \left(A_x^2 S_{31}^2 - A_y^2 S_{32}^2 \right) (K^2 + A_z^2 S_{33}^2) \right.$$
$$\left. + \eta^2 \left(A_x^2 S_{31}^2 - A_y^2 S_{32}^2 \right)^2 + 4\eta^2 K^2 A_z^2 S_{33}^2 \right]$$

Putting together all the bits and pieces of the above perturbation theory treatment of quadrupole coupling effects, we arrive at the following equations:

$$B = B_0 - \frac{mK}{g\mu_B} - \frac{F_1 m^2}{2g^2 \mu_B^2 B} - \frac{F_2}{4g^2 \mu_B^2 B} \left[I(I+1) - m^2 \right]$$
$$+ \frac{8mF_3}{g\mu_B K} \left[I(I+1) - (2m^2 + \tfrac{1}{4}) \right]$$
$$- \frac{mF_4}{g\mu_B K} \left[I(I+1) - (m^2 + \tfrac{1}{2}) \right]$$

where:

$$K^2 = \frac{1}{g^2} \left[A_{zz}^2 g_z^2 \cos^2 \theta + \left(A_{xx}^2 g_x^2 \cos^2 \varphi + A_{yy}^2 g_y^2 \sin^2 \varphi \right) \sin^2 \theta \right]$$

$$F_1(x) = \frac{g_x^2 A_x^4 - K^4}{g^2 K^2}, F_1(y) = \frac{g_y^2 A_y^4 - K^4}{g^2 K^2}, F_1(z) = \frac{g_z^2 A_z^4 - K^4}{g^2 K^2}$$

$$F_2(x) = \frac{g_x^2 A_x^4 \left(A_y^2 + A_z^2 \right)}{g^2 K^2} \quad F_2(y) = \frac{g_y^2 A_y^4 \left(A_x^2 + A_z^2 \right)}{g^2 K^2}$$

$$F_2(z) = \frac{g_z^2 A_z^4 \left(A_x^2 + A_y^2 \right)}{g^2 K^2}$$

$$F_3(x) = F_3(y) = P^2 \eta^2 \left(1 - \cos^2 2\alpha \right), F_3(z) = 0$$

$$F_4(x) = P^2 \left(9 + 6\eta \cos 2\alpha + \eta^2 \cos^2 2\alpha \right)$$
$$F_4(y) = P^2 \left(9 - 6\eta \cos 2\alpha + \eta^2 \cos^2 2\alpha \right)$$
$$F_4(z) = 4P^2 \eta^2$$

7.2.2 Example Application of Analysis of Quadrupole Effects

The ESR spectrum of a Rh-Ir complex[7,8] is shown in Figure 7.2, together with a very satisfactory simulation.

Since ^{103}Rh has $I = 1/2$ and both isotopes of Ir have $I = 3/2$, we might have expected each g-component to be a quartet of doublets. The Rh coupling is barely visible on the high-field features, but there is no trace on the other two g-components; indeed, the low-field and mid-field components are more like 1:2:1 triplets than the expected 1:1:1:1 quartet.

We must first examine the predicted spacing of the expected quartet. The outer and inner spacings are given by:

$$\Delta B_{\text{outer}} = \frac{3K}{g\mu_B} + \frac{24F_3}{g\mu_B K} + \frac{3F_4}{g\mu_B K}$$

$$\Delta B_{\text{inner}} = \frac{K}{g\mu_B} - \frac{24F_3}{g\mu_B K} + \frac{3F_4}{g\mu_B K}$$

Assuming that the quadrupole matrix axes differ from the g-matrix axes by $\alpha = 45°$, F_3 and F_4 simplify to:

$$F_3(x) = F_3(y) = P^2 \eta^2, F_3(z) = 0$$
$$F_4(x) = F_4(y) = 9P^2, F_4(z) = 4p^2 \eta^2$$

Under these circumstances, the inner and outer quartet spacings are:

$$\Delta B_{\text{outer}}(x,y) = \frac{3K}{g\mu_B} + \frac{24P^2 \eta^2}{g\mu_B K} + \frac{27P^2}{g\mu_B K}$$

$$\Delta B_{\text{inner}}(x,y) = \frac{K}{g\mu_B} - \frac{24P^2 \eta^2}{g\mu_B K} + \frac{27P^2}{g\mu_B K}$$
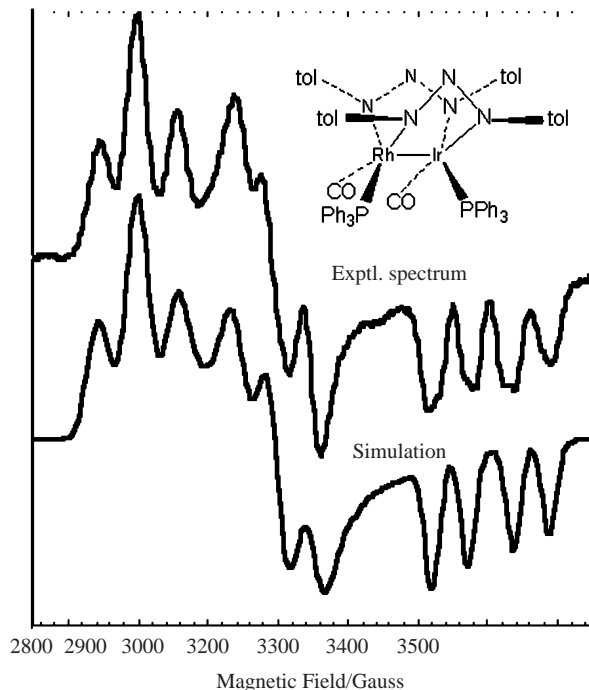
Figure 7.2   ESR spectrum of $[RhLL'\{\mu\text{-}(tol)NNN(tol)\}_2IrLL']^+ PF_6^-$ (tol $=$ p-MeC$_6$H$_4$, L $=$ CO, L' $=$ PPh$_3$).
(Reproduced with permission from ref. 7, copyright (2000) Royal Society of Chemistry. Simulation using methods of ref. 8.)

$$\Delta B_{outer}(z) = \frac{3K}{g\mu_B} + \frac{12P^2\eta^2}{g\mu_B K}$$

$$\Delta B_{inner}(z) = \frac{K}{g\mu_B} + \frac{12P^2\eta^2}{g\mu_B K}$$

Examination of these equations shows that the spacing of the z-component is expected to be a little bigger for the inner $(1/2, -1/2)$ spacing than $1/3$ the outer spacing. In contrast, the inner spacing of the x and y components is expected to be less than $1/3$ the outer spacing. This is entirely consistent with the experimental spectrum of Figure 7.2. Unfortunately, the effect is too big for perturbation theory to be entirely reliable, and it was necessary to perform a matrix diagonalization to get the exact solution of the spin Hamiltonian. For further details, see ref. 8.

One more item needs to be discussed in reference to this spectrum. Why did it turn out that $\alpha = 45°$? Consider the coordination geometry of the Ir atom (**1**).
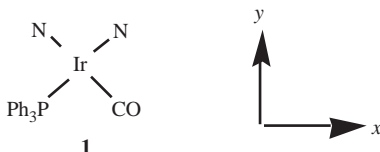
The Rh–Ir vector defines the *z*-axis, and the NN bridges define the *x*- and *y*-axes. The N and P atoms are solely electron donors, but the CO ligand involves a lot of π-back-bonding. Thus the quadrupole matrix, which has large components if there is an electric field gradient at the Ir nucleus, is rotated $45°$ compared with the *g*-matrix principal axes.

References

1. J.A. DeGray, PhD Thesis, Brown University, 1989.
2. H. Watanabe, *Operator Methods in Ligand Field Theory*, Prentice-Hall, Englewood Cliffs, 1966, p. 147.
3. E.B. Wilson, J.C. Decius and P.C. Cross, *Molecular Vibrations*, McGraw-Hill, New York, 1955, p. 286.
4. S.M. Blinder, *J. Chem. Phys.*, 1960, **33**, 748.
5. R.D. Pike, A.L. Rieger and P.H. Rieger, *J. Chem. Soc., Faraday Trans. I*, 1989, **85**, 3913.
6. (*a*) P.H. Rieger, *Specialist Periodical Reports*, *Electron Spin Resonance*, Royal Society of Chemistry, Cambridge, 1993, vol. 13b, ch. 4, p. 178; (*b*) J.A. DeGray and P.H. Rieger, *Bull. Mag. Reson.*, 1987, **8**, 95.
7. N.G. Connelly, O.D. Hayward, P. Klangsinsirikul, A.G. Orpen and P.H. Rieger, *Chem. Commun.*, 2000, 963.
8. N.G. Connelly, D.J.H. Emslie, P. Klangsinsirikul and P.H. Rieger, *J. Phys. Chem. A*, 2002, **106**, 12214.

APPENDIX 1
Physical Constants, Conversion Factors, and Properties of Nuclei (Tables A1.1–A1.4)

Table A 1.1   Physical constants

Name	Symbol	Value
Planck constant	h	6.62607×10^{-34} J s^1
Speed of light	c	2.99792×10^8 m s^{-1}
Avogadro's number	N_A	6.02214×10^{23} mol^{-1}
Boltzmann constant	k	1.38065×10^{-23} J K^{-1}
Bohr magneton	μ_B	9.27401×10^{-28} J G^{-1}
Nuclear magneton	μ_N	5.05078×10^{-31} J G^{-1}
Free electron g-value	g_e	2.002319304
Gas constant	R	8.31447 J mol^{-1} K^{-1}
Electronic charge	e	-1.60218×10^{-19} C
Electron mass	m_e	5.486×10^{-4} amu

Table A 1.2   Conversion factors

1 amu	1.66×10^{-24} g
1 Tesla	10 000 Gauss
10^{-4} cm^{-1}	1.9864×10^{-27} J
A/MHz	$2.8025 \ (g/g_e) \ a$/G
A/10^{-4} cm^{-1}	$0.93481 \ (g/g_e) \ a$/G

Table A1.3 Some properties of stable magnetic nuclei

Nucleus	I	% Abund.[a]	$10^4 A_s\ (cm^{-1})^b$	$10^4 P\ (cm^{-1})^b$	$\mu\ (nm)^a$	$10^{28}Q\ (m^2)^a$
^{1}H	1/2	99.985	473.8		2.7928	0
^{2}H	1	0.012			0.8574	0.00286
^{6}Li	1	7.5	30.7		0.8220	−0.0008
^{7}Li	3/2	92.4	121.7		3.2564	−0.041
^{9}Be	3/2	100.0	−150.6		−1.1776	0.0529
^{10}B	3	19.9	569	35.1	1.8006	0.085
^{11}B	3/2	80.1	850	52.4	2.6886	0.0406
^{13}C	1/2	1.11	1260	89.6	0.7024	0
^{14}N	1	99.63	604	46.3	0.40376	0.0200
^{15}N	1/2	0.37	−424	−32.5	−0.28319	0
^{17}O	5/2	0.04	−1755	−140.4	−1.8938	−0.026
^{19}F	1/2	100.0	2066	109.4	2.6289	0
^{23}Na	3/2	100.0	309.2		2.2175	0.104
^{25}Mg	5/2	10.0	−162.1		−0.8554	0.199
^{27}Al	5/2	100.0	1304	69.28	3.6415	0.1540
^{29}Si	1/2	4.683	−1532	−95.23	−0.5553	0
^{31}P	1/2	100.0	4438	305.9	1.1316	0
^{33}S	3/2	0.76	1155	83.82	0.6438	0.068
^{35}Cl	3/2	75.78	1909	146.4	0.82187	−0.083
^{37}Cl	3/2	24.22	1589	121.9	0.68412	−0.014
^{39}K	3/2	93.258	76.2		0.39146	0.049
^{41}K	3/2	7.730	41.8		0.21487	0.060
^{43}Ca	7/2	0.135	−213.7		−1.3173	−0.05
^{45}Sc	7/2	100.0	941.6	80.2	4.75649	−0.220
^{47}Ti	5/2	7.44	−260.8	−24.56	−0.78848	0.30
^{49}Ti	7/2	5.41	−365.2	−34.40	−1.10417	0.24
^{50}V	6	0.25	1120	117.7	3.3457	
^{51}V	7/2	99.75	1389	146.0	5.148706	−0.04
^{53}Cr	3/2	9.50	−249.6	−34.4	0.47464	−0.15
^{55}Mn	5/2	100.0	1680	207.5	3.4687	0.32
^{57}Fe	1/2	2.12	249.2	32.61	0.0906	0
^{59}Co	7/2	100.0	1984	282.0	4.63	0.41
^{61}Ni	3/2	1.140	−834	−125.2	−0.75002	0.16
^{63}Cu	3/2	69.17	2000	399.0	2.2233	−0.211
^{65}Cu	3/2	30.83	2142	427.0	2.3817	−0.195
^{67}Zn	5/2	4.1	696	117.3	0.8755	0.15
^{69}Ga	3/2	60.11	4073	170.0	2.01639	0.17
^{71}Ga	3/2	39.89	5176	216.0	2.56227	0.11
^{73}Ge	9/2	7.73	−788	−40.1	−0.87947	−0.17
^{75}As	3/2	100.0	4890	278.2	1.43947	0.31
^{77}Se	1/2	7.63	6711	410.0	0.53506	0
^{79}Br	3/2	50.69	10697	682.0	2.1064	0.331
^{81}Br	3/2	49.31	11529	735.0	2.2703	0.276
^{85}Rb	5/2	72.17	346		1.352	0.23
^{87}Rb	3/2	27.83	704		2.7512	0.15
^{87}Sr	9/2	7.00	−584.7		1.0936	0.34
^{89}Y	1/2	100.0	−417	−20.76	−0.13742	0
^{91}Zr	5/2	11.22	−91.8	−51.9	−1.30362	−0.21
^{93}Nb	9/2	100.0	2198	152.5	6.1705	−0.32
^{95}Mo	5/2	15.92	−662	−50.3	−0.9142	−0.02
^{97}Mo	5/2	9.55	−676	−51.3	−0.9335	0.26
^{99}Ru	5/2	12.76	−525	−47.5	−0.6413	0.079
^{101}Ru	5/2	17.06	−588	−53.3	−0.7188	0.46
^{103}Rh	1/2	100.0	−410	−40.4	−0.0884	0
^{105}Pd	5/2	22.33		−62.7	−0.642	0.66

Table A1.3   (*continued*)

Nucleus	I	% Abund.[a]	$10^4 A_s$ (cm^{-1})[b]	$10^4 P$ (cm^{-1})[b]	μ (nm)[a]	$10^{28} Q$ (m^2)[a]
^{107}Ag	1/2	51.84	−611	−68.3	−0.11357	0
^{109}Ag	1/2	48.16	−703	−78.6	−0.13069	0
^{111}Cd	1/2	12.80	−4553	−430.0	−0.59489	0
^{113}Cd	1/2	12.22	−4763	−450.0	−0.62230	0
^{113}In	9/2	4.29	6731	237.1	5.529	0.80
^{115}In	9/2	95.71	6746	236.6	5.541	0.81
^{117}Sn	1/2	7.68	−14002	−584.0	−1.0010	0
^{119}Sn	1/2	8.59	−14650	−611.0	−1.0473	0
^{121}Sb	5/2	57.21	11708	524.0	3.363	−0.4
^{123}Sb	7/2	42.79	8878	397.0	2.550	−0.5
^{125}Te	1/2	7.07	−18542	−875.0	−0.8885	0
^{127}I	5/2	100.0	13876	677.0	2.8133	−0.79
^{133}Cs	7/2	100.0	823		2.582	−0.004
^{135}Ba	3/2	6.59	1220		0.838	0.16
^{137}Ba	3/2	11.23	1324		0.9374	0.245
^{139}La	7/2	99.91	2004	79.1	2.7830	0.20
^{141}Pr	5/2	100.0	4166	295.1	4.275	−0.08
^{143}Nd	7/2	12.18	−793	−60.0	−0.67	−0.60
^{145}Nd	7/2	8.3	−481	−59.0	−0.66	−0.31
^{147}Sm	7/2	14.99	−672	−55.8	−0.815	−0.26
^{149}Sm	7/2	13.82	−554	−46.0	−0.672	0.075
^{151}Eu	5/2	47.81	1086	91.6	−0.872	0.90
^{153}Eu	5/2	52.19	1909	161.0	1.533	2.41
^{155}Gd	3/2	14.80	−647	−21.9	−2.59	1.30
^{157}Gd	3/2	15.65	−849	−28.78	−3.40	1.36
^{159}Tb	3/2	100.0	4546	417.0	2.014	1.43
^{161}Dy	5/2	18.9	−705	−65.1	−0.480	2.51
^{163}Dy	5/2	24.9	988	91.3	0.673	2.65
^{165}Ho	7/2	100.0	4523	429.0	4.17	3.49
^{167}Er	7/2	22.9	−645	−63.2	−0.5639	3.57
^{169}Tm	1/2	100.0	−1946	−195.3	−0.232	0
^{171}Yb	1/2	14.8	889	89.0	0.4937	0
^{173}Yb	5/2	16.1	−1224	−122.6	−0.6799	2.80
^{175}Lu	7/2	97.41	3546	93.2	2.2327	3.49
^{177}Hf	7/2	18.60	1471	41.4	0.7935	0.337
^{179}Hf	9/2	13.62	−1188	−33.4	−0.641	3.79
^{181}Ta	7/2	99.99	5010	148.6	2.370	3.3
^{183}W	1/2	14.31	1927	60.9	0.11778	0
^{185}Re	5/2	37.40	11718	382.0	3.1871	2.18
^{187}Re	5/2	62.60	11838	386.0	3.2197	2.07
^{187}Os	1/2	1.96	431.4	14.74	0.064652	0
^{189}Os	3/2	16.15	4403	150.4	0.65993	0.86
^{191}Ir	3/2	37.3	1072	37.8	0.151	0.82
^{193}Ir	3/2	62.7	1165	41.0	0.164	0.75
^{195}Pt	1/2	33.83	11478	492.0	0.6095	0
^{197}Au	3/2	100.0	959	44.0	0.14575	0.55
^{199}Hg	1/2	16.87	13969	537.4	0.50588	0
^{201}Hg	3/2	13.18	−15470	−595	−0.56023	0.39
^{203}Tl	1/2	29.52	60711	710	1.62226	0
^{205}Tl	1/2	70.48	61308	717.0	1.63822	0
^{207}Pb	1/2	22.1	27188	542.0	0.59258	0
^{209}Bi	9/2	100.0	25860	553.0	4.111	−0.37

[a] Ref. 1.
[b] Ref. 2.

Dipolar hyperfine coupling parameters for the transition metals and $(n + 1)$p-orbitals were computed from SCF Hartree–Fock–Slater atomic orbitals [3]. The parameter P is given by eqn (5) below, and $\langle r^{-3} \rangle_{nd}$ and $\langle r^{-3} \rangle_{(n+1)p}$ are given by eqns (1) and (3). The s-orbital contribution, responsible for the isotropic coupling, is given by eqn (3); Δn_d is the difference between the number of d-electrons present in the ion of interest and the number present in the neutral metal. Using these equations and the parameters given in Table A1.3, the P and isotropic coupling parameters can be computed for each of the transition metals (Table A1.4).

$$\langle r^{-3} \rangle_{nd} = A + B\Delta n_d + Cn_s + Dn_p \tag{1}$$

$$\frac{8\pi}{3} \left[\psi^2(0) \right]_{(n+1)s} = A + B\Delta n_d + Cn_s + Dn_p \tag{2}$$

$$\langle r^{-3} \rangle_{(n+1)p} = A + B\Delta n_d + Cn_s \tag{3}$$

$$F = \frac{g_e g_N \mu_0 \mu_B \mu_N}{4\pi h} \left(6.74834 \times 10^{30} \, \mathrm{au^3 m^{-3}} \right) \left(10^{-6} \, \mathrm{MHz\,s^{-1}} \right) \tag{4}$$

$$P = g_e g_N \mu_B \mu_N \langle r^{-3} \rangle \tag{5}$$

$$P = 4.180 \langle r^{-3} \rangle \times 10^{-4} \, \mathrm{cm^{-1}} \tag{5a}$$

Example

For Cr(II), $3d^{0.9}4s^{0.1}$:

$$\langle r^{-3} \rangle_{3d} = 3.99 - 0.517\,(-2.1) - 0.062\,(0.1) - 0.017\,(0.0) = 5.07$$

$$\left[\psi^2(0) \right]_{4s} = 47.8 - 16.0\,(-2.1) - 6.9\,(0.1) - 3.2\,(0.0) = 80.7$$

$$\langle r^{-3} \rangle_{4p} = 2.69 - 1.70\,(-2.1) - 0.97\,(0.1) = 6.16$$

Using eqn (5a):

$$P_{3d} = 21.2 \times 10^{-4} \, \mathrm{cm^{-1}}$$

$$P_{4p} = 25.7 \times 10^{-4} \, \mathrm{cm^{-1}}$$

Table A1.4   EPR hyperfine coupling parameters for the transition metals

Isotope	*I*	F^a		A^b	$-B^b$	$-C^b$	$-D^b$
^{47}Ti	5/2	−30.13	$\langle r^{-3}\rangle_{3d}$	2.554	0.444	0.057	0.009
^{49}Ti	7/2	−30.14	$[\psi^2(0)]_{4s}$	37.1	12.8	5.5(4)	2.7
			$\langle r^{-3}\rangle_{4p}$	2.15	1.37	0.76	–
^{50}V	6	53.26	$\langle r^{-3}\rangle_{3d}$	3.229	0.479	0.060	0.013
^{51}V	7/2	140.52	$[\psi^2(0)]_{4s}$	42.6	14.3	6.1	2.9
			$\langle r^{-3}\rangle_{4p}$	2.42	1.53	0.86	–
^{53}Cr	3/2	−30.22	$\langle r^{-3}\rangle_{3d}$	3.990	0.517	0.062	0.017
			$[\psi^2(0)]_{4s}$	47.8	16.0	6.9	3.2
			$\langle r^{-3}\rangle_{4p}$	2.69	1.70	0.97	–
^{55}Mn	5/2	132.53	$\langle r^{-3}\rangle_{3d}$	4.841	0.559	0.064	0.020
			$[\psi^2(0)]_{4s}$	53.6	17.8	7.6	3.4
			$\langle r^{-3}\rangle_{4p}$	2.96	1.88	1.08	–
^{57}Fe	1/2	17.31	$\langle r^{-3}\rangle_{3d}$	5.789	0.604	0.066	0.021
			$[\psi^2(0)]_{4s}$	59.8	9.7	8.5	3.7
			$\langle r^{-3}\rangle_{4p}$	3.23	2.07	1.19	–
^{59}Co	7/2	126.4	$\langle r^{-3}\rangle_{3d}$	6.840	0.650	0.067	0.024
			$[\psi^2(0)]_{4s}$	66.2	21.7	9.4	4.0
			$\langle r^{-3}\rangle_{4p}$	3.50	2.26	1.32	–
^{61}Ni	3/2	−47.76	$\langle r^{-3}\rangle_{3d}$	7.997	0.700	0.070	0.024
			$[\psi^2(0)]_{4s}$	73.1	23.7	0.3	4.3
			$\langle r^{-3}\rangle_{4p}$	3.77	2.45	1.44	–
^{63}Cu	3/2	141.58	$\langle r^{-3}\rangle_{3d}$	9.270	0.750	0.072	0.025
^{65}Cu	3/2	151.67	$[\psi^2(0)]_{4s}$	80.3	25.8	11.3	4.6
			$\langle r^{-3}\rangle_{4p}$	4.05	2.65	1.57	–
^{91}Zr	5/2	−49.81	$\langle r^{-3}\rangle_{4d}$	3.407	0.542	0.144	0.036
			$[\psi^2(0)]_{5s}$	75.7	21.3	10.3	4.8
			$\langle r^{-3}\rangle_{5p}$	3.70	2.03	1.20	–
^{93}Nb	9/2	130.98	$\langle r^{-3}\rangle_{4d}$	4.197	0.565	0.142	0.045
			$[\psi^2(0)]_{5s}$	86.1	24.2	11.5	5.4
			$\langle r^{-3}\rangle_{5p}$	4.14	2.27	1.35	–
^{95}Mo	5/2	−34.93	$\langle r^{-3}\rangle_{4d}$	5.04	0.591	0.140	0.050
^{97}Mo	5/2	−35.67	$[\psi^2(0)]_{5s}$	96.0	27.0	12.5	5.6
			$\langle r^{-3}\rangle_{5p}$	4.55	2.51	1.49	–
^{99}Tc	9/2	120.67	$\langle r^{-3}\rangle_{4d}$	5.951	0.619	0.137	0.053
			$[\psi^2(0)]_{5s}$	106.9	−30.4	14.2	6.5
			$\langle r^{-3}\rangle_{5p}$	4.93	2.76	1.64	–
^{99}Ru	5/2	−24.50	$\langle r^{-3}\rangle_{4d}$	6.929	0.648	0.134	0.054
^{101}Ru	5/2	−27.46	$[\psi^2(0)]_{5s}$	117.6	33.7	15.6	7.0
			$\langle r^{-3}\rangle_{5p}$	5.29	3.00	1.78	–
^{103}Rh	1/2	−16.89	$\langle r^{-3}\rangle_{4d}$	7.980	0.678	0.132	0.055
			$[\psi^2(0)]_{5s}$	128.5	37.2	17.0	7.6
			$\langle r^{-3}\rangle_{5p}$	5.64	3.24	1.93	–
^{105}Pd	5/2	−24.53	$\langle r^{-3}\rangle_{4d}$	9.107	−0.710	−0.129	−0.055
			$[\psi^2(0)]_{5s}$	139.7	−40.9	−18.6	−8.1
			$\langle r^{-3}\rangle_{5p}$	5.98	−3.49	−2.08	–
^{107}Ag	1/2	−21.70	$\langle r^{-3}\rangle_{4d}$	10.31	−0.744	−0.127	−0.054
^{109}Ag	1/2	−24.95	$[\psi^2(0)]_{5s}$	151.2	−44.8	−20.2	−8.7
			$\langle r^{-3}\rangle_{5p}$	6.30	−3.73	−2.22	–
^{177}Hf	7/2	21.66	$\langle r^{-3}\rangle_{5d}$	6.34	−0.99	−0.30	−0.07
^{179}Hf	9/2	−13.60	$[\psi^2(0)]_{6s}$	274	−73	−36	−16
			$\langle r^{-3}\rangle_{6p}$	6.80	−3.61	−2.21	–

Table A1. 4   (*continued*)

Isotope	I	F^a		A^b	$-B^b$	$-C^b$	$-D^b$
^{181}Ta	7/2	64.68	$\langle r^{-3}\rangle_{5d}$	7.51	−0.99	−0.29	−0.09
			$[\psi^2(0)]_{6s}$	310	−81	−40	−18
			$\langle r^{-3}\rangle_{6p}$	7.51	−3.96	−2.42	−
^{183}W	1/2	22.50	$\langle r^{-3}\rangle_{5d}$	8.72	−1.00	−0.28	−0.10
			$[\psi^2(0)]_{6s}$	345	−90	−44	−20
			$\langle r^{-3}\rangle_{6p}$	8.16	−4.30	−2.63	−
^{185}Re	5/2	121.77	$\langle r^{-3}\rangle_{5d}$	9.98	−1.02	−0.27	−0.11
^{187}Re	5/2	123.02	$[\psi^2(0)]_{6s}$	387	−103	−52	−25
			$\langle r^{-3}\rangle_{6p}$	8.77	−4.65	−2.84	−
^{187}Os	1/2	12.34	$\langle r^{-3}\rangle_{5d}$	11.30	−1.03	−0.26	−0.11
^{189}Os	3/2	42.02	$[\psi^2(0)]_{6s}$	417	−110	−53	−24
			$\langle r^{-3}\rangle_{6p}$	9.33	−4.98	−3.05	−
^{191}Ir	3/2	9.62	$\langle r^{-3}\rangle_{5d}$	12.68	−1.05	−0.26	−0.11
^{193}Ir	3/2	10.44	$[\psi^2(0)]_{6s}$	454	−120	−58	−26
			$\langle r^{-3}\rangle_{6p}$	9.85	−5.32	−3.26	−
^{195}Pt	1/2	116.44	$\langle r^{-3}\rangle_{5d}$	14.12	−1.08	−0.25	−0.11
			$[\psi^2(0)]_{6s}$	491	−131	−63	−27
			$\langle r^{-3}\rangle_{6p}$	10.34	−5.64	−3.45	−
^{197}Au	3/2	9.285	$\langle r^{-3}\rangle_{5d}$	15.64	−1.10	−0.24	−0.10
			$[\psi^2(0)]_{6s}$	530	−143	−68	−29
			$\langle r^{-3}\rangle_{6p}$	10.80	−5.97	−3.66	−

[a] Factor defined by eqn (4).
[b] Parameters A, B, C, D refer to eqns (1)–(3).

References

1. *Handbook of Chemistry and Physics*, ed. D. R. Lide, 83rd edn, CRC Press, Boca Raton, FL, 2002.
2. J.R. Morton and K.F. Preston, *J. Magn. Reson.*, 1978, **30**, 577.
3. P.H. Rieger, *J. Magn. Reson.*, 1997, **124**, 140.

APPENDIX 2
Advanced ESR Methods

For most of the 60 years since ESR was discovered, the vast majority of experiments have been carried out using CW spectrometers operating at the X-band frequency and employing conventional electromagnets. Indeed, most commercially available instruments are still of the general type described in Chapter 1, albeit with enhancements made possible by advancements in electronics, computers and, to some extent, microwave technology. The last two decades, however, have seen ever increasing development and applications of other ESR techniques. Most of these advanced methods fall into one of three broad categories:

- High field/multifrequency ESR
- Double resonance
- Pulsed methods

Although several of these methods were first applied in the 1950s and 1960s, none would have been possible at their current technical level using the post-World War II technology that gave rise to X-band ESR. In particular:

High frequency ESR has required not only the use of superconducting magnets, developed primarily for NMR, but even more importantly employs stable frequency sources and sensitive detectors in the millimeter and sub-millimeter range that have only recently become available.

Double resonance techniques, on the other hand, of which the earliest was ENDOR (described in Chapter 1), have greatly benefited from advances in signal processing technology, of the sort now employed, for example, in wireless communication systems.

Pulsed methods in ESR, which have by now taken over NMR instrumentation, have required the development of high power amplifiers and fast switches for microwave and higher frequency radiation.

One group of reviewers[1] has actually attributed much of the rapid development in all three categories to declassification of research in high frequency and communications technology that was an outgrowth of the end of the Cold War! The ready availability of this technology is also reflected in the fact that at least one supplier of commercial ESR equipment now offers a high field, pulsed,

double resonance spectrometer, *i.e.*, an instrument that incorporates advanced technology in all three categories.

The impact of these new methods has been felt particularly strongly in two areas:

(i) Improvements in effective resolution using high fields, double resonance, and pulsed methods have made possible the analysis and interpretation of spectra from increasingly complex paramagnetic materials, especially those of biological and solid state relevance.

(ii) Nanosecond pulsed methods have made possible the detection and characterization of various transient paramagnetic intermediates that could be previously studied by optical methods but were inaccessible to ESR. The latter application, which has led to advances in the understanding of reactive intermediates in photochemistry, radiation chemistry and other areas of mechanistic chemistry, is beyond the scope of this book. Reviews of these and other recent chemical applications of ESR have been written by Christopher Rhodes.[6,13]

Presented below are brief descriptions of some of the applications to structure analysis to which each of the three advanced methods are making important contributions. For the reader who wishes to learn more about these methods and applications a list of recent reviews and other leading references to these applications is also included. The titles of the papers that we have referenced will make it clear that we have tried to include applications of relevance not only to organometallic chemistry but also to biochemistry and related fields.

A2.1 High Frequency ESR

The two most obvious advantages of high frequency/high field spectrometers, better sensitivity and improved resolution of field-dependent features, which has revolutionized the field of high-resolution NMR, have proved to have less impact on ESR. For example, the smaller sample sizes that must be used when higher frequency, smaller wavelength, radiation is used have made it necessary in many cases to work with smaller numbers of spins and therefore not fully exploit the sensitivity advantage inherent in use of the higher frequency. Improved resolution with increasing frequency is also not a forgone conclusion, especially with randomly oriented samples. While it is certainly possible, for example, to detect smaller *g*-factor anisotropies at high fields, the first indication of such effects often appears as poorer resolution of individual features because of increased apparent line width as the anisotropy is revealed.

Nevertheless many recent studies simply could not have been carried out without the use of high frequency EPR. One of these is described below. In this,

and most other studies to date, custom-built equipment was necessary because no commercial instruments are available yet at very high frequencies.

A recent example of an application of high field ESR ("HF-EPR") is shown in Figure A2.1. The sample studied is a frozen aqueous solution of Cr^{2+} sulfate ($3d^4$, $S = 2$), cooled to 10 K.

This corresponds to an "EPR-silent" sample that gives no detectable ESR spectrum at X-band frequencies because it possesses a zero-field splitting larger than the Zeeman interaction (see Chapter 6), and the energy spacing between the two lowest levels is too large to be spanned by a microwave quantum at X-band. Nevertheless, higher frequencies are able to induce transitions. Since
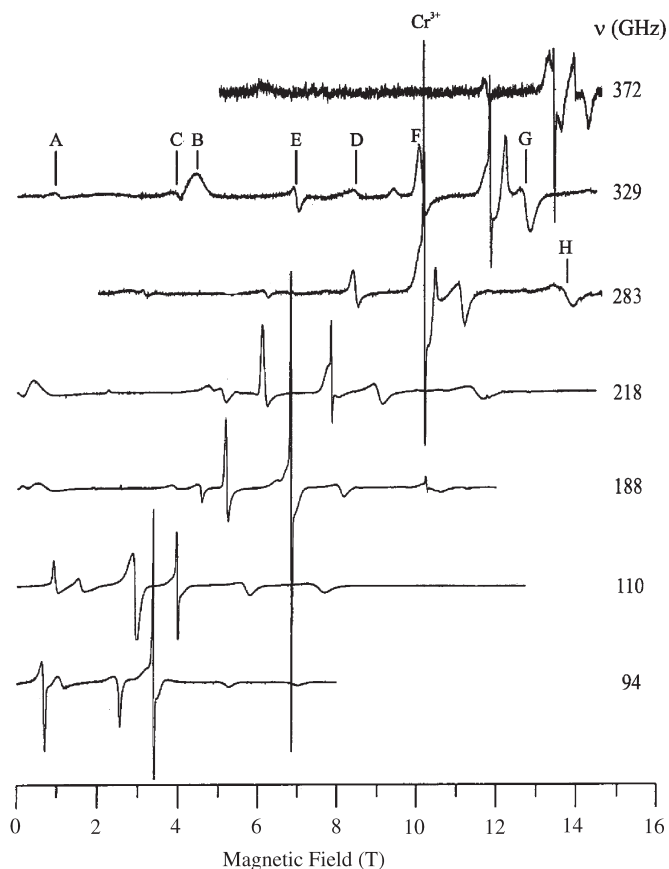
Figure A2.1 Microwave frequency dependent HF-EPR spectra of aqueous Cr^{2+} (0.1–0.2 M), sulfate counterion. Experimental conditions: temperature 10 K; microwave frequency as indicated. In the spectrum taken at 329 GHz a sharp signal from aqueous Cr^{3+} impurity at $g = 2$ is indicated and the resonances due to Cr^{2+} are labeled (Figure A2.2).
(Reprinted with permission from ref. 25, copyright (1998) American Chemical Society.)
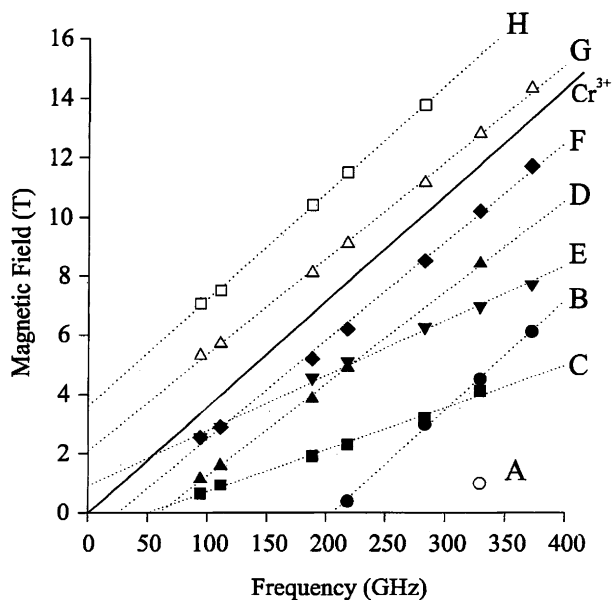
Figure A2.2 Plot of resonance field *versus* microwave frequency for data from Figure A2.1. Least squares fits are given for each Cr^{2+} resonance (dotted line) and for the Cr^{3+} impurity (solid line). C and E correspond to $\Delta m_S > 1$ while the rest correspond to $\Delta m_S = 1$.
(Reprinted with permission from ref. 25, copyright (1998) American Chemical society.)

the energy level scheme is quite complex, as shown in Figure A2.1 the spectrum varies markedly with frequency. Figure A2.2 shows the frequency dependence of the various spectral features.

Analysis of the spectra at different frequencies yielded the parameters $D = -2.20(5)$ cm^{-1}, $E = 0.0(1)$ cm^{-1}, and a nearly isotropic *g*-factor, $g = 1.98(2)$, none of which could have been determined at X-band. Analysis was aided by the observation of different slopes of the *B* vs. *v* plots for $\Delta m_S > 1$ and $\Delta m_S = 1$ transitions. A review of advanced methods, including high-field EPR, is given in ref. 11. Various recent applications of high field and multi-frequency EPR are described in refs 19–31.

A2.2   Double Resonance

In Chapter 2, ENDOR (electron–nuclear double resonance) was briefly described. To perform an ENDOR experiment it is necessary to apply both a radiofrequency and a microwave frequency, effectively performing simultaneous NMR and ESR, respectively, on the sample. The experiment is performed at a fixed magnetic field, with the ESR saturating frequency centered on a

spectral feature usually identified from a CW-ESR experiment. The RF field at the NMR frequency is then varied. When the RF frequency matches the appropriate NMR transition frequency the ESR absorption reappears. The number of observed lines is reduced, making it easier to detect small hyperfine splittings, even though the number of nuclei giving rise to the coupling is not revealed. Furthermore, one immediately knows from the NMR frequency what type of nucleus is involved. We saw, for example, in Chapter 2 that hyperfine patterns from ^{14}N and ^{1}H splittings can be quite similar and proper analysis of the spectrum requires recognition of subtle differences in peak intensities. This in turn demands resolution that is almost never available in randomly oriented samples. In the case of such samples, ENDOR is playing an increasingly important role since careful selection of the saturated features in the ESR spectrum leads to excitation of molecules over only a narrow range of orientations. This makes it possible to extract anisotropic spectral parameters that must otherwise be obtained using single crystals or laborious simulation of the full spectrum.[32–34,39,42,43] The relatively old technique of Dynamic Nuclear Polarization (DNP), originally proposed by Overhauser, in which the NMR spectrum is observed during irradiation of ESR transitions, is being rejuvenated as a method of enhancing the NMR spectra of solids.[35]

As discussed in Chapter 6, in systems with more than one unpaired electron the ESR spectrum contains features that involve electron–electron coupling parameters analogous to the nuclear hyperfine parameters. In those types of samples the advantages of double resonance are carried out by employing the use of two different microwave frequencies, one fixed and saturating, and one variable frequency that searches for transitions. This technique is known as ELDOR (electron–electron double resonance).[38,40,41,44] It has been used much less than ENDOR and usually requires custom-built equipment.

A major limitation of CW double resonance methods is the sensitivity of the intensities of the transitions to the relative rates of spin relaxation processes. For that reason the peak intensities often convey little quantitative information about the numbers of spins involved and, in extreme cases, may be undetectable. This limitation can be especially severe for liquid samples where several relaxation pathways may have about the same rates. The situation is somewhat better in solids, especially at low temperatures, where some pathways are effectively frozen out. Fortunately, fewer limitations occur when pulsed radio and microwave fields are employed. In that case one can better adapt the excitation and detection timing to the rates of relaxation that are intrinsic to the sample.[50] There are now several versions of pulsed ENDOR and other double resonance methods. Some of these methods also make it possible to separate in the time domain overlapping transitions that have different relaxation behavior, thereby improving the resolution of the spectrum.

A2.3 Pulsed Methods

The recent advent of the ability to apply short and very intense microwave pulses to samples and detect the fast response to the excitation has made it

possible to collect an ESR free-induction decay in the time domain and to Fourier transform the result and view the data in the frequency domain. Such experiments are an outgrowth of the pulsed methods commonly used to determine relaxation times. They mimic the ubiquitous pulsed methods that have revolutionized NMR. It has taken the ability to do this much longer to develop for ESR than for NMR, however, due both to the much shorter ESR relaxation times and to the much wider extent of ESR spectra in the frequency domain, both of which require shorter, more intense pulses and much faster detector response[8,16,18] than for pulsed NMR. Applications of Fourier-transform ESR, and related multiple-pulse two-dimensional techniques now common in NMR, are still in their infancy and require custom-built equipment.[47,48,54,55]

Nevertheless, there is one type of pulsed ESR measurement, the phenomenon of Electron Spin Echo Envelope Modulation (ESEEM) that is growing very rapidly and is in some instances replacing ENDOR as a way of extracting parameters from randomly oriented samples, since it can also be used to study weakly coupled nuclei, *i.e.*, cases where $A < 10$ MHz. Interestingly, the most robust version of the method works best in randomly oriented solids with overlapping lines. In its simplest form, the phenomenon appears as modulation of the intensity of the "echo" detected after a sequence of two pulses separated by a time τ, on the order of the reciprocal of a hyperfine coupling in frequency units, typically micro- to nanoseconds. This "envelope" has in it two sorts of information, an approximately exponential decay corresponding to the phase memory time, T_2, as well as information about the amplitude modulation by nuclear spin flips under the influence of A. For an ESEEM experiment to be successful the applied microwave pulse must be such that both allowed and semi-forbidden, *i.e.*, double quantum, transitions are excited. There must also be enough nuclear modulations within the time before the echo decays to define the observable values of A. ESEEM experiments are usually run on frozen samples at low temperatures both to lengthen decay times and to achieve the anisotropic effects that make the desired transitions possible. It is also necessary for the deadtime, the time needed between pulses before the detector can record new information, to be short compared with the time over which the modulations are observable. The echo intensity as a function of τ may then be Fourier transformed to yield a frequency domain "spectrum" that looks a lot like ENDOR. ESEEM experiments can also be performed using more than two pulses, giving somewhat greater flexibility in the range of relaxation times over which modulations can be observed. As with ENDOR, however, ESEEM spectra can be quite sensitive to relaxation behavior so that failure to observe a modulation does not prove the absence of a coupled nucleus. Several recent reviews of the technique are available.[2,9,12,14] ENDOR and ESEEM are also sometimes employed together.[46,49]

The combination of higher fields and pulsed, double resonance methods is now making it possible to use ESR as a tool to determine distances within macromolecules. This is a valuable supplement to the very widespread use of multi-dimensional NMR in structural biology.[33]

References

In developing this short bibliography of advanced ESR methods we have tried to select references primarily from widely available journals, review series and books published after 1990. We have therefore avoided references to meeting abstracts or highly specialized journals with low circulation or earlier publications where the methods were first demonstrated. Citations to these pioneering papers are found in the references.

   For ease of recognition of papers relevant to a particular method or application we have included the title of the review or paper within the citation. The references are grouped by topic and listed in reverse chronological order within each topic. They are numbered consecutively.

Books and Reviews

 1. High-field EPR, *Magn. Reson. Chem.*, *Special Issue*, ed. W. Lubitz, K. Mobius and K.-P. Dinse, 2005, **43**, S1–S266.
 2. G.R. Eaton and S.S. Eaton, Electron-nuclear double resonance spectroscopy and electron spin echo envelope modulation spectroscopy, *Comprehensive Coordination Chemistry II*, Elsevier, Boston, 2004, 49.
 3. C. Coulon and R. Clerac, Electron spin resonance: A major probe of molecular conductors, *Chem. Rev.*, 2004, **104**, 5655.
 4. *Biomedical EPR*, ed. S.S. Eaton, G.R. Eaton and L.J. Berliner, Kluwer Academic/Plenum Publishers, New York, 2004.
 5. L.J. Berliner, ed., *In vivo EPR (ESR): Theory and Applications*, Kluwer Academic/Plenum Publishers, New York, 2004.
 6. C.J. Rhodes, Electron spin resonance (some applications for the biological and environmental sciences), *Annu. Rep. Prog. Chem., Sec. C*, 2004 **100**, 149.
 7. *Paramagnetic Resonance of Metallobiomolecules*, ed. J. Telser, ACS Symposium Series, 858, American Chemical Society, 2003.
 8. T. Prisner, M. Rohrer and F. MacMillan, Pulsed EPR spectroscopy: Biological applications, *Annu. Rev. Phys. Chem.*, 2001, **52**, 279.
 9. N.D. Chasteen and P.A. Snetsinger, ESEEM and ENDOR spectroscopy, in *Physical Methods in Bioinorganic Chemistry, Spectroscopy and Magnetism*, ed. L. Que, Jr, University Science Books, Sausalito, CA, 2000.
10. G. Palmer, Electron paramagnetic resonance of metalloproteins, in *Physical Methods in Bioinorganic Chemistry, Spectroscopy and Magnetism*, ed. L. Que, Jr, University Science Books, Sausalito, CA, 2000.
11. J.H. Freed, New technologies in electron spin resonance, *Annu. Rev. Phys. Chem.*, 2000, **51**, 655.
12. Y. Deligiannakis, M. Louloudi and N. Hadjiliadis, Electron spin echo envelope modulation (ESEEM) spectroscopy as a tool to investigate the coordination environment of metal centers, *Coord. Chem. Rev.*, 2000, **204**, 1.
13. C.J. Rhodes, Electron spin resonance, *Annu. Rep. Prog. Chem., Sect. C*, 1999, **95**, 199.

14. J. McCracken, Electron spin echo modulation, in *Handbook of Electron Spin Resonance*, ed. C.P. Poole and H.A. Farach, Springer-Verlag, New York, 1999, vol. 2.

15. M. Ikeya, *New Applications of Electron Spin Resonance: ESR Dating, Dosimetry and Microscopy*, World Scientific Publishing Co., Singapore, 1993.

16. A. Schweiger, Pulsed electron spin resonance spectroscopy: Basic principles, techniques, and examples of applications, *Angew. Chem. Int. Ed. Engl.*, 1991, **30**, 265.

17. L.R. Dalton, A. Bain and C.J. Young, Recent advances in electron paramagnetic resonance, *Annu. Rev. Phys. Chem.*, 1990, **41**, 389.

18. *Modern Pulsed and Continuous-Wave Electron Spin Resonance*, ed. L. Kevan and M.K. Bowman, John Wiley and Sons, New York, 1990.

Selected Papers from the Recent Literature

High Field/Multifrequency EPR:

19. K. Möbius, A. Savitsky, A. Schnegg, M. Plato and M. Fuchs, High-field EPR spectroscopy applied to biological systems: Characterization of molecular switches for electron and ion transfer, *Phys. Chem. Chem. Phys.*, 2005, **7**, 19.

20. T.A. Konovalova, L.D. Kispert, J. van Tol and L.-C. Brunel, Multifrequency high-field electron paramagnetic resonance characterization of the peroxyl radical location in horse heart myoglobin oxidized by H_2O_2, *J. Phys. Chem. B*, 2004, **108**, 11820.

21. J. Krzystek, S.A. Zvyagin, A. Ozarowski, A.T. Fiedler, T.C. Brunold and J. Telser, Definitive spectroscopic determination of zero-field splitting in high-spin colbalt(II), *J. Am. Chem. Soc.*, 2004, **126**, 2148.

22. K.K. Andersson, P.P. Schmidt, B. Katterle, K.R. Strand, A.E. Palmer, S.-K. Lee, E.I. Solomon, A. Gräslund and A.-L. Barra, Examples of high-frequency EPR studies in bioinorganic chemistry, *J. Biol. Inorg. Chem.*, 2003, **8**, 235.

23. J. van Slageren, R. Sessoli, D. Gatteschi, A.A. Smith, M. Helliwell, R.E.P. Winpenny, A. Cornia, A.-L. Barra, A.G.M. Jansen, E. Rentschler and G.A. Timco, Magnetic anisotropy of the antiferromagnetic ring $[Cr_8F_8Piv_{16}]$, *Chem. Eur. J.*, 2002, **8**, 277.

24. Z. Liang and J.H. Freed, An assessment of the applicability of multifrequency ESR to study the complex dynamics of biomolecules, *J. Phys. Chem. B*, 1999, **103**, 6384.

25. J. Telser, L.A. Pardi, J. Krzystek and L.-C. Brunel, EPR spectra from EPR-silent species: High-field spectroscopy of aqueous chromium(II), *Inorg. Chem*, 1998, **37**, 5769.

26. D. Collison, M. Helliwell, V.M. Jones, F.E. Mabbs, E.J.L. McInnes, P.C. Riedi, G.M. Smith, R.G. Pritchard and W.I. Cross, Single and double quantum transitions in the multi-frequency continuous wave electron paramagnetic resonance (cwEPR) of three six-co-ordinate nickel(II) complexes:

[Ni(EtL)$_2$(Me$_5$dien)] and [Ni(5-methylpyrazole)$_6$]X$_2$, X = (ClO$_4$)$^-$ or (BF$_4$)$^-$. The single crystal X-ray structure at room temperature of [Ni(5-methyl-pyrazole)$_6$]ClO$_4$)$_2$, *J. Chem. Soc., Faraday Trans.*, 1998, **94**, 3019.

27. P.J.M. van Kan, E. van der Horst, E.J. Reijerse, P.J.M. van Bentum and W.R. Hagen, Multi-frequency EPR spectroscopy of myoglobin. Spectral effects for high-spin iron(III) at high magnetic fields, *J. Chem. Soc., Faraday Trans.*, 1998, **94**, 2975.

28. E.J.L. McInnes, F.E. Mabbs, S.M. Harben, P.D. Smith, D. Collison, C.D. Garner, G.M. Sith and P.C. Riedi, Single-crystal and multi-frequency EPR studies on chemical analogues of Amavadin″ V(IV)-doped Ca[Ti (hida)$_2$].6H$_2$O, and Mo(V)-doped [PPh$_4$][Nb(hida)$_2$] and [NEt$_4$][Ta (R,R-hidpa)$_2$] [H$_3$hida = 2,2′-(hydroxyimino)diacetic acid, H$_3$hidpa = 2,2′-(hydroxyimino)dipropionic acid], *J. Chem. Soc., Faraday Trans.*, 1998, **94**, 3013.

29. A. Klein, E.J.L. McInnes, T. Scheiring and S. Zalis, Electronic structure of radical anionic binuclear organoplatinum complexes. A multiple frequency EPR investigation, *J. Chem. Soc., Faraday Trans.*, 1998, **94**, 2979.

30. B. Cage, A.K. Hassan, L. Pard, J. Krzystek, L.-C. Brunel and N.S. Dalal, 375 GHz EPR measurements on undiluted Cr(V) salts. The role of exchange effects and g-strain broadening in determining resolution in high-field EPR spectroscopy of S = 1/2 paramagnets, *J. Magn. Reson.*, 1997, **124**, 495.

31. W.B. Lynch, R.S. Boorse and J.H. Freed, A 250-GHz ESR study of highly distorted manganese complexes, *J. Am. Chem. Soc.*, 1993, **115**, 10909.

Double Resonance:

32. J.C. Wilson, G. Wu, A.-I. Tsai and G.J. Gerfen, Determination of the structural environment of the tyrosyl radical in prostaglandin H$_2$ synthase-1: A high frequency ENDOR/EPR study, *J. Am. Chem. Soc.*, 2005, **127**, 1618.

33. (*a*) D. Goldfarb and D. Arieli, Spin distribution and the location of protons in paramagnetic proteins, *Annu. Rev. Biophys. Biomol. Struct.*, 2004, **33**, 441; (*b*) S.S. Eaton and G.R. Eaton, Measurement of interspin distances by EPR, *Electron Paramagnetic Reson.*, 2004, **19**, 318.

34. O.G. Poluektov, L.M. Utschig, A.A. Dubinskij and M. Thurnauer, ENDOR of spin-correlated radical pairs in photosynthesis at high magnetic field: A tool for mapping electron transfer pathways, *J. Am. Chem. Soc.*, 2004, **126**, 1644.

35. K.-N. Hu, H.-h. Yu, T.M. Swager and R.G. Griffin, Dynamic nuclear polarization with biradicals, *J. Am. Chem. Soc.*, 2004, **126**, 10844.

36. S. Sinnecker, E. Reijerse, F. Neese and W. Lubitz, Hydrogen bond geometries from paramagnetic resonance and electron-nuclear double resonance parameters: Density functional study of quinone radical anion-solvent interactions, *J. Am. Chem. Soc.*, 2004, **126**, 3280.

37. B.M. Hoffman, (*a*) Electron-nuclear double resonance spectroscopy (and electron-spin-echo envelope modulation spectroscopy) in bioinorganic

chemistry, *Proc. Natl. Acad. Sci. U.S.A.*, 2003, **100**, 3575; (*b*) ENDOR of metalloenzymes, *Acc. Chem. Res.*, 2003, **36**, 522.

38. M. Bennati, A. Weber, J. Antonic, D.L. Perlstein, J. Robblee and J. Stubbe, Pulsed ELDOR spectroscopy measures the distance between the two tyrosyl radicals in the R2 subunit of the E. coli ribonucleotide reductase, *J. Am. Chem. Soc.*, 2003, **125**, 14988.

39. J. Kang, S. Tokdemir, J. Shao and W.H. Nelson, Electronic g-factor measurement from ENDOR-induced EPR patterns: Malonic acid and guanine dihydrate, *J. Magn. Reson.*, 2003, **165**, 128.

40. H. Mino and T. Ono, Applications of pulsed ELDOR-detected NMR measurements to studies of photosystem II: Magnetic characterization of Y_D tyrosine radical and Mn^{2+} bound to the high-affinity site, *Appl. Magn. Reson.*, 2003, **23**, 571.

41. C. Elsasser, M. Brecht and R. Bittl, Pulsed electron-electron double resonance on multinuclear metal clusters: Assignment of spin projection factors bsed on the dipolar interaction, *J. Am. Chem. Soc.*, 2002, **124**, 12606.

42. S.K. Smoukov, J. Telser, B.A. Bernat, C.L. Rife, R.N. Armstrong and B.M. Hoffman, EPR study of substrate binding to the Mn(II) active site of the bacterial antibiotic resistance enzyme FosA: A better way to examine Mn(II), *J. Am. Chem. Soc.*, 2002, **124**, 2318.

43. A.R. Raitsimring and F.A. Walker, Porphyrin and ligand protons as internal labels for determination of ligand orientations in ESEEMS of low-spin d^5 complexes in glassy media: ESEEM studies of the orientation of the **g** tensor with respect to the planes of axial ligands and porphyrin nitrogens of low-spin ferriheme systems, *J. Am. Chem. Soc.*, 1998, **120**, 991.

Pulsed Methods:

44. C.W.M. Kay, C. Elsässer, R. Bittl, S.R. Farrell and C. Thorpe, Determination of the distance between the two neutral flavin radicals in augmenter of liver regeneration by pulsed ELDOR, *J. Am. Chem. Soc.*, 2006, **128**, 76.

45. H.-I. Lee, R.Y. Igarashi, M. Laryukhin, P.E. Doan, P.C. Dos Santos, D.R. Dean, L. C. Seefeldt and B.M. Hoffman, An organometallic intermediate during alkyne reduction by nitrogenase, *J. Am. Chem. Soc.*, 2004, **126**, 9563.

46. C. Finazzo, J. Harmer, B. Jaun, E.C. Duin, F. Mahlert, R.K. Thauer, S. Van Doorslaer and A. Schweiger, Characterization of the MCR_{red2} form of methyl-coenzyme M reductase: A pulse EPR and ENDOR study, *J. Biol. Inorg. Chem.*, 2003, **8**, 586.

47. J.M. Lu, J. Geimer, S. Naumov and D. Beckert, A Fourier transform EPR study of uracil and thymine radical anions in aqueous solution, *Phys. Chem. Chem. Phys.*, 2001, **3**, 952.

48. B. Epel and D. Goldfarb, Two-dimensional pulsed TRIPLE at 95 GHz, *J. Magn. Reson.*, 2000, **146**, 196.

49. S. Van Doorslaer, R. Bachmann and A. Schweiger, A pulse EPR and ENDOR investigation of the electronic and geometric structure of cobaltous tetraphenylporphyrin(pyridine), *J. Phys. Chem. A*, 1999, **103**, 5446.

50. M. Bennati, C.T. Farrar, J.A. Bryant, S.J. Inati, V. Weis, G.J. Gerfen, P. Riggs-Gelasco, J. Stubbe and R.G. Griffin, Pulsed electron-nuclear double resonance (ENDOR) at 140 GHz, *J. Magn. Reson.*, 1999, **138**, 232.

51. K. Fukui, Y. Fujisawa, H. Ohya-Nishiguchi, H. Kamada and H. Sakurai, In vivo coordination structural changes of a potent insulin-mimetic agent, bis(picolinato)oxovanadium(IV), studied by electron spin-echo modulation spectroscopy, *J. Inorg. Biochem.*, 1999, **77**, 215.

52. W.R. Hagen, W.A.M. van den Berg, W.M.A.M. van Dongen, E.J. Reijerse and P.J.M. van Kan, EPR spectroscopy of biological iron-sulfur clusters with spin-admixed S = 3/2 ground states, *J. Chem. Soc., Faraday Trans.*, 1998, **94**, 2969.

53. A.M. Raitsimring, P. Borbat, T. Kh. Shokjireva and F.A. Walker, Magnetic field (g-value) dependence of proton hyperfine couplings obrained from ESEEM measurements: Determination of the orientation of the magnetic axes of model heme complexes in glassy media, *J. Phys. Chem.*, 1996, **100**, 5235.

54. B.R. Patyal, R.H. Crepeau, D. Gamliel and J.H. Freed, Two-dimensional Fourier transform ESR in the slow-motional and rigid limits: SECSY-ESR, *Chem. Phys. Lett.*, 1990, **175**, 445.

55. B.R. Patyal, R.H. Crepeau, D. Gamliel and J.H. Freed, Two-dimensional Fourier transform ESR in the slow-motional and rigid limits: 2D-ELDOR, *Chem. Phys. Lett.*, 1990, **175**, 453.

Subject Index

Organometallic complexes have been indexed under their molecular formulae.